

Durham E-Theses

A spectroelectrochemical investigation of arylamine based hole transporting materials

Paterson, Michael A. J.

How to cite:

Paterson, Michael A. J. (2003) *A spectroelectrochemical investigation of arylamine based hole transporting materials*, Durham theses, Durham University. Available at Durham E-Theses Online: <http://etheses.dur.ac.uk/3704/>

Use policy

The full-text may be used and/or reproduced, and given to third parties in any format or medium, without prior permission or charge, for personal research or study, educational, or not-for-profit purposes provided that:

- a full bibliographic reference is made to the original source
- a [link](#) is made to the metadata record in Durham E-Theses
- the full-text is not changed in any way

The full-text must not be sold in any format or medium without the formal permission of the copyright holders.

Please consult the [full Durham E-Theses policy](#) for further details.

A Spectroelectrochemical Investigation of Arylamine Based Hole Transporting Materials

by

Michael A. J. Paterson, M.Sci. (Dunelm)

Ustinov College, University of Durham

A thesis submitted in part fulfilment of the requirements for the
degree of Doctor of Philosophy at the University of Durham

September 2003

**A copyright of this thesis rests
with the author. No quotation
from it should be published
without his prior written consent
and information derived from it
should be acknowledged.**



1 2 MAR 2004

Statement of Copyright

The copyright of this thesis rests with the author. No quotation from it should be published without his prior written consent and information derived from it should be acknowledged.

Declaration

The work described in this thesis was carried out at the University of Durham, Department of Chemistry, between October 2000 and September 2003. All the work is my own unless stated otherwise, and it has not been submitted previously for a degree at this or any other university.

Financial Support

The Engineering and Physical Science Research Council (EPSRC) and Avecia are gratefully acknowledged for providing funding for the work described herein.

Abstract

A Spectroelectrochemical Investigation of Arylamine Based Hole Transporting Materials

This thesis describes exploratory synthetic, structural and electrochemical studies into the molecular and electronic structures of arylamine based hole transporting materials. The principle objectives in these studies were to increase understanding of the electronic structures of the materials involved and to investigate the effect of various substitution patterns on the chemical stability and electronic structure of these materials.

Chapter Summary

Chapter One: *Introduction to Arylamines and their Applications* highlights the industrial applications and importance of the materials studied in this thesis, and introduces the physical and electronic properties required of such materials. Previously studied materials and their properties are also reviewed.

Chapter Two: *Concepts and Techniques* introduces the concept of mixed valence compounds and explains the theory behind this description. The various electrochemical and spectroscopic techniques employed throughout this study are also described here.

Chapter Three: *Triarylamines and Tetra Aryl Biphenyl Diamines* introduces the structural and electrochemical characterisation of triarylamines and *N,N,N',N'*-tetraaryl-1,1'-biphenyl-4,4'-diamines and the analysis and assignment of the electronic structures, both in terms of molecular orbitals and mixed valence materials.

Chapter Four: *Studies of the Molecular Conformation* expands on ideas developed in Chapter Three and describes the synthesis, characterisation and study of *N,N,N',N'*-tetraaryl-1,1'-biphenyl-4,4'-diamines which are conformationally restricted due to their substitution patterns. The effect of these restrictions on the oxidation potential and electronic structure is analysed.

Chapter Five: *Trimeric and oligomeric systems* explores the synthesis and study of trimeric and oligomeric derivatives of triarylamine, concentrating on the effects of various substituents on the chemical stability and electronic structure of the materials across the range of accessible oxidation states.

Chapter Six: *Electrochemical Polymerisation reactions* expands on the study of chemical reactivity of triarylamine derivatives initiated in Chapter Five, covering synthesis of reactive monomers and subsequent polymerisation reactions. The rationale behind the reactivity of the monomers is explored.

Chapter Seven: *Fluorescence, Raman and ESR Studies* are described in this chapter, including a collaborative spectroelectrochemical Raman study of *N,N,N',N'*-tetraaryl-1,1'-biphenyl-4,4'-diamines.

Chapter Eight: *Experimental Procedures* are described, with complete characterisation data for all compounds synthesised during this study

Acknowledgements

I would like to thank Paul Low for three years of encouragement and suggestions. Julian Cherryman, Steve Leeming and the synthetic team at Avecia have been very helpful throughout, Bev Brown, Geoff Dent, Linda Jayes and Dan Tackley have all contributed with ideas and suggestions throughout this project.

A special thank-you must go to Olivia Koentjoro and the past and present inhabitants of Lab Shack 100 for keeping me sane throughout the last three years, and always being willing to enjoy a quiet drink in the New Inn on a Friday night. I am indebted to Mark Fox and Andy Hughes who were instrumental in convincing me to stay in Durham and complete a Ph.D.

Thanks are also due to the technical staff at the Department of Chemistry for all the help and assistance over the past seven years. I would also like to thank Rachael Littleford and Ewen Smith for introducing me to the finer points of Raman Spectroscopy, Eric McInnes for a crash course in ESR, and the crystallographers of the Department Crystallography Service who have solved the molecular structures contained in this thesis.

Abbreviations

Å	Angstrom
Abs	Absorbance
Ar	Aryl
Bu	n-Butyl
^t Bu	tertiary-Butyl
CGL	Charge Generating Layer
COSY	Correlated Nuclear Magnetic Resonance Spectroscopy
CV	Cyclic Voltammetry
ET	Electron Transfer
Et	Ethyl
ETL	Electron Transporting Layer
EL	Electroluminescence
Fc	Ferrocene
FET	Field Effect Transistor
HMBC	Heteroatom Multiple Bond Correlation Nuclear Magnetic Resonance Spectroscopy
HSQC	Heteronuclear Single Quantum Correlation Nuclear Magnetic Resonance Spectroscopy
HTL	Hole Transporting Layer
I _p	Ionisation Potential
Me	Methyl
MO	Molecular Orbital
NIR	Near Infra Red
nm	Nanometer
NMR	Nuclear Magnetic Resonance
OTTLE	Optically Transparent Thin Layer Electrode
PE	Potential Energy
Ph	Phenyl
ppm	parts per million
Pz	Pyrazine
TFT	Thin Film Transistor
Thf	Tetrahydrofuran
TPA	Triphenylamine
TPD	<i>N,N'</i> diphenyl- <i>N,N'</i> -bis(3-methylphenyl)-1,1'-biphenyl-4,4'-diamine
UV-vis	Electromagnetic radiation in the ultraviolet-visible region

Table of Contents

Chapter One

Introduction to Arylamines and their Applications

1.1 Photoconductors in Xerography	2
1.2 Organic Light Emitting Diodes	5
1.2.1 Mechanism of Operation	5
1.2.2 Mechanism of Electroluminescence	7
1.2.3 Charge Transport and Injection	8
1.3 Organic Transistors	10
1.3.1 Mechanism of Hole Movement	11
1.4 Hole Transporting Materials	12
1.4.1 Small Molecules as Hole Transporters	12
1.4.2 Hole Transporting Polymers	20
References for Chapter 1	22

Chapter Two

Concepts and Techniques

2.1 Electron Transfer	26
2.2 Experimental Techniques	33
2.2.1 Electrochemistry	33
2.2.2 Spectroelectrochemistry	35
2.2.3 Fluorescence Spectroscopy	37
2.2.4 Raman and Resonance Raman Spectroscopy	37
2.2.5 Electron Spin Resonance Spectroscopy	40
References for Chapter 2	42

Chapter Three

Triarylamines and Tetra Aryl Biphenyl Diamines

3.1 Introduction	45
3.2 Results and Discussion	53
3.3 Experimental section	68
References for Chapter 3	70

Chapter Four

Studies of the Molecular Conformation

4.1 Introduction	73
4.2 The Ullmann Condensation	84
4.3 Modifications to the Ullmann Condensation	86
4.4 Synthesis of Target Materials by Means of the Ullmann condensation	89
4.5 Cyclic Voltammetry and Spectroelectrochemistry	103
4.5.1 Summary of the Effects of Substituents on the Electrochemical Response of Tetraarylbiophenyldiamines	107
References for Chapter 4	119

Chapter Five

Trimeric and oligomeric systems

5.1 Introduction to Trimeric and Oligomeric Triaryamine Derivatives	122
5.2 Boronic Acid Formation and Palladium Catalysed Couplings	124
5.3 Cyclic Voltammetry and Spectroelectrochemistry	128
References for Chapter 5	139

Chapter Six

Electrochemical Polymerisation reactions

6.1 Introduction	141
6.2 Results and Discussion	142
6.3 Conclusion	151
References for Chapter 6	152

Chapter Seven

Fluorescence, Raman and ESR Studies

7.1 Introduction	156
7.2 Fluorescence Spectra	156
7.3 Electron Spin Resonance Studies	159
7.4 Raman Analysis of Charge Transfer Materials	162
7.4.1 Introduction	162
7.4.2 Aims	162
7.4.3 Results and Discussion	163
7.4.3.1 DFT calculations	163
7.4.3.2 Raman Spectra of Solid State 26^{n+} ($n=0,1$)	166
7.4.3.3 Spectroelectrochemical Raman Data	168
7.4.4 Conclusion	174
7.4.5 Experimental	175
7.4.5.2 Raman analysis	175
References for Chapter 7	176

Chapter Eight

Experimental Procedures

8.1 Experimental Procedures	178
8.2 Instrumentation	178

8.3 General Procedure	179
Synthesis of <i>N,N,N',N'</i> -tetra(phenyl)-(1,1'-biphenyl)-4,4'-diamine (19)	179
Synthesis of <i>N,N,N',N'</i> -tetra(4-methylphenyl)-(1,1'-biphenyl)-4,4'-diamine (27)	180
Synthesis of 2,2'-dimethyl-4,4'-diiodobiphenyl (52)	180
Synthesis of <i>N,N,N',N'</i> -tetraphenyl-(2,2'-dimethyl)-(1,1'-biphenyl)-4,4'-diamine (28)	181
Synthesis of <i>N,N,N',N'</i> -tetra(4-methylphenyl)-(2,2'-dimethyl)-(1,1'-biphenyl)-4,4'-diamine (29)	181
Synthesis of 3,3'-5,5'-tetramethyl hydrazobenzene	182
Synthesis of 2,2',6,6'-tetramethyl-4,4'-diaminobiphenyl (39)	182
Synthesis of 2,2',6,6'-tetramethyl-4,4'-diiodobiphenyl (53)	183
Synthesis of <i>N,N,N',N'</i> -tetra(phenyl)-(2,2',6,6'-tetramethyl)-(1,1'-biphenyl)-4,4'-diamine (30)	184
Synthesis of <i>N,N,N',N'</i> -tetra(4-methylphenyl)-(2,2',6,6'-tetramethyl)-(1,1'-biphenyl)-4,4'-diamine (31)	184
Synthesis of 3,3'-dimethyl-4,4'-diiodobiphenyl (54)	185
Synthesis of <i>N,N,N',N'</i> -tetraphenyl-(3,3'-dimethyl)-(1,1'-biphenyl)-4,4'-diamine (32)	186
Synthesis of <i>N,N,N',N'</i> -tetra(4-methylphenyl)-(3,3'-dimethyl)-1,1'-biphenyl-4,4'-diamine (33)	186
Synthesis of 9,9-diethylfluorene (55)	187
Synthesis of 9,9-diethyl-2,7-diiodofluorene (56)	187
Synthesis of <i>N,N,N',N'</i> -tetraphenyl-9,9-diethyl-2,7-diaminofluorene (34)	188
Synthesis of <i>N,N,N',N'</i> -tetra(4-methylphenyl)-9,9-diethyl-2,7-diaminofluorene (35)	189
Synthesis of 4,4'-dicarbazole-1,1'-biphenyl (36)	189
Trimeric Triarylamine Synthesis	190
Synthesis of bis(4-bromophenyl)phenylamine (60)	190
Synthesis of 4-bromophenyl bis(4-methylphenyl)amine (61)	190
Synthesis of 4-boronic acid bis(4-methylphenyl)phenylamine (62)	191
Synthesis of <i>N,N</i> -bis[4'-(bis {4-methylphenyl} amine)-1,1'-biphenyl-4] <i>N</i> -phenylamine (63)	192
References for Chapter 8	193

Conclusion

Conclusion	194
------------	-----

Appendix A

Experimental and Computational Raman Data

Experimental and calculated Raman Spectrum of 26	195
Experimental and calculated Raman Spectrum of 26⁺	199

Appendix B

First Year Introduction Courses: October 2000	204
Examined Lecture Courses: October 2000 to April 2001	204
Research Colloquia Seminars and Lectures Organised by the Department of Chemistry	205
Conferences and Symposia attended	207

Chapter One

Introduction to Arylamines and their Applications



Arylamines have found application in a number of technological roles due to their electronic and physical properties, a selection of these applications are reviewed here.

1.1 Photoconductors in Xerography

Electrophotography allows the replication of images on paper by arranging 100 million pigmented plastic particles in precise positions. Since its invention in 1942 it has grown to a hundred billion dollar industry. The fundamental process in xerography, as electrophotography became known on commercialisation, is the conversion of a light image into an electric field pattern. This is done through a series of stages. (Figure 1.1)¹

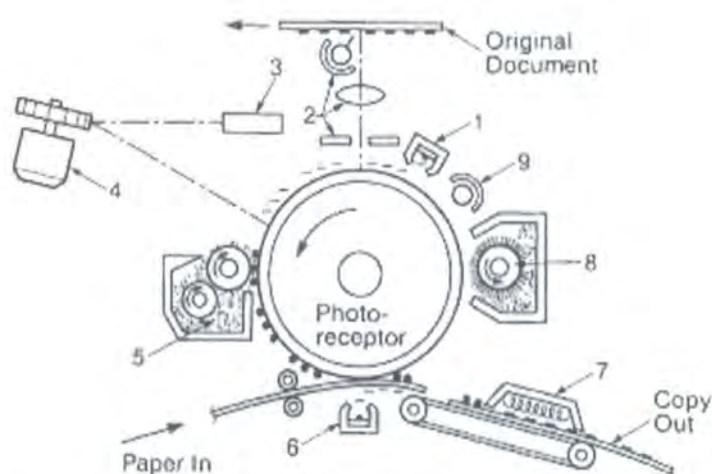


Figure 1.1 Xerographic reproduction machine indicating the important process steps. (1) Corona charging; (2) Exposure with light and lenses; (3) Laser; (4) Rotating polygon; (5) Development; (6) Transfer; (7) Fixing; (8) Cleaning; (9) Erasing.

The first step in the xerographic process is the charging of the photoconductor- a material that is capable of photogenerating and transporting a charge. This is commonly achieved by passing a corotron across the photoconductor surface in order to create a uniform surface charge. The corotron is a thin wire, to which a high voltage is applied, generating a plasma around the wire and charging the photoconductor surface.

The charged photoconductor is then exposed to light. This exposure to light initiates the photogeneration of charges that drift through the photoconductor, neutralising the surface charge in the illuminated areas and producing an electrostatic image of the original. Many different techniques have been applied to this step, including digital scanning of the image to be reproduced and then use of a laser to discharge the photoreceptor. Digital or laser printing emerged as a development of this process through removal of the scanning system and direct connection to a computer.

The latent electrostatic image is developed into a visible image through the application of toner particles. The charged, pigmented toner particles are attracted to the charged image on the photoconductor surface, from which they are transferred to the paper or other copy medium and fused to that surface.

Before repeating the imaging cycle the photoreceptor must be cleared of residual charge and toner. Toner is removed by physically cleaning the photoreceptor surface with a brush, wiper blade or magnetic roller. To remove any residual charge the photoconductor is exposed to an erase lamp that reduces the remaining electrostatic images to a level acceptable for initiation of the next charging step.¹

It is clear from this brief introduction to xerography that the photoconductor is a key component, and that the physical and electrical demands on the photoconductor are not trivial. The main requirements of a photoconductor are as follows:

- (1) The photoconductor film must hold the corona charge prior to exposure and maintain the image exposed charge pattern between exposure and development.
- (2) The photoreceptor must discharge efficiently at all wavelengths in the visible spectrum in a copier application, or in a laser printer, at the wavelength of the laser.
- (3) The photogenerated charge carriers must traverse the photoreceptor faster than the time taken for exposure and development.
- (4) The charged, partially charged and residual voltages must remain stable, during repetitive cycles, with no build up of residual voltage caused by accumulation of charge.
- (5) The photoreceptor materials must be capable of being fabricated into large (0.1 to 2 m²), defect-free films. The material must be stable in a chemically reactive corona

environment containing ozone, oxides of nitrogen, and water, and physically resistant to wear and abrasion by the development and cleaning processes.

The first photoreceptors consisted of amorphous selenium but doping with tellurium or arsenic is required to increase colour sensitivity and reduce crystallinity. The current trend is towards use of organic photoreceptors due to their material variety, economy, flexibility and environmental safety.²⁻⁵ High speed copying machines operating at speeds greater than 100 pages per minute typically use belts coated with multilayered organic photoconductors, while personal copiers and printers employ aluminium drums dip-coated with multilayered organic photoconductors.

These organic photoconductors allow the separation of the roles of charge generation and charge transport and the concept of dual layer devices in which the functions of photogeneration and transport of charge are carried out by different materials has gained wide acceptance within the industry. In these multilayered systems, a thin charge generation layer (CGL) of organic pigment capable of efficient charge generation is combined with a thicker charge transport layer consisting of a charge transporting polymer or of a binary solid solution of a charge transporting molecule dispersed in an inert polymeric binder. This latter approach provides the ability to vary independently the photoelectronic and mechanical properties.¹

1.2 Organic Light Emitting Diodes

Since the first reports of organic electroluminescence (EL) appeared in the 1960s⁶ and the extensive development of the field in the 1980s,⁷⁻¹¹ the prospect of constructing a flexible, energy efficient flat panel display has been the driving force behind a great deal of research conducted into organic electroluminescent molecular materials.¹²⁻¹⁴

The stimulus behind this drive towards new display technology has been the continual demand for lightweight, colourful, power efficient displays for portable electronic devices, such as mobile telephones and computers. These displays need not be limited to small-scale applications and there is considerable interest in applying this technology to high-resolution displays for television sets and VDUs.¹⁵⁻²³

Whereas conventional display methods such as cathode ray tubes,²⁴ plasma displays²⁵ or liquid crystal displays are either bulky or require complicated electronics, organic EL devices are emissive with high luminescence, have high quantum efficiency, low operating voltages and are available in colours across the whole of the visible spectrum.²⁶⁻³⁴

Where these properties are teamed with flexibility,³⁵ fast response time of the individual pixels and the wide viewing angle of up to 160°, EL devices become a very attractive proposition indeed, as has been proven by the rapid uptake of this technology by a wide range of high end technology companies including Avecia,³⁶ Covion,³⁷ CDT,³⁸ IBM/eMagin,³⁹ Kodak,⁴⁰ Motorola,⁴¹ Philips,⁴² Pioneer,⁴³ Samsung/SDI/NEC,⁴⁴ Sanyo,⁴⁵ Sony⁴⁶ and Toshiba.⁴⁷

1.2.1 Mechanism of Operation

The principle behind an organic EL display is conceptually simple. The emissive material, which may be a highly conjugated polymer or specifically designed molecular material, is sandwiched between two electrodes. (Figure 1.2) When an appropriate voltage is applied the material is oxidised at the anode, generating positively charged “holes”, and reduced at the cathode, leading to the introduction of electrons. The charges migrate towards the opposite electrode by an as yet poorly

understood hopping mechanism between molecules/polymer chains. If two opposite charges happen to meet in the same EL molecule/polymer, an excited state “exciton” is formed⁴⁸⁻⁵⁴ which may then decay radiatively, emitting a photon. In conjugated materials these singlet excitons are not confined to a small region of the molecule but are wavelike and are spread over several repeat units, enabling them to move to a region of low energy where they decay. The introduction of dopants which creates sites where these excitons can decay is one method of altering the wavelength of the light emitted.⁵⁵ To enable the emitted light to be observed, a semitransparent material, indium tin oxide (ITO) coated onto glass is used as the anode.

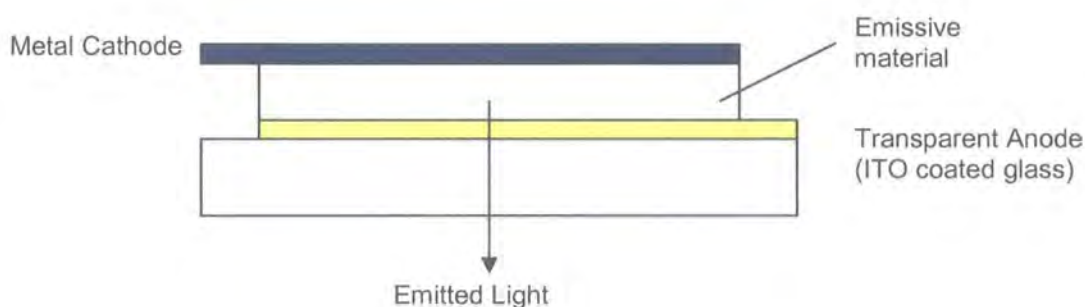


Figure 1.2 Schematic configuration of a single layer OLED

Various methods have been developed in the quest for a full colour display device. These include layering different emissive materials and generating emission from each colour separately, having three separate emissive materials making up the individual pixels (Figure 1.3) or creating a white emitting display with red, green and blue filters.⁵⁶⁻⁵⁸

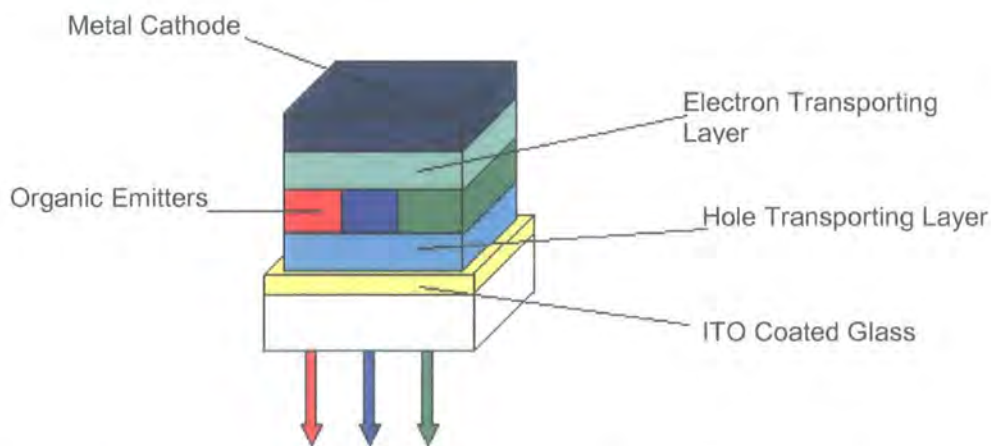


Figure 1.3 Schematic configuration of a three layer OLED with multiple organic emitters

1.2.2 Mechanism of Electroluminescence

The photophysics of electroluminescence is closely related to the principles of photoluminescence. Electroluminescence is generated by application of a field to a material whereas photoluminescence is the re-emission of a photon of absorbed light, usually at a longer wavelength. The electroluminescence and photoluminescence spectra of a particular material are almost always identical as they usually originate from the same energy levels.

Electroluminescence is an inherently inefficient process as statistically 75% of excited states are formed as triplets, which do not decay radiatively. On formation of a singlet excited electronic state, through either absorption of a photon or the presence of an exciton, an electron is promoted into one of the energy levels above the ground state HOMO, 1S ($\nu = n$). Loss of energy through non-radiative decay occurs first to the 1S ($\nu = 0$) state. Then a radiative transition to the ground state can occur and this is observed as emitted light. (Figure 1.4)

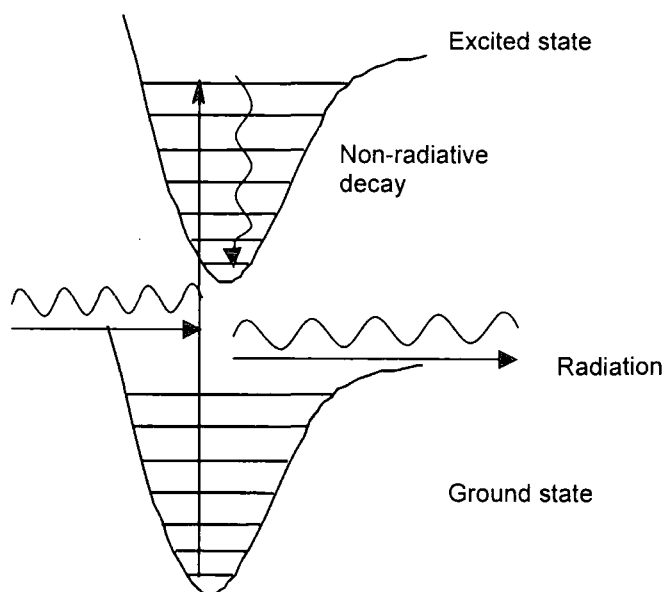


Figure 1.4 Jablonski diagram of photoluminescence

Non radiative decay from the 1S ($\nu = 0$) can occur when inter system crossing occurs. The excited state originates as a singlet state. However, if there is a mechanism for

conversion of the singlet to a triplet state, (converting $\uparrow\downarrow$ to $\uparrow\uparrow$), these triplets can then lose further energy by non-radiative decay. Any emission observed would be weak, often occurring as phosphorescence, long after the excited state is formed. Another pathway for non-radiative decay is the migration to and decay of the excited state at quenching sites, such as the metal contacts, chemical defects or contaminants in the material.

1.2.3 Charge Transport and Injection

Organic materials are generally much more efficient transporters of positive charges than electrons. In a single layer device, the majority of holes will pass through the emissive material without meeting an electron and therefore without emitting light. In addition, the region where electrons and holes meet will be close to the metal contact. This tends to quench electroluminescence. All of these factors serve to cause poor device efficiency i.e. number of photons emitted per electron injected. To increase the efficiency a layered arrangement has been developed, with three or more layers of different organic materials,⁸⁻¹⁰ typically a hole transporting layer, the emissive layer and an electron-transporting layer. These additional layers improve charge carrier injection into the emissive layer. They also effectively control where the combination of hole and electron occurs, through the use of hole and electron injecting materials, which transport only holes or electrons the charges are effectively confined to the emissive material, thus increasing the efficiency of the device.⁵⁹ (Figure 1.5)

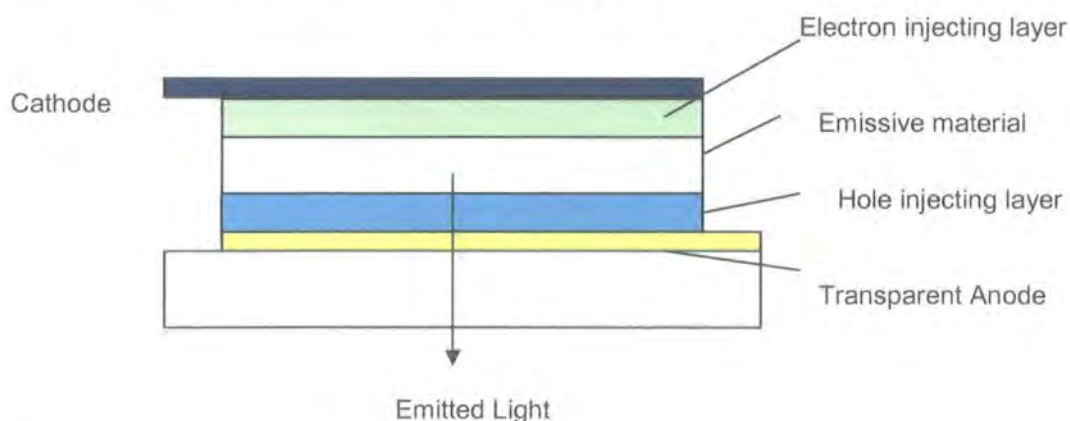


Figure 1.5 Multi-layered device arrangement

The design of suitable materials for device construction requires an understanding of injection and transport of charges between the layers of organic material throughout the device.

Figure 1.6 Band structure diagram for a three-layer system

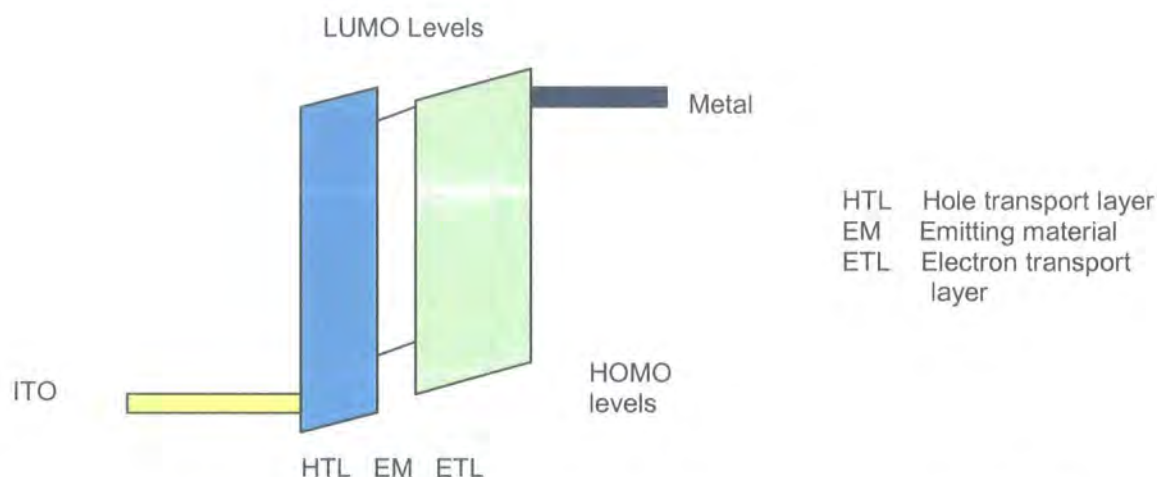


Figure 1.6 illustrates the ideal arrangement for the relative energies of the HOMOs and LUMOs of an EL device. The HOMO of the EM is at a higher energy than the HOMO of the HTL, and the LUMO at a lower energy than LUMO of the ETL. This ensures that both holes and electrons can be efficiently transferred to the emissive layer. The use of ETL and HTL materials also confines the excitons to the emissive layer,^{7-10, 60} minimising non-radiative losses at the electrodes.

For effective hole transport it is essential that the material possess a number of key characteristics:

- (1) The material must have a low ionisation potential so that it will easily form the radical cation through loss of an electron.
- (2) The redox process must be completely reversible; any degree of irreversibility will soon degrade the transporting material and possibly act as a trap to transport.
- (3) The material must be stable in both neutral and oxidised states under the operating conditions of the device.

The use of materials initially developed as charge transporting materials for xerographic applications has advanced this area of research due to the common requirements of the two applications. Use of both charge transporting polymers, and molecularly doped polymers to obtain the optimal electronic and physical properties has been explored, and will be discussed below.

1.3 Organic Transistors

The rapid development of organic LEDs has revealed the possibilities of utilising organic and polymeric devices in other areas of electronics. Organic transistors have been proposed for applications such as display driving circuits and low-cost memory devices for smart cards and price tags. The key building blocks for these circuits are organic thin film field effect transistors (TFTs or FETs). These systems may not replace silicon in high performance or high-density devices; instead they are aimed at applications where ease of fabrication, mechanical flexibility, cost and avoidance of high temperature processes are of particular importance.⁶¹⁻⁶⁴

A typical FET is constructed with the following components, three electrodes (gate, drain and source), a dielectric layer and a semiconducting layer.(Figure 1.7) The semiconductor channel acts as an insulator until a voltage is applied to the gate electrode. When a voltage is applied to the gate, charges can be induced into the semiconducting layer at the interface between the semiconductor and dielectric layer. As a result this allows current to flow through the semiconductor.⁶⁴

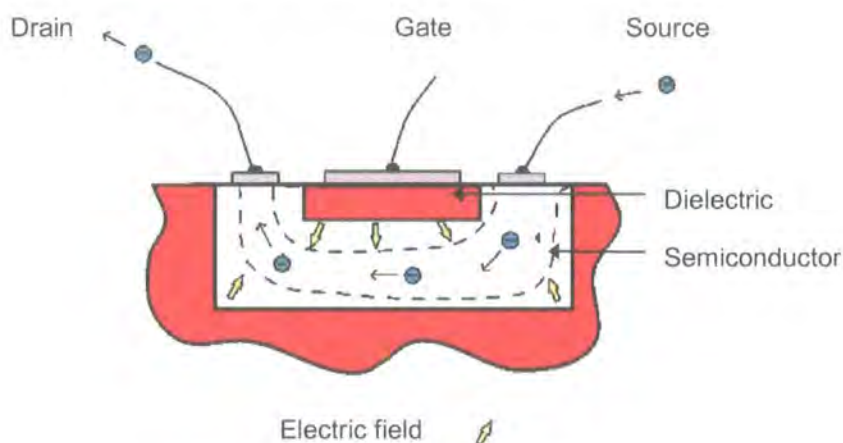


Figure 1.7 Typical arrangement of a FET

The semiconductor must possess several distinct but interrelated attributes:

- (1) The material must accept charge from the source electrode, without a substantial voltage being required.
- (2) The charge must migrate quickly between the source and drain. The mobility must be high enough to allow useful amounts of source-drain current to flow, modulated by an accessible voltage.

(3) The semiconductor must withstand the operating conditions without thermal, electrochemical or photochemical degradation.

These requirements define the necessary band levels, band gaps and surface states for the semiconducting material.⁶⁵

1.3.1 Mechanism of Hole Movement

The role of polymers in the electronics industry has been traditionally associated with insulating properties. However, all of the technologies discussed above employ an organic material as a semiconducting material. The polymers that have found application as semiconducting materials contain a conjugated π -system along the polymer backbone. The multiple bonds or heteroatoms between carbon atoms in the polymer chain provide an electron excess to that normally required for bonding. These 'spare' electrons are in p_z orbitals that overlap with adjacent p_z orbitals to form a delocalized π -electron cloud that can spread over several atomic sites along the polymer backbone. When this occurs, delocalized π valence (bonding) and π^* conduction (antibonding) bands with a defined band gap can be considered to be formed. The delocalised π -electron system confers semiconducting properties to the polymer and gives rise to the ability to support positive and negative charge carriers with high mobility along the polymer chain.^{20, 51}

The charge transport in molecularly doped polymers, where the polymer acts as supporting matrix to the electron donor or acceptor is commonly described by means of a hopping mechanism, in which the hole or electron progresses through the bulk material by an electric field driven chain of redox processes, involving discrete neutral molecules or groups and their charged derivatives.⁶⁶⁻⁶⁸

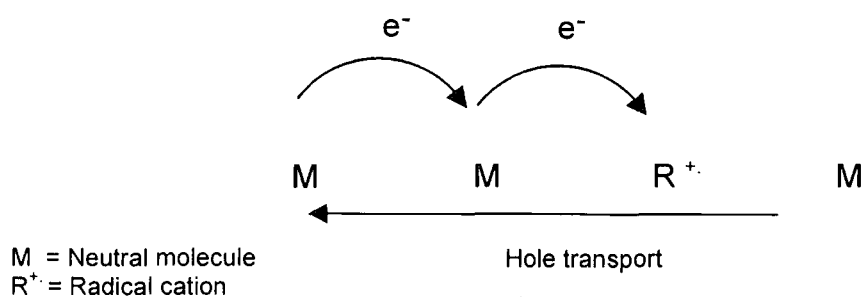


Figure 1.8 A schematic of the hole transport process. The electron hops from a neutral molecule to a neighbouring radical cation. The hole thus moves in the opposite direction.

The interpretation of data differs between the many available systems, but the rate of charge transport has been shown to depend on the type of material, the concentration of active species, the supporting polymer - which is not inert as originally assumed, temperature and most of all, the applied electric field.⁶⁹⁻⁷¹

1.4 Hole Transporting Materials

For hole transport, on which this thesis will now focus, it is essential that the material be an electron donor when neutral, and have a low ionisation potential to facilitate formation of the cation radical, and that the redox processes (oxidation/reduction/oxidation) are completely reversible. Aryl amines were found to possess the required low ionisation potentials which when combined with their physical properties and ease of derivitisation, proved to be the ideal family of materials for application as hole transporting materials.

1.4.1 Small Molecules as Hole Transporters

Triphenylamine and tetraaryl-1,1'-biphenyl-4,4'-diamines were amongst some of the earliest organic materials to be studied as hole transporting materials. However during device operation there is significant thermal stress on the hole transporting material and one of the principal failure modes in devices incorporating these materials involves thermal instability in the molecular thin film.^{11, 72, 73} The main sources of instability in the amorphous films are thought to be dewetting and crystallisation. Crystallisation of the organic layers can cause the contacts between layers to be destroyed and crystal grain boundaries are believed to act as traps to mobility. The formation and stability of amorphous films, is therefore very important for hole transporting materials. Thermally induced dewetting and crystallisation occur most readily in materials with comparatively low glass transition temperatures (T_g). It has been shown that there is a linear relationship between the T_g of the hole transporting material and the temperature at which a device fails. At temperatures above the T_g , drastic morphological changes have been reported in films of N,N'-diphenyl-N,N'-bis(3-methylphenyl)-1,1'-biphenyl-4,4'-diamine (TPD, **1**), leading to the failure of the device.⁷³⁻⁷⁵ A systematic study showed that devices manufactured from hole transporting materials with higher T_g s demonstrated greater thermal stability.⁷³ A considerable amount of research has been directed towards developing hole

transporting materials with the required low ionisation potential, high hole mobility and greater amorphous film stability than the currently available materials, such as N,N'-diphenyl-N,N'-bis(3-methylphenyl)-1,1'-biphenyl-4,4'-diamine (**1**), which has a T_g of only 65 °C.

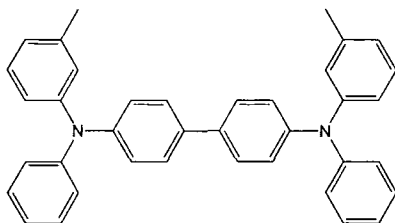


Figure 1.9 N,N'-diphenyl-N,N'-bis(3-methylphenyl)-1,1'-biphenyl-4,4'-diamine (TPD, **1**)

A number of approaches to mediate this film instability have been developed. Incorporation of the hole transporting material into a supporting polymer matrix,^{66-68, 70} although this can give some problems relating to phase separation of the dopant materials and polymeric support.⁷⁶ Incorporation of the hole transporting unit into a polymer, (which will be considered in a later section) and utilisation of a material with inherent greater thermal stability.^{72, 76, 77} Among the methods used in developing materials with an increased thermal stability are synthesis of starburst materials having a triphenylamine or benzene core, use of spiro linkages between established hole transporting units and the addition of bulky groups to the phenyl rings of tetraaryl biphenyl diamine derivatives, often in an asymmetric substitution pattern as this hinders crystallisation. All of the above approaches will be briefly reviewed here.

It was proposed by Tanaka, Kitamura and Yokoyama that charge transport processes in these materials are dominated by the degree of delocalisation of the charge distribution on the molecule, and that high mobilities require that the distribution be highly delocalised.⁷⁷ For hole transport Kitamura and Yokoyama concluded that two structural features are important for high mobilities:

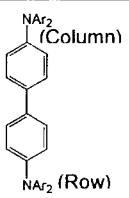
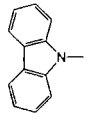
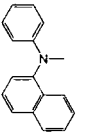
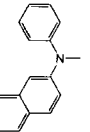
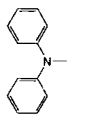
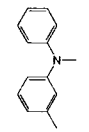
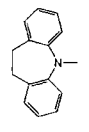
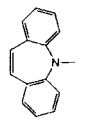
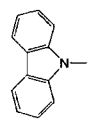
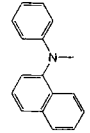
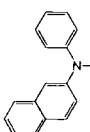
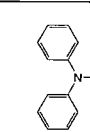
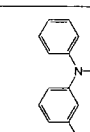
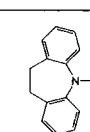
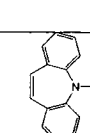
- (1) Polyfunctionality i.e. more than one donor unit within a molecule to afford a greater probability that a hole will hop from a neighbouring molecule.
- (2) A well balanced resonance structure to ensure that a hole has a high intramolecular mobility within a molecule. This was the first realisation that intramolecular charge-transfer was significant to charge transport in these materials.^{78, 79}

Many of the TPD based materials did combine two donor sites, being diamines, with good delocalisation of the charge, these materials are amenable to asymmetric

substitution and a selection of materials and their corresponding oxidation potentials, glass transition temperatures and HOMO energies are displayed in tables 1.1 and 1.2.^{11, 72, 80-85} The drive to synthesise and test a wide range of materials in order to optimise these aforementioned properties led to developments in the synthetic procedures for formation of these materials.^{4, 5, 86, 87} Synthetic procedures will be discussed in more detail in Chapter 4.

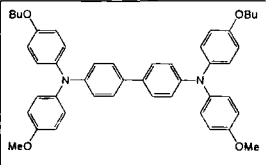
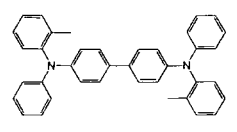
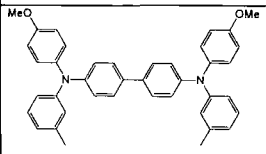
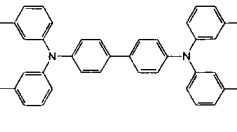
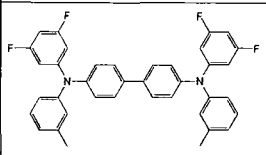
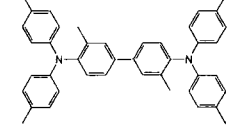
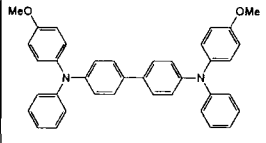
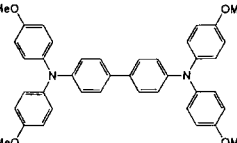
Literature reports of novel hole transporting materials often use different parameters to measure the oxidation potential/ionisation potential and energy of the HOMO. For clarity all oxidation potentials are quoted relative to $\text{Fc}/\text{Fc}^+ = 0.0 \text{ V}$, and HOMO energies are quoted based on the value of -4.8 eV for Fc with respect to zero vacuum level following the procedure adopted by Pommerehne *et al.*⁵⁰

Table 1.1 Selected data for biphenyl diamine based hole transport materials^{72, 80}

							
	- 0.52 -5.32 -	109 0.54 -5.34 5.78	107 0.53 -5.33 -	91 0.52 -5.32 -	85 0.47 -5.27 -	117 0.53 -5.33 5.53	125 0.58 -5.38 -
		100 0.31 -5.11 5.70	106 0.32 -5.12 -	87 0.32 -5.20 -	85 0.29 -5.09 5.58	110 0.25 -5.05 -	117 0.31 -5.11 -
			103 0.33 -5.13 -	92 0.32 -5.12 -	94 0.29 -5.09 -	105 0.28 -5.08 -	117 0.27 -5.07 -
				77 0.29 -5.09 -	71 0.31 -5.11 -	96 0.273 -5.07 -	97 0.29 -5.09 -
					60 0.27 -5.07 5.50	86 0.24 -5.04 -	91 0.26 -5.06 -
						117 0.20 -5.00 5.30	125 0.23 -5.03 -
							110 0.24 -5.04 5.46

The amine found in the column is bound to the 4 position of the biphenyl and the amine in the row is bound to the 4' position. The amines along the diagonal are symmetric, while all the non-diagonal entries are asymmetric. The first line of each entry is the T_g ($^{\circ}$), the second line is the oxidation potential, obtained from CVs in CH_2Cl_2 referenced to $\text{Fc}/\text{Fc}^+ = 0.0\text{V}$. The third line gives the HOMO energy (eV). The fourth line gives the I_p in eV.

Table 1.2 Selected data for biphenyl diamine based hole transport materials^{11, 80-85}

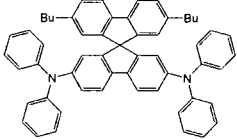
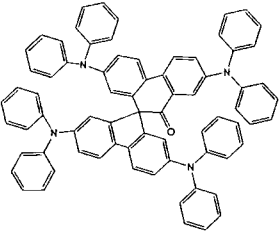
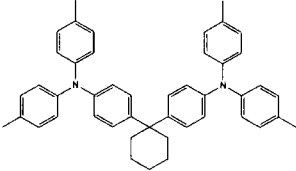
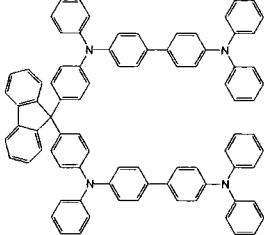
	- 0.17 -4.97 -		56 - - 5.44
	- 0.18 -4.98 -		56 - - 5.20
	- 0.47 -5.27 -		78 - - 5.20
	56 - -5.06 5.32		67 - - 4.97

The first line of each entry is the T_g ($^{\circ}$), the second line is the oxidation potential relative to Fc/Fc^+ . The third line gives the HOMO energy (eV). The fourth line gives the I_p in eV.

These studies have produced a wide range of diamine derivatives, with varying T_g s and ionisation potentials. The highest T_g s are associated with carbazole, iminodibenzyl and iminostilbene end groups and, excepting the carbazole containing materials, these compounds also show relatively low oxidation potentials.

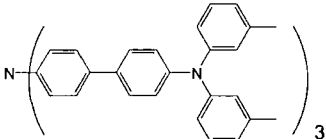
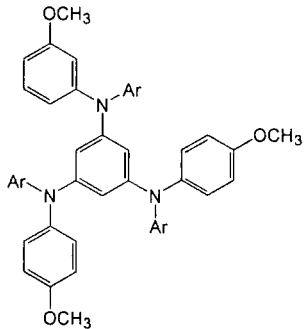
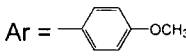
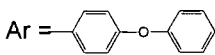
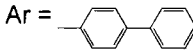
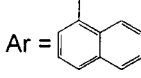
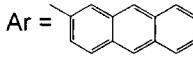
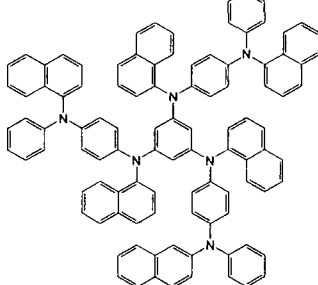
The use of a spiro linkage between the hole transporting units in place of a biphenyl has been investigated by a number of groups.^{8, 11, 88, 89} The spiro linkage imparts better film forming properties and higher T_g values due to the non-planar conformation of the molecular structure. The electronic properties of discrete end units, such as arylamines, are unaffected giving good hole transport. (Table 1.3)

Table 1.3 Selected data for spiro linked hole transporting materials.^{8, 11, 88, 89}

	$T_g = 161^\circ$
	$T_g = 131^\circ$
	$T_g = 74^\circ$ $I_p = 5.43 \text{ eV}$
	$T_g = 153^\circ$ $E_{1/2} = 0.24 \text{ V}$

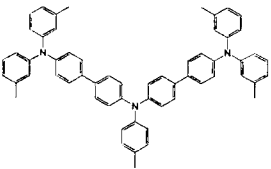
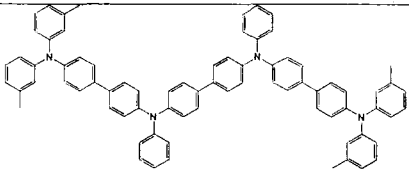
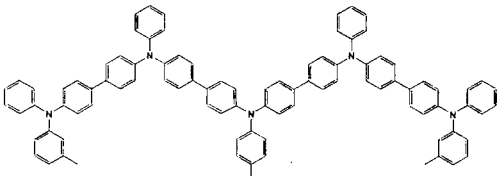
Another approach utilised to raise the film stability and T_g is to form starburst molecules centred about either an arylamine or a benzene core, with arylamine units radiating out. These materials have been shown to have low ionisation potentials and to form stable amorphous films.^{73, 84, 90-94} The majority of these materials have been based around simple arylamines, incorporation of carbazole and naphthyl moieties into the materials has been shown to increase the T_g even further. (Table 1.4)

Table 1.4 Selected data for starburst hole transporting materials.

	$T_g = 106^\circ$
	<p>Ar =  $T_g = -$ $E_{1/2} = -0.01\text{ V}$ HOMO = -4.98 eV</p> <p>Ar =  $T_g = 54^\circ$ $E_{1/2} = 0.07\text{ V}$ HOMO = -5.07 eV</p> <p>Ar =  $T_g = 85^\circ$ $E_{1/2} = 0.11\text{ V}$ HOMO = -5.11 eV</p> <p>Ar =  $T_g = 88^\circ$ $E_{1/2} = 0.12\text{ V}$ HOMO = -5.13 eV</p> <p>Ar =  $T_g = 123^\circ$ $E_{1/2} = 0.07\text{ V}$ HOMO = -5.16 eV</p>
	$T_g = 141^\circ$ $E_{1/2} = 0.02\text{ V}$ HOMO = -4.82 eV

Larger linear systems such as trimers, tetramers and pentameric systems exhibit similar electrochemical properties to the dimeric systems, with higher glass transition temperatures. ^{11, 73, 88, 95} (Table 1.5)

Table 1.5

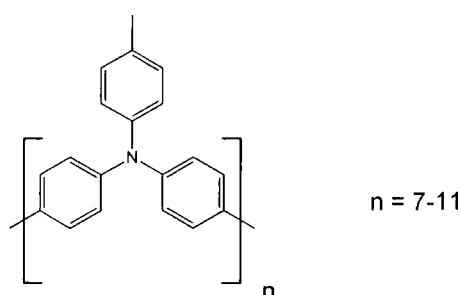
	$T_g = 95^\circ$ $I_p = 5.08 \text{ eV}$
	$T_g = 140^\circ$
	$T_g = 145^\circ$

Larger molecular weight derivatives of triphenylamine and tetraaryl biphenyl diames have been synthesised and these polymeric systems alongside polymers with hole transporting units appended to side chains, will be briefly reviewed here.

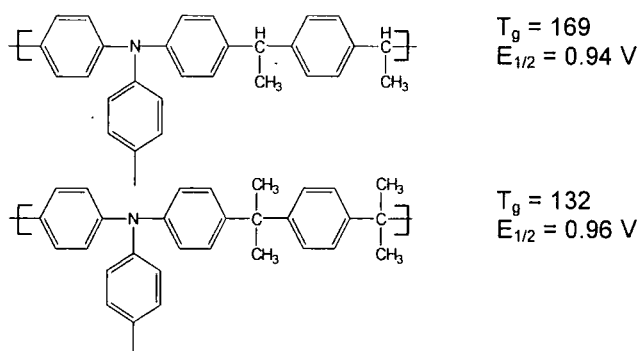
1.4.2 Hole Transporting Polymers

The polymeric materials that have been employed as hole transporting materials can be classified into two types. Those employing the hole transporting units in the backbone and those with hole transporting groups appended on side chains.

The simplest of the former class, polytriphenylamine itself, has been shown to form stable amorphous films from a toluene solution with a T_g of 185 °C, and hole mobility not worse than the TPD based reference device.⁷⁵



Modifications that have been made to the polymer structure include disrupting the biphenyl link between adjacent amine centres through incorporation of methylene groups between the triarylamine units. This approach has been proven to provide a polymer with good solubility and therefore, ease of processing, good film formation and a electrochemical response similar to the monomer.^{3, 96, 97}



Attaching the hole transporting unit to an established polymer backbone allows much greater scope for derivatisation,^{85, 98} although the backbone can play a role in disrupting the charge transport. The incorporation of a variety of amine groups into a poly(methylmethacrylate) backbone with the active amines separated from the polymer backbone by three or four atoms to ensure that they replicate the disordered

solid solutions found for aromatic amines in polymeric binders has been studied.² The resulting polymers were soluble in all common organic solvents and formed films which were subjected to hole mobility testing. It was found that the triphenylamine substituted polymer exhibited the highest hole mobility, this was however lower than the mobility of TPA at 30 wt % in polycarbonate. The polymer itself having a higher concentration of amine centres (71 wt %). This was attributed to the inhibition of overlap of the functional groups due to the covalent attachment of the triphenylamine unit to the polymer backbone.

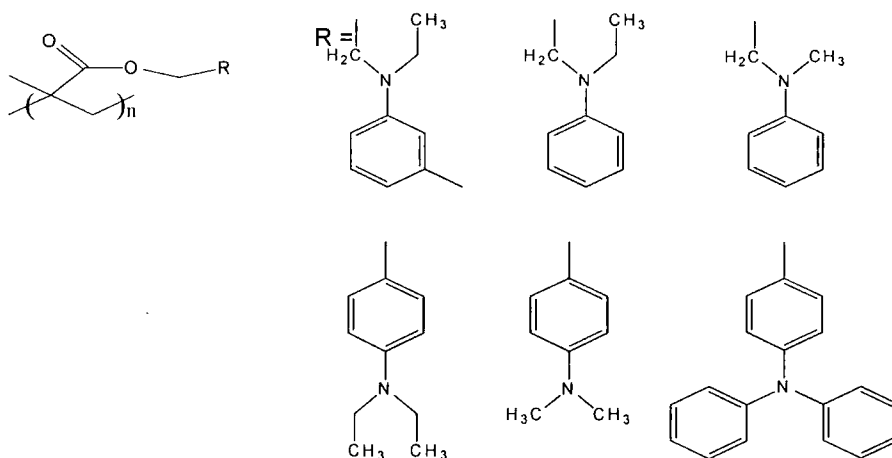
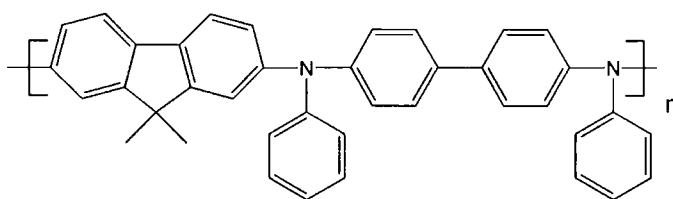


Figure 1.10 Polymers of arylamine-containing methacrylates

A novel fluorene based co-polymer incorporating alternating fluorene and diphenyl benzidine units had a T_g of 148 °C, was soluble in common organic solvents and had better hole transporting properties than most of the 9,9-disubstituted polyfluorenes.⁹⁹



References for Chapter 1

- 1 D. M. Pai and B. E. Springett, *Rev. Mod. Phys.*, 1993, **65**, 163.
- 2 M. Stolka, D. M. Pai, D. S. Renfer, and J. F. Yanus, *J. Polym. Sci. Polym. Chem. Ed*, 1983, **21**, 869.
- 3 X. Wang, M. Nkao, K. Ogino, H. Sato, and H. Tan, *Macromol. Chem. Phys.*, 2001, **202**, 117.
- 4 H. B. Goodbrand, in 'United States Patent 5,654,482', 1997.
- 5 H. B. Goodbrand, in 'United States Patent 5,648,539', 1996.
- 6 W. Helfrich and W. G. Schneider, *Phys. Rev. Lett.*, 1965, **14**, 229.
- 7 C. W. Tang and S. A. VanSlyke, *Appl. Phys. Lett.*, 1987, **51**, 913.
- 8 C. W. Tang, S. A. VanSlyke, and C. H. Chen, *J. Appl. Phys.*, 1989, **65**, 3610.
- 9 C. Adachi, S. Tokito, T. Tsutsui, and S. Saito, *Jpn. J. Appl. Phys.*, 1988, **27**, L269.
- 10 C. Adachi, S. Tokito, T. Tsutsui, and S. Saito, *Jpn. J. Appl. Phys.*, 1988, **27**, L713.
- 11 C. Adachi, K. Nagai, and N. Tamoto, *Appl. Phys. Lett.*, 1995, **66**, 2679.
- 12 U. Mitschke and P. Bäuerle, *J. Mater. Chem.*, 2000, **10**, 1471.
- 13 D. D. C. Bradley, *Synth. Met.*, 1993, **54**, 401.
- 14 J. L. Segura, *Acta Polym.*, 1998, **49**, 319.
- 15 J. H. Burroughes, D. D. C. Bradley, A. R. Brown, R. N. Marks, K. Mackay, R. H. Friend, P. L. Burns, and A. B. Holmes, *Nature*, 1990, **347**, 539.
- 16 R. H. Friend, D. Bradley, and A. B. Holmes, *Phys. World*, 1992, 42.
- 17 P. May, *Physics World*, 1995, March 52.
- 18 R. W. Gymer, *Endeavour*, 1996, **20**, 115.
- 19 J. R. Sheats, H. Antoniadis, M. Heuschen, W. Leonard, J. Miller, R. Moon, D. Roitman, and A. Stocking, *Science*, 1996, **273**, 884.
- 20 A. Kraft, A. C. Grimsdale, and A. B. Holmes, *Angew. Chem. Int. Ed.*, 1998, **37**, 402.
- 21 R. H. Friend, R. W. Gymer, A. B. Holmes, J. H. Burroughes, R. N. Marks, C. Taliani, D. D. C. Bradley, D. A. D. Santos, J. L. Brédas, M. Lögdlund, and W. R. Salaneck, *Nature*, 1999, **397**, 121.
- 22 H. Kikuchi, T. Negishi, and R. Gardner, *Displays*, 2001, **22**, 57.
- 23 C. Py, M. D'Iorio, Y. Tao, J. Stapleton, and P. Marshall, *Synth. Met.*, 2000, **113**, 155.
- 24 L. Ozawa, *Mat. Chem. and Phys.*, 1997, **51**, 107.
- 25 G. Oversluizen, M. Klein, S. d. Zwart, S. v. Heusden, and T. Dekker, *Appl. Phys. Lett.*, 2000, **77**, 948.
- 26 C. Adachi, T. Tsutsui, and S. Saito, *Appl. Phys. Lett.*, 1990, **56**, 799.
- 27 J. A. Osaheni and S. A. Jenekhe, *Macromol.*, 1994, **27**, 739.
- 28 I. D. W. Samuel, G. Rumbles, and C. J. Collison, *Phys. Rev. B*, 1995, **52**, R11 573.
- 29 D. U. Kim, T. Tsutsui, and S. Saito, *Polymer*, 1995, **36**, 2481.
- 30 M. Onada, K. Tada, M. Ozaki, and K. Yoshino, *Thin Solid Films*, 2000, **363**, 9.
- 31 Y. Sakakibara, S. Okutsu, T. Enokida, and T. Tani, *Thin Solid Films*, 2000, **363**, 29.
- 32 D. Zhu, Y. Liu, and F. Bai, *Thin Solid Films*, 2000, **363**, 51.
- 33 M. Cheng, Y. Xiao, W.-L. Yu, Z.-K. Chen, Y.-H. Lai, and W. Huang, *Thin Solid Films*, 2000, **363**, 110.

- 34 L. M. Cheng, L. M. Hung, X. M. Ding, Z. Q. Gao, C. S. Lee, and S. T. Lee, *Displays*, 2000, **21**, 51.
- 35 G. Gustafsson, G. M. Treacy, Y. Cao., F. Klavetter, N. Colaneri, and A. J. Heeger, *Synth. Met.*, 1993, **55-57**, 4123.
- 36 www.avecica.co.uk.
- 37 www.covion.com.
- 38 www.cdttld.co.uk.
- 39 www.emagin.com.
- 40 www.kodak.com.
- 41 www.motorola.com.
- 42 www.research.philips.com.
- 43 www.pioneerelectronics.com.
- 44 www.samsung.com.
- 45 www.sanyo.com.
- 46 www.sony.com.
- 47 www.toshiba.co.jp.
- 48 A. B. Holmes, D. D. C. Bradley, A. R. Brown, P. L. Burns, J. H. Burroughes, R. H. Friend, N. C. Greenham, R. W. Gymer, D. A. Halliday, R. W. Jackson, A. Kraft, J. H. F. Martens, K. Pichler, and I. D. W. Samuel, *Synth. Met.*, 1993, **55-57**, 4031.
- 49 I. D. Parker, *J. Appl. Phys.*, 1994, **75**, 1656.
- 50 J. Pommerehne, H. Vestweber, W. Guss, R. F. Mahrt, H. Bässler, M. Porsch, and J. Daub, *Adv. Mater.*, 1995, **7**, 551.
- 51 D. D. C. Bradley, *Curr. Opin. Solid St. M.*, 1996, **1**, 789.
- 52 M. S. Weaver, D. G. Lidzey, T. A. Fisher, M. A. Pate, D. O'Brien, A. Bleyer, A. Tajbakhsh, D. D. C. Bradley, M. S. Sklnick, and G. Hill, *Thin Solid Films*, 1996, **273**, 39.
- 53 P. D. Rack and P. H. Holloway, *Mat. Sci. Eng. R.*, 1998, **21**, 171.
- 54 Y. Xiaohui, H. Yulin, H. Yanbing, Y. Zheng, and X. Xurong, *Displays*, 2000, **21**, 61.
- 55 C. Hosokawa, H. Higashi, H. Nakamura, and T. Kusumoto, *Appl. Phys. Lett.*, 1995, **67**, 3853.
- 56 M. Hamaguchi and K. Yoshino, *Appl. Phys. Lett.*, 1996, **69**, 143.
- 57 Z. Zhilin, J. Xueyin, and X. Shaohong, *Thin Solid Films*, 2000, **363**, 61.
- 58 S. Liu, J. Huang, Z. Xie, Y. Wang, and B. Chen, *Thin Solid Films*, 2000, **363**, 294.
- 59 D. Troadec, G. Veriot, R. Antony, and A. Moliton, *Synth. Met.*, 2001, **124**, 49.
- 60 D. C. Freeman and C. E. White, *J. Am. Chem. Soc.*, 1956, **78**, 2678.
- 61 H. E. Katz, *J. Mater. Chem.*, 1997, **7**, 369.
- 62 F. Garnier, R. Hajlaoui, A. Yassar, and P. Srivastava, *Science*, 1994, **265**, 1684.
- 63 Z. Bao, *Adv. Mater.*, 2000, **12**, 227.
- 64 H. E. Katz and Z. Bao, *J. Phys. Chem. B*, 2000, **104**, 671.
- 65 A. Dodabalapur, L. Torsi, and H. E. Katz, *Science*, 1995, **268**, 270.
- 66 G. Pfister, S. Grammatica, and J. Mort, *Phys. Rev. Lett.*, 1976, **37**, 1360.
- 67 G. Pfister, *Phys. Rev. B*, 1977, **16**, 3676.
- 68 P. M. Borsenberger, W. Mey, and A. Chowdry, *J. Appl. Phys.*, 1978, **49**, 273.
- 69 W. T. Gruenbaum, L. J. Sorriero, P. M. Borsenberger, and N. Zumbulyadis, *Jpn. J. Appl. Phys.*, 1996, **35**, 2714.
- 70 M. Stolka, J. F. Yanus, and D. M. Pai, *J. Phys. Chem.*, 1984, **88**, 4707.

- 71 S. Heun and P. M. Borsenberger, *Physica B*, 1995, **216**, 43.
72 B. E. Koene, D. E. Loy, and M. E. Thompson, *Chem. Mater.*, 1998, **10**, 2235.
73 S. Tokito, H. Tanaka, K. Noda, A. Okada, and Y. Taga, *Appl. Phys. Lett.*,
1997, **70**, 1929.
74 S. Tokito, H. Tanaka, A. Okada, and Y. Taga, *Appl. Phys. Lett.*, 1996, **69**, 878.
75 I. K. Yakushchenko, M. G. Kaplunov, O. N. Efimov, M. Y. Belov, and S. N.
Shamaev, *Phys. Chem. Chem. Phys.*, 1999, **1**, 1783.
76 P. M. Borsenberger, L. Pautmeier, R. Richert, and H. Bässler, *J. Chem. Phys.*,
1991, **94**, 8276.
77 M. V. d. Auwerer and F. C. D. Schryver, *J. Phys. Chem.*, 1993, **97**, 8808.
78 T. Kitamura and M. Yokoyama, *Jpn. J. Appl. Phys.*, 1991, **30**, 1015.
79 T. Kitamura and M. Yokoyama, *J. Appl. Phys.*, 1991, **69**, 821.
80 D. F. O'Brien, P. E. Burrows, S. R. Forrest, B. E. Koene, D. E. Loy, and M. E.
Thompson, *Adv. Mater.*, 1998, **10**, 1108.
81 L. C. Palilis, A. J. Mäkinen, M. Uchida, and Z. H. Kafafi, *Appl. Phys. Lett.*,
2003, **82**, 2209.
82 S. Thayumanavan, S. Barlow, and S. R. Marder, *Chem. Mater.*, 1997, **9**, 3231.
83 J.-L. Maldonado, M. Bishop, C. Fuentes-Hernandez, P. Caron, B. Domercq,
Y.-D. Zhang, S. Barlow, S. Thuyumanavan, M. Malagoli, J. L. Brédas, S. R.
Marder, and B. Kippelen, *Chem. Mater.*, 2003, **15**, 994.
84 M. Thelakkat, R. Fink, F. Haubner, and H.-W. Schmidt, *Macromol. Symp.*,
1997, **125**, 157.
85 E. Bellmann, S. E. Shaheen, R. H. Grubbs, S. R. Marder, B. Kippelen, and N.
Peyghambarian, *Chem. Mater.*, 1999, **11**, 399.
86 H. B. Goodbrand and N.-X. Hu, *J. Org. Chem.*, 1999, **64**, 670.
87 S. Gauthier and J. M. J. Fréchet, *Synthesis*, 1987, 383.
88 S. Tokito, K. Noda, K. Shimada, S. Inoue, M. Kimura, Y. Sawaki, and Y.
Taga, *Thin Solid Films*, 2000, **363**, 290.
89 R. Fáber, G. F. Mielke, P. Rapta, A. Staško, and O. Nuyken, *Collect. Czech.*
Chem. Commun, 2000, **65**, 1403.
90 Y. Kuwabara, H. Ogawa, H. Inada, N. Noma, and Y. Shirota, *Adv. Mater.*,
1994, **6**, 677.
91 M. Thelakkat, C. Schmitz, C. Hohle, P. Strohhriegl, H.-W. Schmidt, U.
Hofmann, S. Schlöter, and D. Haarer, *Phys. Chem. Chem. Phys.*, 1999, **1**,
1693.
92 M. J. Plater and T. Jackson, *J. Chem. Soc., Perkin Trans. 1*, 2001, 2548.
93 J. P. Chen, H. Tanabe, X.-C. Li, T. Thomas, Y. Okamura, and K. Ueno, *Synth.*
Met., 2003, **132**, 173.
94 S. Tanaka, T. Iso, and Y. Doke, *Chem. Commun.*, 1997, 2063.
95 H. Tanaka, S. Tokito, Y. Taga, and A. Okada, *Chem. Commun.*, 1996, 2175.
96 A. Kraft, P. L. Burns, A. B. Holmes, D. D. C. Bradley, R. H. Friend, and J. H.
F. Martens, *Synth. Met.*, 1993, **55-57**, 4163.
97 M. Thelakkat, J. Hagen, D. Haarer, and H.-W. Schmidt, *Synth. Met.*, 1999,
102, 1125.
98 Y.-D. Zhang, R. D. Hreha, G. E. Jabbour, B. Kippelen, N. Peygambrian, and
S. R. Marder, *J. Mater. Chem.*, 2002, **12**, 1703.
99 B. Liu and W. Huang, *Thin Solid Films*, 2002, **417**, 206.

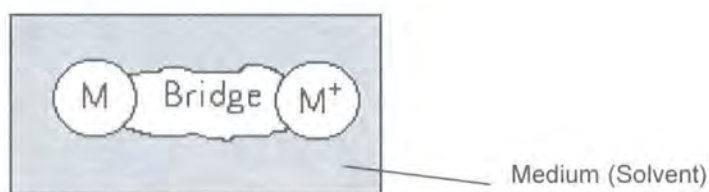
Chapter Two

Concepts and Techniques

The stability of the radical cations formed on oxidation of tetraaryl biphenyl diamines and the idea that the radical is delocalised over multiple sites has led to the description of these materials as mixed valence compounds. A brief review of the theory of mixed valence compounds and electron transfer is presented here.

2.1 Electron Transfer

Inter and intra-molecular electron transfer (ET) reactions are of great importance in chemistry and biology and a great deal of effort has been put into understanding them. In order to study the processes, researchers have typically identified and quantum mechanically treated the electronic manifolds of the localised M and M^+ sites (designated the diabatic states), then formulated the electronic coupling process mediated by the energetic and electronic features of any intervening medium. The medium may be an intramolecular "bridge", as well as the surrounding environment.



Examples of applications of this system are:

Molecule—Molecule—Molecule

Covalently linked

Molecule----Molecule----Molecule

Non-bonded contact

Electrode—Molecule----Electrode

As in scanning tunnelling
microscopy

Figure 2.1 Schematic depiction of two redox active sites linked by a bridge, and some applications of these systems

If the constituents of the two sites are identical, but assuming that the left and right-hand sites can be distinguished, the energy of the electron (or hole) at the two sites is identical since the constituents are the same, that is, the equilibrium constant for figure 2.1 is 1 ($\Delta G = 0$). The species on either side of the equilibrium are energetically degenerate electronic isomers. As stated above, there is no free energy change accompanying the electron transfer, there is however an activation barrier; E_{th} to the process.

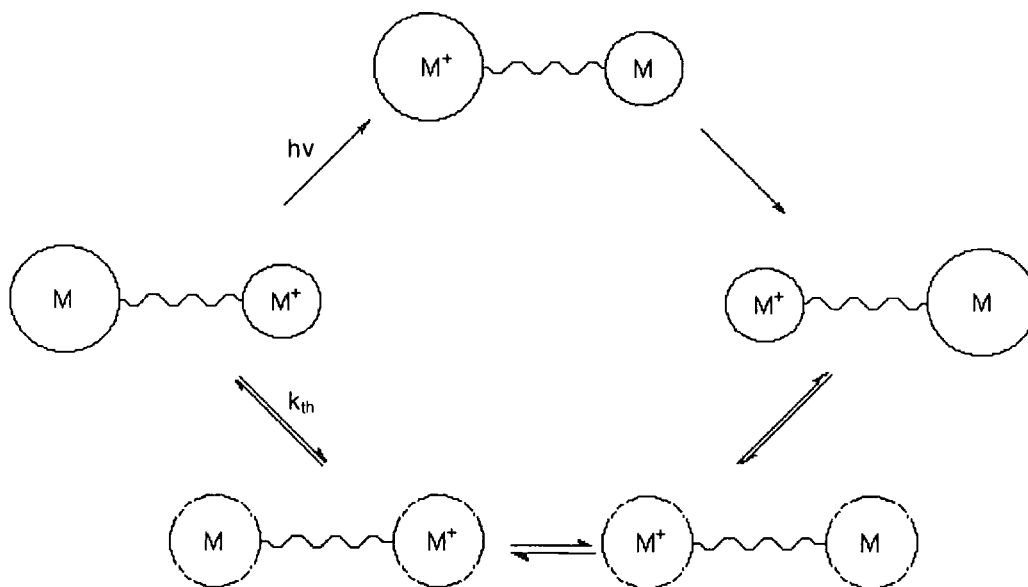


Figure 2.2 Optical and thermal electron transfer paths

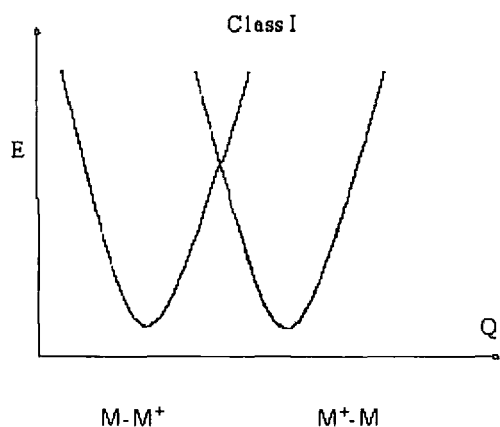
As a consequence of the differing solvent and substituent environments, the electron transfer is accompanied by nuclear rearrangement at each site. As electronic motion occurs at a much shorter time-scale than nuclear motion (the Franck Condon principle), this nuclear rearrangement gives rise to the electron transfer activation barrier E_{th} . If spontaneous electron transfer were to occur between M and M⁺ in their original configurations, the product would be formed in a vibrationally excited state: M⁺ having the substituent bond lengths and solvation of M, and M in a configuration appropriate to M⁺. This would not conserve energy. This thermally ‘forbidden’ pathway is the upper route in figure 2.2. For thermal electron transfer, rearrangement of the substituents and solvent about M and M⁺ precedes the electron transfer step, giving rise to an energy barrier to the process. The electron transfer occurs within an activated complex in which the M-L and M⁺-L (L denotes substituents bound to the redox centre M) bond lengths and solvent environment are the same and are intermediate between the M-L and M⁺-L values. This thermally allowed route is the lower pathway in figure 2.2. The upper pathway in figure 2.2 can be induced when incident light of the correct frequency is absorbed and supplies the energy required to form the excited state.¹ The upper pathway is designated optical electron transfer and occurs when $E_{op} = h\nu$.

Electron transfer theory was initially developed by Marcus,² who introduced the importance of the total reorganisation energy λ and the electronic coupling element H_{ab} , both of which will be discussed in more detail later.

Much of the initial work on mixed-valence compounds stemmed from the work of Creutz and Taube who studied $[(\text{NH}_3)_5\text{-Ru-Pz-Ru}(\text{NH}_3)_5]^{5+}$ in which the two ruthenium centres are in different oxidation states (Pz = Pyrazine). The ultra-violet and visible spectra of $[(\text{NH}_3)_5\text{-Ru-Pz-Ru}(\text{NH}_3)_5]^{5+}$ contained only features expected for a species containing Ru(II) and Ru(III) centres. Examination of the NIR region however contained a band absent in the spectra of the 4+ and 6+ dimers, the optical electron transfer band.³

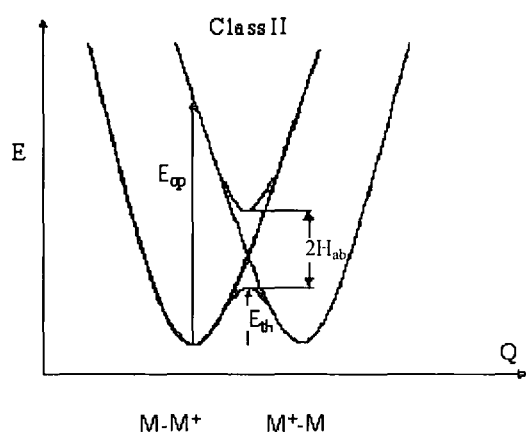
Robin and Day devised a scheme for classifying mixed valence materials. They allocated materials into Class I, II or III depending on the strength of the electronic interaction between the sites of differing oxidation states, ranging from no interaction (Class I) through modest interaction (Class II) to very strong electronic coupling (Class III).⁴

The properties of Class I systems are essentially those of the separate sites. In Class III systems the interaction of the two sites is so great that the system is delocalised and possesses its own unique properties. Class II systems are intermediate, with interaction between the two sites, although this interaction is sufficiently weak so as to transiently localise the charge. These materials generally possess novel optical and electronic properties in addition to those of the separate sites. To fully understand the classification and theory it is beneficial to plot the differing potential energy curves of the three classes of materials. The potential energy surface of a degenerate mixed valence system can be constructed from parabolic functions that represent the diabatic (non-interacting) states. Electronic coupling of these diabatic states leads to an avoided crossing in the intersection region of the two parabolas and, thus, to two adiabatic surfaces where the splitting at the (avoided) intersection is $2H_{ab}$.



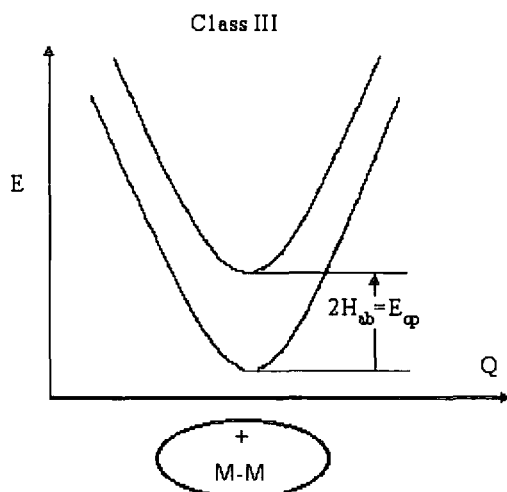
With no interaction the two Potential Energy curves are separate.

(Q = Reaction Coordinate)



When electronic coupling occurs, the wave functions mix in a manner described by the electronic coupling element H_{ab} . If H_{ab} is small (and/or λ is large) there are two minima and two electronic states which can inter-convert by two routes.⁵

The two processes are as outlined above, a thermal process, which is governed by $E_{th} = \lambda/4 - H_{ab}$, and an optical process where the system is photo-excited from one minimum of the lower PE surface to the Franck-Condon state of the upper PE surface. The energy of this excitation E_{op} is the Marcus reorganisation energy λ , which is comprised of an inner (vibronic) component λ_v , which is due to reorganisation of the molecule on transfer of the charge, and a solvent shell reorganisation component λ_s .



As H_{ab} increases, the thermal barrier $E_{th}=(\lambda/4)-H_{ab}$ decreases. When H_{ab} is sufficiently large there is a single symmetrical electronic and nuclear state.

The discrimination between Classes II and III is not simplistic as the observed behaviour is dependent on the rate of the ET process with respect to the time-scale of the experimental technique. For this reason organic materials on the borderline between Classes II and III have recently attracted a great deal of theoretical and experimental study.⁶⁻⁸

For both Class II and III compounds, the absorption bands due to E_{op} , which are usually found in the NIR region, contain a large amount of information, and can be analysed by a number of methods.⁹ The shape of the band provides information on whether a material is Class II or III. For a Class II material, if one constructs a potential energy surface from two diabatic parabolas and assumes a Boltzmann distribution of vibrational states over the ground-state surface, it is reasonable to expect an approximate Gaussian absorption band shape centred at $\tilde{\nu}_{max}$, where $\tilde{\nu}_{max}$ corresponds to E_{op} .

In the case of Class III compounds where H_{ab} is large, a Boltzmann distribution of states is still assumed, but it is important to note that the smallest vertical excitation cannot be less than the smallest energy gap between the ground and excited states, which is $2H_{ab}$ for both Class II and III. The band now displays a band maximum $\tilde{\nu}_{max} \approx \lambda \approx E_{op}$ at the minima of the lower energy surface. As a result the band displays marked asymmetry due to this low energy "cut off" at $2H_{ab}$.^{6, 7, 10, 11}

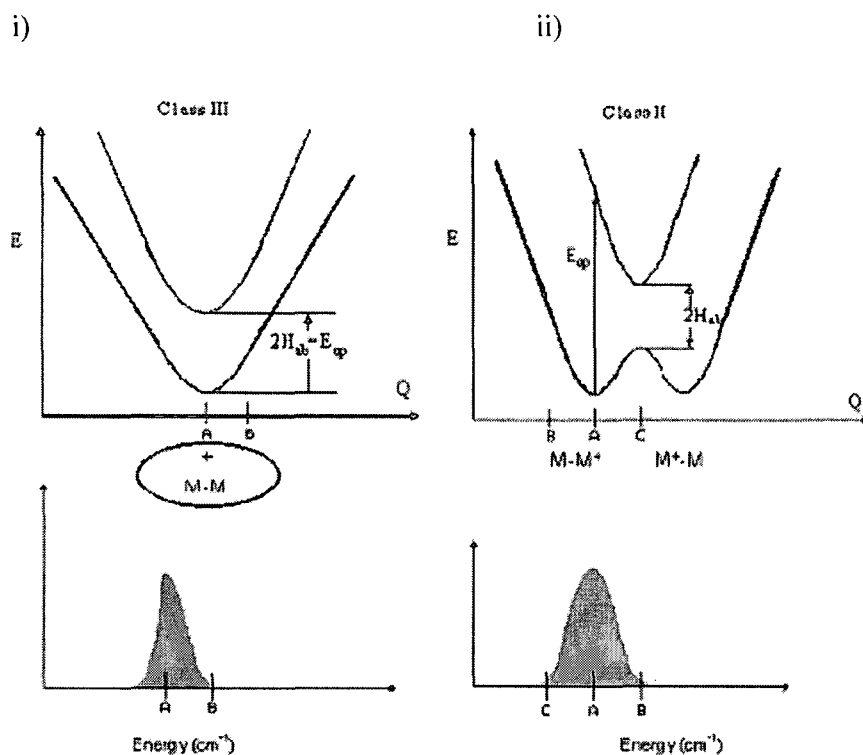


Figure 2.3 Energy plots (top) and resultant spectra illustrating the cutoff using the Marcus-Hush two state model. For i), A Class III system, $H_{ab} > \lambda/2$. The band maximum occurs at $2H_{ab}$ (A) with a high energy bandwidth extending to B. For ii), A Class II system, $H_{ab} < \lambda/2$. The band maximum (ν_{max}) occurs at E_{op} (A) but the band is more symmetric with both high and low energy bandwidth distribution.

A great deal of information can be extracted from analysis of these bands. Hush and others developed theoretical treatments from consideration of Class II mixed valence compounds and their spectroscopic properties. For Class II species, Hush theory can be used to deduce the electronic coupling parameter H_{ab} (in cm^{-1}). For this purpose equation 2.1 is often used.¹²

$$H_{ab} = 0.0206/r (\tilde{\nu}_{max} \tilde{\nu}_{1/2} \epsilon)^{1/2} \quad \text{Equation 2.1}$$

$$\tilde{\nu}_{1/2} (\text{HTL}) = 47.94 (\tilde{\nu}_{max})^{1/2} \quad \text{Equation 2.2}$$

However, the extinction coefficient ϵ , the bandwidth at half height $\tilde{\nu}_{1/2}$ and the electron transfer distance r (in \AA) must all be known. The value of r can be difficult to determine precisely, especially for systems with delocalised frontier orbitals. If the vibrational levels are in the order of $k_B T$ or smaller, the situation relates to the high

temperature limit (HTL) and the bandwidth at 298 K is given by equation 2.2. Equation 2.1 is only valid for true Gaussian shaped curves, which only occur when the diabatic potential surfaces are true parabolas. A more rigorous quantum mechanical formulation of equation 2.1 is equation 2.3.¹³

$$H_{ab} = \tilde{\nu}_{\max} \mu_{eg}/er \quad \text{Equation 2.3}$$

where $\mu_{eg} = 0.09584(\int \epsilon(\tilde{\nu}) d\tilde{\nu} / \tilde{\nu}_{\max})^{1/2}$ Equation 2.4

In this equation μ_{eg} is the transition moment connecting the ground and the excited state, $\tilde{\nu}_{\max}$ is the transition energy, r is the distance between the diabatic (non-interacting) redox active centres and e is the elementary charge. This equation has the advantage that no assumption is made about the band shape as μ_{eg} can be calculated from the integrated absorbance band of any band shape via equation 2.4.

The need for accurate analysis of the NIR absorption band has resulted in the development of a method in which construction of a vibronic matrix allows the fitting of a theoretical band to the experimental data. The adjustment of only three parameters, the electronic coupling parameter H_{ab} , the linear vibronic coupling constant l_y and the reorganisation energy λ enables accurate reproduction of experimental results and makes no assumptions about the electron transfer distance in the molecule.¹⁴

As the surrounding medium is affected by the rearrangement of the material on charge transfer, contributing to the total rearrangement energy through the component λ_s , solvent effects have been studied.^{1, 6, 15} The total reorganisation energy decreases as the solvent becomes less polar, and by assuming that the solvent may be considered as a dielectric continuum, Marcus introduced an equation that relates λ_s to the Pekar factor which depends only on the bulk solvent parameters, the refractive index at the sodium D line and the static dielectric constant.¹⁵

2.2 Experimental Techniques

2.2.1 Electrochemistry

The basis of cyclic voltammetry, a linear sweep method, involves application of a potential gradient to the working electrode, from the initial potential E_i to the first vertex (maximum E_{\max} or minimum potential E_{\min}), the sweep then reverses and sweeps to the second vertex (E_{\min} or E_{\max}) then continues to the final potential, E_f . $I_{p,a}$ and $I_{p,c}$ are the anodic and cathodic peak currents. (Figure 2.5)

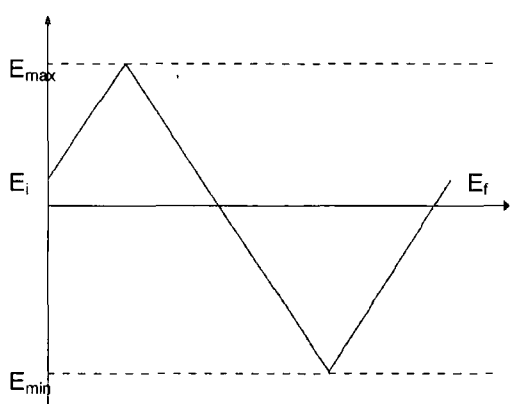


Figure 2.4 Sweep diagram for a cyclic voltammogram process

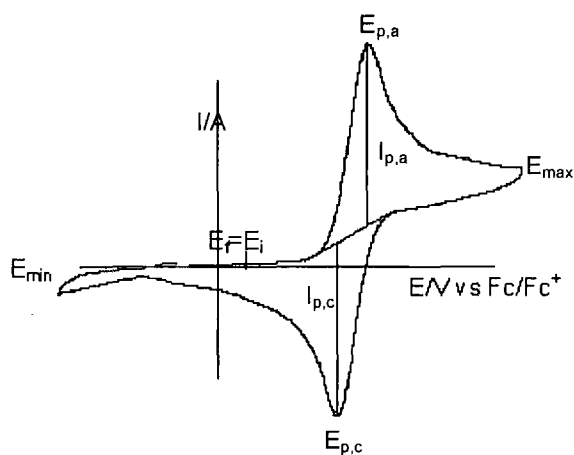
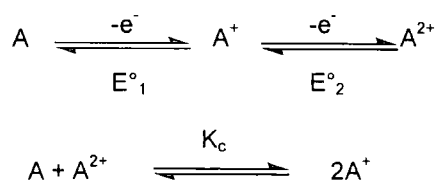


Figure 2.5 Typical cyclic voltammogram for a single oxidation process

The important parameters that are most easily adjusted are: initial potential E_i , initial sweep direction, scan rate, maximum potential E_{\max} , minimum potential E_{\min} , and final potential E_f .¹⁶ For a reversible redox system $E_{p,a} - E_{p,c} = 57.0/n$ mV, where n is the number of electrons involved. In organic solvents there is often solution resistance between the working and reference electrodes. This resistance leads to a shift in the potential of the working electrode of $I_p R$ where R is the uncompensated resistance of the solution. A broadening of the peaks is observed and greater separation between $E_{p,a}$ and $E_{p,c}$ than predicted. For systems where two or more successive oxidations or reductions can occur, $A - e^- \rightarrow A^+$ (E_1°) then $A^+ - e^- \rightarrow A^{2+}$ (E_2°), if E_2° and E_1° are well separated with $E_1^\circ > E_2^\circ$ then 2 or more waves are observed in the voltammogram.¹⁷

Through the use of the electrode potentials of the two processes, $A - e^- \rightarrow A^+$ (E°_1) and $A^+ - e^- \rightarrow A^{2+}$ (E°_2), calculation of the cell potential and then application of the Nernst equation produces the equilibrium constant, or in this specific case the comproportionation constant K_c , which is a measurement of the thermodynamic stability of the cation A^+ .



$$E = E^\circ_2 - E^\circ_1 \quad \text{Equation 2.5}$$

The Nernst equation states that $E = E^\circ - (RT/nF)\ln Q$, where E = cell potential, E° = formal electrode potential and Q = reaction quotient. At equilibrium, $Q = K$, and $E = 0$, therefore

$$\begin{aligned}
 \Delta E &= (RT/nF)\ln K_c \\
 E^\circ_2 - E^\circ_1 &= (RT/F)\ln K_c \\
 (E^\circ_2 - E^\circ_1)F/RT &= \ln K_c
 \end{aligned}
 \quad \text{Equation 2.6}$$

If the value of K_c is large then the equilibrium lies over to the right hand side and A^+ is stable with respect to A and A^{2+} .

In this study cyclic voltammograms were recorded using either an EG & G Versastat II or an Eco Chemie Autolab PGstat 30 controlled by a PC running GPES v.4.9 for Windows. The electrochemical cell used was an EG & G PARC micro cell fitted with an argon feed for the bubbler and purge inlets.

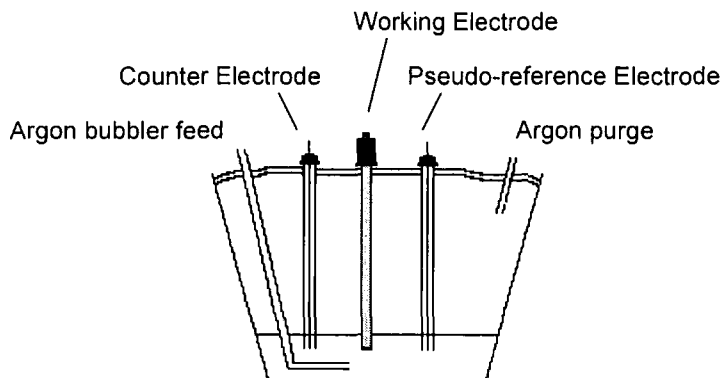


Figure 2.6 Typical cell arrangement for cyclic voltammetry measurements

The working electrodes were EG & G PARC millielectrodes, with a 2 mm diameter electrode surface, counter and pseudo-reference electrodes were platinum wire.

The solvent, CH_2Cl_2 , was deoxygenated by through bubbling of argon prior to taking measurements, and blanketed with argon during the scans.

The supporting electrolyte tetrabutylammonium tetrafluoroborate was synthesised from aqueous fluoroboric acid and tetrabutylammonium bromide and recrystallised from ethyl acetate and cyclohexane, until a CV showed no impurities. Tetrabutylammonium hexafluorophosphate (98 %) from Aldrich Chemical Company was used as received.

All potentials are given vs the ferrocene/ferrocenium couple as recommended by IUPAC, by addition of ferrocene as an internal standard.¹⁸ Where the ferrocene/ferrocenium couple would have obscured the peaks of interest decamethylferrocene was used as the internal standard, the decamethylferrocene/decamethylferrocenium couple occurring at $E^\circ -0.48$ V in CH_2Cl_2 vs Fc/Fc^+ .

2.2.2 Spectroelectrochemistry

The *in situ* UV-visible spectroscopic technique widely utilised in this research is a transmission technique. It is the simplest and most widely employed approach to obtaining the UV-Vis spectra of an electrogenerated species in solution. The technique involves passing the probe light beam directly through a solution of the analyte in close proximity to the working electrode.¹⁹⁻²² This allows any change in the intensity of absorbed light on oxidation/reduction to be measured directly. One of the methods adopted for this procedure is to have an electrode that is optically transparent, three approaches to achieving this have been developed: Metal minigrids, coating a thin layer of a semiconductor or metal onto glass or use of a reticulated vitreous carbon working electrode. Reticulated vitreous carbon is a sponge like form of glassy carbon, the transmittance of a 0.12 cm thick slice being ~24%. Use of a thin layer of In/SnO₂ (ITO) on a glass substrate provides a transparent metallic surface, enabling the ITO coated glass to be used as one of the solution cell windows although the solubility of ITO can cause problems.²³

Metal minigrids are perhaps the simplest electrode to use, consisting of a fine mesh of any selected metal (platinum, silver or gold are commonly used) which is inserted into a normal short pathlength cell, with an accompanying set of reference and counter electrodes to produce an optically transparent thin layer electrode (OTTLE) cell.^{24, 25} (Figure 2.7)

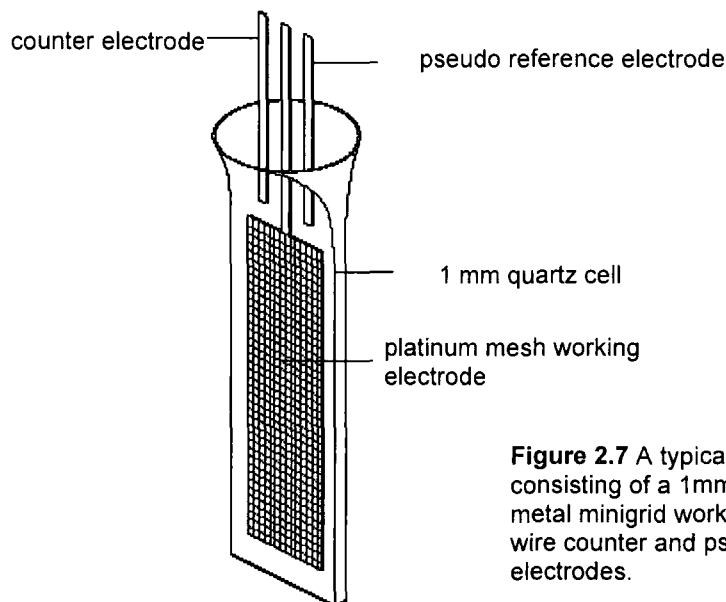


Figure 2.7 A typical OTTLE consisting of a 1mm pathlength cell, metal minigrad working electrode and wire counter and pseudo reference electrodes.

The use of a small solution volume cell allows bulk electrolysis to be achieved within a short period of time. Thus for the oxidation, $R - e^- \rightarrow O$ the spectrum would be recorded at a potential where R was stable, then the applied potential increased incrementally, with a spectrum being recorded at each step after the cell current has dropped to zero, i.e. the system has reached electrochemical equilibrium. This provides sequential spectra and if R and O have distinct absorption bands the oxidation of R can be monitored by the disappearance of bands associated with R and the growth of bands relating to O.²³

The OTTLE cell employed in this work consisted of a 30 x 10 x 1 mm quartz cuvette, containing a solution volume of ~0.3 ml in the thin layer region. The 3 electrode system was made up of a platinum mesh working electrode (0.06 mm wire diameter, 82 x 82 wires per inch, 65% open area) with platinum wire (0.40 mm diameter) pseudo reference and counter electrodes.²⁴

2.2.3 Fluorescence Spectroscopy

Emission and excitation spectroscopy, were used to obtain further information on the chromophore responsible for the UV/Vis absorption spectra. The emission spectrum of a species is obtained by irradiation of a dilute solution of a sample with a tuneable source of radiation.

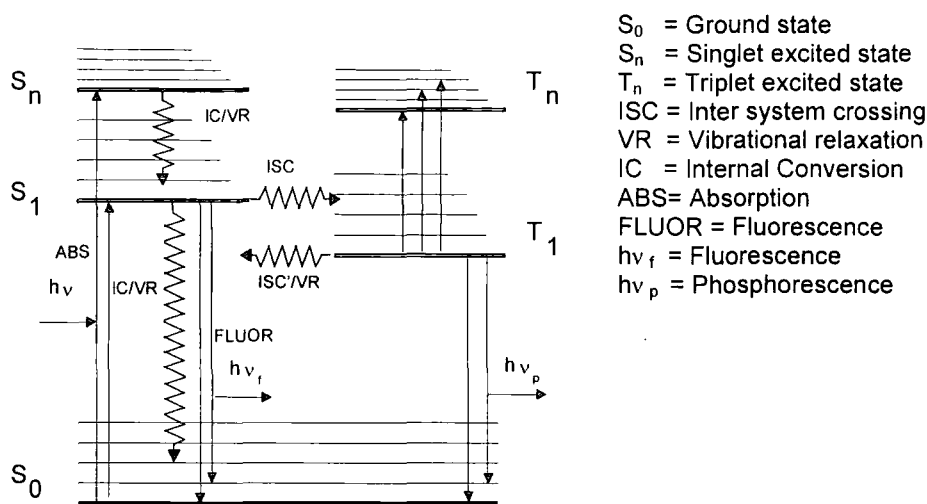


Figure 2.7 Jablonski diagram illustrating the processes that can occur on absorption of a photon.

The excitation spectrum is obtained by the monitoring of the intensity of fluorescence at a pre-selected wavelength as a function of excitation wavelength.

For a pure sample the excitation spectrum is normally identical to the absorption spectrum, any deviation is indicative of either an impure sample or, less commonly anomalous emission behaviour. If the spectra are observed to differ then more detailed studies, including the recording of total excitation-emission matrices and time resolved spectra, are necessary.

2.2.4 Raman and Resonance Raman Spectroscopy

Raman spectroscopy probes the vibrational energy levels of a sample, through examination of the frequencies present in the radiation scattered by the sample. A typical experiment involves the irradiation of the sample with a monochromatic light source, usually a laser, and monitoring of the scattered radiation. The incident photons interact with the electron cloud around the nucleus of the molecule, distort it, and then scatter. Most of the scattered light will be of the same frequency as the incident light

and is termed Rayleigh scattering. This is an elastic process where little or no energy is transferred to the analyte molecules.

However, approximately one photon in every million is scattered inelastically, emerging with a different energy to that of the incident photons. This is termed Raman scattering and is an inherently weak effect. The difference in energy between the scattered and incident photons is equal to the energy required to change the molecule from one vibrational state to another. Energy can either be transferred from the photon to the molecule or from the molecule to the photon. This results in two series of Raman bands being observed.

When the molecule is in the lowest vibrational energy state of the ground electronic state it can be excited to a virtual state of equal energy to the photon beam. The molecule then relaxes to an excited vibrational energy level of the ground electronic state. This relaxation occurs by the emission of light from the molecule and is termed Stokes Raman scattering. Anti-Stokes Raman scattering occurs when the molecule is in an excited vibrational energy level of the ground electronic state, and the photon beam excites it to a virtual state. The molecule then relaxes back down to the lowest vibrational energy level of the ground electronic state by emission of light. These processes are shown in figure 2.9.

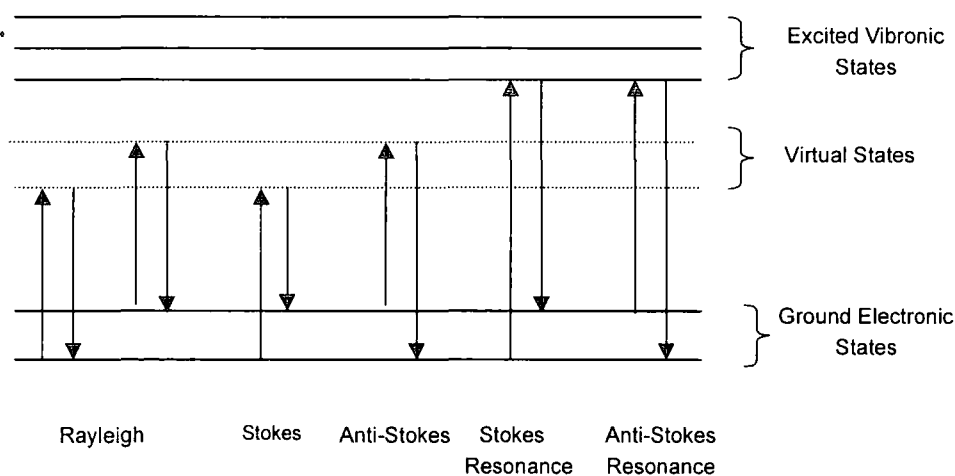


Figure 2.9 Schematic diagram of Rayleigh, Raman, and resonance Raman scattering

A diffraction grating is employed to distinguish between the Rayleigh, Stokes and anti-Stokes radiation, with the Rayleigh radiation being removed by a notch filter, allowing only the Stokes and anti-Stokes radiation through to the detector.

The selection rules for Raman spectroscopy state that a molecule is Raman active if the molecule is anisotropically polarisable. A molecule is anisotropically polarisable if the polarisation of the molecule induced by an electric field is dependent on the direction of the field.²⁶

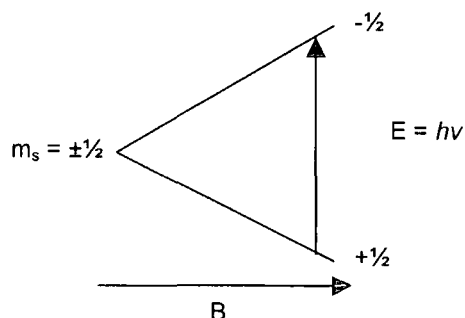
If a scattering system has an absorption band close to or coincident with the excitation frequency, resonance Raman results, producing a significant enhancement in the intensity of certain Raman bands. Resonance Raman results from the promotion of an electron into an excited electronic-vibrational state, accompanied by immediate relaxation into a vibrational level of the ground state.(Figure 2.10) This allows both electronic and vibrational information to be gained from the resulting spectrum, whereas Raman scattering only produces vibrational information. Resonance Raman provides enhancement by a factor of up to 10^4 over normal Raman scattering. It also has the advantage of being able to be used as a probe of chromophore structure since only the vibrational modes associated with the chromophore are enhanced.^{26, 27}

2.2.5 Electron Spin Resonance Spectroscopy

The electronic spin of an electron can be described in terms of the selection rule $S = \frac{1}{2}$, $m_s = \pm\frac{1}{2}$, usually the two spin states $m_s = \pm\frac{1}{2}$, are degenerate. When the electron is placed in a magnetic field the degeneracy splits, and the energy levels of an electron spin are given by equation 2.8.

$$E_{m_s} = g_e \mu_B m_s B, \quad m_s = \pm\frac{1}{2} \quad \text{(Equation 2.7)}$$

where B is the strength of the magnetic field and μ_B is the Bohr magneton. The energy of an α electron ($m_s = +\frac{1}{2}$) increases and the energy of a β electron ($m_s = -\frac{1}{2}$) decreases as the field is increased.



The separation of the levels is given by equation 2.9

$$\Delta E = E_\alpha - E_\beta = g_e \mu_B B = h\nu \quad \text{(Equation 2.8)}$$

Exposing the sample to electromagnetic radiation of frequency ν , causes resonant absorption to occur. ESR is the study of molecules containing unpaired electrons by observing the magnetic fields at which they come into resonance with monochromatic microwave radiation, usually 9-10 GHz or X-band radiation. It is the coupling of the electronic spin with nuclear spins of other atoms in the molecule that provides the most information in an ESR spectrum, as this leads to hyperfine coupling, the splitting of individual resonances due to interaction of the electron with other nuclei in the material. This is caused by the interaction of the electronic spin with the localised magnetic field due to the spin orientation of the nucleus. $^{14}\text{Nitrogen}$ has $I = 1$, so coupling of the electron to nitrogen gives three lines of equal intensity in the spectrum, because the nitrogen nucleus has three possible spin orientations, and each spin orientation is possessed by one third of all the radicals in the sample.²⁸ The technique is very sensitive and adaptable to running at both elevated and low

temperatures and also to *in-situ* radical generation through electrochemical generation of oxidised or reduced samples.

This is achieved through the use of a modified cell fitted with a three electrode arrangement, allowing *in-situ* electrochemistry, in an entirely analogous manner to that seen for UV/Vis spectroelectrochemistry.

References for Chapter 2

- 1 C. Creutz, *Prog. Inorg. Chem.*, 1980, **30**, 1.
- 2 R. A. Marcus and N. Sutin, *Biochim. Biophys. Acta*, 1985, **811**, 265.
- 3 C. Creutz and H. Taube, *J. Am. Chem. Soc.*, 1969, **91**, 3988.
- 4 M. B. Robin and P. Day, *Adv. Inorg. Chem. Radiochem.*, 1967, **10**, 247.
- 5 N. S. Hush, *Coord. Chem. Rev.*, 1985, **64**, 135.
- 6 C. Lambert and G. Nöll, *J. Am. Chem. Soc.*, 1999, **121**, 8434.
- 7 S. F. Nelsen, *Chem. Eur. J.*, 2000, **6**, 581.
- 8 M. Holzapfel, C. Lambert, C. Selinka, and D. Stalke, *J. Chem. Soc., Perkin Trans. 2*, 2002, 1553.
- 9 S. F. Nelsen, H. Q. Tran, and M. A. Nagy, *J. Am. Chem. Soc.*, 1998, **120**, 298.
- 10 B. S. Brunshwig, C. Creutz, and N. Sutin, *Chem. Soc. Rev.*, 2002, **31**, 168.
- 11 V. Coropceanu, M. Malagoli, J. M. André, and J. L. Brédas, *J. Chem. Phys.*, 2001, **115**, 10409.
- 12 C. Lambert and G. Nöll, *Angew. Chem. Int. Ed.*, 1998, **37**, 2107.
- 13 C. Lambert and G. Nöll, *J. Chem. Soc., Perkin Trans. 2*, 2002, 2039.
- 14 V. Coropceanu, M. Malagoli, J. M. André, and J. L. Brédas, *J. Am. Chem. Soc.*, 2002, **124**, 10519.
- 15 S. F. Nelsen and H. Q. Tran, *J. Phys. Chem. A*, 1999, **103**, 8139.
- 16 C. M. A. Brett and A. M. O. Brett, 'Electrochemistry: Principles, Methods and Applications', Oxford University Press, 1994.
- 17 A. J. Bond and L. R. Faulkner, 'Electrochemical Methods', Wiley, 1980.
- 18 N. G. Connelly and W. E. Geiger, *Chem. Rev.*, 1996, **96**, 877.
- 19 F. Hartl, H. Luyten, H. A. Nieuwenhuis, and G. C. Schoemaker, *Appl. Spectrosc.*, 1994, **48**, 1522.
- 20 R. W. Murray, W. R. Heineman, and G. W. O'Dom, *Anal. Chem.*, 1967, **39**, 1666.
- 21 J.-S. Yu, C. Yang, and H.-Q. Fang, *Anal. Chim. Acta*, 2000, **420**, 45.
- 22 L. Kavan, L. Dunsch, and H. Kataura, *Chem. Phys. Lett.*, 2002, **361**, 79.
- 23 P. A. Christensen and A. Hamnett, 'Techniques and Mechanisms in Electrochemistry', Blackie Academic & Professional, 1994.
- 24 C. M. Duff and G. A. Heath, *Inorg. Chem.*, 1991, **30**, 2528.
- 25 A. Neudeck and L. Kress, *J. Electroanal. Chem.*, 1997, **437**, 141.
- 26 D. A. Long, 'Raman Spectroscopy', McGraw-Hill International Book Company, 1977.
- 27 J. T. Hupp and R. D. Williams, *Acc. Chem. Res.*, 2001, **34**, 808.
- 28 P. W. Atkins, 'Physical Chemistry', OUP, 1995.

Chapter Three

Triarylamines and Tetra Aryl Biphenyl Diamines

3.1 Introduction

Many hole transporting materials are oligo or polymeric compounds based on a triarylamine moiety.¹⁻⁹ In order to understand the properties of these materials, it is beneficial to first consider the behaviour of the isolated fragment. The electrochemical response of a wide range of substituted triarylamines have been studied in considerable detail, and in general terms NAr_3 species undergo a chemically reversible one electron oxidation. The radical cations of these materials have found application as mild oxidising agents, as through the careful selection of substituents, materials with a range of oxidation potentials are accessible. (Table 3.1)

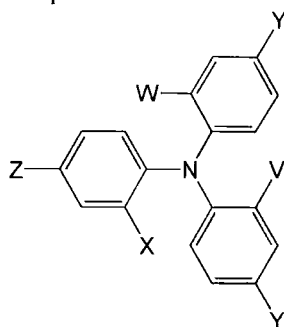
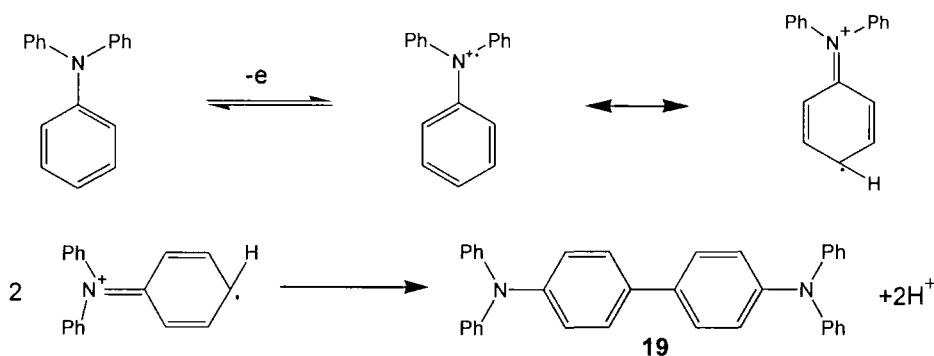


Table 3.1

	V	W	X	Y	Z	E° vs Fc/Fc^+
2	H	H	H	Br	Br	0.67
3	Br	Br	Br	Br	Br	1.09
4	H	H	H	COCH_3	COCH_3	0.85
5	H	H	H	NO_2	NO_2	1.15
6	H	H	H	CN	CN	1.03
7	H	H	H	Br	COCF_3	0.8
8	Br	Br	Br	Br	COCF_3	1.2
9	H	H	H	Br	$\text{C}(\text{CF}_3)=\text{CH}_2$	0.63
10	Br	Br	Br	Br	$\text{C}(\text{CF}_3)=\text{CH}_2$	1.07
11	H	H	H	NO_2	Br	0.99
12	H	H	H	$\text{Si}(\text{CH}_3)_3$	$\text{Si}(\text{CH}_3)_3$	0.43
13	H	H	H	COCF_3	COCF_3	1.03
14	H	H	COOH	Br	Br	0.76
15	H	H	COOCH_3	Br	Br	0.77
16	H	H	COOCH_2 (4- NO_2)Ph	Br	Br	0.74
17	H	H	H	CF_3	CF_3	0.95
18	H	H	H	C_2F_5	C_2F_5	0.99

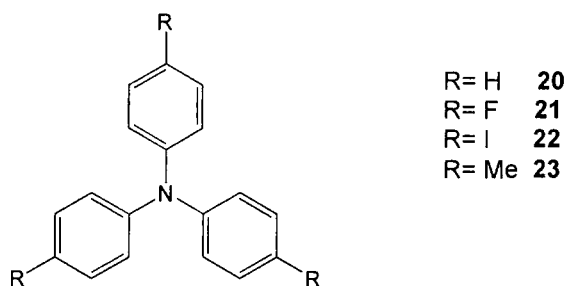
Stable radical cations are formed on oxidation only if all *para* positions are blocked by substituents. The anodic oxidation of triphenylamine is followed by a chemical reaction to form a tetraarylbi(biphenyl)diamine.^{10, 11} (Scheme 3.1) For example oxidation of triphenylamine (TPA) affords the chemically reactive monocation radical, TPA^{•+}. The cation rapidly dimerizes through a *para* position of one of the aryl rings to form *N,N,N',N'*-tetraphenyl-1,1'-biphenyl-4,4'-diamine (**19**). This is accompanied by the loss of two protons per dimer, but it has not been ascertained if the proton loss occurs before or after coupling.



Scheme 3.1 The reaction of triphenylamine radical cation to form **19**

The reaction product, **19**, is more easily oxidised than the TPA and undergoes further oxidation to the dication at the applied potential. Reduction of the dication reveals two successive one electron waves, indicating that the oxidation and reduction occur in discrete steps.

There have been a very small number of structural studies of triarylamines, and selected bond lengths and angles are summarised in table 3.2.¹²⁻¹⁴



In each case the nitrogen atom displays essentially trigonal planar geometry, with the three aryl rings displaying a propeller like geometry about the nitrogen centre. An

interesting point to note is that one of the rings is usually twisted at a greater angle than the others, 44-60° compared to 33-46°. The C-N bond lengths and twist angles of the rings are correlated, with the larger twist angle producing decreased overlap between the aromatic π system and the nitrogen lone pair resulting in a longer bond length.^{13, 14}

Table 3.2 Crystallographic and calculated structural parameters

Crystallographic data	N-C Bond length (Å)	Ring twist angle
23 ¹⁴	1.413, 1.414, 1.431	34.8°, 30.9°, 59.7°
20 ¹³	1.408, 1.419, 1.427	37.0°, 46.0°, 50.5°
21 ¹²	1.411, 1.417, 1.431	32°, 32°, 59°
22 ¹²		33°, 43°, 44°
Computational results		
20 ¹⁵	1.42	41.7°
20 ^{+1 15}	1.41	38.9°
20 ¹⁶	1.433	41.3°
20 ^{+1 16}	1.427	39.0°
23 ¹⁶	1.433	41.6°
23 ^{+1 16}	1.426	38.6°

The molecular structures of both the neutral and cationic states of an amine with appended biphenyls, tri(*p*-biphenyl)amine have been reported.^{17, 18} (Figure 3.1)

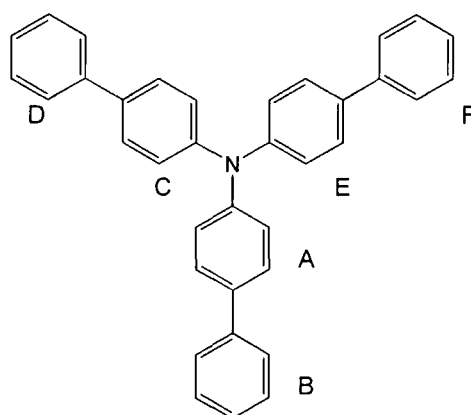


Figure 3.1 Molecular structure of tri(*p*-biphenyl)amine

The central triphenylamine moiety has a propeller-like structure about the nitrogen, with torsion angles of 45.7° for ring A, 56.8° for ring C and 35.4° for ring E similar values as seen for discrete triphenylamines. The biphenyl units however are twisted around the inter-ring C-C bonds, ring F is rotated clockwise 39.8° against the inner phenyl ring E, rings B and D are twisted counter clockwise by 27.0° and 40.1° respectively against inner rings A and C.

The radical cation, as the perchlorate salt, also describes a propeller-like geometry around the nitrogen, with angles of 43.5° , 45.3° and 26.5° , showing an average reduction of 8° . The twist angles in the biphenyls are 14.5° , 23.0° and 36.4° with associated bond lengths of 1.481, 1.47 and 1.487 Å. Although the dihedral angles of these outer rings about the nitrogen are reduced relative to the neutral, which would be consistent with increased delocalisation of the positive charge, this particular pattern of angles is considered to result from crystal packing.

Although many derivatives of tetraarylbiphenylamines have been synthesised, solid state structural data is scarce, with only a single report describing the solid state structures of **1** and N,N'-diphenyl-N,N'-bis(4-methylphenyl)-1,1'-biphenyl-4,4'-diamine. These studies were determined using synchrotron based single crystal and powder X-ray diffraction methods, with the single-crystal data complicated by a degree of rotational disorder (Table 3.3).¹⁹

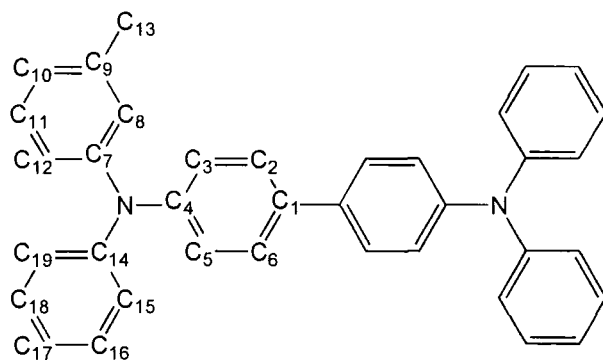


Figure 3.2 The molecular structure of **1**

The molecular structure of **1** revealed a planar configuration at the nitrogen centres, with the torsion angles of the surrounding aryl rings defining a propeller like geometry about the nitrogen centres with respect to the plane defined by the 3 N-C bonds. The N-C(4)_(biphenyl) bond length is slightly shorter than the N-C(7,14) bond

lengths at 1.411 Å compared to 1.427 and 1.422 Å. The central C-C bond length is 1.507 Å. The dihedral angle between the two rings of the biphenyl is 35.6°. There have been a number of structural studies on biphenyl, in the gas phase it has been shown to have a non-planar conformation with a dihedral angle of 40°. Solid state X-ray diffraction studies however have repeatedly found a planar structure with a central C-C bond of 1.496 Å. This bond length has been taken as an indication of an absence of conjugation between the rings.²⁰⁻²²

In light of the scarcity of experimental structural data it is not surprising that there have been few attempts at an experimental study relating structural aspects to the electronic properties of this important class of materials.²³

In contrast there have been a number of theoretical studies on the effects of oxidation on the both the electronic and molecular structure of the molecule. In terms of a Marcus theory-type approach, the energy necessary to reorganise the molecule from the preferred geometry of the neutral to the preferred energy of the radical cation can be estimated as the sum of λ_1 and λ_2 , where λ_1 is the difference between vertical and adiabatic ionisation energies of a neutral amine and λ_2 is that between vertical and adiabatic electron affinities of the cation radical. (Figure 3.3)^{24, 25}

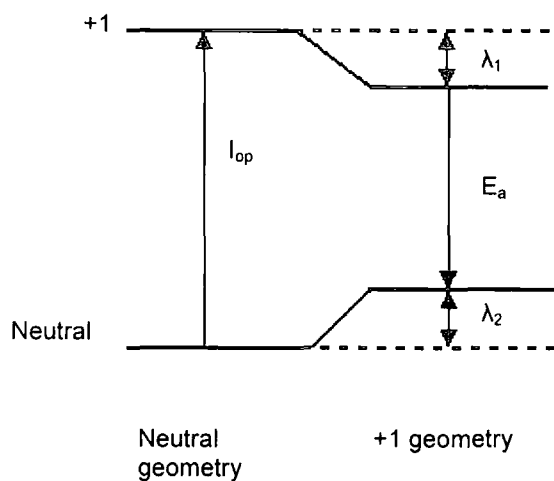
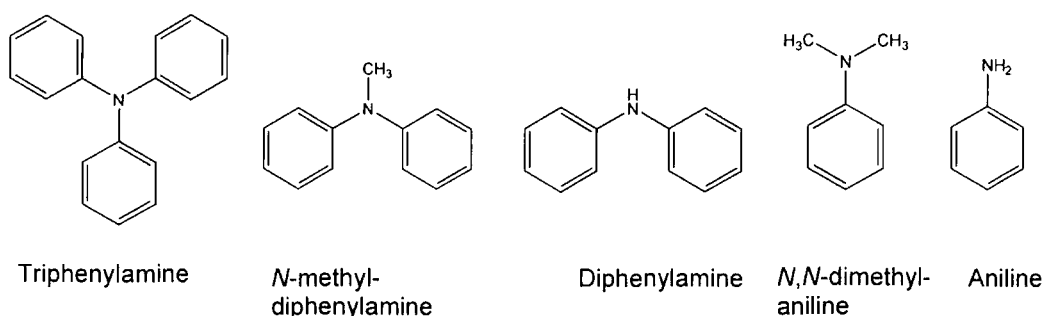


Figure 3.3
 I_{op} Ionization potential
 E_a Electron affinity
 λ_1 Reorganisation energy of +1
 λ_2 Reorganisation energy of neutral species

As the mechanism of hole transport through these materials is regarded as being through a hopping mechanism, charge moving from one molecule to another,^{26, 27} if the reorganisation energy related to formation of the radical cation can be reduced, then the energy of hole transport will also be reduced, leading to more effective hole transport.

Treating the data chronologically, one of the earliest computational studies on the geometry of **1** and its derivatives, investigated the single nitrogen centre molecules, aniline, *N,N*-dimethyl-aniline, diphenylamine, *N*-methyl-diphenylamine and triphenylamine, assuming that the properties of the two nitrogen centre molecule would be reflected in the half molecule.²⁵ The calculations were carried out using semi-empirical Austin Model 1 (AM1), Hartree Fock (HF) *ab initio* and density functional theory (DFT) methods. The geometries of the neutral and radical cation were calculated and the results from the different methods compared. It was found that the DFT method gave the best agreement, with the total λ value estimated from the difference between the neutral and radical geometries decreasing in the order *N,N*-dimethyl-aniline > Methyl-diphenylamine > triphenylamine which agrees with the increasing order of reported hole mobilities of dimers of the amines (Table 3.3).²⁴



A more comprehensive study by the same group using AM1 methods confirmed that rearrangement of the aryl rings to greater dihedral angles about the nitrogen centre was the dominating factor.²⁴ Both Tackley and Malagoli *et al.* have since used DFT to investigate the geometric and electronic structures of **1** as a whole molecule.^{15, 16} The geometries of both the neutral and radical cation states were optimised, and the energy corresponding to the neutral and cationic configurations was then calculated for each of the optimised geometrical structures. This provided four energy values, corresponding to the neutral species in the neutral geometry, the cation in the neutral geometry, the neutral species in the cation geometry and the cation in the cation geometry. From these energies the I_p and reorganisation energies can be estimated, (Table 3.3) as described in figure 3.2. All calculations were carried out using DFT with the B3LYP functional²⁸ and either the 6-31 G or 6-31G** basis set. The major differences reported between the neutral and radical cation species are found in the

biphenyl unit, the central C-C bond is shortened and the dihedral angle between the two rings is decreased.

In a combined experimental and theoretical study on the electronic structure of TPD and its derivatives through the use of gas-phase ultraviolet photoelectron spectroscopy with theoretical calculations a wide range of fluoride and methoxy substituted TPDs were investigated.²³ The neutral geometries were optimised using the semi-empirical Hartree-Fock AM1 method. On the basis of the structural data, the energy of the lowest transition was calculated by means of the semi-empirical intermediate neglect of differential overlap (INDO) Hamiltonian combined to a single configuration interaction scheme (SCI). The calculated gas-phase ionisation potential agreed with the experimental data with the calculated HOMO levels localised mostly on the biphenyl core, with the largest weights on the nitrogen atoms and the carbon on the biphenyl moiety bonded to the nitrogen atoms. It was observed that different conformers caused slight variation of the calculated ionisation energies, typically less than 50meV on 180° rotation of the NAr₂ group around the N-C bond. This change in conformation did not effect the HOMO energy.

A detailed study of the effect of different conformations of **1** was carried out by Brédas *et al.* who considered the six conformers illustrated in figure 3.4.²⁹

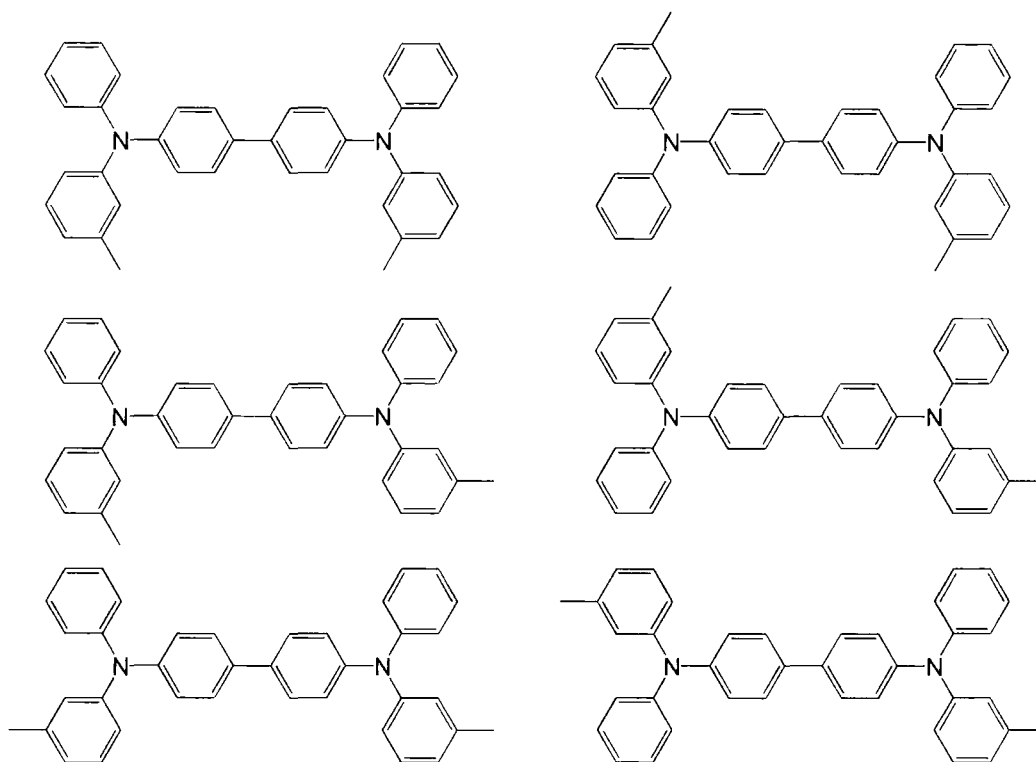


Figure 3.4 The 6 conformers of **1** considered by Brédas *et al.*

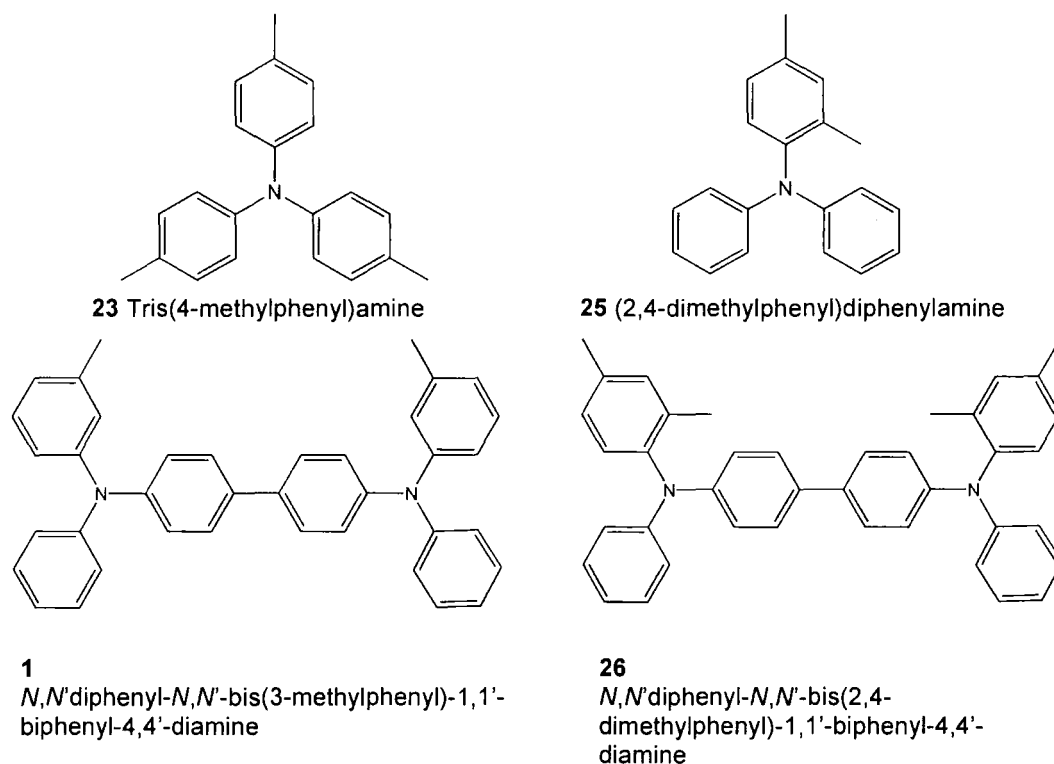
It was found that the DFT total energies of these six conformers differed by less than 0.42 kJ/mol. This indicates that all six conformers are equally likely to be present in an amorphous film. The main geometric parameters were found to be nearly identical, as was the value of the I_p , this was related to the HOMO mostly being localised on the central N-biphenyl-N moiety and thus being insensitive to ring twists on the periphery. A recent time dependent DFT study on TPD derivatives including *N,N,N',N'*-tetra(4-methoxyphenyl)-1,1'-biphenyl-4,4'-diamine (**24**) carried out geometry optimisations using DFT with the B3LYP functional, on the neutral, radical ground state and radical first excited state geometry,³⁰ these were used as part of a study to understand the charge transfer absorption bands present in the electronic spectra of TPD radical cations.

TABLE 3.3 Calculated molecular structure and electronic parameters for a selection of arylamines

	Method	Material	N-C (Å)	C(1)-C(1#) (Å)	Biphenyl twist	N-C torsion angle	Reorganisation energy (eV)	I_p (eV)
Sakanoue ²⁵	HF AM1	23	1.413					
	MO HF	23	1.417					
	DFT	23	1.423					
Sakanoue ²⁴	AM1 MO	1	1.412	1.459	38°		0.132	
	AM1 MO	1^{††}	1.388	1.439	26°			
Malagoli ¹⁵	DFT	1	1.42 1.42 _{biphenyl}	1.48	33.8°	42.3°, 40.6°, 42.0° _{biphenyl}	0.29	5.73
	DFT	1^{††}	1.43, 1.39 _{biphenyl}	1.46	23.0°	47.6°, 49.3°, 25.8° _{biphenyl}		
Tackley ¹⁶	DFT	1	1.435 1.430 _{biphenyl}	1.486	32.7°	42.6°, 39.5° _{biphenyl}	0.16	5.22
	DFT	1^{††}	1.407 _{biphenyl}	1.469	23.1°	44.0°, 30.1° _{biphenyl}		
Cornil ²³	HF AM1							8.07
	INDO							6.74
	DFT B3 LYP 6- 31G*	Cis 1	1.418 _{biphenyl}	1.481	34.9°	43.1°		4.68
	DFT B3 LYP 6- 31G*	Trans 1	1.419 _{biphenyl}	1.481	34.9°	42.4°		4.68
Coropceanu ³⁰	DFT B3 LYP 6 31**	24	1.413 _{biphenyl}	1.480	36°	48°, 32° _{biphenyl}		
		24^{††}	1.393 _{biphenyl}	1.459	25°	48°, 27° _{biphenyl}		
		24^{††*}	1.426 _{biphenyl}	1.487	39°	38°, 47° _{biphenyl}		
Experimental data ¹⁹		1	1.427, 1.422 1.411 _{biphenyl}	1.507	35.6°	56.8°, 49.8°, 46.0° _{biphenyl}		6.69
Experimental data ¹⁹		<i>N,N</i> -diphenyl- <i>N,N'</i> -bis(4-methylphenyl)-1,1'-biphenyl-4,4'-diamine			-44.5°	54.6°, 47.0°, 18.5° _{biphenyl}		

3.2 Results and Discussion

In order to conduct an experimental study of the electrochemical properties of tetraaryl biphenyl amines and tris(4-methylphenyl)amine, compound **23** was purchased from Aldrich chemical company, (2,4-dimethylphenyl)diphenylamine, compound **25** was synthesised by a palladium catalysed coupling reaction and compounds **1** and **26** were supplied by Avecia. Compound **26** differs from **1** by virtue of the methyl groups *ortho* and *para* to the amine centres on two of the four peripheral ring systems which were introduced to improve the solubility and reduce the crystallinity of the product. The *ortho* groups were expected to have some impact on the overall geometry of the compound in both the neutral and oxidised forms, particularly with respect to the orientation adopted by the substituted rings.



Cyclic voltammetry (CV) studies of **23** revealed a reversible oxidation wave as reported for similar compounds in the literature.(Table 3.4)¹⁰ Room temperature UV-Vis-NIR spectroelectrochemical studies of the oxidation of **23** revealed a set of π - π^* bands in the electronic spectrum, which shift to lower energy upon the oxidation from the neutral material (**23** 304 nm/20,810 mol⁻¹dm³cm⁻¹), through to the cation (**23**⁺ 348, 359, 370, 585, 674 nm/ 23,270 mol⁻¹dm³cm⁻¹). (Figure 3.5).

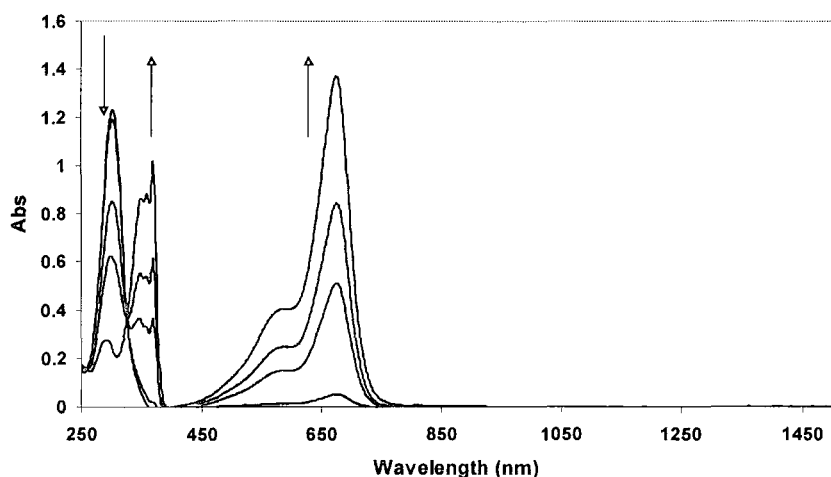


Figure 3.5 UV-Vis-NIR spectroelectrochemistry of **23** during sequential oxidation to 23^{+} . The arrows indicate the bands which grow and decay during the electrolysis. λ (nm)/ ϵ ($\text{mol}^{-1}\text{dm}^3\text{cm}^{-1}$) **23** 304/20,810; 23^{+} 674/23,270.

Cyclic voltammetry of **1** and **26** revealed two, reversible one electron waves associated with the formation of the cation radicals $[1]^+$, $[26]^+$ and dications $[1]^{2+}$, $[26]^{2+}$ (Table 3.4). The first oxidation of the bis-methylated compound **26** was thermodynamically more favourable than in the case of **1**, possibly due to the inductive effect of the methyl groups in the *ortho* and *para* positions. The second oxidation potentials were essentially the same. The potential difference between these two redox processes allows an estimate of the thermodynamic stability of the radical cation, 26^+ , with respect to disproportionation to **26** and 26^{2+} at ambient temperature ($1 K_c = 4,300$, $26 K_c = 20,500$). For similar systems, K_c values of similar magnitude are common, and suggest that the radical cations may be suitable targets for preparative studies.³¹

Table 3.4. Half-wave Potential ($E_{1/2}$ vs Fc/Fc^+) and the difference between First and Second Redox Process (ΔE) for **1**, **26** and **24** from Cyclic Voltammetry.

	$E_{1/2}$ (V)	$E_{1/2}$ (V)	ΔE (V)	K_c
23 [a]	0.347	-	-	-
1 [a]	0.292	0.507	0.215	4,300
26 [a]	0.250	0.505	0.255	20,500
24 [b]	0.085	0.305	0.220	5,250

[a] 0.1M $\text{NBu}_4\text{BF}_4/\text{CH}_2\text{Cl}_2$ at 200 mV/s.

[b] 0.1M $\text{NBu}_4\text{PF}_6/\text{CH}_2\text{Cl}_2$ at 250 mV/s (from reference [31])

Chemical oxidation of **1** with one equivalent of SbCl_5 in CH_2Cl_2 resulted in the immediate formation of a dark orange solution of the radical cation, although it has not yet been possible to isolate crystalline material from this solution. Oxidation of **26** produced a similarly coloured solution, from which dichroic, needle-like crystals of $[\mathbf{26}]\text{SbCl}_6$ with a metallic lustre were obtained following addition of hexane. The electronic spectrum of material isolated in this way was essentially identical to that observed spectroelectrochemically for the radical cation, with only minor deviations in band shape and energy of the NIR band arising from ion-pairing effects with the supporting electrolyte.

Given the interest in molecular conformation of species such as **26** and $\mathbf{26}^+$ single crystal X-ray diffraction studies of **26** and $[\mathbf{26}]\text{SbCl}_6$ were undertaken, using crystals grown from CH_2Cl_2 /hexane mixtures (Table 3.5). For the neutral molecule **26**, a planar conformation is found at the nitrogen centres, with N-C(7, 13) bond lengths of 1.417(5) and 1.443(5) Å to the peripheral phenyl groups, with the longer N-C distance being associated with the 2,4-dimethyl substituted ring. The N-C(4)_(biphenyl) bond length is 1.415(5) Å. The central C(1)-C(1') bond in the biphenyl moiety is 1.484(7) Å, and the bond lengths within the rings of the biphenyl group range between 1.385(5)-1.408(6) Å. There are no unusual C-C bond lengths within the peripheral phenyl groups. The torsion angles are summarised in table 3.5, and define the propeller like geometry about the nitrogen centres with respect to the plane defined by the three N-C bonds. The *ortho* methyl groups are found in a *trans*-type configuration, and reside on the same side of the biphenyl moiety. The twist angles between the biphenyl rings is 37.16° [C(2)-C(1)-C(1')-C(6')].

When compared to the orientation of the unsubstituted ring [C(4)-N(1)-C(7)-C(8) – 34.2(6)°], the methyl substituted ring [C(13)-C(18)] is rotated out of the NC_3 plane [C(14)-C(13)-N(1)-C(4) -67.9°], no doubt due to the steric effect of the C(19) methyl group. The decreased overlap between the aromatic π system and the nitrogen lone pair which results is responsible for the increased N-C(13) bond length noted above. With the exception of these steric constraints, the structure is very similar to the optimised geometry of **1** obtained using DFT methods.

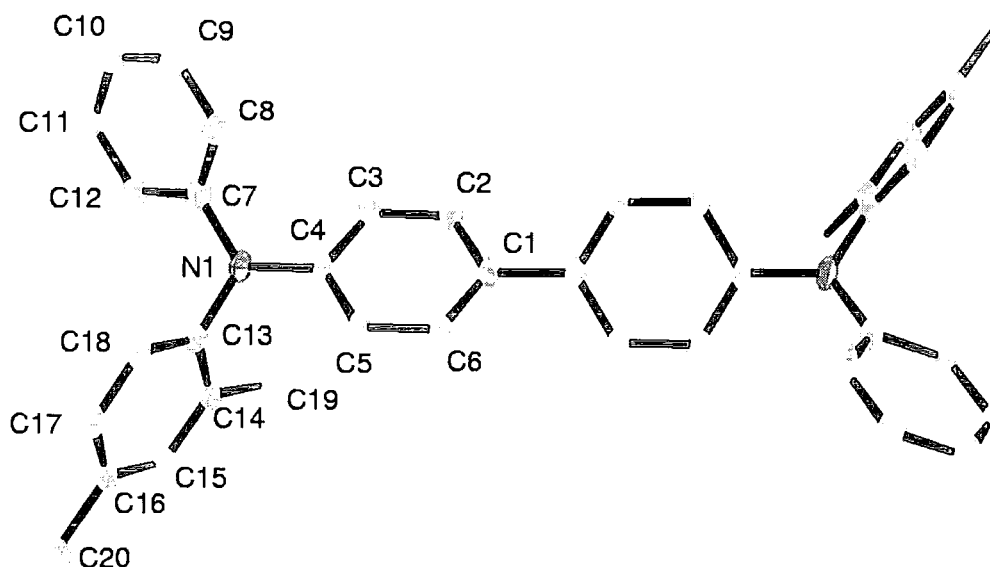


Figure 3.6 Molecular Structure of 26

Table 3.5. Selected bond lengths (Å), bond and torsion angles (°) for **1**^[a], **1**⁺^[b], **26**^[c], **26**⁺^[c]

	1	1 ⁺	26	26 ⁺
N(1)-C(4)	1.42	1.39	1.415(5)	1.391(8)
N(1)-C(7)	1.42	1.43	1.417(5)	1.420(8)
N(1)-C(13)			1.433(5)	1.445(9)
C(1)-C(1')	1.48	1.46	1.484(7)	1.458(12)
C(1)-C(2)	1.41	1.42	1.408(6)	1.419(9)
C(2)-C(3)	1.39	1.38	1.388(5)	1.386(9)
C(3)-C(4)	1.40	1.42	1.399(6)	1.392(9)
C(4)-C(5)			1.397(6)	1.409(9)
C(5)-C(6)			1.385(5)	1.366(8)
C(4)-N(1)-C(7)	120	120	122.3(3)	122.3(5)
C(4)-N(1)-C(13)	120	120	119.2(3)	119.5(5)
C(7)-N(1)-C(13)	120	120	118.1(3)	118.1(5)
C(2)-C(1)-C(1')-C(6')	33.8	23.0	37.1(3)	3.83
C(7)-N(1)-C(4)-C(3)	42.0	25.8	-37.0(6)	166.3(7)
C(13)-N(1)-C(4)-C(3)			150.5(4)	-16.5(9)
C(4)-N(1)-C(7)-C(8)	40.6	47.6	-34.2(6)	-54.7(10)
C(13)-N(1)-C(7)-C(8)			138.3(4)	128.1(8)
C(4)-N(1)-C(13)-C(14)	42.3	49.3	-66.0(5)	110.7(8)
C(7)-N(1)-C(13)-C(14)			121.2(4)	-71.9(9)

[a] Molecular structure data from Kennedy *et al.*¹⁹[b] DFT optimised structural parameters from Malagoli and Brédas¹⁵

[c] This work

In the crystal of **26** (Figure 3.8), a layered structure is found, with the layers running perpendicular to the *b*-axis. The molecules of each layer are out of register with those in the layer immediately above and below, giving an ABA motif. When viewed along the *b*-axis, the molecules form column-like stacks, with the adjacent stacks interdigitated to accommodate the *para* methyl groups. The disordered solvent molecules are found in the channels formed between these columns.

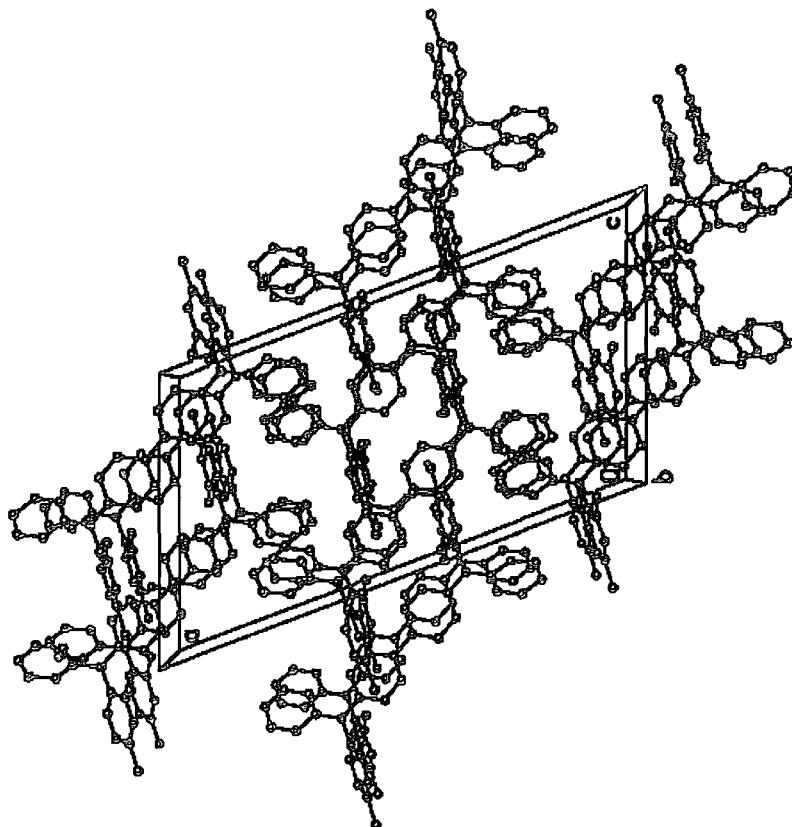


Figure 3.7 The molecular packing in the crystal of **26** viewed down the *b*-axis. The disordered solvent molecules have been omitted for clarity.

The radical cation **26**⁺ (Figure 3.7, Table 3.5) also displays a planar geometry about the nitrogen centres, and N-C(7, 13) bond lengths to the peripheral aryl ring systems are similar to those found in **26** [1.420(8), 1.445(9) Å]. The substituted ring is disordered over two sites (66/34 occupancy), which are related by a 180° rotation of the substituted ring systems around the N(1)-C(13) bond. In contrast to the structure of **26**, these methyl groups are now found on opposite sides of the biphenyl plane. The biphenyl group has rotated into a position closer to the NC₃ plane [C(3)-C(4)-N(1)-C(13) -16.5(9)°], and the twist angle between the biphenyl ring systems [C(6)-C(1)-C(1')-C(2')] has decreased to only 3.83°. The N-C(4)_(biphenyl) bond length [1.391(4) Å] is significantly shorter than the N-C(7, 13) bonds in either structure. However, the

C(1)-C(1') bond length [1.46(1) Å] in 26^+ is equivalent, within error, to that in **26**. While not strictly of statistical significance, it is still worth noting that the C(2)-C(3) [1.386(9) Å] and C(5)-C(6) [1.366(8) Å] fall at the shorter end of the range of C-C bond lengths in the biphenyl bridge [1.366(8) – 1.419(9) Å]. Electronic structure calculations indicate that the HOMO in species such as 26^+ is delocalised over the N-C₆H₄-C₆H₄-N moiety.^[12] Consequently, the bond lengths in **26** and 26^+ are not expected to be particularly sensitive to the oxidation state of the compound, as the fraction of electronic charge lost upon oxidation will be divided over all the atoms in the biphenyldiamine moiety. Nevertheless, the net result of oxidation is a marginal decrease in the N...N separation from 9.98 Å in **26** to 9.88 Å in the radical cation 26^+ . When the structure of the radical cation 26^+ is compared with that of the neutral molecule **26**, using the C4-C7-C13 plane as a point of reference, the greatest changes to the structure are associated with the relative orientation of the C(7)-C(12) aryl ring and the biphenyl moiety. These geometric changes observed between **26** and 26^+ are largely in agreement with those predicted using high-level (6-31G***-*B3LYP-DFT) calculations (Table 3.5).

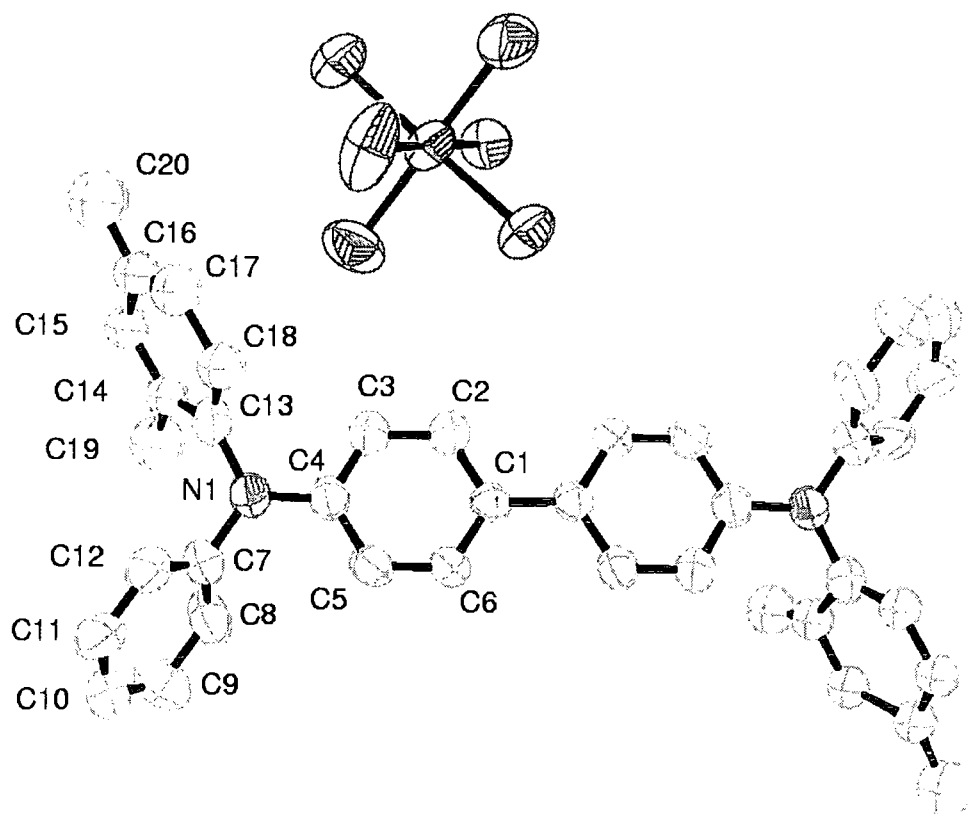


Fig 3.8 Molecular structure of [26]SbCl₆

In the crystal, layers of radical cations are found arranged perpendicular to the a-axis, in a herringbone motif (Figure 3.9). Between these layers, the SbCl_6^- anions and molecules of CH_2Cl_2 are found forming a second layer. The crystal structure can therefore be regarded as alternating layers of opposite charges, which is similar to the structural motifs found in many conducting organic materials. Within the solvent and anion layer, the anions form chains aligned with the c-axis by symmetry constraints, with an inter-anion $\text{Cl}\dots\text{Cl}$ distance of $3.201(5)$ Å, which is 0.3 Å less than twice the Van der Waals radius of Cl. In addition to the electrostatic interactions between the layers of opposite charge, there is a close contact between H(2) and Cl(5) from the SbCl_6^- anion ($\text{H2}\dots\text{Cl5}$ 2.76 Å, C3-H3-Cl5 145.6°).

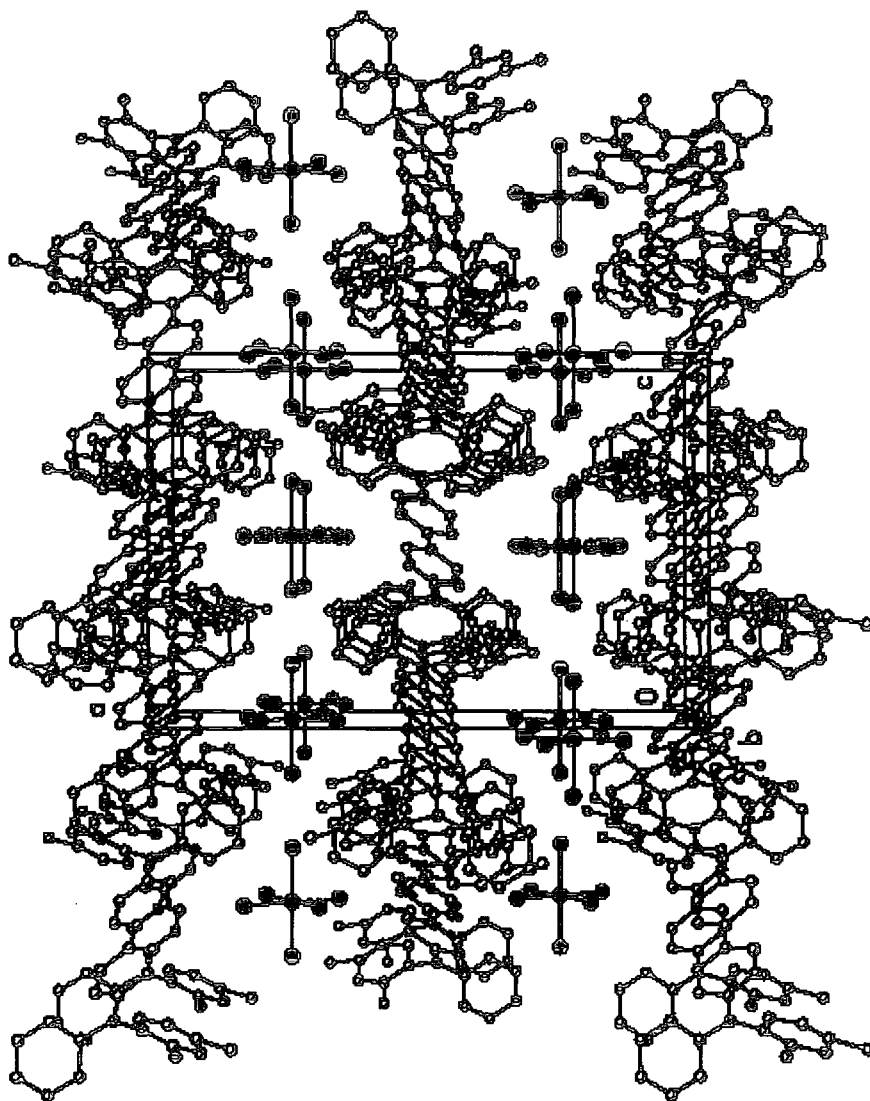


Figure 3.9 The molecular packing in the crystal of $[\mathbf{26}]\text{SbCl}_6$ showing the layered structure. The disordered solvent has been omitted for clarity

In order to assess the kinetic stability of these compounds, and to follow the oxidation events *in situ*, room temperature UV-Vis-NIR spectroelectrochemical studies were undertaken. The observation of sharp isosbestic points during the electrolytic cycle $A \rightarrow A^+ \rightarrow A^{2+} \rightarrow A^+ \rightarrow A$, and recovery of the original spectra of **A** at the end of the cycle confirm both the chemically reversible nature of the redox system in CH_2Cl_2 and the chemically distinct nature of each member of the redox series (Figure 3.10).

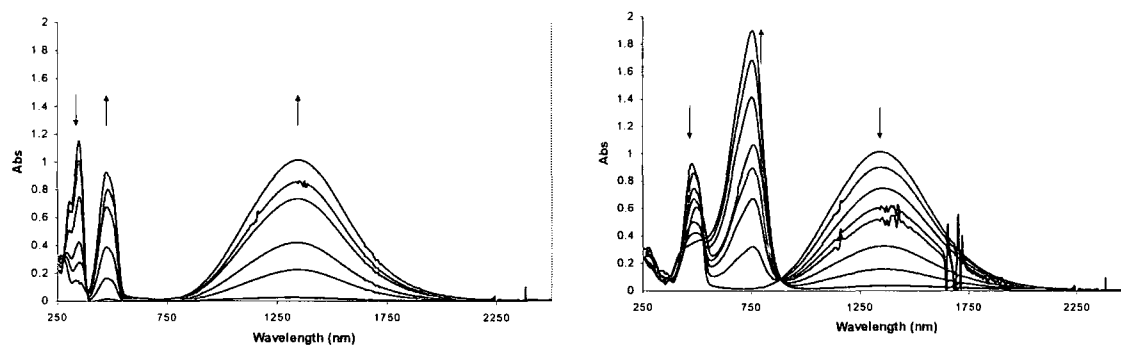


Figure 3.10 UV-Vis-NIR spectroelectrochemistry of **26** during sequential oxidation to 26^+ (left) and 26^{2+} (right). The arrows indicate the bands which grow and decay during the electrolysis. $\lambda(\text{nm})/\epsilon (\text{mol}^{-1}\text{dm}^3\text{cm}^{-1})$ **26** 302/24,279, 350/35,300 26^+ 477/28,015, 1335/30,680; 26^{2+} 750/56,590.

For each compound, a set of $\pi\text{-}\pi^*$ bands are observed in the electronic spectrum, which shift to lower energy upon the oxidation from the neutral material (**1** 310, 353 nm, **26** 305, 350 nm), through the radical cations (1^+ 484; 26^+ 476 nm) to the dicationic (1^{2+} 730; 26^{2+} 749 nm). The spectra of the neutral and dicationic materials are comparable with the spectra of neutral and cationic **23**. The monocationic forms of **1** and **26** show a very different spectrum, with a unique band in the NIR region (**1** 1400; **26** 1347 nm) which is analysed in more detail below. Molecular modelling (see below) suggests that of the two bands observed in the spectrum of the neutral species, the one at higher energy involves a greater proportion of orbitals with π^* character on the peripheral aromatic rings, while the lower energy transition involves more biphenyl π^* character. The neutral spectrum of **25** was recorded to investigate the effects of the methyl substitution, and displayed only a single absorption band at 297 nm. In the case of the dicationic, the $\pi\text{-}\pi^*$ transition is similar in energy and band shape to that observed for oxidised triaryl (mono)amines $[\text{NAr}_3]^+$, and indicates that 1^{2+} and 26^{2+} can be approximately described in terms of two localised triaryl cations.

However, 26^{2+} is ESR silent at room temperature, presumably due to strong antiferromagnetic coupling. (See Chapter 7)

It is useful to consider the electronic transitions in terms of the orbitals involved, which in turn are best displayed graphically. Time dependant DFT methods (TDDFT) as contained within the Gaussian 98 package were employed to model the transitions in each of 1^{n+} , 26^{n+} and the parent compound 19^{n+} ($n = 0, 1$), and the results displayed graphically using Molekel, as described in the experimental section.³² Geometry optimisations for both the neutral and radical cation states were carried out, and the results found to be in excellent agreement with the available crystallographically determined data. Analysis of the electronic transitions using TDDFT methods gave essentially identical results for each compound, which are summarised in table 3.6, and the agreement between calculated transition energies and the experimentally observed results (0.06eV) are remarkably good.

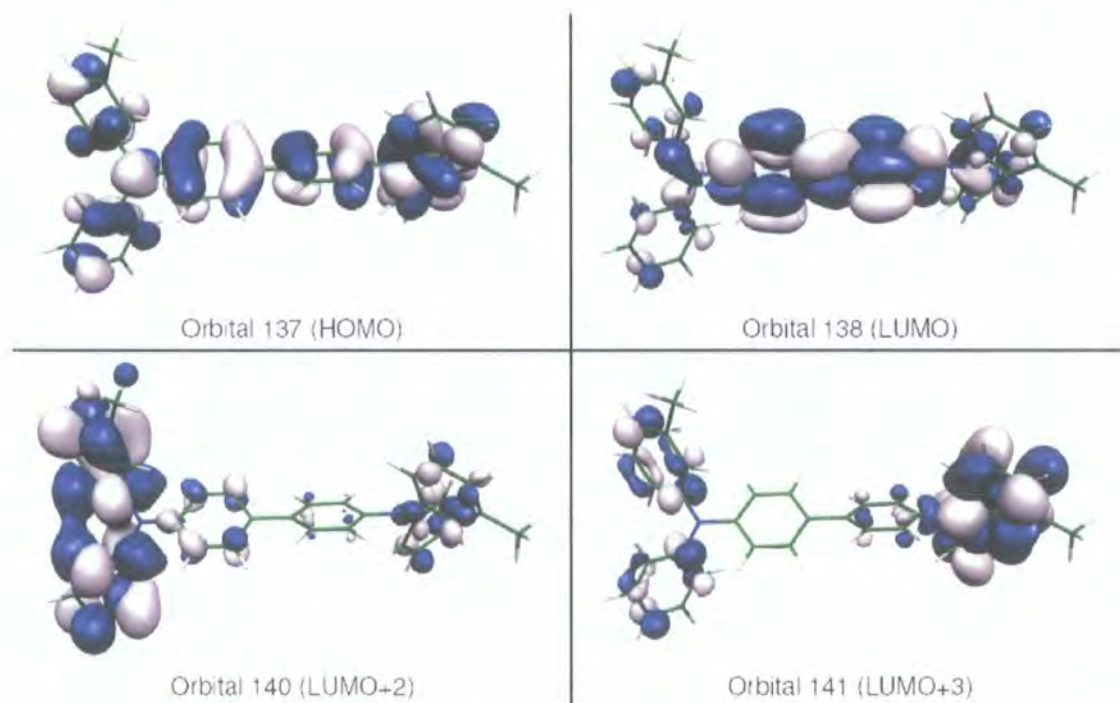
Table 3.6 Observed and calculated electronic transitions

	λ_{max}			
	Observed		Calculated	
	nm	eV	nm	eV
1	310	3.9995	305, 306	4.0588, 4.0508
	353	3.5123	358	3.4604
1⁺	484	2.5616	426	2.9105
	1400	0.8856	1423	0.8709
26	305	4.0651	304	4.0792
	350	3.5424	353	3.5041
26⁺	476	2.6047		
	1347	0.9205		
19	308	3.8332	304	4.0179
	349	3.5823	357	3.4682
19⁺	482	2.5724	424	2.9210
	1368	0.8399	1417	0.8744

The critical orbitals involved in the major transitions are illustrated here for **1** (Fig 3.11), **1⁺** (Figure 3.12) and **26** (Figure 3.13). Those of **19** and **19⁺** are similar, and are included in the supporting CD. The lowest energy absorption band in the neutral species arises from the HOMO-LUMO transition (illustrated by the transition between orbitals **137** – **138**). The HOMO contains appreciable character from the amine nitrogen centres, the biphenyl moiety and the *ortho* and *para* carbons of the peripheral ring systems. The LUMO is heavily centred on the biphenyl group, and may be approximately described as the biphenyl π^* system. The higher energy UV transition is comprised of two almost degenerate transitions arising from HOMO -

(LUMO+2) (orbitals 137 – 140) and HOMO - (LUMO+3) (orbitals 137 – 141). These higher lying unoccupied orbitals display extensive aromatic π^* character localised on the peripheral ring systems. The two transitions in the UV spectrum of the neutral tetraarylbenzidine moiety can therefore be satisfactorily described in terms of π^* _{biphenyl} and π - π^* _{peripheral} transitions.

Figure 3.11 TDDFT representations of the electronic transitions for neutral 1,



Geometry: RBPW91/6-31G(d,p), Symmetry: C1, TDDFT: RPBE1PBE/6-31G(d)

Table 3.7: Selected TDDFT results for the neutral 1 species.

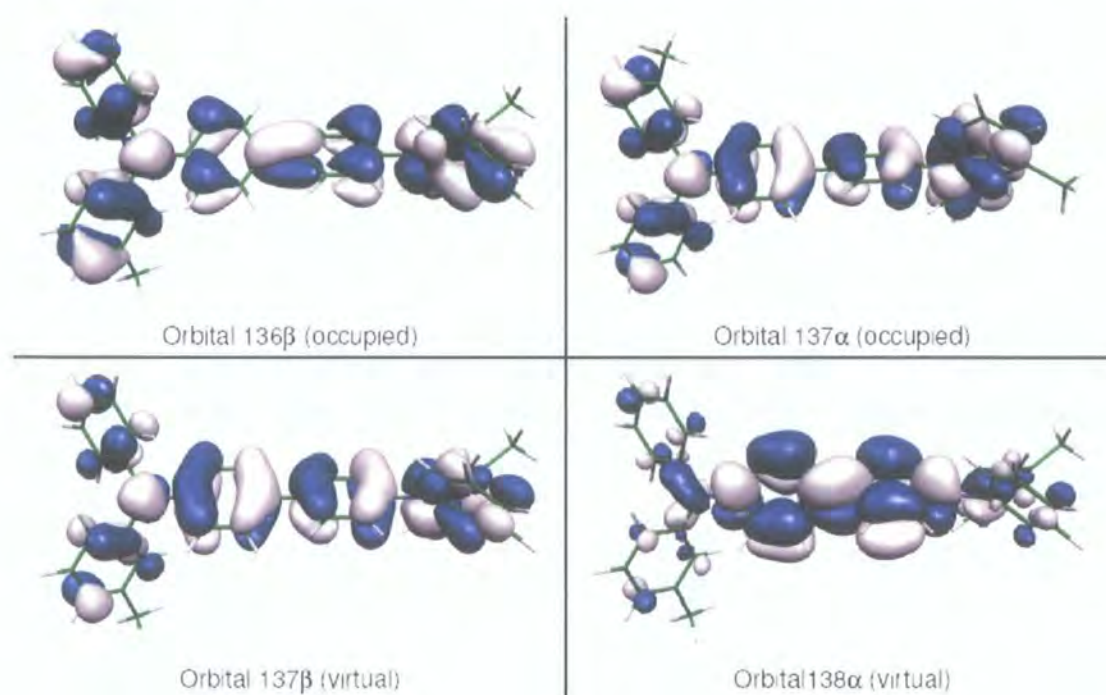
E.S. Number	Energy /eV	Energy /nm	Oscillator Strength (f)	Orbitals Involved	Contribution
1	3.4604	358.30	1.1297	136 – 143 137 – 138	-0.11071 0.67004
5	4.0508	306.07	0.1943	136 – 140 137 – 140 137 – 141 137 – 142	0.24073 0.53396 0.22808 0.21766
6	4.0588	305.47	0.1856	136 – 141 137 – 140 137 – 141 137 – 142	-0.25266 -0.15179 0.55349 -0.22186

Text in bold highlights the major contribution to the transition

Upon oxidation, the π - π^* bands are replaced by a new transition in the visible region. Not surprisingly, analysis of the TDDFT results indicated this transition to be the

SOMO - LUMO (α -spin) transition (orbitals **137 α** – **138 α**) while the NIR absorption band corresponds to the (HOMO-1) – SOMO (β -spin) transition (orbitals **136 β** –**137 β**) in keeping with conventional ideas. The graphical representation of these orbitals (Figure 3.12) clearly shows the (HOMO-1) and SOMO to be delocalised over the molecular framework which strongly supports the conclusions drawn from the band shape analysis below.

Figure 3.12 TDDFT representations of the electronic transitions for the radical cation of **1**



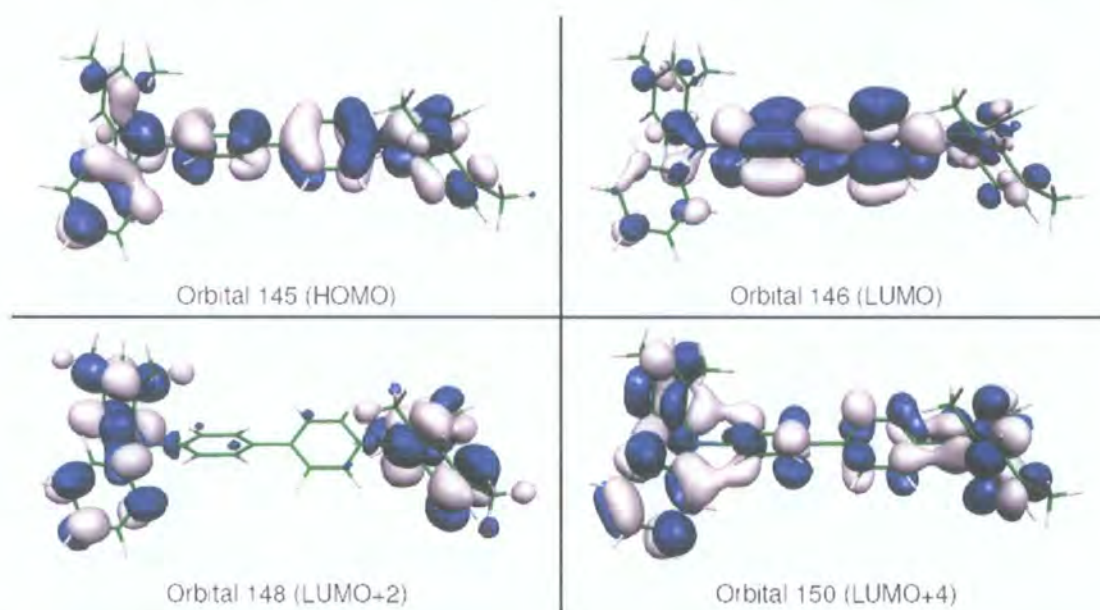
Geometry: UBPW91/6-31G(d,p), Symmetry: C1, TDDFT: UPBE1PBE/6-31G(d)

Table 3.8: Selected TDDFT results for the **1** radical cation.

E.S. Number	Energy /eV	Energy /nm	Oscillator Strength (f)	Orbitals Involved	Contribution
1	0.8709	1423.66	0.6550	137α – 138α 136β - 137β	0.18608 0.83240
12	2.9105	425.99	0.5949	127 β – 140 β 127 β – 145 β 128 β – 139 β 131 β – 138 β 133 β – 138 β 135 β – 138 β 136 β – 143 β 137β – 138β 128 β – 139 β 133 β – 138 β 135 β – 138 β 136 β – 143 β	-0.11896 0.11049 0.17754 -0.10775 0.12549 -0.10439 0.20426 0.89432 -0.12218 -0.13487 0.18722 -0.12418

The calculated transitions for **26** reproduce the excellent agreement with the experimental data seen for **19** and **1**, with the lowest energy absorption band in the neutral species arising from the HOMO-LUMO transition (illustrated by the transition between orbitals **145** – **146**). The HOMO contains no character from the methyl groups on the peripheral rings, the biphenyl moiety and the *ortho* and *para* carbons of the peripheral ring systems again being the dominant contributors. The LUMO also has no character from the methyl groups. The higher energy UV transition is comprised of two almost degenerate transitions arising from HOMO - (LUMO+4) (orbitals **145** – **150**) and HOMO - (LUMO+2) (orbitals **145** – **148**).

Figure 3.13 TDDFT representations of the electronic transitions for neutral **26**



Geometry: RBPW91/6-31G(d,p), Symmetry: C2, TDDFT: RPBE1PBE/6-31G(d)

Table 3.9: Selected TDDFT results for the neutral **26** species.

E.S. Number	Energy /eV	Energy /nm	Oscillator Strength (f)	Orbitals Involved	Contribution
1	3.5041	353.82	1.2348	145 – 146	0.66720
5	4.0792	303.94	0.3303	144 – 147	-0.14224
				144 – 149	-0.21290
				145 – 148	0.45128
				145 – 150	0.43759

Formally the radical cations **1**⁺ and **26**⁺ can be considered as organic mixed-valence compounds (Chapter 2), and the NIR absorption bands present in these species are related to the inter-valence charge transfer (IVCT) band described in Hush theory for moderately coupled (Class II) mixed-valence compounds.³³ The stability of the radical

cation of 26^+ as $[26]SbCl_6$ enabled the recording of spectra in a range of solvents without the complications of supporting electrolyte inherent in spectroelectrochemically generated data. The spectrum of 26^+ in pure CH_2Cl_2 was obtained by titration of a CH_2Cl_2 solution of 26 with a solution of $SbCl_5$ in the same solvent.

While the high energy side of the NIR band in $[26]SbCl_6$ can be fitted to a single Gaussian function, the band as a whole is distinctly non-Gaussian in shape, as expected for these strongly coupled radicals (Table 3.10). In the case of 26^+ the band energy, $\tilde{\nu}_{max}$, and shape was remarkably independent of solvent, only shifting appreciably from the values measured in CH_2Cl_2 in strongly polar solvents, such as propionitrile, where the band maximum is *ca.* 400 cm^{-1} higher in energy.

The asymmetric band shape, and independence of the band maximum with solvent observed for 26^+ suggests that, at least in a relatively non-polar media, these cations are approaching fully delocalised (Class III) structures. As such, the electronic coupling parameter H_{ab} for $1^+/26^+$ can be estimated to be $3560/3680\text{ cm}^{-1}$ in CH_2Cl_2 (Equation 3.1).

$$2H_{ab} = \nu_{max} \quad \text{(Equation 3.1)}$$

Alternatively, semi-classical Marcus-Hush theory for the degenerate case may be used to extract the relevant parameters from the spectroscopic data.³⁴ In order to perform this analysis, a vibronic matrix (Equation 3.2) with one asymmetric mode x (the ET coordinate) and one totally symmetric mode y , similar to the one given by Piepho³⁵ and Schatz³⁶, was constructed.

$$\begin{vmatrix} V + I_x x + \lambda_x x^2 + I_y y + \lambda_y y^2 - \epsilon & V + I_y y \\ V + I_y y & V - I_x x + \lambda_x x^2 + I_y y + \lambda_y y^2 - \epsilon \end{vmatrix} = 0 \quad \text{(Equation 3.2)}$$

The vibronic matrix is presented here in the context of a localised electronic basis, where the basis functions represent diabatic (non-interacting) states in which the hole (or unpaired electron) is localised at one of the two redox centres. The diabatic

potentials are expanded as power series which are terminated after the quadratic terms for the diagonal elements and after the linear terms for the off-diagonal elements. In this matrix, H_{ab} is the electronic coupling parameter, λ_x and λ_y are the reorganisation energies for the x and y modes, respectively, l_x and l_y are the linear vibronic coupling constants. The (dimensionless) displacement of the upper adiabatic surface and the ground state surface along the y mode is given by $\delta Q_y = l_y/\lambda_y$ and along the x mode it is $\delta Q_x = l_x/2\lambda_x$. Thus, choosing $l_x = \lambda_x$ places the minima of the diabatic potentials at $x = \pm 0.5$. Furthermore a simplification is made that $\lambda_x = \lambda_y = \lambda$. Diagonalisation of the matrix gives two adiabatic potential energy surfaces. Using a Boltzmann distribution of infinitesimally spaced vibrational states and the energy difference between the two adiabatic potential energy surfaces the absorption spectra was calculated. As long as the coupling H_{ab} is rather strong, the spectra can be accurately fitted by adjusting H_{ab} , l_y and λ , making no assumptions about any effective electron transfer distance.

Fitting the experimental spectra of $\mathbf{1}^+$ and $\mathbf{26}^+$ in the manner described by equation 3.2 allows an estimate of not only the electronic coupling parameter H_{ab} ($\mathbf{1}^+$ 3200 cm^{-1} ; $\mathbf{26}^+$ 3300 cm^{-1}), but also the reorganisation energy λ ($\mathbf{1}^+$ 7500 cm^{-1} ; $\mathbf{26}^+$ 7800 cm^{-1}), and the linear coupling constant l ($\mathbf{1}^+$ 3100 cm^{-1} ; $\mathbf{26}^+$ 2700 cm^{-1}) of the symmetric mode (Table 3.10). These parameters are similar to those derived from the radical cation derived from *N,N,N',N'*-tetra-4-methoxyphenyl-4,4'-diamino-1,1'-biphenyl (**24**) (Table 3.10), which has been shown to fall near the Class II/III borderline and exhibits a modestly solvent dependent IVCT band.^{30, 37, 38} This band in the NIR region has been shown to contain a significant contribution from redistribution of charge from the peripheral aromatic rings to the benzidene core, and should therefore be expected to be sensitive to the solvent medium and substituent groups.³⁰ In the case of $\mathbf{24}^+$ the internal contribution to the reorganisation energy has been evaluated from plots of the NIR band energy against the Dimroth-Reichardt solvent parameters. Extrapolation of the plot to the gas phase gives λ_v 3200 cm^{-1} /0.397 eV, a value approximately half of the total reorganisation energy $\lambda = \tilde{\nu}_{\text{max}}$ in 0.1M NBu_4PF_6 CH_2Cl_2 (6360 cm^{-1}). Similar treatment of data from $\mathbf{26}^+$ gives $\lambda_v = 6830 \text{ cm}^{-1}$ /0.847 eV, or ca. 90% of the total reorganisation energy in CH_2Cl_2 (Table 3.10). Clearly, direct comparisons between calculated gas phase results and experimental data must make allowance for the solvent environment. Also comparison of compounds **1**, **26**

and **24** are to be made with caution as the influence of the solvent medium, including supporting electrolyte in the case of **24**, and the CH₃ and OMe groups on the data are not entirely clear at present.

The fit of the IVCT bands of **1**⁺, **26**⁺ and **24**⁺ also yields the activation barrier ΔG^\ddagger of the intramolecular ET which is ca. 50 cm⁻¹ for all the radical cations. Together with the symmetrical structure of **26**⁺ as derived from X-ray crystallography the optical features and the parameters derived by the IVCT band fit strongly suggest that the benzidine radical cations are right at the border between Class II and Class III.

Table 3.10. NIR band and derived parameters from of **1**⁺,^[a] **26**⁺,^[a] and **24**⁺.^[39] at 298K

	26 ⁺ PhBr	26 ⁺ CHCl ₃	26 ⁺ PhCN	26 ⁺ EtCN	1 ⁺ CH ₂ Cl ₂	26 ⁺ CH ₂ Cl ₂	24 ⁺ CH ₂ Cl ₂ / NBu ₄ PF ₆
$\tilde{\nu}_{\max}$ (cm ⁻¹)	7363	7363	7545	7770	7120	7380	6360
ϵ (M ⁻¹ cm ⁻¹)	22,600	30,750	23,160	16,700	37,800	24,600	28,040
E_T^N	0.209	0.259	0.333	0.401	0.309	0.309	0.323 ^[c]
$\tilde{\nu}_{1/2(\text{high})}$ (cm ⁻¹) ^[d]	3574	3614	3650	3360	3630	3880	3750
$\tilde{\nu}_{1/2(\text{low})}$ (cm ⁻¹) ^[e]	2526	2486	2590	2490	2400	2460	2590
$\tilde{\nu}_{1/2(\text{obs})}$ (cm ⁻¹) ^[f]	3050	3050	3120	2925	3015	3170	3170
$\tilde{\nu}_{1/2(\text{HTL})}$ (cm ⁻¹) ^[g]	4113	4113	4164	4225	4045	4118	3820
$\tilde{\nu}_{1/2(\text{High})}/\tilde{\nu}_{1/2(\text{HTL})}$	0.87	0.87	0.87	0.79	0.89	0.94	0.98
$\tilde{\nu}_{1/2(\text{High})}/\tilde{\nu}_{1/2(\text{Low})}$	1.41	1.45	1.41	1.35	1.51	1.57	1.45
H_{ab} (cm ⁻¹)					3200	3300	2800
$\lambda(\text{cm}^{-1})/\text{eV}$					7500/ 0.930 ^[h]	7800/ 0.967 ^[h]	6800/ 0.843 ^[h]
$l(\text{cm}^{-1})$					3100 ^[h]	2700 ^[h]	2800 ^[h]
$\Delta G^\ddagger(\text{cm}^{-1})$					50 ^[h]	50 ^[h]	60 ^[h]

[a] As SbCl₆⁻ salt.

[b] Spectroelectrochemically generated data from reference [8].

[c] Pseudo- E_T^N parameter calculated to allow for the effects of the supporting electrolyte used in the spectroelectrochemical experiment. See reference [8].

[d] Twice the bandwidth at half-height of the high-energy side.

[e] Twice the bandwidth at half-height of the low-energy side.

[f] Observed halfwidth at half-height.

[g] Calculated from $\tilde{\nu}_{1/2(\text{HTL})} = 47.94[\tilde{\nu}_{\max}]^{1/2}$

[h] Calculated from fitted data as described in the text

3.3 Experimental section

Recrystallisation of **26** by slow diffusion of methanol into a concentrated CH_2Cl_2 solution afforded small block shaped crystals suitable for single crystal X-ray diffraction.

Treatment of a solution of **26** (101 mg, 0.18 mmol) in CH_2Cl_2 (5 ml) with a solution of SbCl_5 (150 mg, 0.18 mmol) in CH_2Cl_2 (150 ml) resulted in the immediate formation of a dark orange solution. The solvent was removed *in vacuo* and the dark brown residue obtained re-dissolved in a minimum volume of CH_2Cl_2 , and filtered. The filtrate was treated with hexane (10 ml), and allowed to slowly evaporate to give red-green needle-like crystals of $[\mathbf{26}]\text{SbCl}_6$ with a metallic lustre which were suitable for X-ray diffraction.

Cyclic voltammetry was carried out on solutions in CH_2Cl_2 containing 0.1M NBu_4BF_4 as supporting electrolyte, and values obtained referenced against an internal ferrocene standard. Spectroelectrochemical studies were carried out in an OTTLE cell (1 mm pathlength) of standard design,⁴⁰ using a 0.5 mM solution of **1** in CH_2Cl_2 containing 0.1 M NBu_4BF_4 supporting electrolyte.

The construction of the vibronic matrix and subsequent band shape analysis was carried out by Lambert (Wurzburg).

All DFT calculations were carried out by Tackley and Cherryman (Avecia) using the Gaussian 98 program.⁴¹ For each molecule, the geometry was optimised for both the neutral and radical cation states at a DFT level using the BPW91 functional (Becke's 1998 exchange functional,²⁸ with Perdew and Wang's 1991 gradient-corrected correlation functional^{42, 43}) in conjunction with the 6-31G(d,p) basis set.⁴⁴⁻⁴⁸ Where possible, molecular symmetry was used to simplify the calculations and aid in the interpretation of the results. Using the optimised geometries, Time-Dependant Density Functional Theory (TDDFT) calculations were run to solve for excited states. For these calculations, the PBE1PBE functional was used in conjunction with the 6-31G(d) basis set.⁴⁹⁻⁵² The TDDFT calculation was solved for 10 excited states in the

case of the neutral species and 20 excited states in the case of the radical cation species. In both cases the calculation was only solved for singlet excitations. Post-processing for visualisation of the molecular orbitals generated by the TDDFT calculation was performed using the Molekel programme.⁵³

References for Chapter 3

- 1 M. Stolka, J. F. Yanus, and D. M. Pai, *J. Phys. Chem.*, 1984, **88**, 4707.
- 2 C. W. Tang and S. A. VanSlyke, *Appl. Phys. Lett.*, 1987, **51**, 913.
- 3 C. Adachi, S. Tokito, T. Tsutsui, and S. Saito, *Jpn. J. Appl. Phys.*, 1988, **27**, L269.
- 4 C. W. Tang, S. A. VanSlyke, and C. H. Chen, *J. Appl. Phys.*, 1989, **65**, 3610.
- 5 D. U. Kim, T. Tsutsui, and S. Saito, *Polymer*, 1995, **36**, 2481.
- 6 C. Adachi, K. Nagai, and N. Tamoto, *Appl. Phys. Lett.*, 1995, **66**, 2679.
- 7 S. Thayumanavan, S. Barlow, and S. R. Marder, *Chem. Mater.*, 1997, **9**, 3231.
- 8 E. Bellmann, S. E. Shaheen, R. H. Grubbs, S. R. Marder, B. Kippelen, and N. Peyghambarian, *Chem. Mater.*, 1999, **11**, 399.
- 9 B. E. Koene, D. E. Loy, and M. E. Thompson, *Chem. Mater.*, 1998, **10**, 2235.
- 10 E. T. Seo, R. F. Nelson, J. M. Fritsch, L. S. Marcoux, D. W. Leedy, and R. N. Adams, *J. Am. Chem. Soc.*, 1966, **88**, 3498.
- 11 W. H. Bruning, R. F. Nelson, L. S. Marcoux, and R. N. Adams, *J. Phys. Chem.*, 1967, **71**, 3055.
- 12 G. R. Freeman, H. A. Levy, and G. M. Brown, *Acta Cryst.*, 1969, **A25**, S145.
- 13 A. N. Sobolev, V. K. Belsky, I. P. Romm, N. Y. Chernikova, and E. N. Guryanova, *Acta Cryst.*, 1985, **C41**, 967.
- 14 S. L. Reynolds and R. P. Scaringe, *Cryst. Struct. Comm*, 1982, **11**, 1129.
- 15 M. Malagoli and J. L. Brédas, *Chem. Phys. Lett.*, 2000, **327**, 13.
- 16 D. R. Tackley, University of Strathclyde.
- 17 M. Inada, K. Ohnishi, S. Nomura, A. Higuchi, H. Nakano, and Y. Shirota, *J. Mater. Chem.*, 1994, **4**, 171.
- 18 G. M. Brown, G. R. Freeman, and R. I. Walter, *J. Am. Chem. Soc.*, 1977, **99**, 6910.
- 19 A. R. Kennedy, W. E. Smith, D. R. Tackley, W. I. F. David, K. Shankland, B. Brown, and S. J. Teat, *J. Mater. Chem.*, 2002, **12**, 168.
- 20 G.-P. Charbonneau and Y. Delugeard, *Acta Cryst.*, 1976, **B32**, 1420.
- 21 A. Hargreaves and S. H. Rizvi, *Acta Cryst.*, 1961, **15**, 365.
- 22 J. Trotter, *Acta Cryst.*, 1961, **14**, 1135.
- 23 J. Cornil, N. E. Gruhn, D. A. d. Santos, M. Malagoli, P. A. Lee, S. Barlow, S. Thayumanavan, S. R. Marder, N. R. Armstrong, and J. L. Brédas, *J. Phys. Chem. A*, 2001, **105**, 5206.
- 24 K. Sakanoue, M. Motoda, M. Sugimoto, and S. Sakaki, *Nonlinear optics*, 2000, **26**, 271.
- 25 K. Sakanoue, M. Motoda, M. Sugimoto, and S. Sakaki, *J. Phys. Chem. A*, 1999, **103**, 5551.
- 26 T.-Q. Nguyen, V. Doan, and B. J. Schwartz, *J. Chem. Phys.*, 1999, **110**, 4068.
- 27 J. Cornil, D. Beljonne, D. A. d. Santos, J. P. Calbert, and J. L. Bredas, *Thin Solid Films*, 2000, **363**, 72.
- 28 A. D. Becke, *Phys. Rev. A*, 1988, **38**, 3098.
- 29 M. Malagoli, M. Manoharan, B. Kippelen, and J. L. Brédas, *Chem. Phys. Lett.*, 2002, **354**, 283.
- 30 V. Coropceanu, M. Malagoli, J. M. André, and J. L. Brédas, *J. Am. Chem. Soc.*, 2002, **124**, 10519.
- 31 C. Lambert and G. Nöll, *J. Am. Chem. Soc.*, 1999, **121**, 8434.
- 32 J. Cherryman and D. Tackley, 2003.

- 33 M. B. Robin and P. Day, *Adv. Inorg. Chem. Radiochem.*, 1967, **10**, 247.
34 C. Lambert, 2003.
35 S. B. Piepho, *J. Am. Chem. Soc.*, 1988, **110**, 6319.
36 P. N. Schatz, 'Mixed Valency Systems: Applications in Chemistry, Physics
and Biology', ed. K. Prassides, Kluwer Academic Publishers, 1991.
37 V. Coropceanu, M. Malagoli, J. M. André, and J. L. Brédas, *J. Chem. Phys.*,
2001, **115**, 10409.
38 S. F. Nelsen, *Chem. Eur. J.*, 2000, **6**, 581.
39 T. Ito, T. Hamaguchi, H. Nagino, T. Yamaguchi, J. Washington, and C.
Kubiak, *Science*, 1997, **277**, 660.
40 C. M. Duff and G. A. Heath, *Inorg. Chem.*, 1991, **30**, 2528.
41 M. J. Frisch, G. W. Trucks, H. B. Schlegel, G. E. Scuseria, M. A. Robb, J. R.
Cheeseman, V. G. Zakrzewski, J. A. M. Jr., R. E. Stratmann, J. C. Burant, S.
Dapprich, J. M. Millam, A. D. Daniels, K. N. Kudin, M. C. Strain, O. Farkas,
J. Tomasi, V. Barone, M. Cossi, R. Cammi, B. Menucci, C. Pomelli, C.
Adamo, S. Clifford, J. Ochterski, G. A. Petersson, P. Y. Ayala, Q. Cui, K.
Morokuma, P. Salvador, J. J. Dannenberg, D. K. Malick, A. D. Rabuck, K.
Raghavachari, J. B. Foresman, J. Cioslowski, J. V. Ortiz, A. G. Baboul, B. B.
Stefanov, G. Liu, A. Liashenko, P. Piskorz, I. Komaromi, R. Gomperts, R. L.
Martin, D. J. Fox, T. Keith, M. A. Al-Laham, C. Y. Peng, A. Nanayakkara, M.
Challacombe, P. M. W. Gill, B. Johnson, W. Chen, M. W. Wong, J. L.
Andres, C. Gonzalez, M. Head-Gordon, E. S. Replogle, and J. A. Pople, in
'Gaussian 98 (Revision A.11)', Gaussian Inc., Pittsburgh PA, 2001.
42 J. P. Perdew, K. Burke, and Y. Wang, *Phys. Rev. B*, 1996, **54**, 16533.
43 Erratum, *Phys. Rev. B*, 1998, **57**, 14999.
44 R. Ditchfield, W. J. Hehre, and J. A. Pople, *J. Chem. Phys.*, 1971, **54**, 724.
45 W. J. Hehre, R. Ditchfield, and J. A. Pople, *J. Chem. Phys.*, 1972, **56**, 2257.
46 P. C. Hariharan and J. A. Pople, *Mol. Phys.*, 1974, **27**, 209.
47 M. S. Gordon, *Chem. Phys. Lett.*, 1980, **76**, 163.
48 P. Hariharan and J. A. Pople, *Theo. Chim. Acta*, 1973, **28**, 213.
49 J. P. Perdew, K. Burke, and M. Ernzerhof, *Phys. Rev. Lett.*, 1996, **77**, 3865.
50 Erratum, *Phys. Rev. Lett.*, 1997, **78**, 1386.
51 C. Adamo and V. Barone, *J. Chem. Phys.*, 1999, **110**, 6158.
52 M. Ernzerhof and G. E. Scuseria, *J. Chem. Phys.*, 1999, **110**, 5029.
53 S. Portmann and H. P. Lüthi, *Chimia*, 2000, **54**, 766.

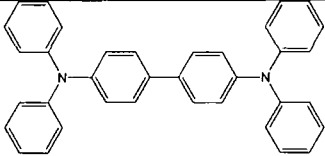
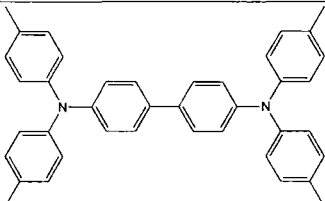
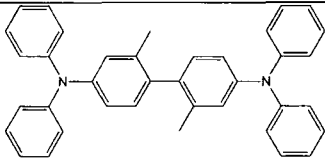
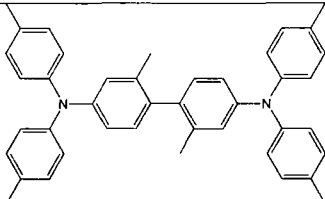
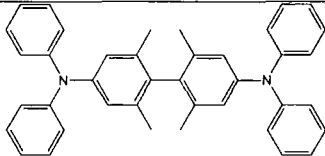
Chapter Four

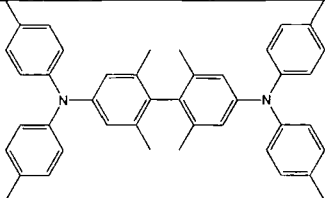
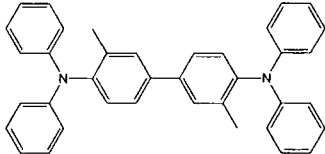
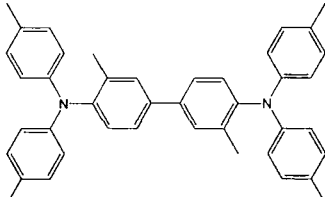
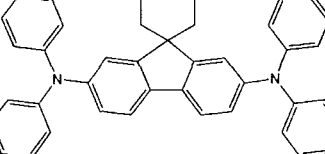
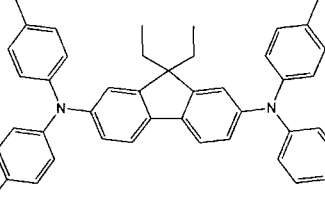
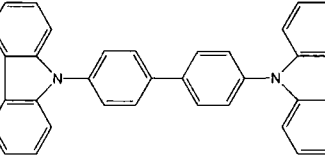
Studies of the Molecular Conformation

4.1 Introduction

In order to investigate the effect of molecular conformation on the electrochemical response and electronic spectra of tetraarylbiophenyldiamines, a range of compounds with varying degrees and patterns of methyl substitution were prepared and studied (Table 4.1). The conformationally unrestricted parent compound *N,N,N',N'*-tetra(phenyl)-(1,1'-biphenyl)-4,4'-diamine, **19**, was employed as a reference material. To help distinguish the role of molecular conformation from the inductive effects of methyl substituents, *N,N,N',N'*-tetra(4-methylphenyl)-(1,1'-biphenyl)-4,4'-diamine, **27** was prepared and studied as in contrast to compounds such as **28/29**, **30/31** and **32/33** the methyl groups at positions *para* to the amine nitrogen centre were not expected to distort the molecular conformation.

Table 4.1

19	
27	
28	
29	
30	

31	
32	
33	
34	
35	
36	

The use of methyl groups to influence the molecular structure of biphenyl-based materials and the consequences of such distortions on bulk properties has been studied in a wide range of contexts. For example, recent work on the incorporation of 2,2'-dimethyl substituted biphenyls into a variety of polymer chains has shown that the methyl groups at the 2,2' positions force adjacent phenyl rings into a non-coplanar conformation with respect to each other, decreasing the intermolecular interactions between the polymer chains. This change in molecular structure served to markedly decrease the crystallinity, but increase the solubility, of the substituted polymer in comparison with the unrestricted parent materials. However, the rod-like structure of

the polymer backbone and the mechanical properties of the materials are less dramatically affected.¹⁻⁵

The influence of methyl substituents on the conformation of a molecule has been the subject of a number of studies which have employed a variety of spectroscopic techniques, such as electron transmission spectroscopy.⁶ Despite claims by Chuang *et al.* in 1997, the molecular structure of 2,2'-dimethyl-1,1'-biphenyl-4,4'-diamine was first reported in 1952 by Fowweather. These crystallographically determined structures show that the dihedral angle between the phenyl rings in 2,2'-dimethyl-1,1'-biphenyl-4,4'-diamine falls in the range 86-75°. In the dihydrochloride salt this angle is decreased to 70.6° probably due to the strong ionic forces between the NH₃⁺ groups and the Cl⁻ ions.⁷ In the solid state, the biphenyl portion of the 2,2'-dimethylbiphenylene bridged dithiadiazolyl diradical (37)(Figure 4.1) has been shown to adopt a dihedral angle of 74°. In each case, the 2,2' methyl groups reside in a *syn* arrangement on the same side of the molecule, with those in the dithiadiazolyl being found disordered over two positions, and successfully modelled in terms of 50:50 occupancy of each site.

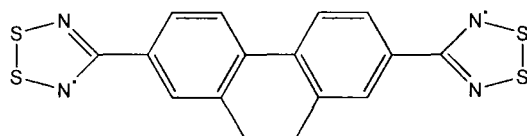


Figure 4.1 Structure of 2,2'-dimethylbiphenylene dithiadiazolyl diradical (37)

The role of molecular conformation on intramolecular electron transfer rates between biphenyl bridged bis-porphyrins has been inferred from fluorescence lifetimes of these compounds. The somewhat surprising result that maximum electron transfer rates occur when the dihedral angle between the biphenyl rings was not only 0°, but also 90° was rationalised in terms of the nodal structure of the molecular orbitals involved in the porphyrin-biphenyl-porphyrin assembly.⁸ Work by Maus *et al.* has studied how the rate of intramolecular electron transfer is influenced by conformation through investigation of a series of biphenyls exhibiting varying twist angles. The fluorene derivative showed very little rearrangement following the photoinduced charge transfer, due to the prearranged planarity.⁹

The ability to control the dihedral angle in biphenyl systems through the introduction of methyl substituents has been applied to manipulation of the linear and nonlinear optical properties of quinopyrans such as **38**.

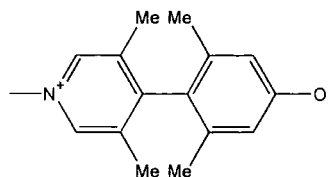


Figure 4.2 Quinopyran (**38**)

The effect of conformation on the oxidation potential of a range of redox-active biphenyl-based compounds has also been investigated in some detail. While the barrier to rotation around the biphenyl C-C single bond is essentially non-existent, as a bridging moiety in a delocalised, mixed-valance system the tendency to adopt a planar structure is considerable. A theoretical study with the AM1 MO method calculated the geometries of selected neutral amines and their radical cations and the reorganisation energy between the two. These calculations predicted that substituents at the 2,2' positions would enlarge the reorganisation energy, λ from 0.132 eV to 0.591 eV due to the steric repulsion introduced by the methyl groups. A dihedral angle between the biphenyl rings of 58° was predicted for *N,N,N',N'*-tetraphenyl-(2,2'-dimethyl)-(1,1'-biphenyl)-4,4'-diamine (**28**), compared to 38° in the unsubstituted biphenyl.¹⁰

The increased re-organisation energy, and increased steric repulsion encountered upon forcing the 2,2'-substituted biphenyl to be planar can be observed indirectly via the increased potentials associated with these materials. For example, despite the electron donating nature of the methyl groups 2,2'-dimethyl-4,4'-dimethoxybiphenyl has an oxidation potential 160mV more positive than the 4,4'-dimethoxybiphenyl.¹¹ In order to investigate whether these observed trends would be applicable to tetraarylbiophenyldiamines the 2,2'-dimethyl substituted materials *N,N,N',N'*-tetraphenyl-(2,2'-dimethyl)-(1,1'-biphenyl)-4,4'-diamine, **28** and *N,N,N',N'*-tetra(4-methylphenyl)-(2,2'-dimethyl)-(1,1'-biphenyl)-4,4'-diamine, **29** were prepared as described below.

Other structural modifications around the biphenyl moiety have been employed in these studies. The rearrangement of 3,3',5,5'-tetramethylhydrazobenzene to 2,2',6,6'-tetramethylbenzidine **39** was reported in 1945 by Carlin,¹² and since that time a number of reports describing the effects of introducing a 2,2',6,6'

substituted biphenyl group on the physical and electronic properties of both polymeric and small molecule systems have been made. For example introducing a 2,2',6,6' tetramethyl substituted biphenyl into a polyimide backbone results in an increase in the solubility and glass transition temperature of the materials, no doubt as a result of disruption in the various inter-chain interactions.^{5, 13}

The introduction of a 2,2',6,6'-tetramethyl substitution pattern to the biphenyl group of the quinopyran **38** results in a conformationally induced localisation of the π -conjugated system, which in turn enforces zwitterionic behaviour.¹⁴ More recently a study into the effect of dihedral angle on aromatic linked bis(hydrazine) radical cations showed that incorporation of a 2,2',6,6-tetramethylbiphenyl unit led to loss of the IVCT band which was observed for the biphenyl linked system.¹⁵ It is interesting to note that despite this long standing interest in the use of 2,2',6,6'-tetramethyl biphenyl as a structural unit, the molecular structure of **39** was only recently reported and confirmed that the tetramethyl substitution pattern around the central C-C bond enforced a dihedral angle of 83° in the biphenyl moiety.⁵

The fluorene unit may be regarded as a conformationally restricted *planar* biphenyl moiety, and has been widely used in the backbone of numerous conjugated polymers due to the thermal and photochemical stability this group can impart.^{16, 17} These materials have found application as fluorophores in two-photon microscopy, while other fluorene-based π -conjugated polymers incorporating phenyl, biphenyl and thiophene units are highly emissive materials with the precise emission wavelengths dependant upon the composition of the copolymer.^{18, 19} Incorporation of arylamine units into the polymer backbone has been shown to increase the hole transporting properties of the polymer although the mechanism responsible for this increased mobility (improved interchain interactions, lower/higher T_g , modified ionisation potentials) is not yet fully understood.^{20, 21} The charge transfer through a fluorene bridge, has been compared to that through biphenyl and sterically hindered bridges, in both neutral and cationic systems.

A study comparing the stability of aromatic cation radicals of biphenyls in various conformations has shown that a fluorene bridge reduces the oxidation potential of the radical cation, and stabilises the radical formed, relative to the biphenyl system. This

was ascribed to the transition state for the formation of the cation radicals requiring assumption of a planar conformation, thus the activation energy for the fluorene is greatly reduced.²² The electron transfer rate constants and Hush's coupling element were measured for the mixed valance system. The fluorene linked bis(hydrazine) radical cations showed larger intramolecular electron transfer rate constants values and Hush's coupling element, H_{ab} , than the comparable biphenyl systems, demonstrating the greater efficacy of the planar bridge with regards to the transfer of charge.^{15, 22}

In addition to the influence of methyl substituents at the 2 and 6 positions of the 1,1'-biphenyl group on the intra-ring dihedral angle, it is also possible to influence the conformation of the tetraarylbenzidine skeleton through the introduction of groups at the 3 (and 3') positions. A theoretical study using the AM1 MO method predicted that the phenyl groups in the diarylamine unit would be twisted almost perpendicular to the biphenyl unit due to steric repulsion with the methyl group.¹⁰ This calculated structure is broadly in agreement with the crystallographically determined structure of 3,3'-dimethyl-1,1'-biphenyl-4,4'-diamine, which revealed a dihedral angle between the two phenyl rings of the biphenyl of 41° with a C-N bond length of 1.43 \AA .²³

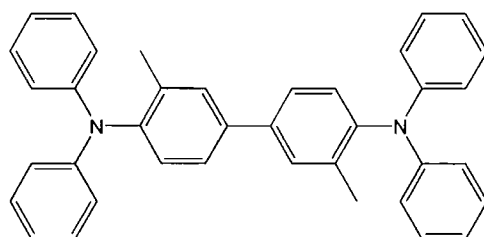


Figure 4.3 Molecular structure of tetraphenyl-3,3'-dimethyl-1,1'-biphenyl-4,4'-diamine (**32**)

Related studies by Nelson *et al.* on the intramolecular electron transfer rate of *p*-phenylenedihydrazine radical cations (Figure 4.4) demonstrated that incorporation of methyl groups *ortho* to the nitrogen atoms *destabilised the neutral species* due to inhibition of resonance through steric conflicts with the amine moieties.²⁴

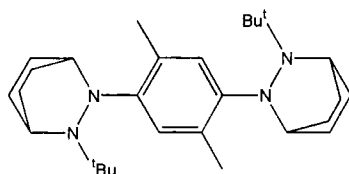
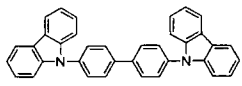
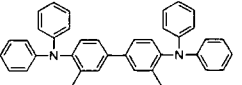
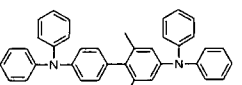
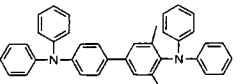
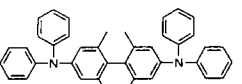
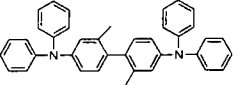


Figure 4.4 2,5-dimethyl-1,4-bis(2-*tert*-butyl-2,3-diazabicyclo[2.2.2]oct-3-yl)benzene-1,4-diyl (**40**)

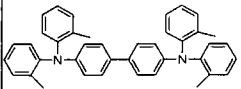
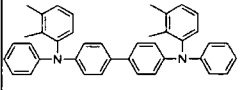
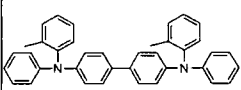
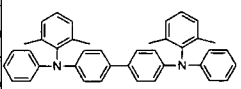
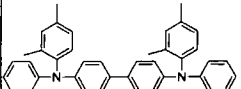
Materials containing the carbazole sub-unit have been investigated as the incorporation of the structurally rigid carbazole unit serves to increase the glass transition temperature of polymeric materials.²⁵ The material 4,4'-dicarbazole-1,1'-biphenyl, **36** is used extensively as a host for dopants in light emitting diodes, however there is very little information available in the open literature relating to the structural or electronic properties of the material itself.

As many of the literature reports of the electronic properties only describe selected properties, the computational chemistry group at Avecia has undertaken a comprehensive study of the effects of introducing substituent groups. Twenty molecules were studied, the neutral structures were first optimised at AM1 semi-empirical level, and the energy of the HOMO level and also the HOMO/LUMO gap calculated. The structure of the radical cation was then optimised and the ionisation potential and reorganisation energy associated with oxidation from the neutral to mono cation calculated. As structural features are of particular interest to the present study, the dihedral angle of the central biphenyl and the dihedral angles between the peripheral phenyl rings and the N-C plane bond were measured from the optimised structures in both the neutral and radical cation (Table 4.2).

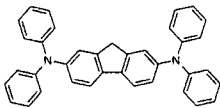
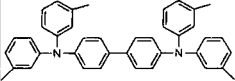
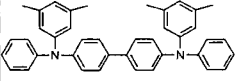
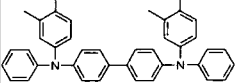
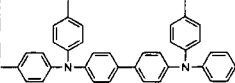
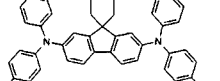
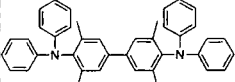
Table 4.2 Calculated electronic and structural parameters²⁶

Material	IP (eV)	Neutral			Neutral			Radical cation		
		Neutral HOMO (eV)	HOMO/LUMO Gap (eV)	Reorg. energy (eV)	Biphenyl twist (°)	Sub. Peripheral/biphenyl (°)	Unsub. Peripheral/biphenyl (°)	Biphenyl twist (°)	Sub. Peripheral/biphenyl (°)	Unsub. Peripheral/biphenyl (°)
	7.0738	-8.111	7.4789	-0.567	39.86	6.68	9.08	29.88	3.12	3.11
	6.7717	-8.038	7.6884	-0.243	39.37	50.18	16.41	29.64	33.13	30.79
	6.7578	-7.884	7.9117	-0.076	77.86	34.59	34.86	70.28	41.30	38.95
	6.7483	-7.93	7.6026	-0.085	39.86	40.62	19.58	29.61	35.36	30.24
	6.6899	-7.917	8.6637	-0.078	89.79	34.41	34.84	89.65	39.96	40.25
	6.6829	-7.811	7.791	-0.097	58.72	34.69	35.44	50.40	34.61	34.88

Chapter Four: Studies of the Structural Conformation

Material	IP (eV)	Neutral HOMO (eV)	HOMO/LUMO Gap (eV)	Reorg. energy (eV)	Biphenyl twist (°)	Sub. Peripheral/ biphenyl (°)	Unsub. Peripheral/ biphenyl (°)	Biphenyl twist (°)	Sub. Peripheral/ biphenyl (°)	Unsub. Peripheral/ biphenyl (°)
	6.673	-7.871	7.8396	-0.337	38.78	43.20	80.11	22.67	76.02	52.63
	6.6613	-7.846	7.6729	-0.285	38.83	75.53	21.19	22.98	66.77	57.22
	6.6532	-7.867	7.6648	-0.280	38.95	73.41	21.46	23.14	66.61	40.38
	6.6222	-7.737	7.4657	-0.115	38.95	35.28	35.03	26.22	35.56	35.74
	6.6058	-7.784	7.6556	-0.21	38.85	71.62	39.21	22.40	75.74	47.66
	6.6034	-7.83	7.6475	-0.271	38.95	73.46	21.66	23.81	63.82	38.60
	6.5977	-7.704	7.434	-0.113	38.93	34.93	35.48	26.52	34.37	35.69

Chapter Four: Studies of the Structural Conformation

Material	IP (eV)	Neutral HOMO	HOMO/LUMO Gap (eV)	Reorg. energy (eV)	Biphenyl twist (°)	Sub. Peripheral/biphenyl (°)	Unsub. Peripheral/biphenyl (°)	Biphenyl twist (°)	Sub. Peripheral/biphenyl (°)	Unsub. Peripheral/biphenyl (°)
	6.5826	-7.672	7.2533	-0.399	0	33.81	35.83	0.13	38.17	38.35
	6.5771	-7.711	7.4641	-0.115	38.97	34.76	35.90	26.07	46.95	45.70
	6.5737	-7.707	7.4631	-0.115	38.93	35.60	35.02	26.24	35.17	35.62
	6.5529	-7.680	7.4327	-0.115	38.88	34.07	36.43	26.41	47.03	46.26
	6.5298	-7.650	7.4001	-0.110	38.77	35.73	34.87	27.00	35.06	34.20
	6.4264	-	7.2103	-0.130	0	30.04	39.46	0.12	35.70	35.65
	-	-	-	-	40.79	40.67	19.97	-	-	-

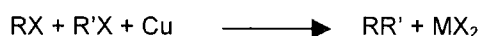
The calculations predict a number of trends within this series of tetraarylbiphenyldiamines. Introducing methyl groups on the biphenyl has a marked effect on the ionisation potential, with disruption of the conjugation between the diarylamine unit and the biphenyl appearing to have a larger effect than disrupting the conjugation through the biphenyl unit, i.e. the second to sixth entries in table 4.2. The substitution at *ortho* positions of the peripheral rings is predicted to raise the ionisation potential, relative to that of **1**, associated with an increase in the reorganisation energy. The dihedral angles of the *ortho* substituted rings are also greatly increased, relative to *meta* substituted rings. This suggests that the *ortho* methyl groups are having an influence due to the steric demands of a substituent at that position, and not just an inductive effect. The introduction of methyl substituents at *meta* and *para* positions appears to reduce the ionisation potential as would be expected due to the inductive effect, with little increase in steric demand. The incorporation of a fluorene unit as the central bridge is also predicted to reduce the I_p of the material, relative to **1**, and when the fluorene bridge is combined with tetra(4-methylphenyl) substitution the I_p is greatly reduced, although the reorganisation energy is higher than that for **1**. This suggests that the reorganisation energy is due to the movement of peripheral rings, with the central biphenyl planarisation being a low energy process.

The calculated data show reasonable agreement with the crystal structure obtained for the neutral **26**, although the optimised geometry for the radical cation does not show such good agreement, with the planarisation of the central biphenyl being underestimated by 20 ° and the rotation of both of the peripheral rings to a more orthogonal angle being underestimated. This confirms that whilst the AM1 MO method can be useful for suggesting general trends, it is not as accurate as DFT methods, which show closer agreement with experimentally determined structures (Chapter 3).

The synthesis of a series of conformationally restricted systems was undertaken in order to study the molecular and electronic structures experimentally. Key to the synthetic strategy was the use of the Ullmann Condensation which is reviewed here.

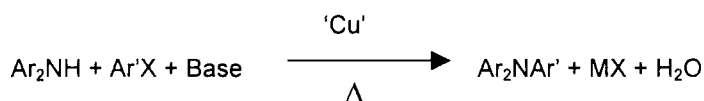
4.2 The Ullmann Condensation

The preparation of biaryl systems from two molecules of an aromatic halide in the presence of copper was developed by Ullmann in 1903, and this reaction is now known as the Ullmann coupling.²⁷



The nature of the active copper species acting as the catalyst has for a long time been uncertain, and early literature reported varying success for differing copper sources with no apparent explanation. Copper sources included copper bronze 'NaturKupfer C' and freshly precipitated copper from treatment of CuSO_4 solution with Zn. Despite the uncertainty over the nature of the catalytically active species, the Ullmann coupling has been applied to a wide range of many symmetrical and unsymmetrical biaryls, which would otherwise be difficult to obtain.^{28, 29} The coupling reaction is dependant on the nature of the aromatic halides used, the order of reactivity of the halogens being $\text{I} > \text{Br} > \text{Cl}$, with the latter two substituents undergoing reaction only when activating electronegative groups are present in the *ortho* and *para* positions, with halides having no influence in any position around the ring.

An extension of the C-C bond forming Ullmann Coupling, is the Ullmann Condensation, which is a copper catalysed C-N or C-O bond forming reaction, entailing the condensation of an arylamine or phenol with an aryl halide.

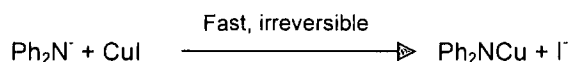


The Ullmann Condensation shares a number of characteristics with its namesake: the variation in reaction success with different copper sources and the need to carry out the reaction at temperatures between 100° and 300° being the more notable similarities. The trends in halide reactivity $\text{I} > \text{Br} > \text{Cl}$ holds, although the presence of

electron withdrawing groups are not as critical. The reaction is notoriously capricious with side reactions such as halide reduction and homocoupling often encountered.

Interestingly the mechanism of the Ullmann Condensation, a copper catalysed aromatic substitution of an unactivated aryl halide, has never been explicitly elucidated,³⁰ although the synthetic method has been utilised widely for over 90 years.

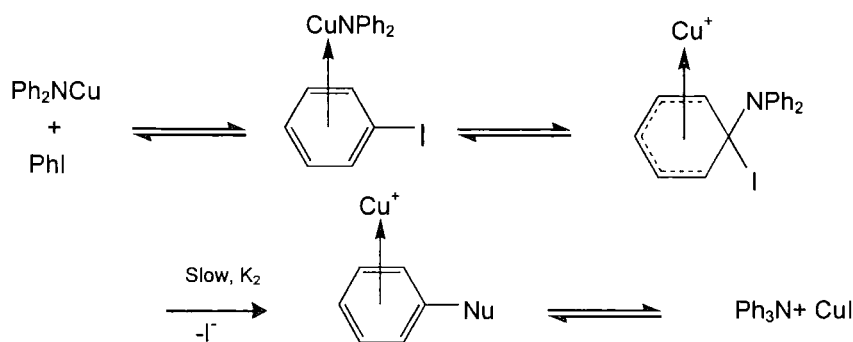
In 1987 a detailed study of both homogeneous and heterogeneous catalytic conditions employing three different oxidation states of copper greatly enhanced the understanding of the mechanism of reaction.³¹ The study confirmed earlier suggestions that a cuprous nucleophile formed from coordination of the amine to the copper species is involved in the reaction.³⁰ For homogeneous reactions the reaction rate was found to be zero order with respect to the nucleophile, but as the rate responded to substituents in the aromatic nucleophile ring it was concluded that the nucleophile must be involved in the transition state, suggesting formation of a cuprous nucleophilic species 'Ph₂NCu'



Cuprous nucleophiles are not unusual, and examples such as PhSCu and PhOCu react with haloaromatics to give thioethers and ethers respectively.³²

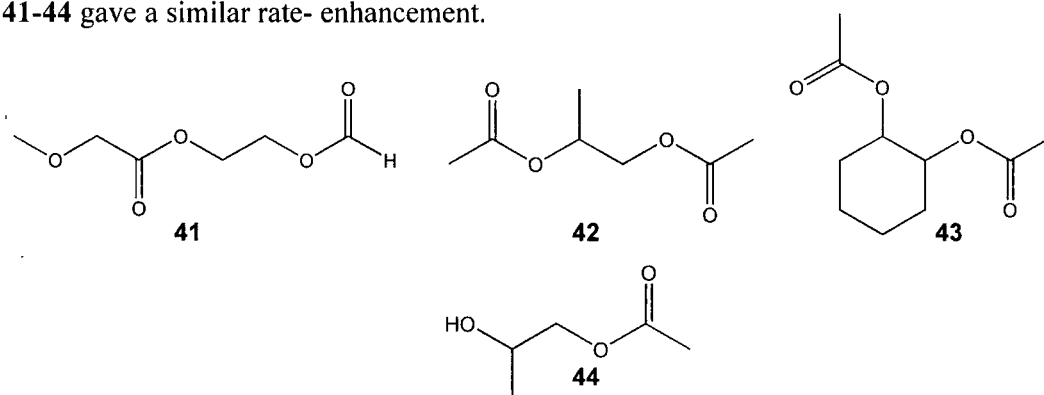
Scanning electron microscopy studies on recovered copper metal from heterogeneous reactions identified a coating of oxide layer Cu₂O, which would have to be removed for clean metal surface catalysis. Amines being excellent ligands for cuprous ion, would remove this layer however, and the amount of cuprous oxide that would be present in solution would be more than adequate to complete the reaction, through a cuprous catalysed mechanism, consistent with the observed homogeneous reaction rate. Confirmation of the catalytic species as solvated Cu(I) was complete, after demonstration of catalytic activity in solution, after removal of the solid copper metal catalyst. The effect of the choice of halide on reaction rate has been studied in some detail, the observation of reactivity trends I>Br>Cl is consistent with a rate limiting halide elimination step.³³ So with identification of the catalytic copper species the current best hypothesis of the mechanism is a π-complexed organocuprate

intermediate. The intimate mechanistic detail is unusual in that it requires electron transfer to the higher energy σ^* CX orbital, rather than the π^* aromatic orbital.



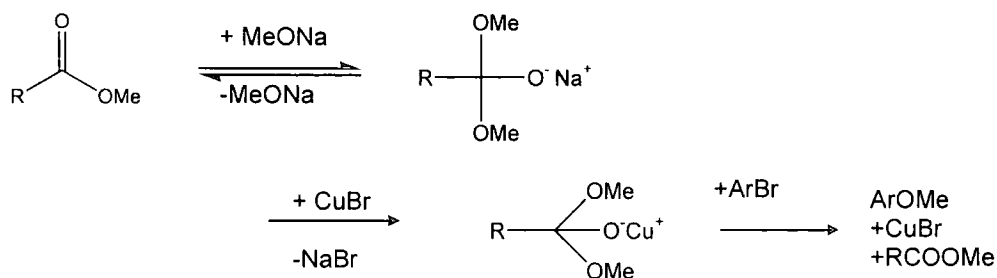
4.3 Modifications to the Ullmann Condensation

As the original conditions for the Ullmann Condensation require long reaction times at high temperatures, there have been a number of modifications employed to reduce the harshness of the conditions. Many of these modifications stem from the serendipitous observation made by Weingarten during a mechanistic study.³⁰ It was noted that on purification of the solvent, diglyme, the reaction rate was greatly decreased on comparison to undistilled solvent. A diester was identified as the active component in the solvent. Several other esters of ethylene glycol and related glycols **41-44** gave a similar rate-enhancement.

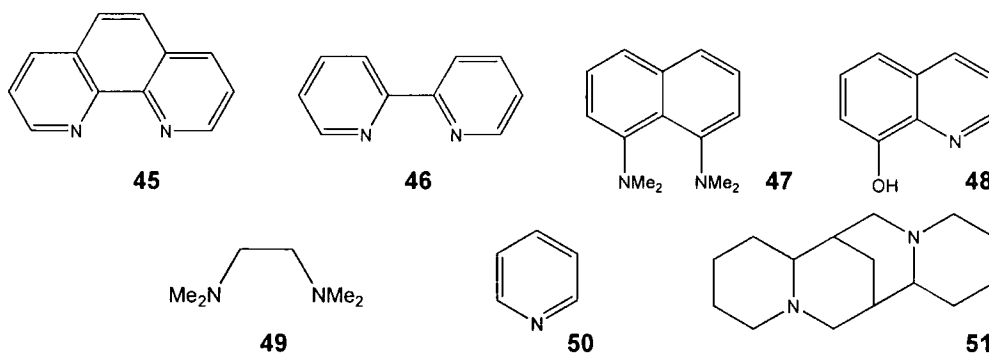


While the study was not comprehensive, the rate increase was taken as a result of enhancement of the solubility of the cuprous ion, and a similar rate increase was reported for the copper-catalysed methanolysis of aryl bromides where the presence of any ester was found to co-catalyse the methanolysis.³⁴ The increased solubility and

stability of the cuprous ion catalyst was ascribed to the formation of an adduct with methoxide ion and an ester.



However, the production of water as a by-product, together with the large excess of hydroxide commonly employed prevents the direct transfer of this co-catalyst to the amine Ullmann Condensation. This has led to the investigation of hydrolytically stable ligands known to co-ordinate Cu(I) salts to co-catalyse Ullmann Condensation reactions.³⁵⁻³⁷ Ligands studied comprised alkyl and aryl, mono and bidentate nitrogen containing compounds: 1,10-phenanthroline (**45**), 2,2'-dipyridyl (**46**), 1,8-bis(dimethylamino)-naphthalene (**47**), 8-hydroxyquinoline (**48**), N,N,N',N',tetramethyl-ethylenediamine (**49**), pyridine (**50**) and racemic sparteine (**51**).



Of these, 1,10-phenanthroline was found to produce significant rate acceleration for the Ullmann Condensation, enabling use of lower reaction temperatures and shorter reaction times. Greater halide selectivity is also introduced by these mild conditions, as bromide is no longer reactive under these mild reaction conditions. This selectivity enables preparation of brominated triarylamines from both bromo-iodobenzenes and bromide containing nucleophiles.

Whereas 1,10 phenanthroline is applicable for reactions utilising Cu(I) salts as the catalyst, for copper metal catalysed Ullmann Condensations a phase transfer catalyst

has been employed. The use of 18-crown-6 was found to increase yields and reduce reaction times, although the use of high boiling point solvents is still necessary.³⁵ These reactions are carried out using K_2CO_3 as the base to remove the possibility of attack of the iodo- substrate by the hydroxide ion.

While Ullmann protocols have been widely adopted, metal catalysed aromatic carbon nitrogen coupling reactions are not limited solely to copper, and in the last 10 years there have been many interesting developments in this area.^{38, 39} In particular, Pd based catalysts have been rapidly developed, and general aromatic carbon-nitrogen bond forming reactions catalysed by palladium were realised by both the Buchwald and Hartwig research groups, who simultaneously published their results of reactions of aryl halides with the combination of an amine and either an alkoxide or silylamide base.⁴⁰⁻⁴² The catalytically active species was initially generated from $[PdCl_2 \{P(o-C_6H_4Me)_3\}_2]$ or a combination of $[Pd_2(dba)_3]$ ⁴³⁻⁴⁵ (dba = trans, trans-dibenzylidene-acetone)⁴⁶ and $P(o-C_6H_4CH_3)_3$.⁴⁷ For these systems secondary amines were viable substrates, whereas primary amines gave substantial yields with only electron-poor aryl halides.⁴⁸ Second generation catalysts featured chelating phosphines. Palladium complexes of DPPF⁴⁹ (DPPF = 1,1'-bis(diphenylphosphino)ferrocene)⁵⁰ and BINAP^{51, 52} (BINAP = 2,2'-bis(diphenylphosphino)-1,1'-binaphthyl) catalyse aminations of electron-rich, electron-poor, hindered, or unhindered aryl bromides or iodides aryl bromides and iodides with primary alkylamines, cyclic secondary amines and anilines. Palladium complexes with BINAP ligands provide higher yields for electron neutral aryl halides than with DPPF ligands, and provide a reliable route to secondary arylamines, whereas often the DPPF system will convert the amine to the tertiary amine. Although the mechanism has not been explicitly revealed, current data provides a reasonable mechanism which is illustrated in figure 4.5.

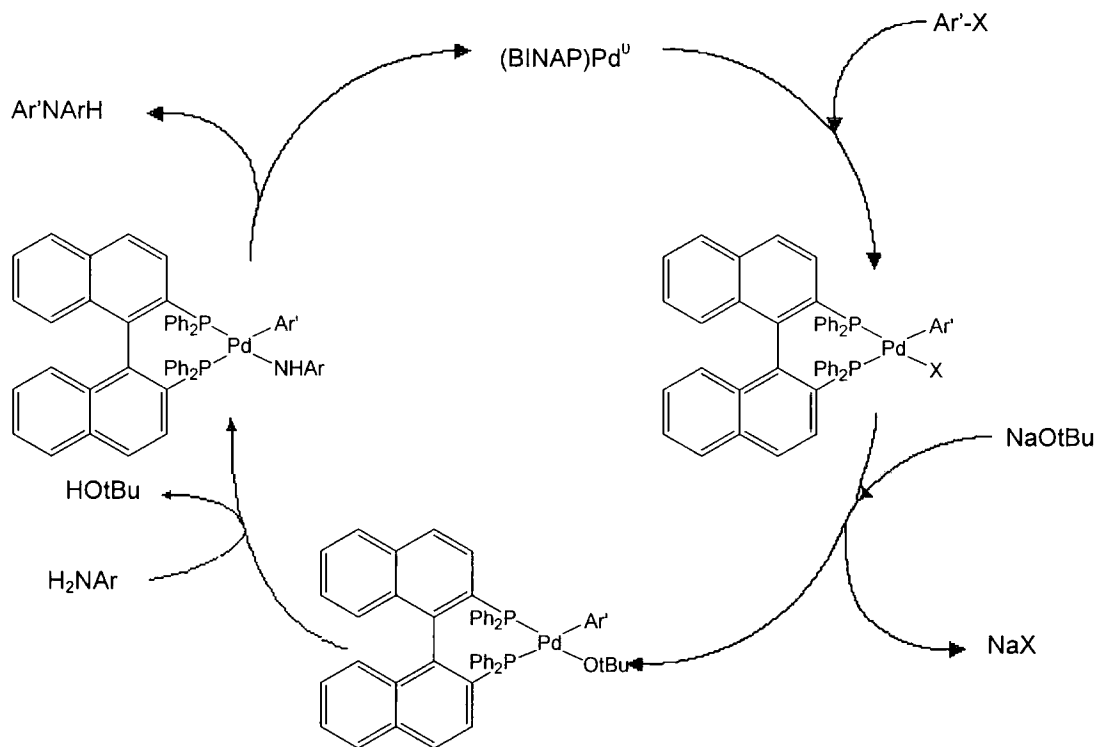


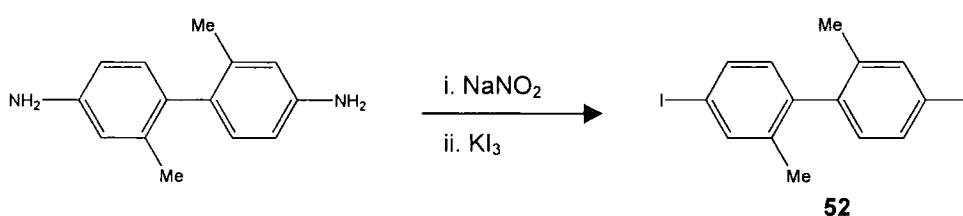
Figure 4.5 Catalytic cycle for the palladium catalyzed coupling

4.4 Synthesis of Target Materials by Means of the Ullmann Condensation

The tetraaryldiaminobiphenyls **19** and **27** were prepared by Ullmann Condensations of 4-4'-diiodobiphenyl with diphenylamine and di(4-methylphenyl)amine respectively by reaction in refluxing *ortho*-dichlorobenzene in the presence of potassium carbonate and copper powder. The resulting mixture of product and excess diarylamine was separated by chromatography. The ¹H NMR spectrum for **19** displayed a doublet at δ 7.48 ppm, $J_{\text{HH}} = 9\text{Hz}$, due to hydrogens on the biphenyl, a pseudo triplet due to the hydrogens at the *meta* position of the peripheral rings at 7.16 ppm, $J_{\text{HH}} = 15\text{Hz}$, two overlaid doublets due to the hydrogens at the *ortho* position of the peripheral rings and hydrogens on the biphenyl moiety at 7.03 ppm, $J_{\text{HH}} = 9\text{Hz}$, and a triplet at 6.93

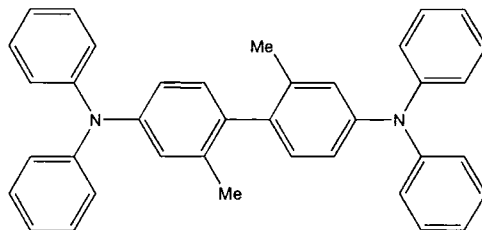
ppm, $J_{\text{HH}} = 14$ Hz, assigned to the hydrogen at the *para* position of the peripheral rings. The ^1H NMR spectrum for **27** contained a doublet at δ 7.31 ppm, $J_{\text{HH}} = 8$ Hz due to one of the hydrogens on the biphenyl, and a doublet at 6.97 ppm consisting of resonances due to the remaining proton of the biphenyl and the hydrogens on the peripheral rings. A singlet due to the methyl hydrogens present on the peripheral rings was present at 2.2 ppm. Mass spectroscopy (EI) also proved useful in the characterisation of these materials, with molecular ions at m/z 488 and 544 and fragmentation patterns consistent with loss of aryl rings, and amine sub-units being observed in the mass spectra. Crystals of **19** suitable for single crystal X-ray analysis were obtained from slow evaporation of a saturated CH_2Cl_2 solution. Selected bond lengths, angles and torsion angles for all molecular structures obtained are given in table 4.3

The 2,2'-dimethyl-4,4'-diiodo-1,1'-biphenyl **52** was prepared by literature methods.^{15, 53} Thus the parent diamine 2,2'-dimethyl-(1,1'-biphenyl)-4,4'-diamine dihydrochloride was diazotised by treatment with sodium nitrite then di-iodinated through reaction with potassium triiodide, producing the diiodide **52** which was isolated as an orange solid. The ^1H NMR spectrum showed a pattern of four resonances. At δ 7.56 ppm a singlet due to the proton at the 3 position of the biphenyl. At 7.13 and 6.72 ppm doublets, $J_{\text{HH}} = 8$ Hz, due to the protons at the 5 and 6 positions and a singlet at 1.93 ppm due to the protons on the methyl groups, in agreement with the literature values. The molecular ion was found in the mass spectrum at m/z 434 with a fragmentation pattern consistent with sequential loss of each iodide.



Similar Ullmann Condensation conditions to those used in the preparation of **19** and **27** were employed for the synthesis of **28** and **29**, using **52** in place of 4-4'-diiodobiphenyl. The products were obtained as white solids after chromatography on silica gel. The ^1H NMR spectrum for **28** showed a pattern of multiplets in the aromatic region at δ 7.22, 7.19, 7.06, 6.93, 6.92, 6.85 ppm in the ratio 2:8:8:2:4:2, consistent with the expected product, with a singlet corresponding to the methyl

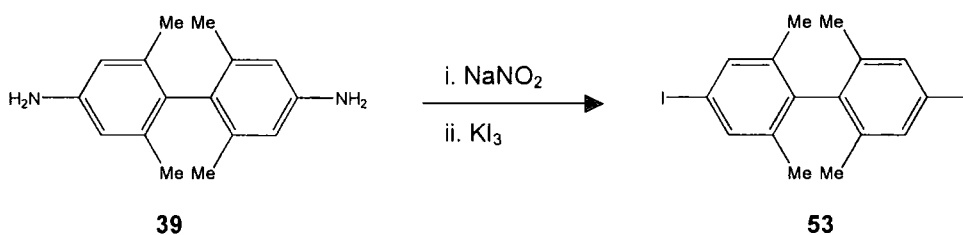
protons at 1.94 ppm. For **29** the ^1H NMR spectrum contained a multiplet at δ 7.14 ppm with two singlets at 2.32 and 1.99 ppm corresponding to the methyl groups on the peripheral rings and the biphenyl moiety respectively. The mass spectra of these compounds were also consistent with the proposed structure, with molecular ions at m/z 516 and 572 respectively, being observed.



28

The preparation of the key intermediate 2,2',6,6'-tetramethyl-1,1'-biphenyl-4,4'-diamine **39** followed literature methods.¹² 5-Nitro-xylene was reduced to the corresponding aniline by treatment with zinc in an acidic solution then azotised to form 3,3-5,5-tetramethyl hydrazobenzene as white needles. On treatment with acid this underwent the benzidine rearrangement to form buff crystals of the diamine. The diamine **39** was characterised by ^1H NMR with a singlet at δ 6.48, a broad resonance at 3.48 and a singlet at 1.82 ppm assigned to the aromatic protons, amino protons and methyl protons respectively. The melting point was measured and showed good agreement with the reported value, 166-167°(lit 167-168°). The molecular ion was identified in the mass spectrum at m/z 240 with a fragmentation pattern consistent with loss of the amine moieties.

The synthesis of **53** was carried out in a manner similar to that described for **52**.^{15, 53} The biphenyl diamine **39** was diazotised by treatment with sodium nitrite then diiodinated through reaction with potassium triiodide, producing a buff coloured solid. The ^1H NMR spectrum contained a singlet at δ 7.40 ppm due to the aromatic protons and a singlet at 1.75 ppm corresponding to the methyl protons. The molecular ion was identified in the mass spectrum at m/z 462 with a fragmentation pattern consistent with sequential loss of each iodide.

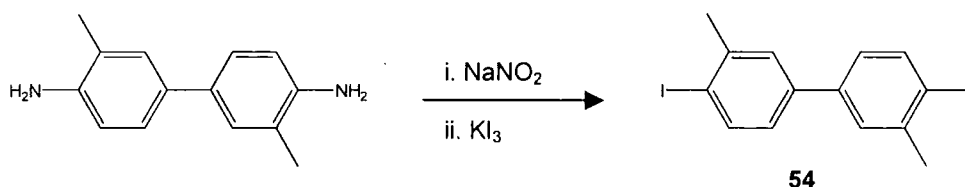


39

53

The tetraaryl substituted compounds **30** and **31** were prepared by an Ullmann Condensation of **53** with diphenylamine and di(4-methylphenyl)amine respectively in refluxing *ortho*-dichlorobenzene in the presence of potassium carbonate and copper powder. The resulting mixture of product and excess diarylamine was separated by fractional crystallisation from cold ethanol. The ^1H NMR spectrum for **30** showed a pattern of a pseudo triplet at δ 7.26 ppm $J_{\text{HH}} = 16$ Hz, due to coupling of the *meta* proton of the peripheral aryl ring with those either side of it, a doublet at 7.12 ppm, $J_{\text{HH}} = 7$ Hz, due to the *ortho* protons of the peripheral rings, a triplet at 7.00 ppm, $J_{\text{HH}} = 7$ Hz, due to the *para* protons of the peripheral aryl rings, a singlet at 6.86 ppm due to the protons of the biphenyl and a singlet at 1.86 ppm corresponding to the protons of the methyl groups. The ^1H NMR spectrum for **31** contained two doublets at 6.97 ppm $J_{\text{HH}} = 22$ Hz, due to the AA'BB' coupling pattern of the protons of the peripheral tolyl rings, a singlet at 6.73 ppm due to the protons of the biphenyl and two singlets at 2.54 and 1.76 ppm corresponding to the methyl groups on the peripheral rings and the central biphenyl respectively. The mass spectra confirmed the molecular ions with masses of m/z 544 and 600 respectively with appropriate fragmentation patterns showing loss of aryl and amino units.

The synthesis of **54** followed the same procedure as employed for **52**. The parent diamine, 3,3'-dimethyl-(1,1'-biphenyl)-4,4'-diamine was diazotised and iodinated, producing **54** as a buff coloured powder. The ^1H NMR spectrum showed a pattern of four resonances, at δ 7.76 ppm a doublet, $J_{\text{HH}} = 8$ Hz, due to the proton at the 5 position of the biphenyl. At 7.33 ppm a doublet, $J_{\text{HH}} = 2$ Hz, due to the proton at the 2 position, the coupling is small as it is long range through bond w coupling to the proton at the 6 position. The resonance for the proton at the 6 position is at 6.97 ppm and is a doublet of doublets, $J_{\text{HH}} = 11$ Hz. The singlet resonance for the protons on the methyl groups occurred at 2.41 ppm. The molecular ion was identified in the mass spectrum at m/z 434 with the appropriate fragmentation pattern for loss of iodide.



The preparations of **32** and **33** were analogous to those of **28** and **29**, using **54** in place of **52**. The ^1H NMR spectrum for **32** showed a pattern of multiplets in the aromatic region at δ 7.52, 7.47, 7.26, 7.21, 7.05, 6.97 ppm in the ratio 2:2:8:2:8:4, consistent with the expected product, with a singlet corresponding to the methyl protons at 2.12 ppm. The spectra were explicitly assigned through the use of correlated 2D NMR.

Correlated 2D NMR is one of the more commonly used 2D techniques. These methods can be applied to homonuclear spin systems, in this case proton-proton, hereon referred to as COSY, and heteronuclear spin systems in this case proton-carbon, known as Heteronuclear Single Quantum Correlation, (HSQC). A third technique was also applied to the systems of interest here, Heteroatom Multiple Bond Correlation (HMBC) spectroscopy.⁵⁴⁻⁵⁶

The basis of the correlation experiment is the process of coherence transfer of magnetisation between coupled spins. The experiment consists of two 90° pulses separated by a time period. The result of performing this experiment for the nucleus A of an AX spin system (A and X both protons) can be explained as follows. There are two distinct cases which may be considered, $J_{(A-X)} = 0$ and, $J_{(A-X)} \neq 0$ Hz. For both situations the effect of the initial 90° pulse is the same, the bulk magnetization being flipped into the $x'y'$ plane. The second pulse is called the mixing pulse and essentially mixes the components of the transverse magnetization, causing coherence transfer between the coupled systems. When $J_{(A-X)} = 0$ Hz this second pulse has no effect on the information contained in the transverse magnetization and is therefore invariant to any time delay before the second pulse. This produces a contour in the 2D spectrum with the coordinates (δ_x, δ_x) : this is called a diagonal contour. When $J_{(A-X)} \neq 0$ Hz the second pulse results in coupling information being transferred between the spins of the X and A nuclei. The A magnetization vectors precessing at frequency ν_a are partially transferred to ν_x . The 2D COSY spectrum of the spin-coupled AX system therefore consists of the diagonal contours (δ_A, δ_A) , (δ_x, δ_x) and also the off-diagonal contours with coordinates (δ_A, δ_x) and (δ_x, δ_A) . These contours indicate that A is indeed spin coupled to X. Figure 4.7 shows an expansion of the aromatic region of the COSY contour plot for **32**.

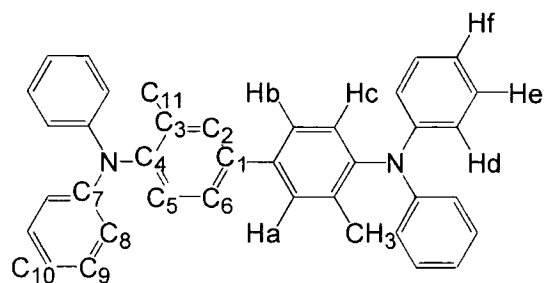


Figure 4.6 Carbon and hydrogen labelling diagram for NMR assignment of **32**

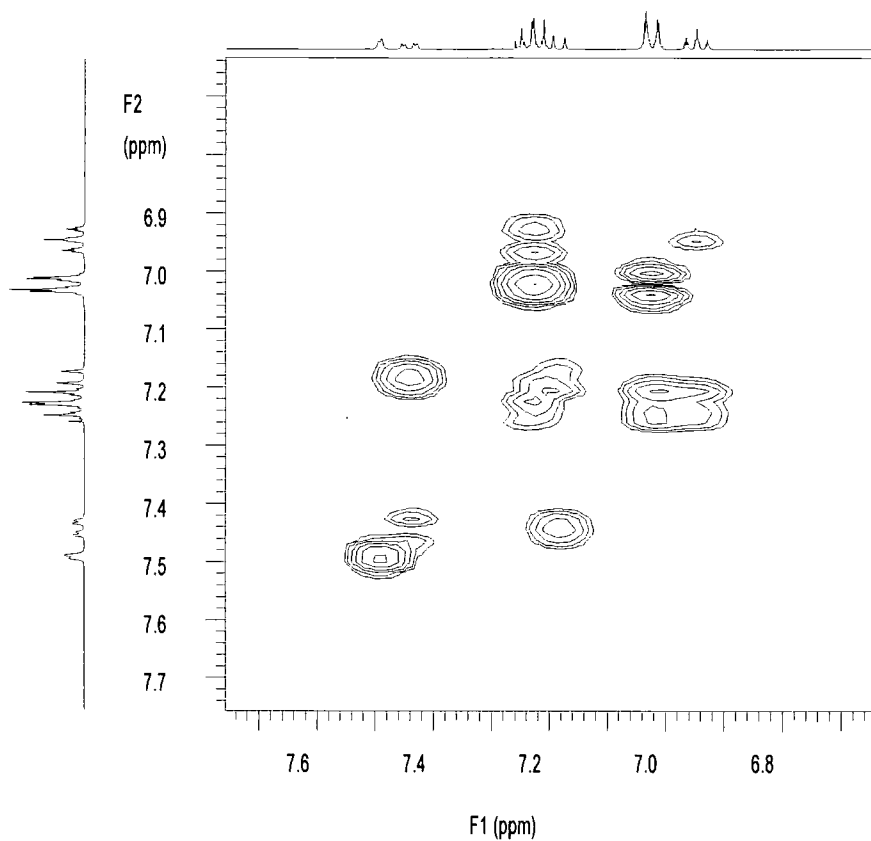


Figure 4.7 Expansion of the aromatic region of the COSY contour plot for **32**.

The doublet at 7.52 ppm, $J_{\text{HH}} = 2$ Hz, has one off diagonal contour relating to the doublet of doublets at 7.47 ppm, the coupling is very small however, indicating that the coupling is a w coupling to the proton H_b , therefore we can assign this peak to H_a . The doublet of doublets, at 7.47 ppm, $J_{\text{HH}} = 8$ Hz has two off diagonal contours, relating to H_a and to the doublet at 7.21 ppm, $J_{\text{HH}} = 8$ Hz, and these are the only off diagonal contours for that set of resonances. We can therefore relate this set of resonances to H_b and the resonances at 7.21 ppm are assigned to H_c . The triplet at 7.26 ppm, $J_{\text{HH}} = 16$ Hz, displays contours relating to both signals at 7.05 and 6.97 ppm, so is assigned to H_e . The doublet at 7.05 ppm, $J_{\text{HH}} = 8$ Hz, has off diagonal contours relating to H_e only and taking account of the integration of the peak is assigned to H_d . The final aromatic signal, a triplet at 6.97 ppm, $J_{\text{HH}} = 14$ Hz, has an off-diagonal contour relating to H_e only, and therefore must be due to H_f .

In contrast to the COSY experiment, which uses the ^1H - ^1H spin-spin couplings as the means for the transfer of magnetisation, HSQC utilises the ^1H - ^{13}C one bond couplings and therefore shows directly which protons are attached to which carbons. Figure 4.8 shows the HSQC contour plot for **32**.

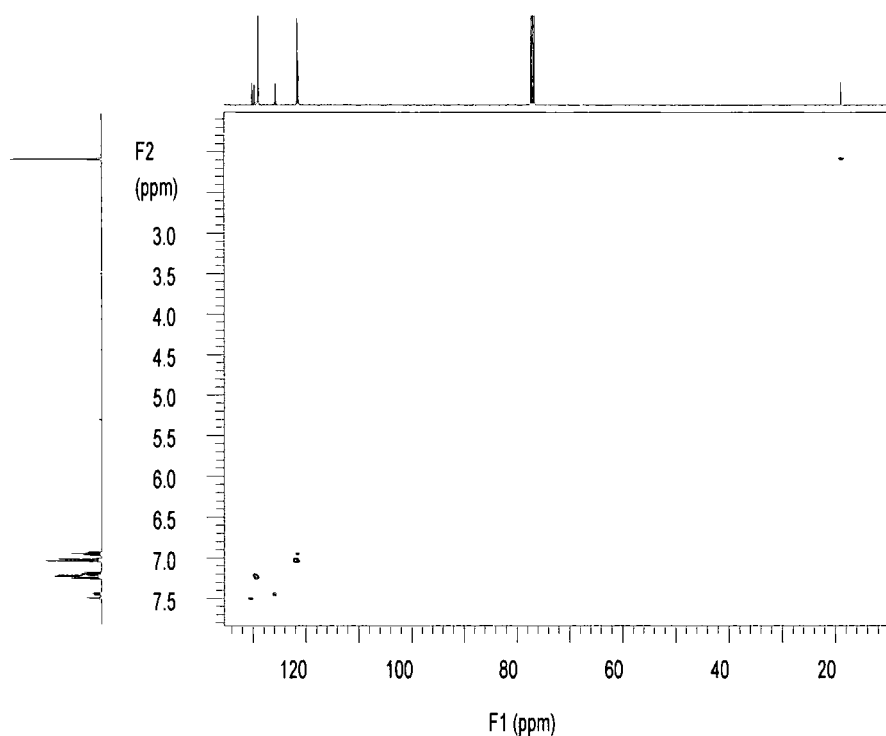


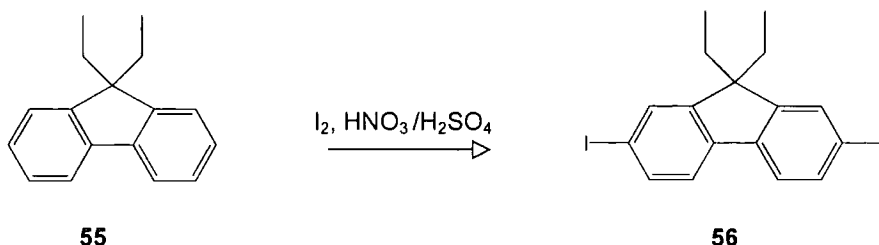
Figure 4.8 HSQC spectrum showing ^{13}C and ^1H spectra of **32**

The HSQC spectrum is assigned in the same manner as the COSY, through the contours that relate the two spectra. The signal assigned to H_a at 7.52 ppm has a contour plot with the carbon signal at 130.21 ppm, which we can assign as C2. The next carbon signal at 129.75 ppm, has a contour with H_c, and is assigned C5. The signal at 129.07 ppm has a contour relating to H_e and is therefore due to C9. The signal at 125.83 ppm has a contour relating to H_b and is therefore due to C6. Of the two closely grouped signals in the spectrum at 121.69 and 121.51 ppm, the first is assigned to C8 and the second to C10 due to the appropriate contours with H_d and H_f. The third technique employed, HMBC, provides information on coupling through 2, 3 or 4 bonds, and was used to assign the signals due to the quaternary carbons. The signal at 147.48 ppm showed contours with H_d, H_e and H_f and is therefore due to C7. The C4 carbon would show coupling to H_c, H_a and H_b and would be shifted to low field due to the N-C bond, this is consistent with the signal at 144.65 ppm. The signal at 136.52 ppm displays a contour relating to H_c and no others and is assigned to C3. The remaining signal at 138.03 ppm is consistent with that expected for C1, completing the assignment.

The ¹H NMR spectrum of **33** contained a pattern of multiplets at δ 7.38, 7.19 and 6.88 ppm in the ratio 2:4:16, relating to the aromatic protons, with two singlets at 2.22 and 2.00 ppm in the ratio 12:6 assigned to the methyl groups on the peripheral and biphenyl respectively. Both **32** and **33** were also characterised by mass spectral analysis with molecular ions at *m/z* 516 and 572 respectively, being observed with accompanying fragmentation patterns consistent with the expected product.

The acidic methylene protons of fluorene are known to cause complications during the Ullmann Condensation,⁵⁷ and consequently diethyl fluorene **55** was used to prepare the fluorene derivatives.^{17, 19} Fluorene was treated sequentially with BuLi and bromoethane, to yield diethylfluorene almost quantitatively. The ¹H NMR spectrum contained a multiplet at δ 7.22 ppm assigned to the aromatic protons on fluorene, with the quartet and triplet resonances at δ 1.92 and 0.22 ppm characteristic of the ethyl groups.

Compound **56** was prepared by a modified literature procedure.⁵⁸ Treatment of a solution of finely divided iodine and **55** in acetic acid, with fuming nitric acid in concentrated sulfuric acid yielded **56** as a yellow solid. This was characterised by the ¹H NMR which contained a series of multiplets at δ 7.49, 7.26 and 7.11 ppm in the ratio 2:2:2:4:6 with a quartet and triplet at 1.82 and 0.16 ppm respectively, corresponding to the protons on the ethyl chain.



Preparation of **34** and **35** from **56** followed the same coupling procedure as previously described for **19**. The resultant products were purified by chromatography and recrystallisation from ethanol and CH_2Cl_2 , producing crystals suitable for X-ray analysis in the case of **34**. The products were characterised by their ¹H NMR spectra, which for **34** contained a complex multiplet centred at δ 7.0 ppm assigned to the signals due to the aromatic protons of the fluorene and phenyl rings overlying each other, and a quartet at 1.72 ppm, $J_{\text{HH}} = 7\text{Hz}$, with a triplet at 0.29 ppm, $J_{\text{HH}} = 7\text{Hz}$, due to the ethyl chains. The molecular ion was identified in the mass spectrum at m/z 556. The ¹H NMR spectrum for **35** also displayed a complex multiplet at δ 7.0 ppm corresponding to all the aromatic protons, with a singlet at 2.2 ppm assigned to the methyl protons. At 1.71 ppm, was the expected quartet, $J_{\text{HH}} = 8\text{Hz}$ and at 0.29 ppm the triplet, $J_{\text{HH}} = 8\text{Hz}$ from the protons, on the ethyl chains. The molecular ion was identified in the mass spectrum at m/z 612.

The synthesis of **36** was analogous to that of **19**, using carbazole in place of the diarylamine. The crude product was purified by recrystallisation from cold ethanol or CH_2Cl_2 solutions. From a CH_2Cl_2 solution crystals suitable for X-ray analysis were obtained. The ¹H NMR spectrum for **36** displayed a series of multiplets arising at δ 8.19, 7.93, 7.53, 7.47 and 7.33 ppm in the ratio 4: 4: 4: 4: 4: 4 for the aromatic protons. The molecular ion was identified in the mass spectrum at m/z 484 with an appropriate fragmentation pattern for the loss of carbazole sub-units.

Due to the dearth of published solid state structures for this class of compounds, obtaining suitable crystals for X-ray analysis was a prime objective. Here are presented the molecular structures recorded during this work.

The molecular structure of **27** shows an almost planar configuration at the nitrogen centres, with the torsion angles of the surrounding aryl rings defining a propeller like geometry about the nitrogen centres with respect to the plane defined by the 3 N-C bonds. The N-C(4)_(biphenyl) bond length is slightly shorter than the N-C(7,14) bond lengths at 1.410(1) Å compared to 1.426(1) and 1.429(1) Å. The central C-C bond length is 1.480(2) Å with bond lengths of 1.383(2)-1.405(2) Å within the biphenyl. The dihedral angle between the two rings of the biphenyl fragment is 32.8°.

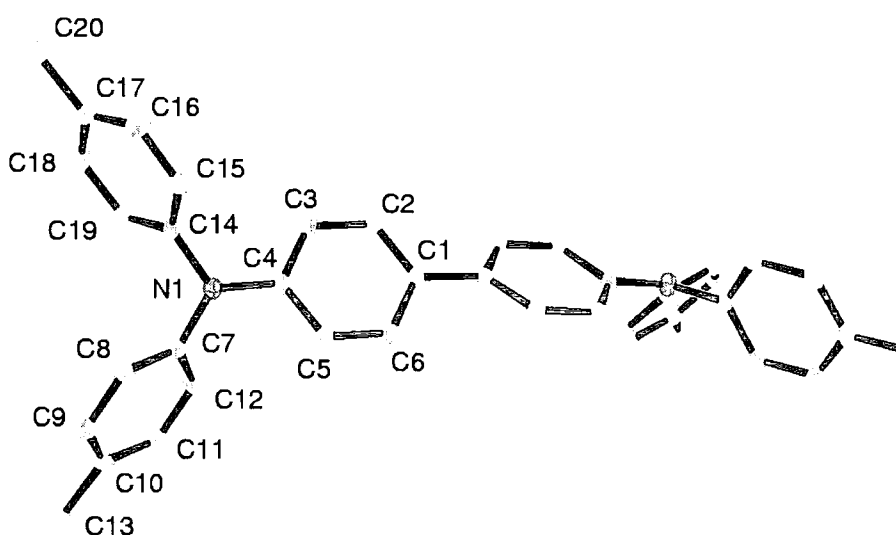


Figure 4.9 Molecular structure of **27**

Crystals of the tetramethyl substituted biphenyl, **30** suitable for single crystal X-ray analysis were obtained by slow evaporation of a saturated thf solution. The molecular structure exhibits a planar conformation at the nitrogen centres, with a N-C(1)_(biphenyl) bond length of 1.42(2) Å, comparable in length to the peripheral ring N-C (7,12) bond lengths of 1.41(2) and 1.42(2) Å. The phenyl rings around the nitrogen centres define a propeller like geometry with respect to the plane defined by the 3 N-C bonds. The central C-C bond length is 1.5(2) Å with bond lengths of 1.39(2)-1.40(2) Å in the biphenyl with a dihedral angle of 84.98° enforced by the steric requirements of the four methyl groups.

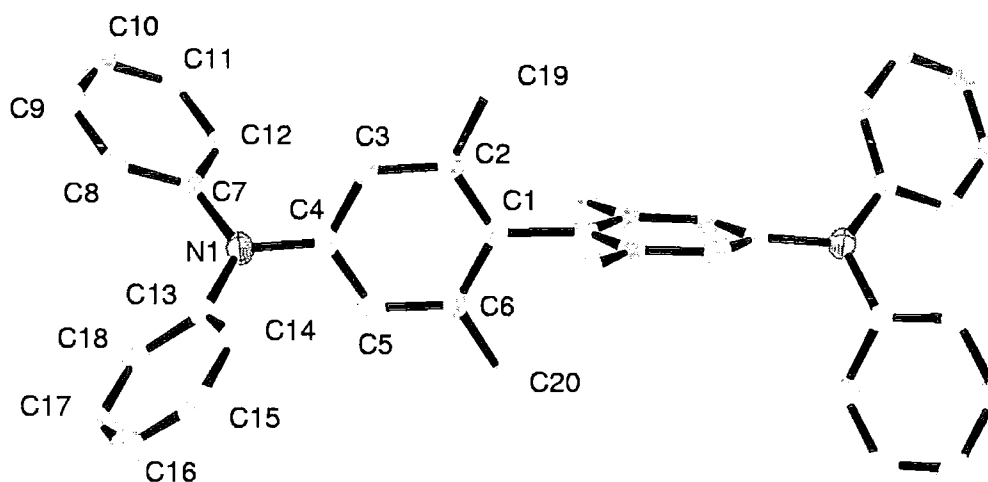


Figure 4.10 Molecular structure of 30

Slow diffusion of hexanes into a benzene solution of **32** produced a crystal suitable for X-ray analysis. The molecular structure exhibits a planar conformation at the nitrogen centres, the plane defined by the N-C bonds is at an angle of 66.50° to the plane of the adjacent phenyl ring of the biphenyl unit. This is due to the steric effect of the methyl group on the biphenyl. The N-C(1)_(biphenyl) bond length of $1.4414(13)$ Å is longer than the N-C (7,13) bond lengths of only $1.4080(14)$ and $1.4215(14)$ Å, due to the reduced interaction between the aromatic π system and the nitrogen lone pair. The phenyl rings around the nitrogen define a propeller like geometry with respect to the plane defined by the 3 N-C bonds. The central C-C bond length is 1.496 Å with bond lengths of $1.3948(16)$ - $1.4060(15)$ Å in the biphenyl with a dihedral angle of 10.17° between the two rings.

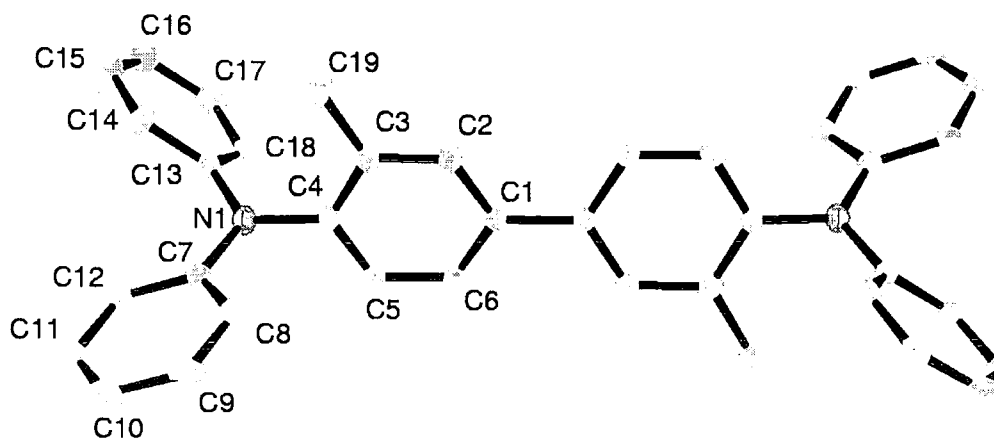


Figure 4.11 Molecular structure of 32

The molecular structure of the fluorene bridged **34**, as with the previous diamines displayed a planar conformation at the nitrogen centres, with the phenyl rings defining a propeller like geometry about the nitrogen centre with respect to the plane defined by the three N-C bonds. All N-C bonds were comparable in length with a N-C(4)_(fluorene) bond length of 1.427(2) Å and N-C(7, 13) bond lengths of 1.408(2) and 1.425(2) Å to the peripheral phenyl groups. The fluorene sub-unit is essentially planar with a central C-C bond of 1.481(3) Å, the bond lengths within the rings of the fluorene moiety range between 1.382(3)-1.519(2) Å.

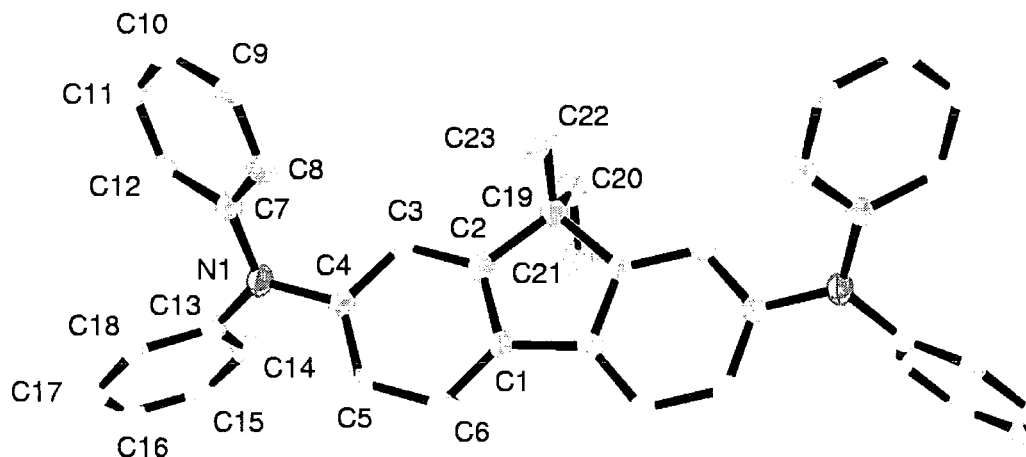


Figure 4.12 Molecular structure of **34**

In the molecular structure of **36** the carbazole unit is planar with a dihedral angle of 46.1(2)° with respect to the biphenyl. The (C7-N1-C14) angle of 108.11(13)° is enforced by the C12-C13 bond. The N-C(4)_(biphenyl) bond length is 1.417(2)Å, comparable with N-C(4)_(biphenyl) lengths in diaryl substituted diamines. The central C-C bond length is 1.489(3)Å with bond lengths of 1.380(2)-1.396(2)Å within the biphenyl.

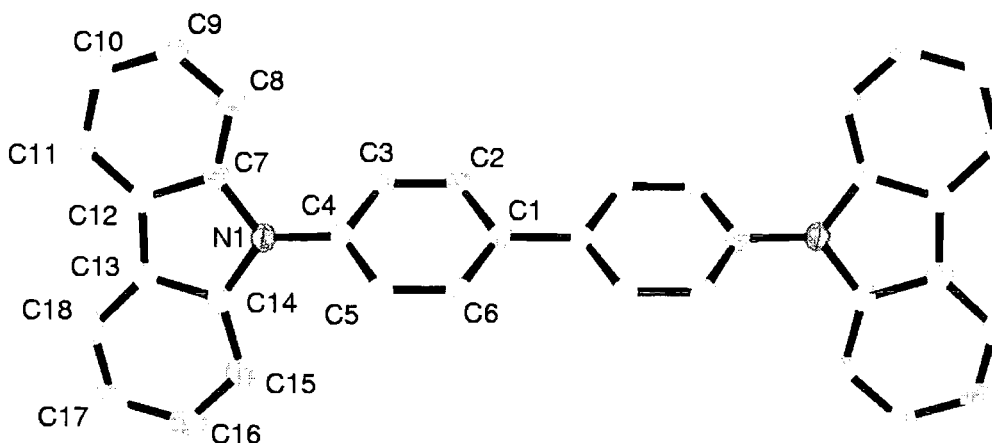


Figure 4.13 Molecular structure of **36**

Table 4.3 Selected crystallographically determined bond lengths, bond angles and torsion angles (Data for **26** is included for comparison)

	26	27	32	34	36	30
Bond lengths (Å)						
N1 C4						
N1 C7	1.415(5)	1.410(1)	1.4414(13)	1.427(2)	1.417(2)	1.4276(16)
N1 C14	1.417(5)	1.426(1)	1.4080(14)	1.408(2)	1.407(2)	1.4109(17)
C1 C6	1.443(5)	1.429(1)	1.4215(14)	1.425(2)	1.399(2)	1.4237(17)
C1 C2	1.400(6)	1.405(2)	1.4039(16)	1.391(3)	1.396(2)	1.4036(18)
C1 C1'	1.408(6)	1.398(2)	1.4060(15)	1.400(3)	1.396(2)	1.4037(18)
C2 C3	1.484(7)	1.480(2)	1.496(15)	1.481(3)	1.489(3)	1.500(2)
C3 C4	1.388(5)	1.391(2)	1.3990(15)	1.382(3)	1.380(2)	1.3973(18)
C4 C5	1.399(6)	1.397(2)	1.3994(17)	1.393(3)	1.386(2)	1.3902(19)
C5 C6	1.397(6)	1.401(2)	1.3948(16)	1.398(3)	1.395(2)	1.3904(19)
	1.385(5)	1.383(2)	1.3959(15)	1.394(3)	1.381(2)	1.3947(18)
Bond angles (°)						
C4 N1 C7	122.3(3)	119.52(9)	119.06(9)	121.03(15)	125.13(13)	120.10(11)
C4 N1 C14	119.2(3)	120.03(9)	117.78(9)	119.88(15)	126.39(13)	117.87(11)
C7 N1 C14	118.1(3)	116.51(9)	123.12(9)	118.70(16)	108.11(13)	120.83(11)
C3 C4 N1	120.6(3)	121.9(1)	119.80(10)	120.01(17)	120.88(14)	121.27(12)
C5 C4 N1	120.8(4)	119.7(1)	119.84(10)	119.91(17)	120.30(14)	119.14(12)
C8 C7 N1	121.6(4)	119.2(1)	120.47(10)	121.00(17)	129.55(15)	121.44(12)
C12 C7 N1	120.1(4)	121.6(1)	120.99(10)	121.22(17)	108.76(14)	119.87(12)
C19 C14 N1	119.5(4)	120.4(1)	119.53(10)	120.24(18)	109.11(14)	120.29(13)
C15 C14 N1	120.7(4)	120.5(1)	121.27(10)	120.17(18)	129.46(15)	120.33(13)
Torsion angles (°)						
C6 C1 C1' C6'	37.16	32.8	36.1	-	-0.21	85.0
C7 N1 C4 C3	-37.0(6)	136.64(11) -	52.3	-43.4(3)	-46.1(2)	44.55(19)
C14 N1 C4 C3	150.5(4)	20.27(16)	74.30	129.5(2)	126.11(16)	-123.02(15)
C4 N1 C7 C8	-34.2(6)	146.32(11)	45.0	-26.4(3)	-10.7(3)	-144.10(14)
C14 N1 C7 C8	138.3(4)	-55.98	-147.8	160.93(18)	-	23.1(2)
C4 N1 C14 C15	-66.0(5)	-68.18(14)	28.8	-46.1(3)	7.7(2)	39.7(2)
C7 N1 C14 C15	121.2(4)	134.24(11)	139.7	126.7(2)	173.01(13)	-127.75(15)



4.5 Cyclic Voltammetry and Spectroelectrochemistry

The electrochemical response of **1** and **26** has been described in detail in Chapter 3. Cyclic voltammetry (CV) studies of compounds **19-36** (Table 4.4) illustrate the marked effect of the different substitution patterns of these materials on the oxidation potentials. The electrochemistry of compounds **28**, **30** and **32** were complicated by the reactivity of the cations, and will be discussed in greater detail in Chapter 6.

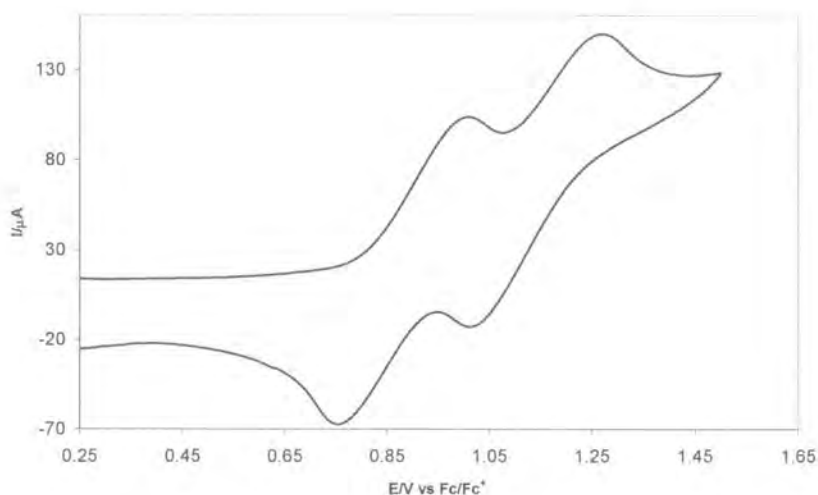


Figure 4.13 Cyclic voltammogram of **19**

The parent material **19** undergoes two sequential, one electron oxidation processes at $E_{1/2} = 0.386$ and 0.638 V (vs $\text{Fc}/\text{Fc}^+ = 0.0$ V). (Figure 4.14) The introduction of four methyl groups, at the *para* positions of the peripheral rings in **27** again produced two reversible oxidation waves in the CV, but with the first oxidation occurring at a potential 0.135 V lower than the first oxidation of **19**. The second oxidation occurred at a potential 0.084 V lower than the corresponding oxidation for **19**. These results are due to the inductive effects of the additional methyl groups. It can also be seen that addition of more methyl groups stabilises the radical cation, as the comproportionation constant for $\mathbf{27}^{\cdot+}$ is an order of magnitude larger than that for **19**.

The introduction of methyl groups at the 2,2' positions, around the central C-C bond was expected to greatly increase the thermodynamic barrier of formation of the radical cation, as it would hinder the planarisation which has been shown to occur on oxidation of these tetraarylbiophenyldiamines (Chapter 3). This was indeed the case, with the first oxidation of **29**, occurring at 0.442 V with the second oxidation occurring at a potential only 0.158 V more positive, indicating that the radical cation is destabilised relative to the unhindered systems.

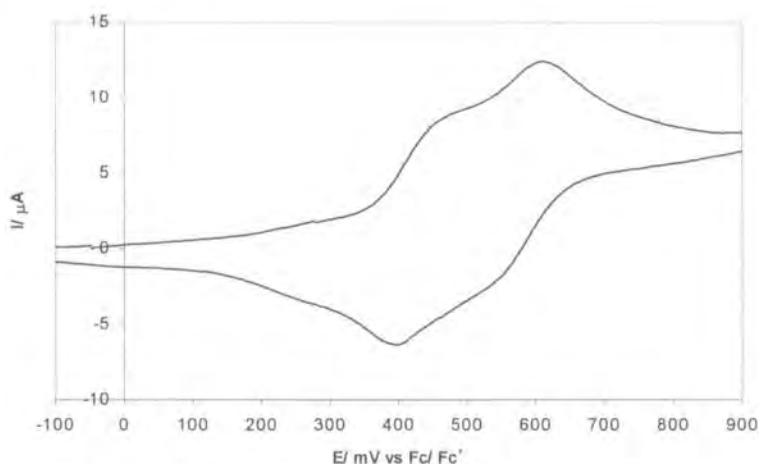


Figure 4.14 Cyclic voltammogram of **29**

As a consequence of the introduction of four methyl groups at the 2,2',6,6' positions in **31**, this compound displayed only one oxidation process, at $E_{1/2}$ 0.463 V. This oxidation potential is markedly high, some 0.116 V more positive than oxidation of tri(4-methylphenyl)amine, **23**. If the two centres are totally isolated, then the oxidation potential would be expected to be at a similar value to that of the simple triarylamine. That the oxidation potential in **31** is significantly higher, suggests that the confinement of two positively charged centres in such close proximity is thermodynamically unfavourable. This suggestion is supported by inspection of the second oxidation potentials of **1**, **19**, **26** and **27** which all have second oxidation potentials in the range 0.505-0.638 V.

The CV of the fluorene bridged material **34** showed two reversible oxidation waves, the first oxidation at a potential of 0.276 V, a much lower potential than the comparable biphenyl containing compound **19**. The stability of the radical cation was also greatly increased over all the other materials, with a comproportionation constant an order of magnitude greater than **27**.

The CV of **35** had a first oxidation potential 0.157 V less positive than **34**, evidencing the inductive effect of the methyl groups on the first oxidation potential. Having seen that enforcing the geometry of the central biphenyl rings orthogonal to each other removes any delocalisation between the two nitrogen centres in **31**, enforcing the central biphenyl in a planar geometry lowers the thermodynamic barrier to oxidation. The energy associated with the planarisation of the biphenyl is removed completely.

Introducing methyl groups at the 3,3' position of the biphenyl introduces steric interactions between the arylamine moieties and the introduced methyl group. This has the potential to have an effect on the electrochemistry of the material if it significantly reduces the overlap between the biphenyl aromatic π system and the nitrogen lone pair.

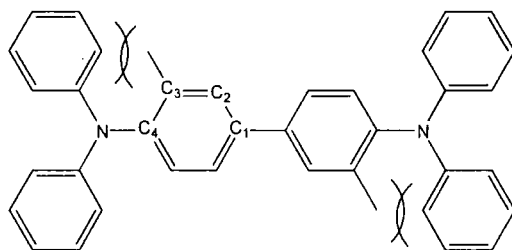


Figure 4.16 Steric conflict in **32** and **33** due to the introduction of methyl groups at the 3,3' positions

Comparison of the N-C(4) bond lengths acquired from the molecular structures support this idea, with N-C(4) bond lengths of 1.410(1) Å (**19**), 1.415(5) Å (**26**), 1.427(2) Å (**34**) and 1.4276(16) Å (**31**) compared to 1.4414(13) Å for **32**.

The CVs of the two 3,3'-dimethyl substituted materials **32** and **33** showed two oxidation waves corresponding to formation of the cation, and dication. The separation of the two half wave potentials of **33** was 0.223 V, this value is comparable to those obtained for compounds **1**, **19** and **26**. This indicates that once the radical cation is formed it is as stable as the cations of the unhindered systems, any reorganisation that occurs acts to reduce the steric conflict. This is consistent with the molecular structure data of **26** and **26⁺** that shows a rotation of the unsubstituted ring from an angle of $-34.2(6)^\circ$ to $-54.7(10)^\circ$ relative to the N-C plane about the nitrogen centre. The starting geometry of **32** has a dihedral angle of 45.0° for the ring closest to the methyl group at the 3 position of the biphenyl, therefore if a similar rotation

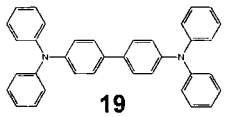
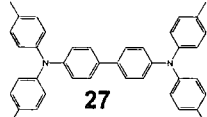
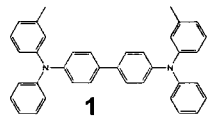
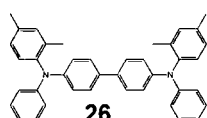
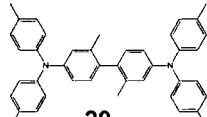
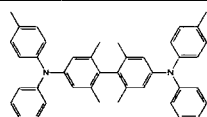
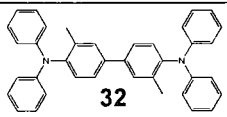
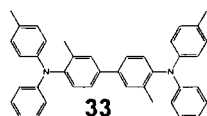
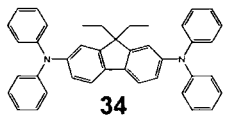
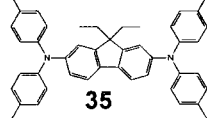
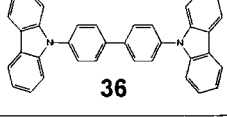
occurs in 32^+ it will act to further reduce the steric conflict between the aryl ring and the methyl group. The electrochemical response of **33** appears to be different, as the reduced stability of the radical cation 33^+ appears to run counter to the trends previously seen. However using the comproportionation constant, which for **33** is the lowest value of any material studied, and the crystal structure data it is possible to provide a hypothesis for the processes occurring. The diarylamine moiety in **33** is rotated by 52.3° relative to the adjacent phenyl ring of the biphenyl, from the structural data of 26^+ it is known that on oxidation these molecules rearrange to increase the aromatic biphenyl- π nitrogen- π orbital overlap. The methyl group in the 3,3' position will obviously prevent this, however **33** has a methyl group in each *para* position of the peripheral aryl rings, and the inductive effect of these groups is able to aid the stabilisation of a positive charge on the diarylamino moiety, with a smaller amount of delocalisation through the biphenyl. This could make the formation of the dication more favourable, relative to the cation, giving the low value of K_c seen for **33**.

The electrochemical response of **36** was complicated by the apparent insolubility of the radical cation in the presence of common anions (BF_4^- , PF_6^-). The initial scan (thf, 0.1M TBABF₄) revealed two chemically irreversible oxidation waves at peak potentials 1.03 and 1.50 V vs Fc/Fc⁺. There was no evidence of reduction processes associated with these oxidation steps and inspection of the working electrode revealed an obvious film on its surface. In CH_2Cl_2 , 0.1M TBAPF₆, a broad oxidation wave was observed at 0.95 V, upon repeated cycling the peak current associated with the oxidation wave at 0.95 V increased and a new oxidation wave was observed at 0.41 V in addition to the original oxidation wave. Further cycling led to further increase in the peak current and loss of definition of the two waves as they coalesced into a broad feature. The electronic spectrum of **36** exhibited a set of bands at 293, 317 and 340 nm however on oxidation in an OTTLE cell, these collapsed and no other bands were seen to appear. Inspection of the electrode again revealed a deposition product on the electrode. Previous studies on **36** have commented on the complicated electrochemistry, but failed to provide any explanation of the processes occurring.⁵⁹ Unfortunately due to the lack of detailed electrochemical and spectroscopic results we too were unable to elucidate the processes any further.

4.5.1 Summary of the Effects of Substituents on the Electrochemical Response of Tetraarylbiophenyldiamines.

The introduction of two methyl groups at the 2,2' positions increases the thermodynamic barrier to formation of the radical cation and destabilises that radical cation to such an extent that the dication is formed at a potential only 0.150 V more positive. Methyl substitution at the *para* position of the peripheral rings reduces the thermodynamic barrier to formation of the cation, following the trend seen with **19** and **27** and stabilises the cation once it has been formed. Confinement of the central biphenyl to a geometry of $\sim 90^\circ$ removes any delocalisation of the positive charge between the two nitrogen centres, producing a single oxidation wave. Enforcing a planar geometry on the central biphenyl in the form of a fluorene moiety reduces the thermodynamic barrier to formation of the radical cation by ~ 0.120 V and increases the stability of the radical cation relative to the biphenyl containing materials. Introducing a methyl group at the 3,3' position of the biphenyl disrupts the aromatic biphenyl π system-diarylamine π system and results in a greater localisation of charge on the peripheral aryl rings.

Table 4.4 Oxidation potentials of **19** – **36** (in CH₂Cl₂ vs Fc/Fc⁺ = 0.0 V)

Compound	E _{1/2} (V)	E _{1/2} (V)	ΔE (V)	Comproportion constant K _c
 19	0.386	0.638	0.250	17,920
 27	0.251	0.554	0.303	133,140
 1	0.292	0.507	0.215	4,320
 26	0.250	0.505	0.255	20,500
 29	0.390	0.550	0.158	550
 31	0.463	-	-	-
 32	0.337	0.560	0.223	5,906
 33	0.347	0.466	0.119	103
 34	0.276	0.648	0.372	1,955,370
 35	0.119	0.473	0.354	970,100
 36	1.03 (thf)	1.50 (thf)	0.470	-

In order to assess the kinetic stability of compounds **19-36**, to follow the oxidation event in situ, and to explore the electronic structures, room temperature UV-Vis-NIR spectroelectrochemical studies were undertaken. As described in Chapter 3 the observation of sharp isosbestic points during the electrolytic cycle $A \rightarrow A^+ \rightarrow A^{2+} \rightarrow A^+ \rightarrow A$, and recovery of the original spectra of **A** at the end of the cycle would confirm both the chemically reversible nature of the redox system in CH_2Cl_2 and the chemically distinct nature of each member of the redox series. Observation of a different spectrum on reduction of the oxidised form at the end of the cycle is indicative of an electrochemical reaction occurring on the timescale of the spectroelectrochemical experiment that may not have been observed from CV studies.

The electronic spectrum of **19** contained a set of $\pi-\pi^*$ bands which shift to lower energy on oxidation from the neutral, through the radical cation to the dication, in a similar manner to those the closely related compounds **1** and **26** (Table 4.5)(Figure 4.17).

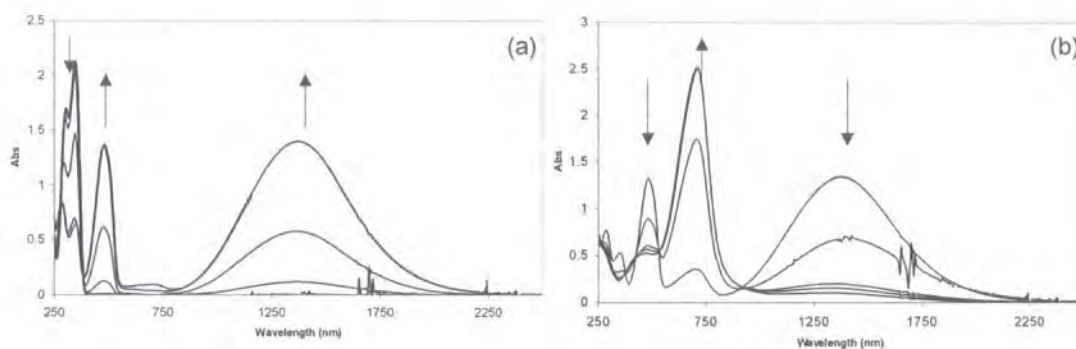
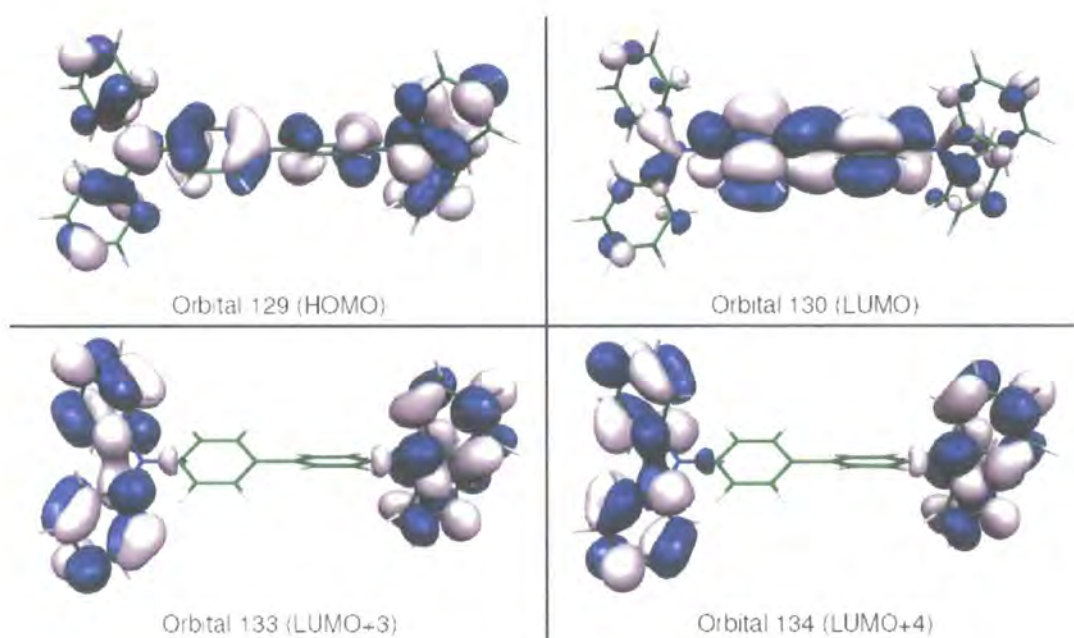


Figure 4.17 UV-Vis-NIR spectroelectrochemistry of **19** during sequential oxidation through 19^+ (a) to 19^{2+} (b). The arrows indicate the bands which grow and decay during the electrolysis. $\lambda(\text{nm})/\epsilon (\text{mol}^{-1}\text{dm}^3\text{cm}^{-1})$ **19** 351/41,764; 19^+ 1367/27,350; 19^{2+} 708/749272

Molecular modelling suggests that of the two bands observed in the spectrum of the neutral species, the lowest energy absorption band in the neutral species arises from the HOMO-LUMO transition (illustrated by the transition between orbitals **129** – **130**, Figure 4.18). The HOMO contains appreciable character from the amine nitrogen centres, the biphenyl moiety and the *ortho* and *para* carbons of the peripheral ring systems. The LUMO is heavily centred on the biphenyl group, and may be approximately described as the biphenyl π^* system. The higher energy UV transition is comprised of two almost degenerate transitions arising from HOMO –

(LUMO+4) (orbitals 129 – 134) and HOMO – (LUMO+3) (orbitals 129 – 133). These higher lying unoccupied orbitals display extensive aromatic π^* character localised on the peripheral ring systems. The two transitions in the UV spectrum of the neutral tetraarylbiophenyldiamine can therefore be satisfactorily described in terms of π - π^* _{biphenyl} and π - π^* _{peripheral} transitions in total agreement with the studies described in Chapter 3.

Figure 4.18 TDDFT representations of the orbitals involved in the electronic transitions for neutral **19**



Geometry: RBPW91/6-31G(d,p), Symmetry: D2, TDDFT: RPBE1PBE/6-31G(d)

Table 4.5: Selected Data from the TDDFT Results for the neutral **19** species.

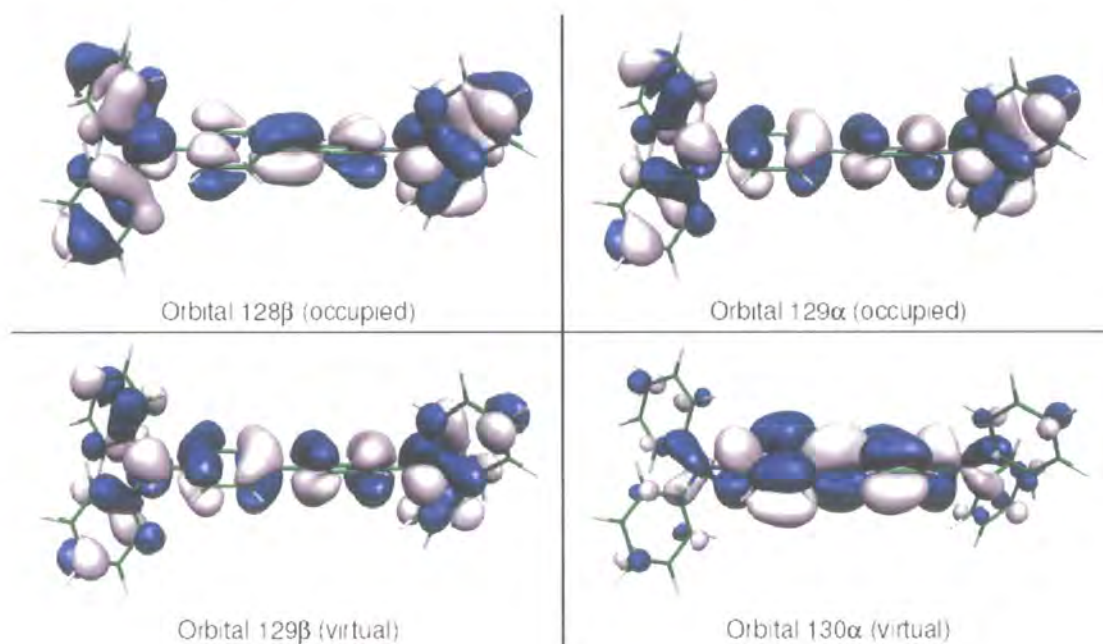
E.S. Number	Energy /eV	Energy /nm	Oscillator Strength (f)	Orbitals Involved	Contribution
1	3.4682	357.48	1.1117	128 – 135 129 – 130	0.11042 0.66993
5	4.0719	304.48	0.2537	128 – 132 128 – 133 129 – 134	-0.10212 0.24707 0.61596
6	4.0728	304.42	0.1249	128 – 134 129 – 133	0.26447 0.61175

(Text in bold highlights the major contribution to the transition)

Upon oxidation, the changes in the spectra are similar to those seen for **1** and **26** with the original π - π^* bands replaced by a new transition in the visible region. Analysis of the TDDFT results indicated this transition to again be the SOMO - LUMO (α -spin) transition (orbitals **129 α** – **130 α**) while the NIR absorption band corresponds to the

(HOMO-1) – SOMO (β -spin) transition (orbitals 128β – 129β) in keeping with the ideas discussed previously in this thesis. The graphical representation of these orbitals (Figure 4.19) again clearly shows the (HOMO-1) and SOMO to be delocalised over the molecular framework which strongly supports the conclusions drawn from the band shape analysis in Chapter 3.

Figure 4.19 TDDFT representations of the electronic transitions for the radical cation of **19**



Geometry: UBPW91/6-31G(d,p), Symmetry: D2, TDDFT: UPBE1PBE/6-31G(d)

Table 4.6: Selected Data from the TDDFT Results for the **19** radical cation

E.S. Number	Energy /eV	Energy /nm	Oscillator Strength (f)	Orbitals Involved	Contribution
1	0.8744	1417.96	0.6446	$129\alpha - 130\alpha$ $128\beta - 129\beta$	-0.18618 0.82803
12	2.9210	424.45	0.5851	$119\alpha - 132\alpha$ $119\alpha - 137\alpha$ $120\alpha - 131\alpha$ $123\alpha - 130\alpha$ $127\alpha - 130\alpha$ $128\alpha - 135\alpha$ $129\alpha - 130\alpha$ $119\beta - 137\beta$ $120\beta - 131\beta$ $127\beta - 130\beta$ $128\beta - 135\beta$	-0.12400 -0.11753 0.17411 0.13992 -0.14253 -0.20446 0.89512 0.10698 -0.12015 0.22455 0.12623

Unsurprisingly the electronic spectra of **27** were virtually identical to those of **19**, with a set of π - π^* bands which shift to lower energy on oxidation. The band in the NIR region associated with the inter-valence charge transfer is shifted to longer wavelength however. This can be ascribed to the inductive effect of the methyl groups decreasing the difference in energy between the SOMO and HOMO-1.

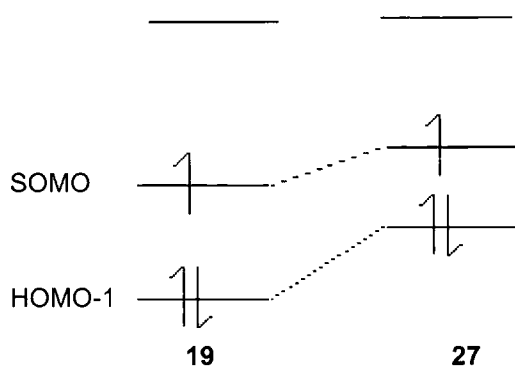


Figure 4.20 Illustration of the difference in magnitude of the SOMO/HOMO-1 gap between **19** and **27**

The electronic spectrum of **29** displayed only a single absorption band suggesting that the methyl groups at the 2,2' positions had enforced a geometry that prohibited any π - π^* _{biphenyl} transition, restricting the absorption to a π - π^* _{phenyl} transition only. In the absence of crystallographic data the geometry of a tetraaryl-2,2'-dimethyl-1,1'-biphenyl-4,4'-diamine was computed using DFT methods, the two rings of the biphenyl were predicted to be twisted at an angle of 89.7° (Figure 4.21). This calculated dihedral angle is somewhat larger than any of the reported crystal structure data for similarly 2,2' disubstituted biphenyls in which the dihedral angle falls between 70 and 86°. ^{5, 7, 60, 61}

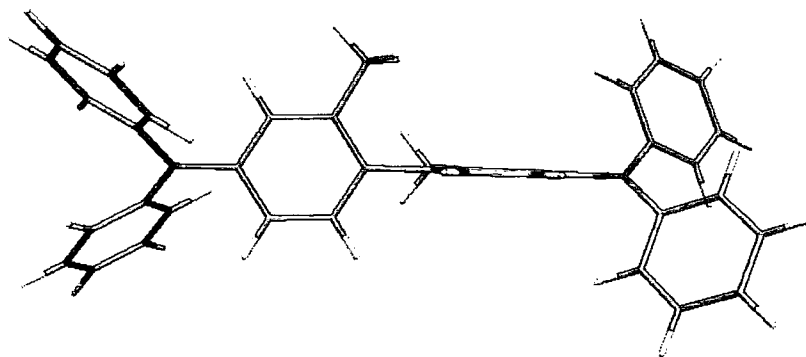


Figure 4.21 Geometry optimised structure of tetraaryl-2,2'-dimethyl biphenylamine (**28**)

The HOMO of this material is quite different to that seen for **19**, with much less character coming from the biphenyl rings, and being more localised on the triaryl amine fragment.

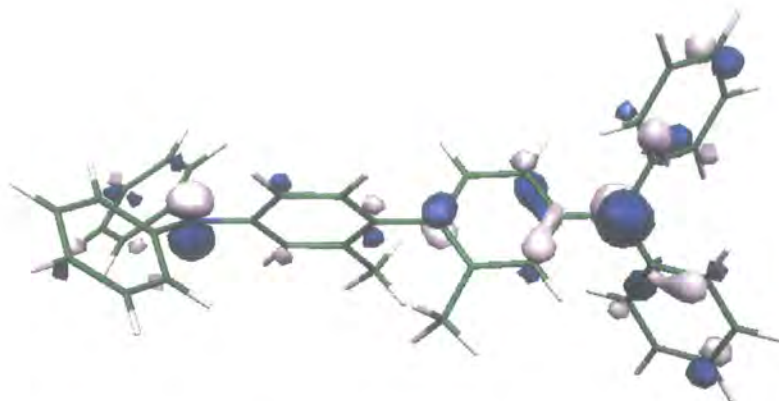


Figure 4.22 Geometry optimised structure of tetraphenyl-2,2'-dimethyl biphenyldiamine overlaid with the calculated HOMO

Oxidation of **29** saw the coherent growth of bands at 360, 439, 693 nm and in the NIR region. Bands at 439 nm and in the NIR assigned to the monocation by analogy with the previous compounds while that at 693 nm was characteristic of oxidised triaryl amines or dioxidised tetraaryl biphenyl diamines. Due to the small separation of the half waves in the CV and therefore the subsequent low value of K_c , it is unsurprising that electrolysis results in formation of equilibrium mixtures containing all three species.

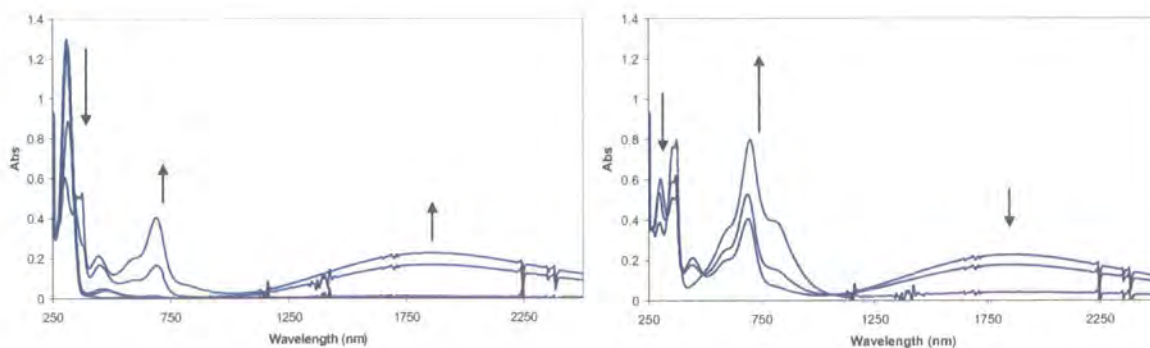


Figure 4.23 UV-Vis-NIR spectroelectrochemistry of **29** during sequential oxidation to **29**^{+•} and **29**²⁺. The arrows indicate the bands which grow and decay during the electrolysis. $\lambda(\text{nm})/\epsilon$ ($\text{mol}^{-1}\text{dm}^3\text{cm}^{-1}$) **29** 309/27; **29**²⁺ 699/16,721

Continued oxidation saw the reduction and disappearance of the bands at 308, 439 nm and in the NIR region leaving only two sets of bands at 360 and 690 nm, almost identical to the spectrum of tri(4-methylphenyl)amine, **23**. Reduction of the dication reproduced the spectral bands observed during the oxidation cycle on oxidation and after exhaustive reduction the spectrum of neutral **29** was regained. The similarity of the spectral profiles and band positions to those of systems such as tri(4-methylphenyl)amine, **23** suggests that the presence of the two methyl groups at the 2,2' positions destabilises the radical cation but do not prevent delocalisation through the central biphenyl.

The electronic spectrum of the more sterically restricted tetramethyl derivative **31** displayed only a single peak, at a wavelength similar to that found for oxidised tri(4-methylphenyl)amine, **23** appeared, supporting the idea that orientation of the two rings orthogonal replicates the behaviour of two independent triarylamines within the one molecule. Oxidation of **31** results in the collapse of this band and the appearance of a lower energy band, again replicating the behaviour of **23**, with no bands seen in the NIR region.

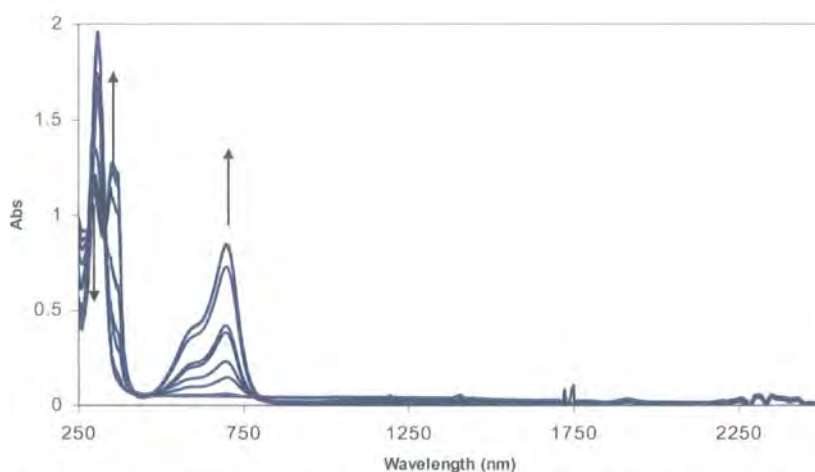


Figure 4.24 UV-Vis-NIR spectroelectrochemistry of **31** during oxidation to 31^{2+}
 $\lambda(\text{nm})/\epsilon (\text{mol}^{-1}\text{dm}^3\text{cm}^{-1})$ **31** 308/44,374; 31^{2+} 698/77,750

The calculated HOMO is not delocalised over the central C-C bond of the biphenyl moiety, but does contain character associated with both amine centres (Figure 4.24).

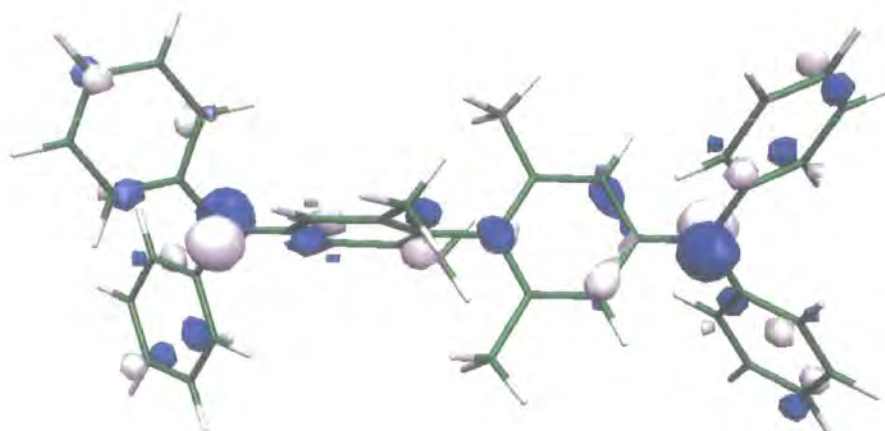


Figure 4.25 Calculated HOMO of **31**

Incorporation of methyl groups at the 3,3' positions of **33** produced a number of changes to the electronic spectral profile observed during oxidation. The bands relating to the neutral species are opposite in intensity relative to the unhindered biphenyl derivatives, with the higher energy band dominating the spectrum. This suggests that there is a larger contribution to the HOMO from the peripheral rings, which is consistent with decreased N(p)-biphenyl(π) conjugation inferred by the solid state molecular structure.

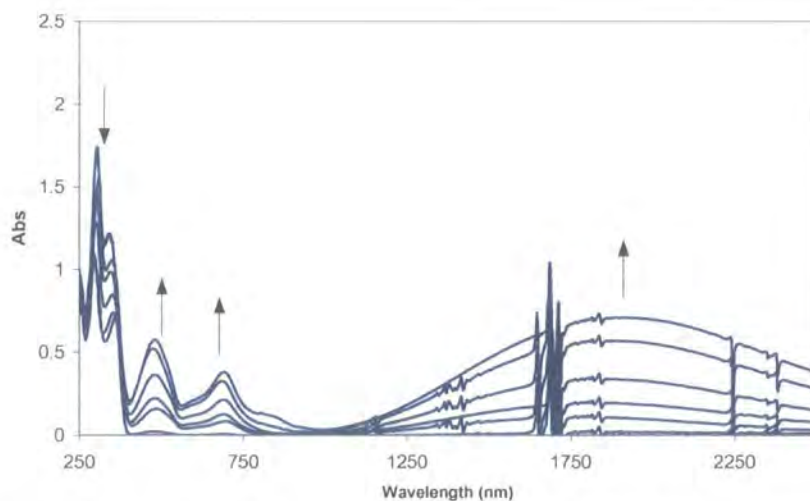


Figure 4.26 UV-Vis-NIR spectroelectrochemistry of **33** during oxidation to **33⁺**. The arrows indicate the bands which grow and decay during the electrolysis. $\lambda(\text{nm})/\epsilon (\text{mol}^{-1}\text{dm}^3\text{cm}^{-1})$ **33** 304/34,457; **33⁺** 1600/14,215. **33²⁺** 830/56,625

On oxidation to **33⁺** there are a number of differences from the unhindered biphenyl spectra evident. The growth of a band at 684 nm coincided with the growth of the band in the visible region, previously assigned to the SOMO-LUMO (α -spin)

transition. The band at 684 nm is at an almost identical position to the band seen on oxidation of **23**, suggesting that the hindered rotation due to the methyl group maintains a higher degree of HOMO character on the peripheral rings. Molecular modelling of the HOMO showed that the proportion of character emanating from the peripheral rings is much larger than in the unhindered systems, therefore the new band was assigned to a $\pi - \pi^*$ peripheral transition. (Figure 4.27)

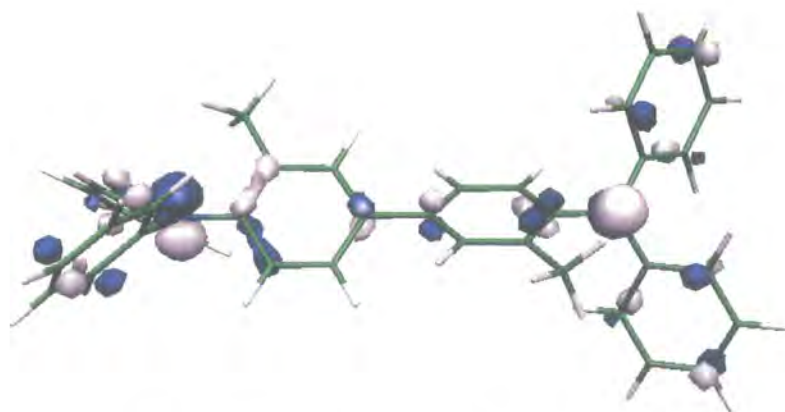


Figure 4.27 Calculated HOMO of tetraaryl-3,3'-dimethyl biphenyldiamine

Oxidation to the dication 33^{2+} produced the collapse of the band due to the SOMO-LUMO (α -spin) and the band in the NIR, and the emergence of a band in a similar position to those previously seen for the unhindered biphenyls. (Figure 4.28) The novel band at 684 nm continued to grow but was rapidly incorporated as a shoulder of the familiar band in the visible region.

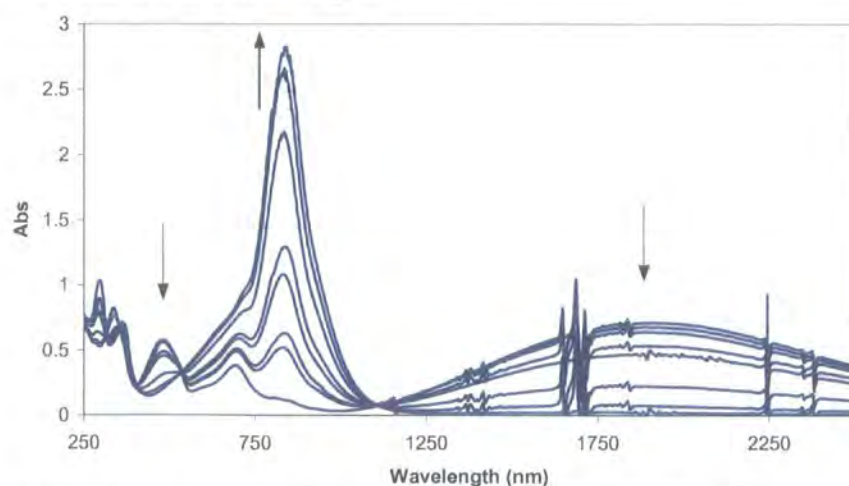


Figure 4.28 UV-Vis-NIR spectroelectrochemistry of 33^+ during oxidation to 33^{2+} . The arrows indicate the bands which grow and decay during the electrolysis. $\lambda(\text{nm})/\epsilon (\text{mol}^{-1}\text{dm}^3\text{cm}^{-1})$ 33^{2+} 830/56,625

The fluorene derivatives **34** and **35** displayed a virtually identical set of spectra, with a set of $\pi\text{-}\pi^*$ bands in the electronic spectrum. The bands at higher energy can be assigned to a $\pi\text{-}\pi^*$ _{peripheral} transition by comparison with the biphenyl derivatives. The band at lower energy can therefore be assigned to a $\pi\text{-}\pi^*$ _{fluorene} transition.

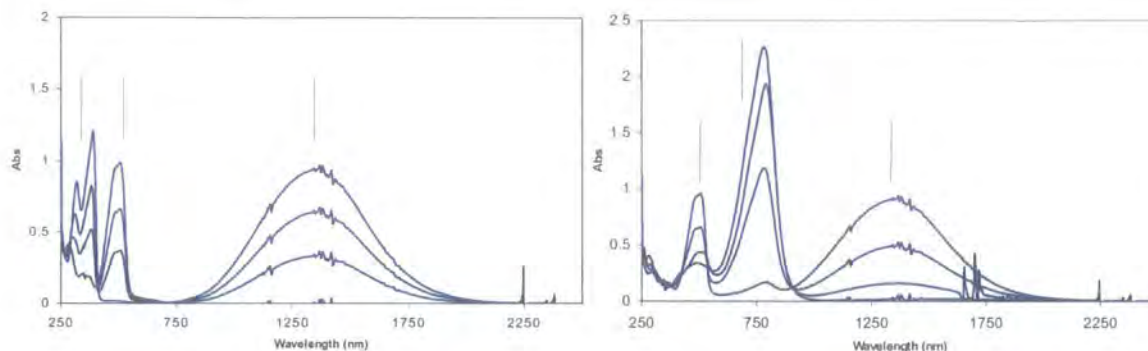


Figure 4.29 UV-Vis-NIR spectroelectrochemistry of **35** during sequential oxidation to **35²⁺**. The arrows indicate the bands which grow and decay during the electrolysis. $\lambda(\text{nm})/\epsilon (\text{mol}^{-1}\text{dm}^3\text{cm}^{-1})$ **35** 386/31,746; **35⁺** 1330/26,030; **33²⁺** 780/59,787

Modelling of the HOMO of **34** showed that the majority of the HOMO character stemmed from the nitrogen centres and the fluorene moiety, with only a small proportion being due to the peripheral aryl rings. This is consistent with the assignment of the electronic spectra above.(Figure 4.30)

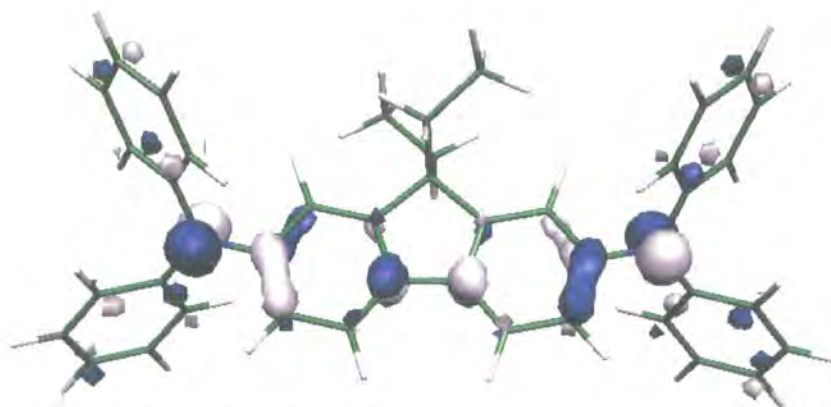


Figure 4.30 Calculated HOMO of **34**

The NIR band present in the electronic spectra of **34⁺** and **35⁺** was almost identical in energy and bandshape to that seen for **1** and **26** indicating that the reorganisation energy that is removed by enforcing a planar geometry across the bridge between the amine centres is very low.

Table 4.7 Table of electronic spectra absorption band data for compounds **19-36**

Material	Oxidation State	Peak Position (nm)/Extinction Coefficient ($\text{mol}^{-1}\text{dm}^3\text{cm}^{-1}$)
19	0	303/33,137 351/41,764
	+1	482/26,078 1367/27,350
	+2	708/49,272
27	0	304/29,902 356/36,990
	+1	468/30,679 1467/32,620
	+2	785/66,406
29	0	309/27,204
	+1	439/4,255 1863/4680
	+2	373/16,595 699/16,721,
31	0	308/44,374
	+2	349/28,832 698/77,750
33	0	304/34,457 340/23,895
	+1	468/11,044 684/7,228 1900/14,215
	+2	830/56,625
34	0	314/44,414 381/59,574
	+1	495/37,234 1222/30,319
	+2	669/64,627
35	0	316/23,676 381/33,404
	+1	483/26,685 1330/30,319
	+2	780/65,425
36	0	293, 317, 340/15,960

References for Chapter 4

- 1 D.-J. Liaw, P.-N. Hsu, and B.-Y. Liaw, *J. Polymer Sci. A. Poly. Chem.*, 2001, **39**, 63.
- 2 D.-J. Liaw, I.-W. Chen, W.-H. Chen, and S.-L. Lin, *J. Polymer Sci. A. Poly. Chem.*, 1999, **37**, 4591.
- 3 H.-W. Schmidt and D. Guo, *Makromol. Chem*, 1988, **189**, 2029.
- 4 W. R. Krigbaum and K. J. Krause, *J. Polymer Sci.*, 1978, **16**, 3151.
- 5 K. C. Chuang, J. D. Kinder, D. L. Hull, D. B. McConville, and W. J. Youngs, *Macromol.*, 1997, **30**, 7183.
- 6 A. Modelli, G. Distefano, and D. Jones, *Chem. Phys.*, 1983, **82**, 489.
- 7 F. Fowweather, *Acta Cryst.*, 1952, **5**, 820.
- 8 A. Helms, D. Heiler, and G. McLendon, *J. Am. Chem. Soc*, 1991, **113**, 4325.
- 9 M. Maus, W. Rettig, D. Bonafoux, and R. Lapouyade, *J. Phys. Chem. A*, 1999, **103**, 3388.
- 10 K. Sakanoue, M. Motoda, M. Sugimoto, and S. Sakaki, *Nonlinear optics*, 2000, **26**, 271.
- 11 A. Ronlan, J. Coleman, O. Hammerich, and V. D. Parker, *J. Am. Chem. Soc*, 1974, **96**, 845.
- 12 R. B. Carlin, *J. Am. Chem. Soc*, 1945, **67**, 928.
- 13 K. C. Chuang, *High Perform. Polym.*, 1995, **7**, 81.
- 14 I. D. L. Albert, T. J. Marks, and M. A. Ratner, *J. Am. Chem. Soc*, 1998, **120**, 11174.
- 15 S. F. Nelsen, R. F. Ismagilov, K. E. Gentile, and D. R. Powell, *J. Am. Chem. Soc*, 1999, **121**, 7108.
- 16 B. Liu, W.-L. Yu, J. Pei, S.-Y. Liu, Y.-H. Lai, and W. Huang, *Macromol.*, 2001, **34**, 7932.
- 17 B. Tsuie, J. L. Reddinger, G. A. Sotzing, J. Soloducho, A. R. Katritzky, and J. R. Reynolds, *J. Mater. Chem.*, 1999, **9**, 2189.
- 18 A. Donat-Bouillud, I. Lévesque, Y. Tao, M. D'Iorio, S. Beaupré, P. Blondin, M. Ranger, J. Bouchard, and M. Leclerc, *Chem. Mater.*, 2000, **12**, 1931.
- 19 M. Ranger, D. Rondeau, and M. Leclerc, *Macromol.*, 1997, **30**, 7686.
- 20 B. Liu and W. Huang, *Thin Solid Films*, 2002, **417**, 206.
- 21 C.-W. Ko and Y.-T. Tao, *Synth. Met.*, 2002, **126**, 37.
- 22 A. Ronlán, J. Coleman, O. Hammerich, and V. D. Parker, *J. Am. Chem. Soc*, 1974, **96**, 845.
- 23 S. A. Chawdhury, A. Hargreaves, and R. A. L. Sullivan, *Acta Cryst.*, 1968, **B24**, 1222.
- 24 S. F. Nelsen, R. F. Ismagilov, and D. R. Powell, *J. Am. Chem. Soc*, 1997, **119**, 10213.
- 25 Y. Kuwabara, H. Ogawa, H. Inada, N. Noma, and Y. Shirota, *Adv. Mater.*, 1994, **6**, 677.
- 26 R. Brook, 2003.
- 27 F. Ullmann, *Ber. Dtsch. Chem. Ges.*, 1903, **36**, 2382.
- 28 P. E. Fanta, *Chem. Rev.*, 1946, **38**, 139.
- 29 P. E. Fanta, *Chem. Rev.*, 1964, **64**, 603.
- 30 H. Weingarten, *J. Am. Chem. Soc*, 1964, **29**, 3624.
- 31 J. A. Paine, *J. Am. Chem. Soc*, 1987, **109**, 1496.
- 32 R. G. R. Bacon and H. A. O. Hill, *Q. Rev.*, 1965, **19**, 95.

- 33 H. Weingarten, *J. Am. Chem. Soc.*, 1964, **29**, 977.
34 P. Capdevielle and M. Maumy, *Tetrahedron. Lett.*, 1993, **34**, 1007.
35 S. Gauthier and J. M. J. Fréchet, *Synthesis*, 1987, 383.
36 H. B. Goodbrand, in 'United States Patent 5,648,539', 1996.
37 H. B. Goodbrand, in 'United States Patent 5,654,482', 1997.
38 C. G. Frost and P. Mendonça, *J. Chem. Soc., Perkin Trans. 1*, 1998, 2615.
39 J. F. Hartwig, *Angew. Chem. Int. Ed.*, 1998, **37**, 2046.
40 A. S. Guram, R. A. Rennels, and S. L. Buchwald, *Angew. Chem. Int. Ed. Engl.*, 1995, **34**, 1348.
41 J. Louie and J. F. Hartwig, *Tetrahedron. Lett.*, 1995, **36**, 3609.
42 B. C. Hamann and J. F. Hartwig, *J. Am. Chem. Soc.*, 1998, **120**, 7369.
43 Y. Takahashi, T. Ito, S. Sakai, and Y. Ishii, *Chem. Commun.*, 1970, 1065.
44 T. Ukai, H. Kawazura, and Y. Ishii, *J. Organometal. Chem.*, 1974, **65**, 253.
45 S. M. Reid, J. T. Mague, and M. J. Fink, *J. Organometal. Chem.*, 2000, **616**, 10.
46 C. R. Conard and M. A. Dolliver, *Org. Synth.*, **2**, 167.
47 A. S. Guram, R. A. Rennels, and S. L. Buchwald, *Angew. Chem. Int. Ed. Engl.*, 1995, **34**, 1348.
48 J. P. Wolfe and S. L. Buchwald, *J. Org. Chem.*, 1996, **61**, 1133.
49 M. S. Driver and J. F. Hartwig, *J. Am. Chem. Soc.*, 1996, **118**, 7217.
50 J. J. Bishop, A. Davison, M. L. Katcher, D. W. Lichtenberg, R. E. Merrill, and J. C. Smart, *J. Organometal. Chem.*, 1971, **27**, 241.
51 J. P. Wolfe, S. Wagaw, and S. L. Buchwald, *J. Am. Chem. Soc.*, 1996, **118**, 7215.
52 J. P. Wolfe and S. L. Buchwald, *J. Org. Chem.*, 2000, **65**, 1144.
53 A. Helms, D. Heiler, and G. McLendon, *J. Am. Chem. Soc.*, 1992, **114**, 6227.
54 R. J. Abraham, J. Fisher, and P. Loftus, 'Introduction to NMR Spectroscopy', Wiley, 1988.
55 G. E. Martin and A. S. Zektzer, 'Two-Dimensional NMR Methods for Establishing Molecular Connectivity', VCH, 1988.
56 H. Friebolin, 'Basic One- and Two-Dimensional NMR Spectroscopy', VCH, 1993.
57 C. Orizu, Personal communication, 2002.
58 R. C. Bansal, E. J. Eisenbraun, and R. J. Ryba, *Oppi Briefs*, 1987, **19**, 258.
59 B. E. Koene, D. E. Loy, and M. E. Thompson, *Chem. Mater.*, 1998, **10**, 2235.
60 F. Fowweather and A. Hargreaves, *Acta Cryst.*, 1950, **3**, 81.
61 T. M. Barclay, A. W. Cordes, N. A. George, R. C. Haddon, M. E. Itkis, and R. T. Oakley, *Chem. Commun.*, 1999, 2269.

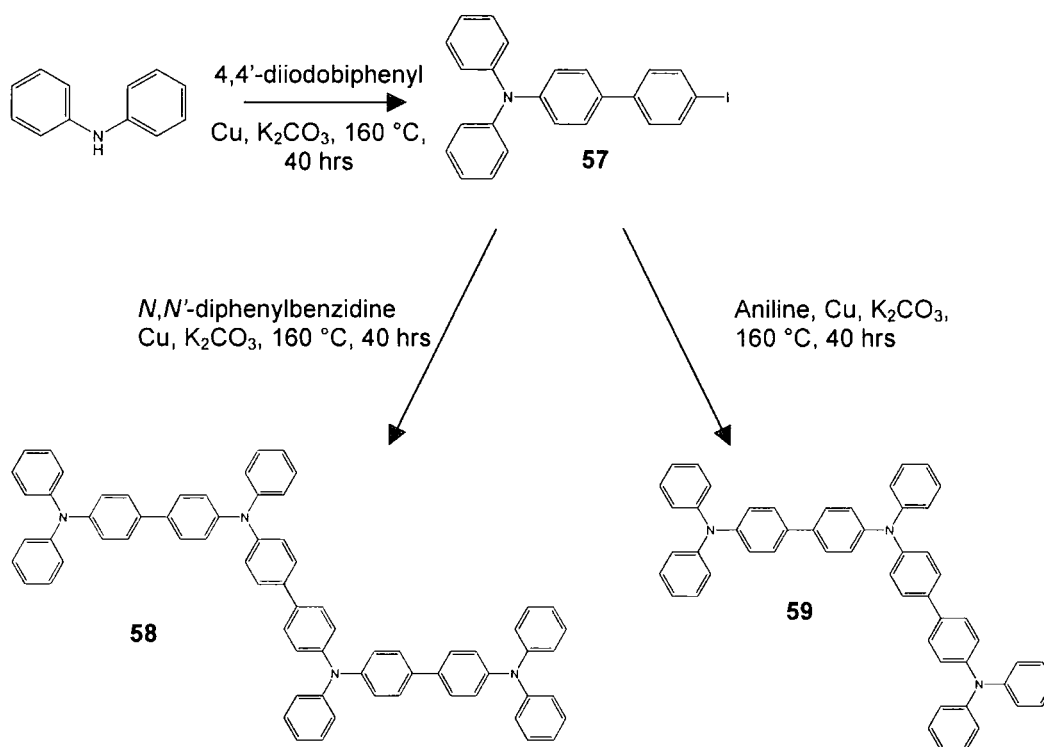
Chapter Five

Trimeric and Oligomeric Systems

5.1 Introduction to Trimeric and Oligomeric Triarylamine Derivatives

There are a number of reports in the literature describing the synthesis of trimeric, tetrameric, pentameric and extended polymeric materials based around the triphenylamine moiety.¹⁻⁷ These materials have been shown to have lower ionisation potentials and enhanced amorphous film forming properties when compared with the dimeric systems such as **1**. These oligomeric materials have typically been synthesised by a series of Ullmann Condensation reactions and therefore require extended reaction times at high temperature. However detailed information regarding specific reaction conditions employed (e.g. solvent, reaction stoichiometry) and yields of the materials obtained were not reported in this earlier literature.

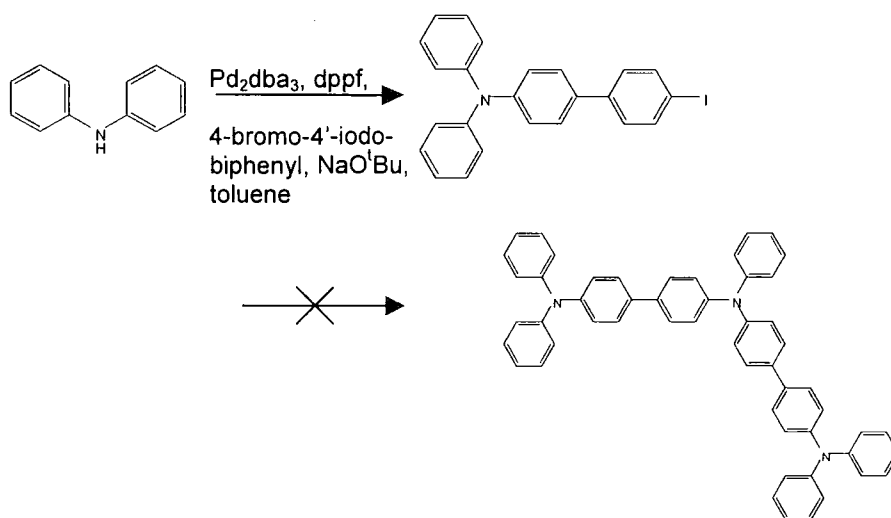
Scheme 5.1 Reaction scheme of the synthesis of **58** and **59**^{2,4}



Tanaka and Goodbrand have described the preparation of **58** and **59** from the 4-iodo-1,1'-biphenyl-4'-diphenylamine, **57** and *N,N'*-diphenylbenzidine or aniline, respectively. The key reagent **57** was reported to be prepared in moderate yield by condensation of diphenylamine with excess diiodobiphenyl under standard Ullmann conditions.^{2,5}

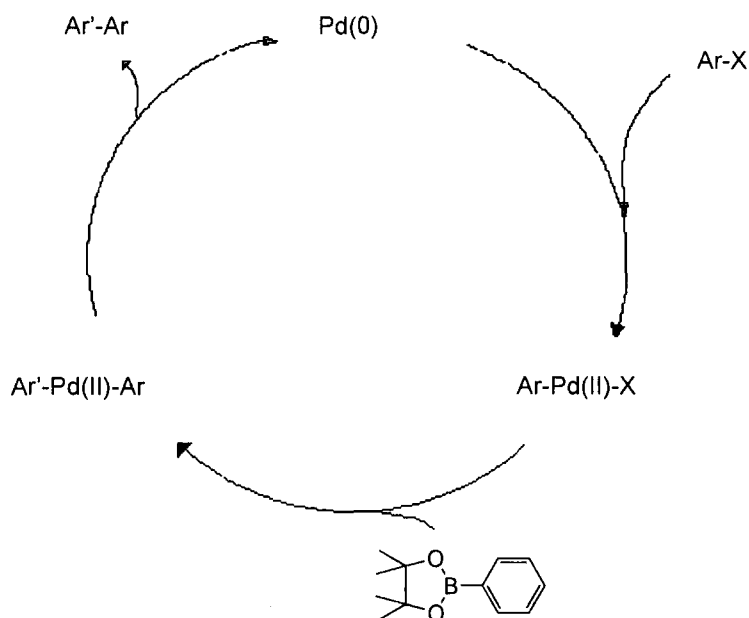
In our laboratory although we were able to prepare the initial precursor **57** through an Ullmann Condensation, we were unable to obtain the product of the second coupling, **59**. While a Hartwig/Buchwald style palladium catalysed C-N coupling protocol provided an alternative route to **57**⁸ these methodologies again failed to achieve the second coupling reaction. Clearly an alternative synthetic approach was required.

Scheme 5.2 The reaction scheme for the palladium catalysed synthesis of **57** and **59**



5.2 Boronic Acid Formation and Palladium Catalysed Couplings

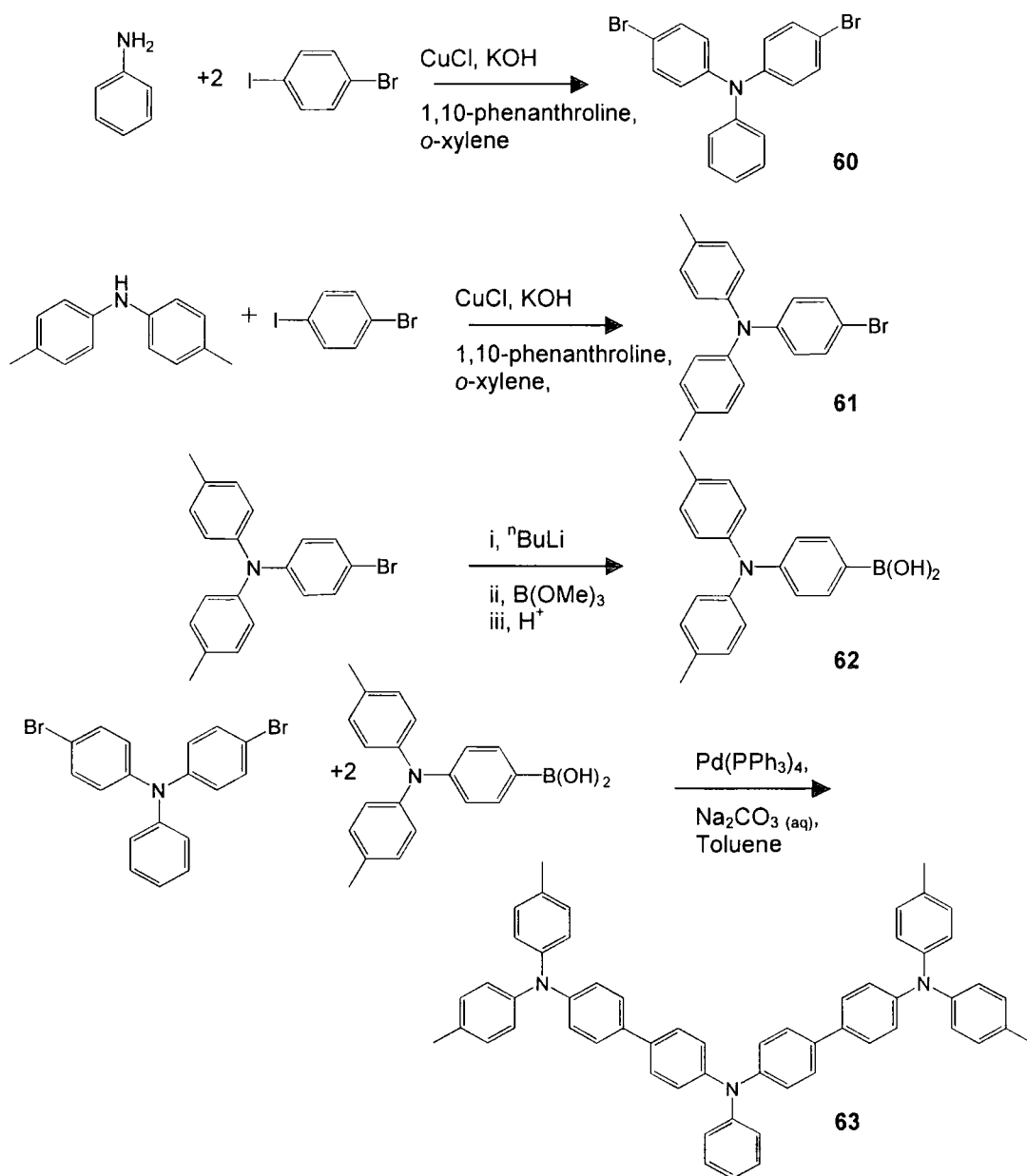
Aryl boronic acids and esters have attracted considerable interest in recent times as useful intermediates that allow a wide range of synthetic transformations under mild conditions.⁹⁻¹³ For example, the Suzuki coupling, in which an organoborane is cross-coupled with an aryl halide in the presence of a catalytic amount of a palladium (0) complex and base, is now one of the more useful C-C bond forming reactions available.^{9, 10, 12} Among the most important virtues of the Suzuki coupling are its tolerance to a wide range of functional groups and the ease of preparation of the precursors.¹¹ A wide range of palladium pre-catalysts can be used for the cross coupling such as $\text{Pd}(\text{PPh}_3)_4$ and $\text{Pd}(\text{OAc})_2$ with PPh_3 which are relatively stable to air and readily dissociate phosphine ligands or are reduced in situ to the active $\text{Pd}(0)$ complexes. While the intimate mechanism for these reactions is complex, in general terms they proceed via oxidative addition of the catalyst to the aryl halide, which is followed by a transmetallation step giving a diaryl palladium species. Reductive elimination then affords the desired biaryl product and regenerates the $\text{Pd}(0)$ catalyst.¹⁰



Scheme 5.3 A general mechanism for the boronic acid cross coupling

In our hands, the use of Suzuki coupling protocols to form key C-C bonds in the assembly of trimeric triarylamine derivatives from the dibromo and boronic acid

triarylamine derivatives proved successful (Scheme 5.4). The precursors **60** and **61** were prepared through Ullmann Condensations of 1-bromo-4-iodobenzene with aniline and di(4-methylphenyl)amine then conversion of the 4-bromophenyl bis(4-methylphenyl)amine to the corresponding boronic acid for the final Suzuki C-C bond forming coupling.

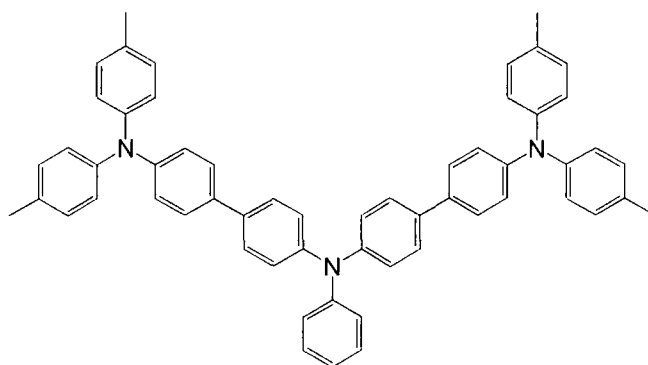


Scheme 5.4 The reaction scheme for the synthesis of *N,N*-bis[4'-(di(4-methylphenyl)amine)-1,1'-biphenyl]-*N*-phenylamine, **63**

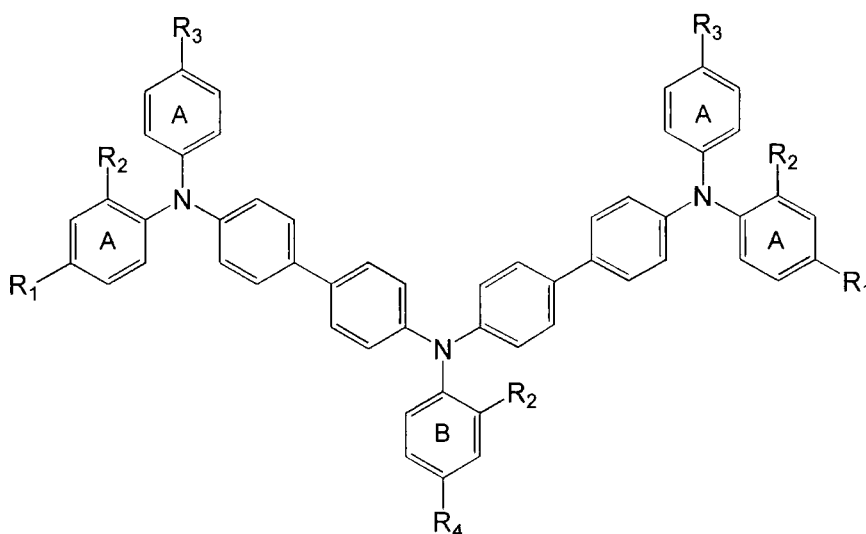
A modified Ullmann Condensation^{5, 14, 15} employing 1,10-phenanthroline as a ligand, CuCl as the catalyst and *ortho*-xylene as solvent gave **60** in good yield. The product was purified by flash chromatography and recrystallised from MeOH until a white crystalline solid was obtained. The material was characterised by ¹H NMR spectroscopy, and through comparison of HPLC retention time with an authentic sample. The 4-bromophenyl bis(4-methylphenyl)amine, **61**, was prepared and characterised in the same manner as **60**, utilising bis (4-methylphenyl)amine in place of aniline, and purified by flash chromatography and recrystallisation from MeOH.

In tetrahydrofuran solution, **61** was lithiated through treatment with butyllithium. The anion was trapped with trimethylborate,¹⁶ and hydrolysed to form the boronic acid, producing **62** as a pale grey powder, which was sufficiently pure to be used directly in the subsequent coupling step.

A Suzuki coupling protocol was employed in the synthesis of **63** from **60** and **62**.¹⁰ The precursors **60** and **62** were heated at reflux overnight with tetrakis (triphenylphosphine) palladium and sodium carbonate in a mixture of toluene and water, with vigorous stirring in order to mix the two phases. The organic layer was separated and the product purified by flash chromatography. The ¹H NMR spectrum contained several overlapping multiplets in the aromatic region and a singlet at 2.25 ppm in the ratio 37: 12. The ¹³C NMR spectrum contained 15 resonances due to the aromatic carbon atoms and a resonance at 21.16 ppm assigned to the carbon of the methyl group. The molecular ion was identified in the mass spectrum at *m/z* 787 with a fragmentation pattern consistent with loss of aryl groups.



The synthetic team at Avecia supplied the compounds **59**, **64-66**, which were prepared in an entirely analogous manner to that described for **63**. This series was chosen to allow a comprehensive study of trimeric materials with both electron donating and electron withdrawing substituents, and varying methyl substituent patterns around both the peripheral and pendant aryl rings (Figure 5.1). The rings labelled “A” are referred to as peripheral aryl rings, whilst the ring labelled “B” is termed the pendant aryl ring



Material	R ₁	R ₂	R ₃	R ₄
59	H	H	H	H
63	Me	H	Me	H
64	F	H	H	F
65	Me	Me	H	Me
66	Me	H	Me	Me

Figure 5.1 The trimeric materials investigated in this study

5.3 Cyclic Voltammetry and Spectroelectrochemistry

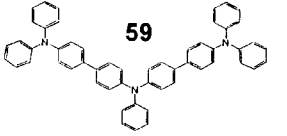
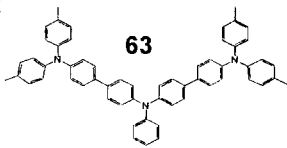
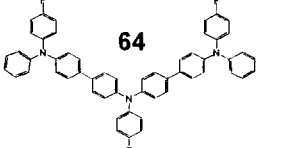
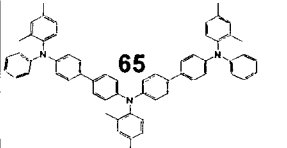
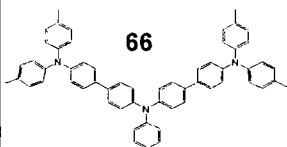
The electrochemical responses of the five trimeric materials **59**, **63-66**, were characterised by three reversible oxidation waves corresponding to sequential formation of the cation radical A^+ , dication A^{2+} , and trication A^{3+} (Table 5.1).

The first oxidation potential of **64**, substituted with electron withdrawing fluorine groups was approximately 30 mV more positive than that of the unsubstituted material. In contrast introduction of electron donating methyl substituents around the peripheral and pendant rings had the effect of lowering the first oxidation potential. The most dramatic decrease was observed for **65**, with the 2,4-dimethyl substitution pattern on three of the rings, this material has the most methyl substituents of the materials here examined and therefore the low oxidation potential is unsurprising. The second oxidation potentials followed a similar trend. The third oxidation potentials of all the samples, with the exception of **63**, were essentially the same. The third oxidation potential of **63** was some 80 mV less positive than the 2,4-dimethyl substituted material **65**.

In conclusion, the introduction of inductively electron withdrawing and donating groups increased and decreased the oxidation potentials respectively. However it is unclear why the third oxidation potential of **63** occurs at a potential lower than expected from the trends in inductive effects established by other members of the series.

The difference between successive oxidation potentials can be used to estimate the thermodynamic stability of the cations being formed by the first oxidation. The 2,4-dimethyl substitution pattern of **65** clearly stabilises the dicationic state more effectively than any other material, although all other values are too similar to provide any real differentiation.

Table 5.1 Table of oxidation potentials of 59, 63-66

	$E_{1/2}$ (V)	$E_{1/2}$ (V)	$E_{1/2}$ (V)	ΔE_1 (V)	ΔE_2 (V)	K_{c1}	K_{c2}
	0.27	0.47	0.65	0.20	0.18	2,410	1,100
	0.22	0.37	0.56	0.15	0.19	340	1,630
	0.30	0.50	0.66	0.20	0.16	2,410	510
	0.20	0.42	0.64	0.22	0.22	5,255	5,225
	0.26	0.46	0.63	0.20	0.17	2,410	750

The kinetic stability and the electronic structures of compounds [59, 63-66]^{nt} were probed using room temperature UV-Vis-NIR spectroelectrochemical studies. As described in Chapters 3 and 4 the observation of sharp isosbestic points during the electrolytic cycle $A \rightarrow A^+ \rightarrow A^{2+} \rightarrow A^{3+} \rightarrow A^{2+} \rightarrow A^+ \rightarrow A$, and recovery of the original spectra of A at the end of the cycle would confirm both the chemically reversible nature of the redox system in CH₂Cl₂ and the chemically distinct nature of each member of the redox series. The observation of a new spectral profile at the end of the cycle is indicative of an electrochemical reaction occurring on the spectroelectrochemical experiment timescale that may not have been observed from CV studies.

The electronic spectrum of 66 contained a set of π - π^* bands near 350 nm (Table 5.2)(Figure 5.2). On oxidation these π - π^* bands shift to lower energy in a manner similar to the dimeric materials. In addition to the shift in the π - π^* band a broad absorption in the NIR region, with multiple bands present in the absorption envelope was recorded. Exhaustive oxidation to the trication resulted in the collapse of the NIR bands and the continued growth of the low energy π - π^* band to a maximum in a manner similar to that seen for the dimeric systems (Figure 5.3).

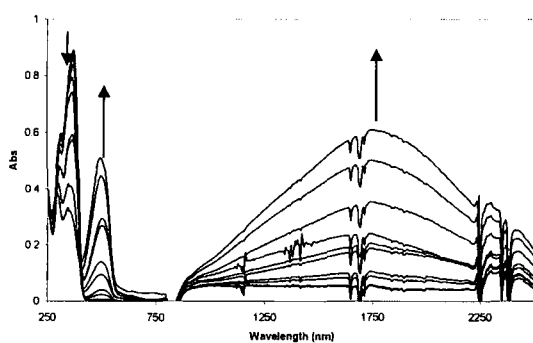


Figure 5.2 Appearance of NIR band of 66 on oxidation. $\lambda(\text{nm})/\epsilon (\text{mol}^{-1}\text{dm}^3\text{cm}^{-1})$ 66 367/70,960;

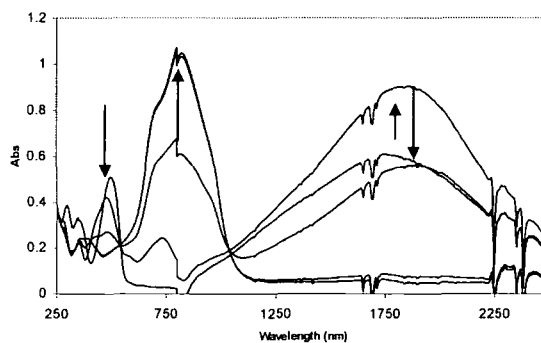


Figure 5.3 Growth then subsequent collapse of NIR band of 66 on exhaustive oxidation. $\lambda(\text{nm})/\epsilon (\text{mol}^{-1}\text{dm}^3\text{cm}^{-1})$ 66³⁺ 820/84,000

The reduction of the fully oxidised **66** saw the collapse of the low energy π - π^* band and the reappearance of the NIR absorption envelope, reproducing the spectra seen on oxidation. Continued reduction saw the collapse of the NIR envelope and the growth of the π - π^* bands associated with the neutral **66**. (Figures 5.4 and 5.5)

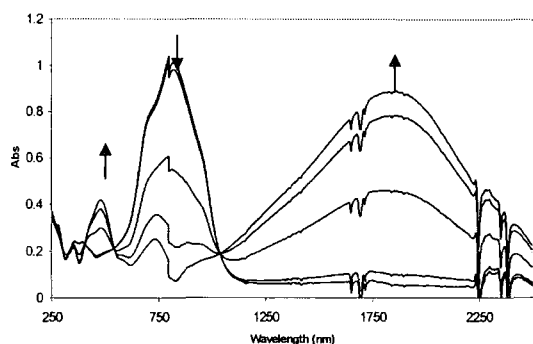


Figure 5.4 Growth of NIR band of **66** on reduction

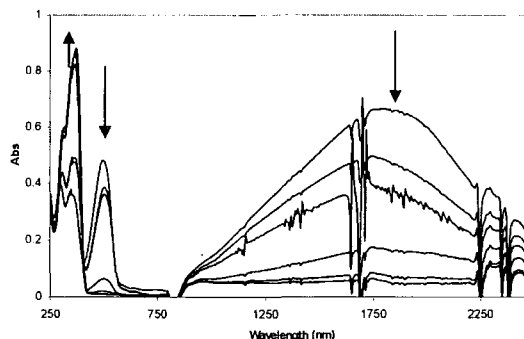


Figure 5.5 Collapse of NIR band of **66** on reduction

The electronic spectrum of **59** initially resembled that of **66**, with a set of π - π^* bands around 340 nm which shifted to lower energy on oxidation alongside the appearance of a set of bands in the NIR region, which had at least two components. Exhaustive oxidation saw the growth of a lower energy π - π^* band at 747 nm replicating the behaviour of **66**.

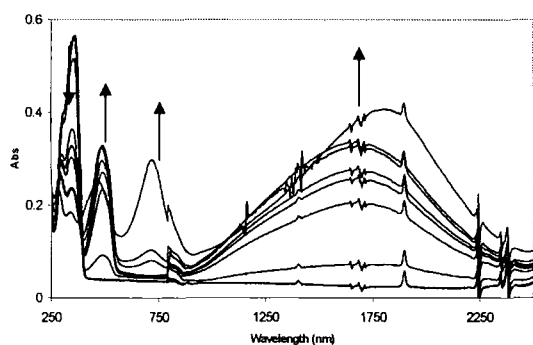


Figure 5.6 UV-Vis spectroelectrochemistry on oxidation of **59**. $\lambda(\text{cm}^{-1})/\epsilon (\text{mol}^{-1}\text{dm}^3\text{cm}^{-1})$ **59** 357/52,000

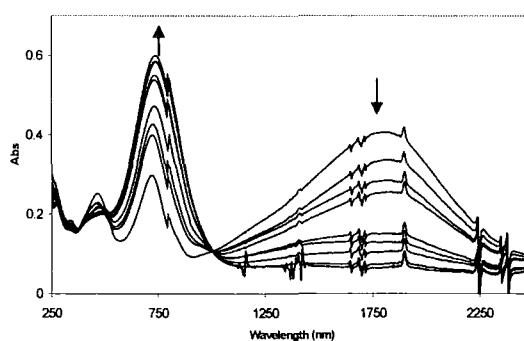


Figure 5.7 UV-Vis spectroelectrochemistry of exhaustive oxidation of **59**. $\lambda(\text{cm}^{-1})/\epsilon (\text{mol}^{-1}\text{dm}^3\text{cm}^{-1})$ **59**³⁺ 747/74,000

In order to assess the stability of the oxidised species, reduction back to the neutral material was instigated. The reduction of $[\mathbf{59}]^{+3}$ revealed a different set of spectra to those seen during oxidation. As the low energy π - π^* band collapsed and a band in the NIR region began to grow in the spectra it became clear that the position of the dominant band in the NIR region was shifted to higher energy, and the overall shape

of the band was markedly different. Oxidation to the cation and dication then subsequent reduction did produce the original spectral profile, indicating that a chemical reaction is occurring in the +3 state. (Figure 5.8)

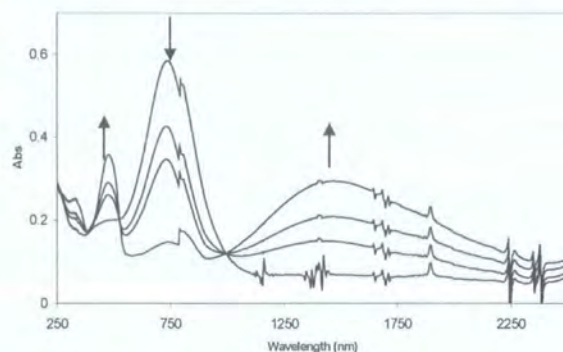


Figure 5.8 UV-Vis spectroelectrochemistry of reduction of fully oxidised **59**

The spectroelectrochemical responses of **64** and **65** were similar to those described for **59**. (Figures 5.9 and 5.10, Table 5.2) Both compounds displayed similar evidence of reaction in the tricationic state, with NIR band maxima shifting from 1819 and 1718 nm to 1560 and 1600 nm respectively.

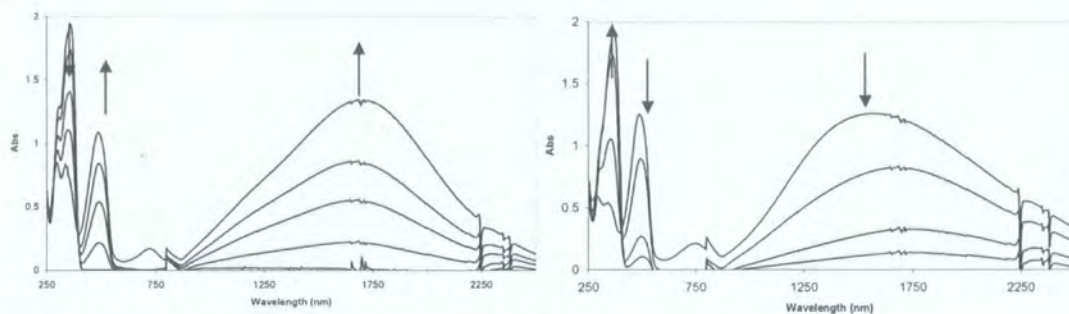


Figure 5.9 Comparison of the NIR band of **64** on oxidation (left) and reduction (right)

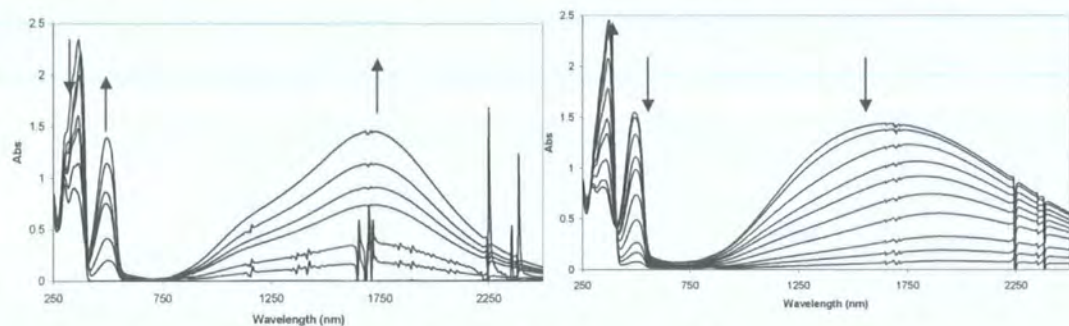
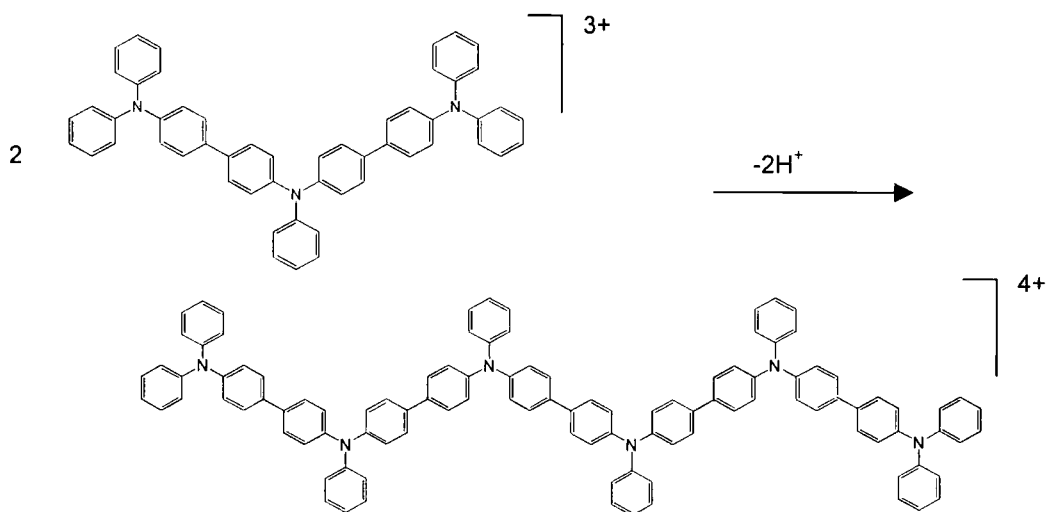


Figure 5.10 Comparison of the NIR band of **65** on oxidation (left) and reduction (right)

These observations give some clues as to the underlying electronic structure of the trimeric materials in their various oxidation states. In the tricationic state there must be at least one unpaired electron. Electronic structure calculations of the dimeric systems suggest that a proportion of the electron density is localised at the *para* position of the peripheral rings. This leads to behaviour reminiscent of triphenylamine, which when oxidised undergoes a coupling reaction through the *para* position of one of the aryl rings.^{17, 18} Compound **66**, which carries a methyl group at the *para* position of each peripheral and pendant aryl group, is stable in this trioxidised state. Compounds **64** and **65** with an unsubstituted peripheral ring are chemically reactive as is the “parent” material **59**. The spectroelectrochemical response of the series can be rationalised in terms of scheme 5.5.



Scheme 5.5, Proposed electrochemical coupling reaction of the trimeric triarylamine systems

The methyl substitution pattern of **63** only allows reaction through the *para* position of the pendant ring as all four of the *para* positions of the peripheral rings are protected. The spectroelectrochemical data for **63** (Figures 5.11 and 5.12) shows no evidence for reaction, with identical profile NIR bands on both oxidation and reduction, indicating that the coupling reaction is only occurring through the *para* position of the peripheral rings.

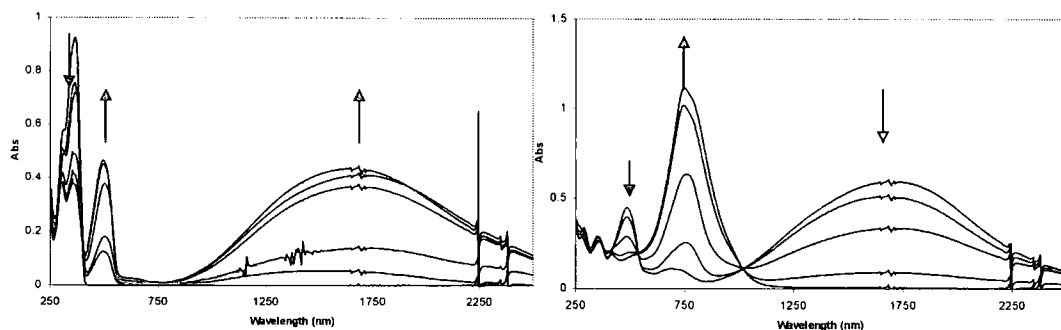


Figure 5.11 Comparison of the NIR band of **63** on oxidation

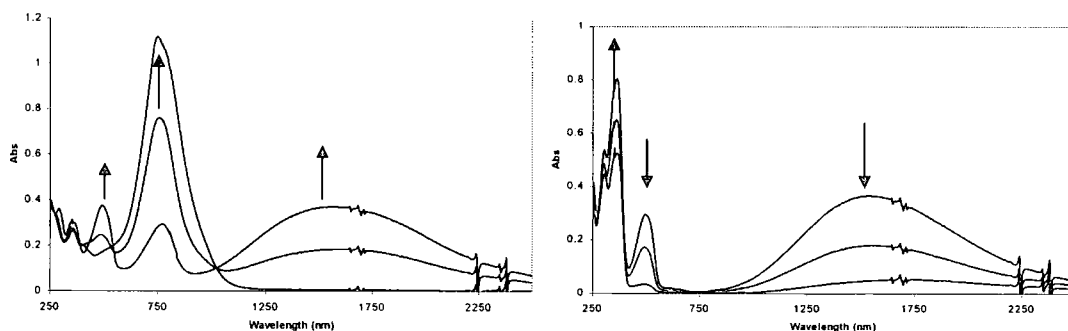
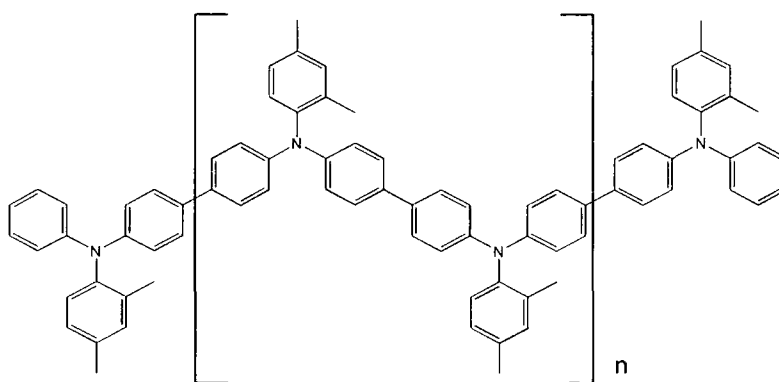


Figure 5.12 Comparison of the NIR band on reduction of **63**

Table 5.2 UV-Vis absorption band data for compounds 59, 63-66

Material	Oxidation state	Peak position (nm)/Extinction Coefficient ($\text{mol}^{-1}\text{dm}^3\text{cm}^{-1}$)
59	0	310/41,639, 344/50,436, 360/52,000
	+1	490, 1684/40,600
	+2	462, 718, 1819/66,000
	+3	747/74,000
63	0	310/34,792, 364/55,475
	+1	501, 1647/41,850
	+2	487, 689, 1693/68,980
	+3	749 /80,500
64	0	306/37,734, 346/55,384, 361/57,515
	+1	491, 1698/39,390
	+2	462, 718, 1819/53,940
	+3	753/72,730
65	0	305/43,517, 340/59,645, 367/71,210
	+1	495, 1710/44,240
	+2	448, 728, 1781/90,910
	+3	815/87,880
66	0	310/47,030, 350/65,185, 367/70,960
	+1	496, 1756/48,800
	+2	477, 1843/72,000
	+3	820/84,000

In order to compare the spectroscopic properties of the electrochemical reaction product of the trimers with the proposed hexameric product, samples of the tetrameric, hexameric and a polymeric blend of hexa-octameric chain length lengths were supplied by Avecia, and subjected to electrochemical and spectroelectrochemical study.



Material	n =
67	1
68	2
69	2-4

The electrochemical response of **67** and **68** revealed oxidation waves, with the third wave having a larger peak current than the first two waves suggesting a superposition of two 1 electron events. The cyclic voltammogram of **69** contained two broad oxidation waves (Table 5.3).

Table 5.3 Table of oxidation potentials of **67-69**

	$E_{1/2}$ (V)	$E_{1/2}$ (V)	$E_{1/2}$ (V)	ΔE_1 (V)	ΔE_2 (V)	K_{c1}	K_{c2}
67	0.20	0.64	0.87	0.44	0.23	27,620,977	7,757
68	0.28	0.41	0.62	0.13	0.21	157	3,560
69	0.22	0.50	-	0.28	-	54,366	-

The electronic spectrum of **67** contained a set of π - π^* bands near 340 nm on oxidation these π - π^* bands shift to lower energy in a manner similar to the dimeric materials, with the associated appearance of a broad set of bands in the NIR, with at least two bands clearly discernable (Table 5.4)(Figure 5.13). Further oxidation again saw a shift of the NIR band maximum, however in this case the band shifts to higher energy. Exhaustive oxidation resulted in the collapse of the NIR band and associated π - π^* band at 497 nm, and the appearance of a new lower energy π - π^* band at 779 nm which proceeded to grow to a maximum in a manner similar to that seen for the dimeric systems. This is distinct from the behaviour of the trimeric materials, where the lowest π - π^* energy band appeared before the NIR band had reached its maximum intensity.

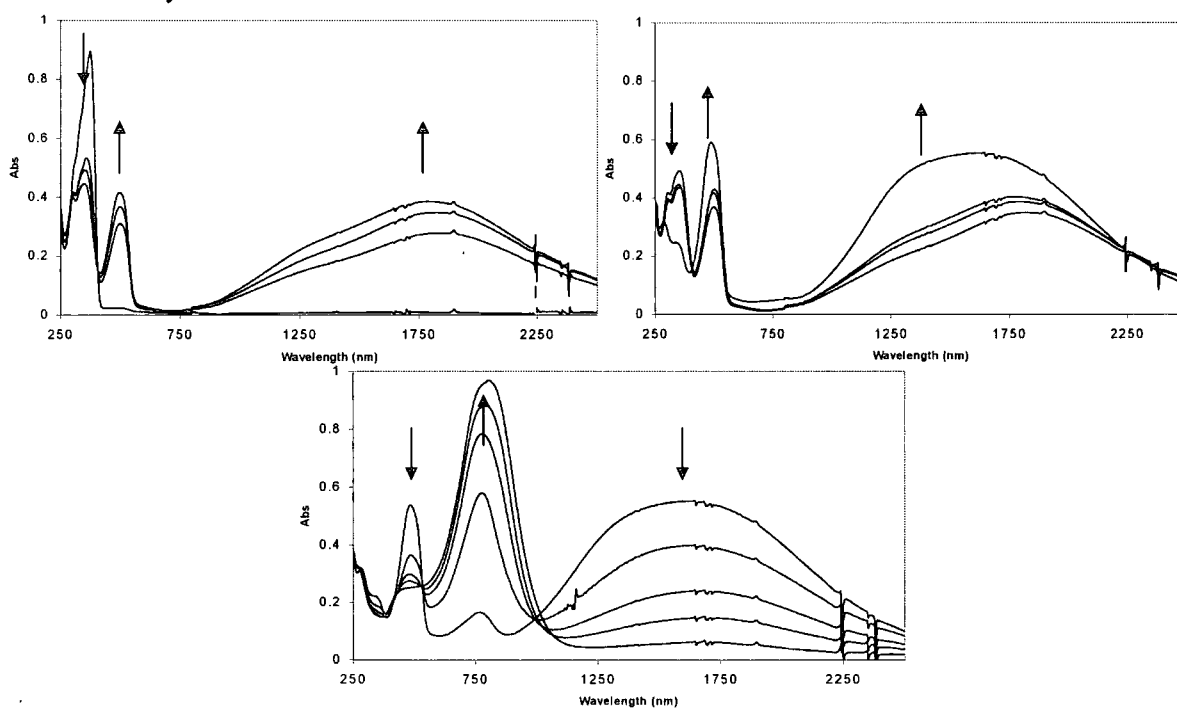


Figure 5.13 UV-Vis-NIR spectroelectrochemistry of **67** during oxidation. The arrows indicate the bands that grow and decay during the electrolysis.

The electronic spectrum of **68** contained a set of π - π^* bands near 375 nm (Table 5.4)(Figure 5.14) resembling closely the spectrum of **67**. On oxidation these π - π^* bands shift to lower energy in a manner similar to **68** however the set of bands in the NIR were not as well resolved and extended to lower energy than the corresponding bands in the spectrum of **67**. Exhaustive oxidation, as for **67**, resulted in the collapse of the NIR band and associated π - π^* band at 498 nm, and the appearance of a new lower energy π - π^* band at 800 nm which proceeded to grow in a manner replicating the behaviour of **67**.

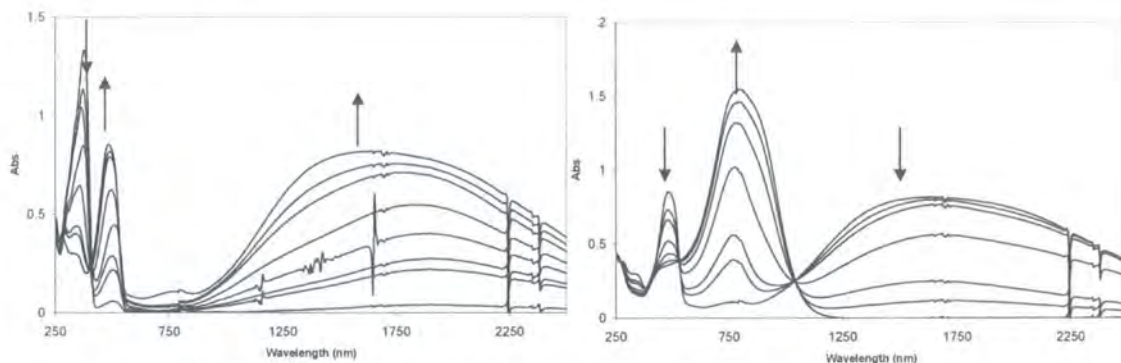


Figure 5.14 UV-Vis-NIR spectroelectrochemistry of **68** during oxidation. The arrows indicate the bands that grow and decay during the electrolysis.

The electronic spectrum of **69** contained a set of π - π^* bands at 377 nm (Table 5.4) and throughout the oxidation/reduction cycle, the spectra recorded closely resembled those seen for **68**.

Table 5.4 UV-Vis absorption band data for compounds **67-69**

Material	Oxidation state	Peak position (nm)
67	0	308/40,800
		336/53,600
		373/71,200
	+n	497, 1578
	Fully oxidised	779/76,800
68	0	308/54,400
		332/75,200
		375/112,000
	+n	498, 1640
	Fully oxidised	800/122,400
69	0	326/48,180
		377/71,515
		492, 1871
	+n	820/73,939
	Fully oxidised	

Due to the different cell geometry of the CV and OTTLE cells the applied potential in the OTTLE cell can not be defined against a reference, hence the intermediate oxidation state is undefined.

Comparison of the NIR band in the absorption spectrum of the product of the electrochemical oxidation of the trimeric triarylamine **65** with the NIR band seen on oxidation of the analogous hexameric triarylamine **68** shows very close agreement of both band shape and energy. This confirms the proposed reaction scheme of dimerisation of the fully oxidised trimeric materials (Scheme 5.5).

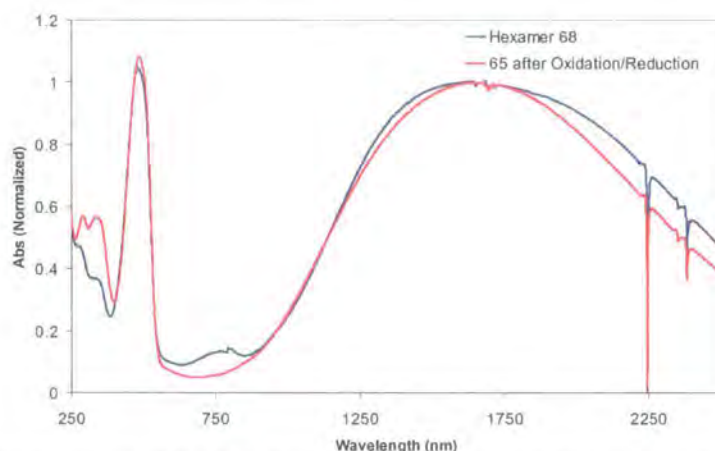


Figure 5.15 Comparison of the NIR bands of the hexameric triarylamine **68**, and the product of the oxidation/reduction cycle of **65**

There are a number of conclusions that can be drawn from these results. It is clear that materials with an even number of amine centres ($n = 0, 1, 2, 3$) are stable to chemical reaction even when fully oxidised. Materials with an odd number of amine centres are reactive in the +3 oxidation state, unless the *para* positions of the peripheral rings are blocked by a non electro-active substituent. This reactivity of the *para* position of the peripheral rings indicates that there must be significant electron density at this location, in the tricationic state.

The spectroelectrochemical spectra obtained on oxidation to the fully oxidised states also display differences, the trimeric materials display both NIR bands and low energy π - π^* bands around 800 nm for the dicationic states. The even number amine centre materials only display low energy π - π^* bands at 800 nm, after the NIR band has reached a maximum absorbance.

References for Chapter 5

- 1 C. Adachi, K. Nagai, and N. Tamoto, *Appl. Phys. Lett.*, 1995, **66**, 2679.
- 2 H. Tanaka, S. Tokito, Y. Taga, and A. Okada, *Chem. Commun.*, 1996, 2175.
- 3 S. Tokito, H. Tanaka, A. Okada, and Y. Taga, *Appl. Phys. Lett.*, 1996, **69**, 878.
- 4 S. Tokito, H. Tanaka, K. Noda, A. Okada, and Y. Taga, *Appl. Phys. Lett.*, 1997, **70**, 1929.
- 5 H. B. Goodbrand and N.-X. Hu, *J. Org. Chem.*, 1999, **64**, 670.
- 6 M. Ishikawa, M. Kawai, and Y. Ohsawa, *Synth. Met.*, 1991, **40**, 231.
- 7 W.-L. Yu, J. Pei, W. Huang, and A. J. Heeger, *Chem. Commun.*, 2000, 681.
- 8 J. F. Hartwig, *Angew. Chem. Int. Ed.*, 1998, **37**, 2046.
- 9 A. Suzuki, *Pure & Appl. Chem.*, 1994, **66**, 213.
- 10 N. Miyaoura and A. Suzuki, *Chem. Rev.*, 1995, **95**, 2457.
- 11 T. Ishiyama, M. Mutata, and N. Miyaoura, *J. Org. Chem.*, 1995, **60**, 7508.
- 12 P. Lloyd-Williams and E. Giralt, *Chem. Soc. Rev.*, 2001, **30**, 145.
- 13 C. Klärner and A. Greiner, *Macromol. Rapid Commun.*, 1998, **19**, 605.
- 14 H. B. Goodbrand, in 'United States Patent 5,648,539', 1996.
- 15 H. B. Goodbrand, in 'United States Patent 5,654,482', 1997.
- 16 M. Nicolas, B. Fabre, J. M. Chapuzet, J. Lessard, and J. Simonet, *J. Electroanal. Chem.*, 2000, **482**, 211.
- 17 E. T. Seo, R. F. Nelson, J. M. Fritsch, L. S. Marcoux, D. W. Leedy, and R. N. Adams, *J. Am. Chem. Soc.*, 1966, **88**, 3498.
- 18 W. H. Bruning, R. F. Nelson, L. S. Marcoux, and R. N. Adams, *J. Phys. Chem.*, 1967, **71**, 3055.

Chapter Six

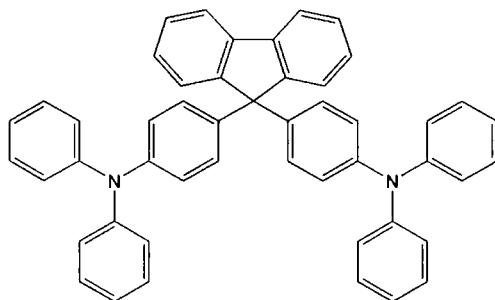
Electrochemical Polymerisation Reactions

6.1 Introduction

As it has been previously noted, while compounds such as **1** display hole-transport properties, these small molecular materials are often incorporated into multi-layer devices as dispersions in an inert polymer matrix in order to reduce problems associated with crystallisation during device fabrication or device operation.¹⁻³ Alternatively, linear or star shaped oligomers, dendrimers and polymeric polyarylamine derivatives may be used. These relatively high molecular weight materials are more resistant to crystallisation than smaller molecular analogues, and offer improved bulk morphological properties, such as interchain interactions, yet typically remain sufficiently soluble for ready processing.⁴⁻⁹

Polymeric polyarylamines are usually prepared from Ullmann-style coupling reactions, or nickel catalysed amine-aryl halide cross coupling reactions.¹⁰⁻¹⁴ Alternatively, the boronic acid coupling protocols described in Chapter 5 could be readily extended to the synthesis of polymeric materials. In each case metal catalyst residue must be removed from the product polymer before it can be employed in electronics based applications. The difficulties associated with purification of polymers prepared in the conventional chemical manner have prompted us to consider alternative synthetic strategies.

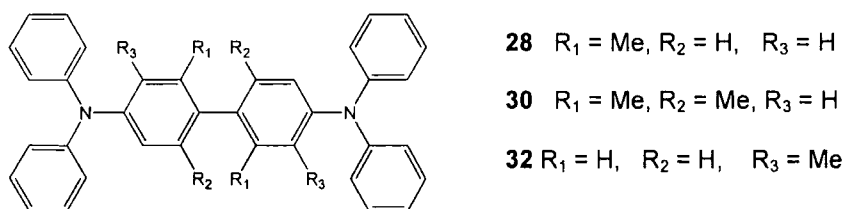
The oxidative dimerisation of triphenyl amine has long been known, Dunsch *et al* have reported the polymerisation of triphenyl amine by anodic oxidation at high current densities in non-polar solvents.^{15, 16} In addition, oxidation of a small number of diphenyl amines has been shown to afford oligomeric materials in low yield. More recently, Lambert and Nöll, as well as Leung's team,¹⁷ have demonstrated that *bis*-triarylamines spanned by a variety of conjugated bridges can be electrochemically polymerised to give conjugated poly{tetra(aryl)benzidene} polymers whilst Staško's group have reported the anodic oxidation of two triphenylamines linked by a non-conjugated fluorene bridge, which disrupts any conjugation between the two amine centres (**72**) (Figure 6.1).¹⁸

Figure 6.1 Structure of 9,9'-bis(triphenylamine)fluorene (**72**)

6.2 Results and Discussion

The structure of the SOMO of triphenylamine radical cation **23**⁺ suggests that an appreciable amount of the unpaired electron character in **23**⁺ resides on the aromatic ring carbons *para* to the nitrogen centre and is clearly the underlying electronic basis for the observed chemical reactivity of this species. In contrast, the frontier orbital structures of tetra(aryl)benzidine radicals, such as **19**⁺, are dominated by contributions from the benzidine core (Chapter 3). The SOMOs are extensively delocalised over the central portion of the molecule which lends significantly greater chemical stability to these species. This orbital description demands a relatively planar structure to the benzidine core in these radical cations, and indeed this is observed in the solid state structure of [**26**⁺]₂SbCl₆. We considered that placement of bulky substituents at the 2 and 6 positions of the biphenyl moiety might be used to disrupt the biphenyl π -system and give a range of electrochemically polymerisable monomers suitable for the production of poly(tetraarylbenzidines).

The series of compounds **28**, **30** and **32** were prepared using the methods described in Chapter 4.

Figure 6.2 The substitution patterns of compounds **28**, **30** and **32**

The electronic spectra of simple triarylamines, such as **23**, typically feature a single UV π - π^* absorption band (Figure 6.3a). In contrast, tetra(aryl)benzidenes such as **1** exhibit two absorption bands arising from π - π^* transitions which may be more precisely defined as transitions between the delocalised HOMO to unoccupied orbitals more or less localised on the biphenyl (λ_{max} ca. 350 nm) and peripheral aryl (λ_{max} ca. 300 nm) groups (Chapter 4). However, in the case of **28** (Figure 6.3b) and **30** (Figure 6.3c) only a single, intense absorption band is observed. This indicates that the triarylamine moieties are effectively electronically decoupled due to the presence of the methyl groups at the bridgehead positions, which favour a molecular conformation that disrupts the extended biphenyl π^* system. The electronic spectrum of **32** exhibits two absorption bands, although the relative intensity of the bands is reversed from that seen for unhindered systems. (Figure 6.3d) This is indicative of the different electronic structure imposed by the methyl substituent at the 3,3' position on the biphenyl.

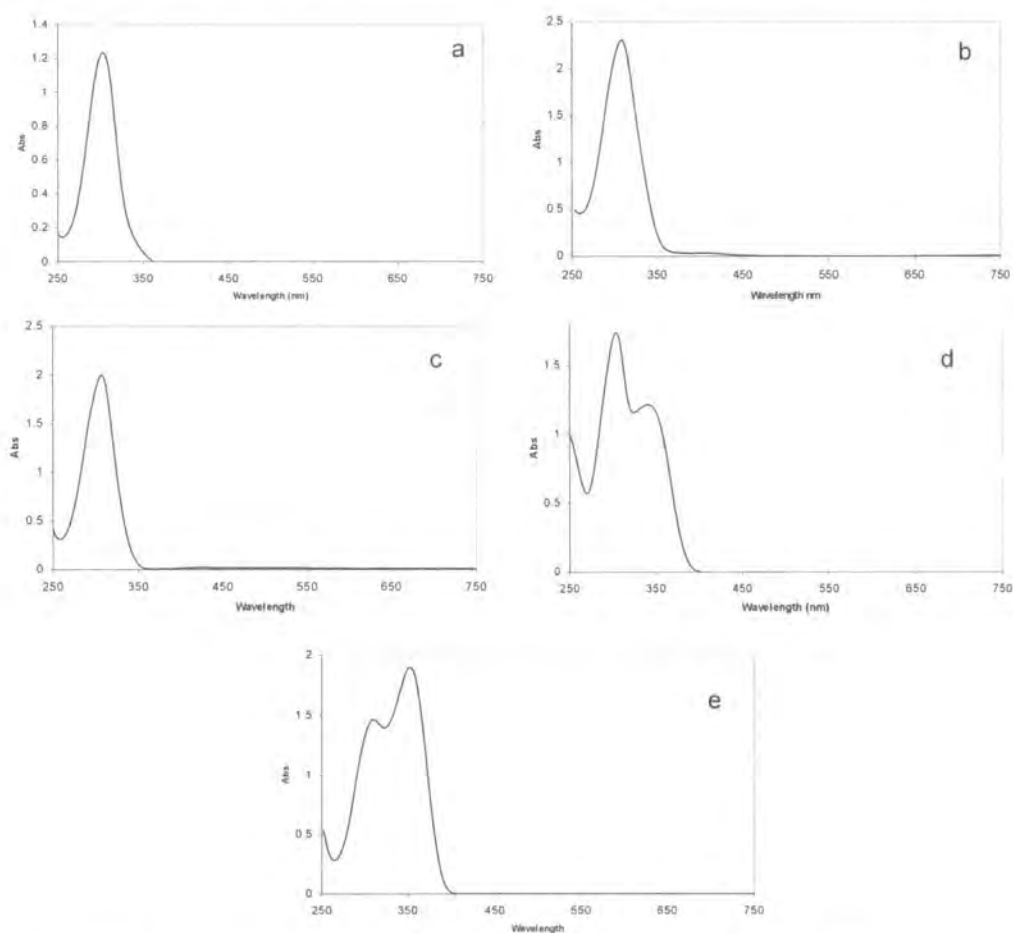


Figure 6.3 The UV-Vis absorption spectra of **23** (a), **28** (b), **30** (c), **32** (d) and **1** (e)

The electrochemical response of **28** and **30** were examined by cyclic and differential pulse voltammetry (Table 6.1).

Relative to the electrochemistry of the unhindered systems explored in Chapter 3 the introduction of additional methyl groups at the 2 and 6 positions resulted in an increase in the first oxidation potential, and a decrease in the separation of the redox events which became a single, presumably two electron, process in **30**. Therefore, despite the presence of the additional inductively electron donating methyl groups, the formation of the radical cation became thermodynamically less favourable **1** > **28** > **30**, presumably due to the greater steric strain associated with driving the biphenyl moiety into a planar conformation.

The electrochemical response of **30** was complicated by the chemical instability of the redox product even on the CV timescale. Thus while the initial oxidative sweep displayed an oxidation wave at 0.90 V, when the potential was cycled between 2.0 and -1.5 V, this wave became broader, and a new wave at 0.58 V was also detected. A thin film of material was clearly evident when the surface of the working electrode was examined and it is likely that this deposition on the electrode is leading to the curiously high oxidation potential by effectively increasing the cell resistance.

Table 6.1 Oxidation potentials of compounds **1**, **28** and **30**

Compound	$E_{1/2}$	$E_{1/2}$	ΔE^0 CH ₂ Cl ₂ (V)	K_c
1	0.292	0.507	0.215	4,320
28	0.442	0.588	0.146	295
30	0.90	-	-	-

Spectroelectrochemical studies on **28** and **30** further revealed the extent of chemical reactivity of the oxidised forms of these materials. Attempts to oxidise **28** to **28⁺** in the OTTLE cell resulted in a collapse of the original spectral profile which was replaced by new bands at 485 and 740 nm together with a broad NIR band. During the oxidation process, the peak maximum of the NIR band shifted from 1600 – 1400 nm. Continued oxidation at higher potentials caused the collapse of the bands at 485 and the NIR envelope and the continued growth of the band at 740 nm.(Figure 6.4)

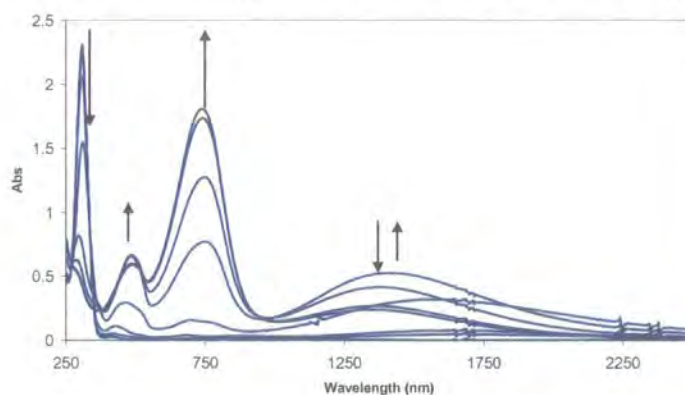


Figure 6.4 The spectroelectrochemical response of **28** on oxidation

When the potential was reversed, there was a smooth transition to a species characterised by intense bands centred at 1400 nm and 480 nm, reminiscent of a tetraaryl biphenyl diamine monocation. Continued reduction saw these bands collapse and the growth of absorption bands at λ_{max} 320 and 350 nm (Figure 6.5).

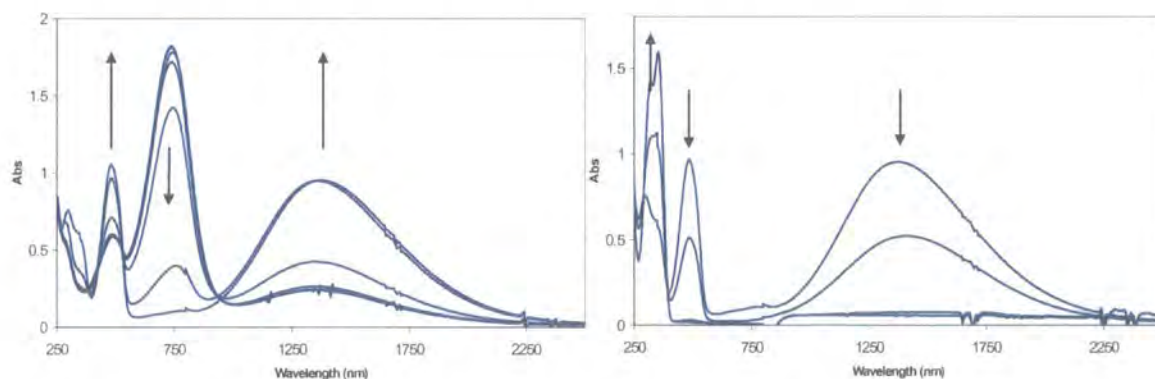


Figure 6.5 The spectroelectrochemical response of **28** on reduction

Oxidation of **30** gave a spectral trace with a different profile, which despite the absence of a conjugated π -system linking the amine centres in the starting material exhibited an absorption spectrum similar to that of 1^+ ($\lambda_{\text{max}} = 480, 1350 \text{ nm}$) in addition to a band near 700 nm. Further oxidation resulted in the collapse of the bands at 480 and 1350 nm and the continued growth of the band at 700 nm. (Figure 6.6)

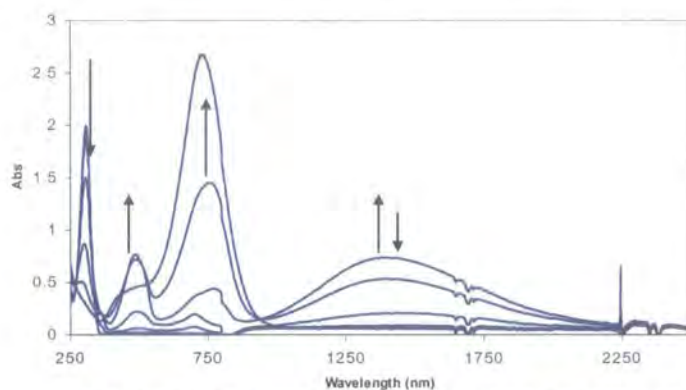


Figure 6.6 The spectroelectrochemical response of **30** on oxidation.

Reduction of the exhaustively oxidised solution resulted in the collapse of the band at 700 nm and re-appearance of the bands at 480 and 1350 nm with an associated isosbestic point at 920 nm. Further reduction gave a clean spectral profile with new band maxima at $\lambda = 320, 353 \text{ nm}$.

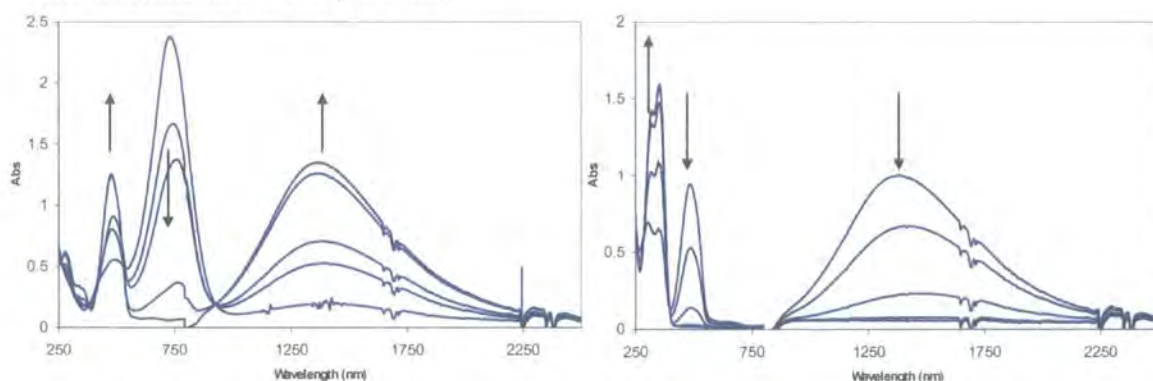


Figure 6.7 Spectral traces of the reduction of **30**

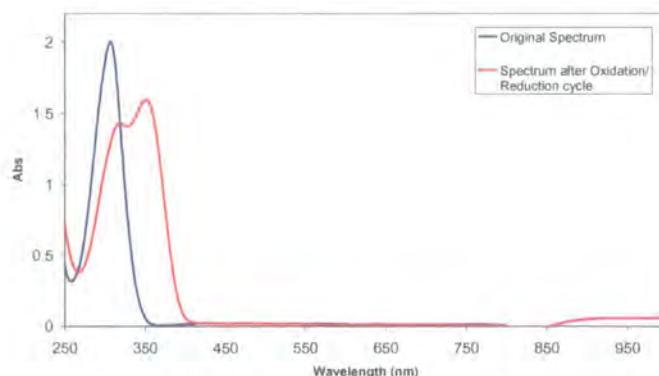


Figure 6.8 Comparison of the spectra recorded before and after the oxidation/reduction cycle of **30**

The electronic spectra observed both during reduction and in the fully reduced state bore a close resemblance to that seen for unhindered biphenyl diamines such as **1**. Comparison of the spectra confirmed how close this resemblance was, suggesting that a chemical reaction was occurring that was forming an unhindered biphenyl diamine moiety. (Figures 6.8 and 6.9)

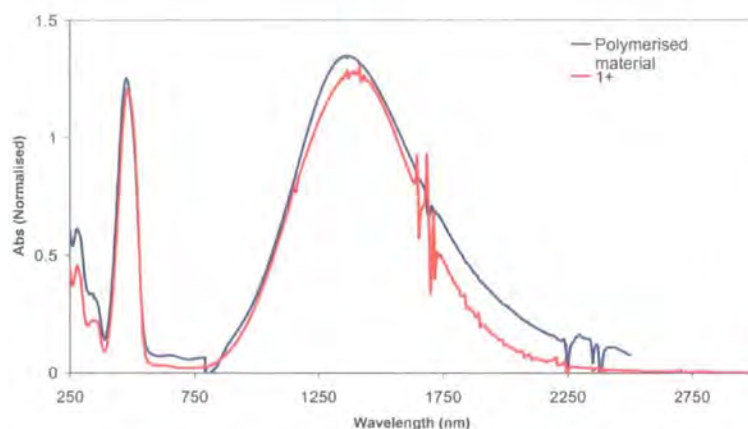


Figure 6.9 Comparison of electronic spectrum of **1**⁺ and electrochemically polymerised **30**⁺

Oxidation of **32** in the OTTLE cell resulted in a collapse of the original spectral profile of bands at 300 and 336 nm and growth of a broad NIR band at 1395 nm accompanied by a band at 486 nm. Further oxidation resulted in the collapse of the band at 486 nm and appearance of a new band 737 nm. Associated with this was a shift of the band maximum of the band in the NIR to higher energy. Continued oxidation then saw the collapse of the NIR band envelope and continued growth of the band at 737 nm. (Figure 6.10)

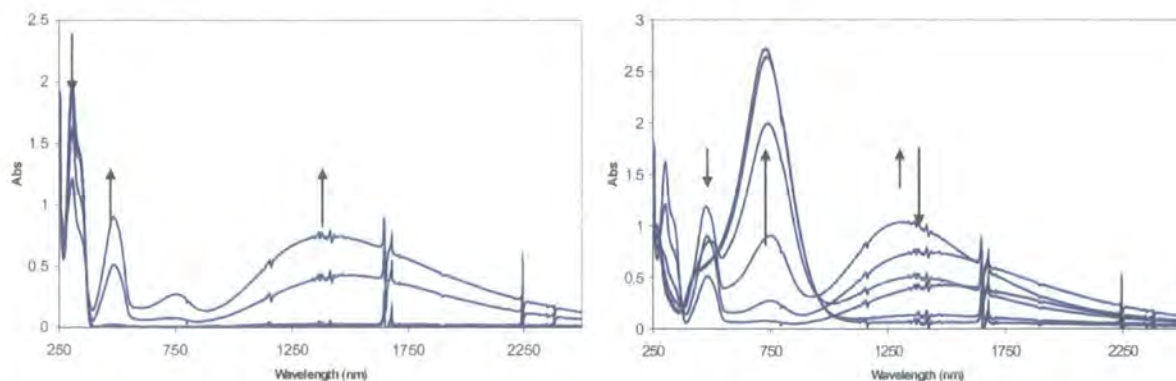


Figure 6.10 The spectroelectrochemical response of **32** on oxidation

Reduction of the exhaustively oxidised solution resulted in the collapse of the band at 737 nm and re-appearance of the band at 486 nm. An intense absorption band was observed in the NIR at 1290 nm, very similar to the spectrum seen for the monocation of **1**. Further reduction saw the collapse of these bands and the growth of a broad set of bands at 355 nm, quite different to those seen for the original neutral solution. (Figure 6.11)

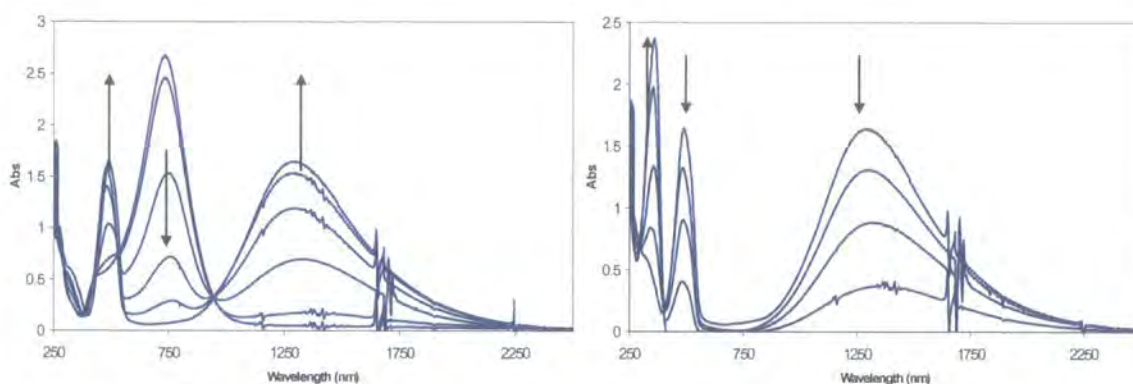


Figure 6.11 The spectroelectrochemical response of **32** on reduction

The change in the spectrum on reduction and in the neutral state after the oxidation/reduction cycle of **32** again suggested that a chemical reaction was occurring in the oxidised state. (Figure 6.12)

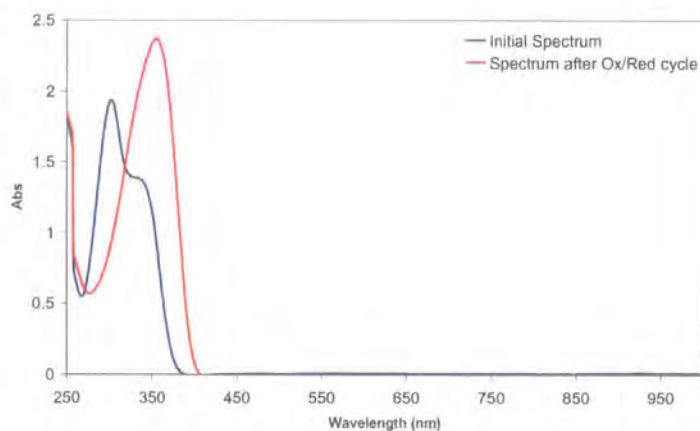
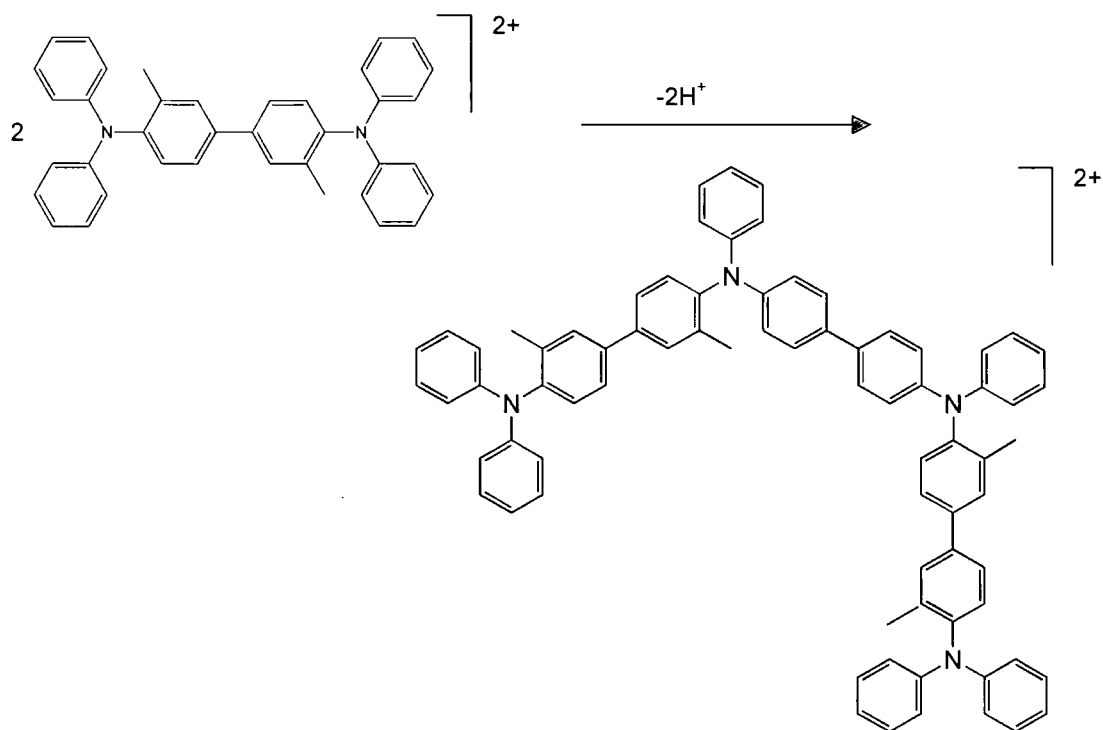


Figure 6.12 Comparison of the spectra recorded before and after the oxidation/reduction cycle of **32**

Only a single absorption band was observed in the spectrum after oxidation. Comparison of the position of the band with those recorded for tri(4-methylphenyl)amine, **23** and tetraaryl biphenyl diamines suggests that the transition is a $\pi - \pi^*_{\text{biphenyl}}$ transition. This is consistent with the formation of an unhindered

biphenyl through coupling of two molecules of **32** at the *para* position of the peripheral rings. The methyl groups at the 3,3' positions would still disrupt the conformation about the N-C bond disrupting the conjugation.



Scheme 6.1 The proposed reaction scheme for the coupling of **32**

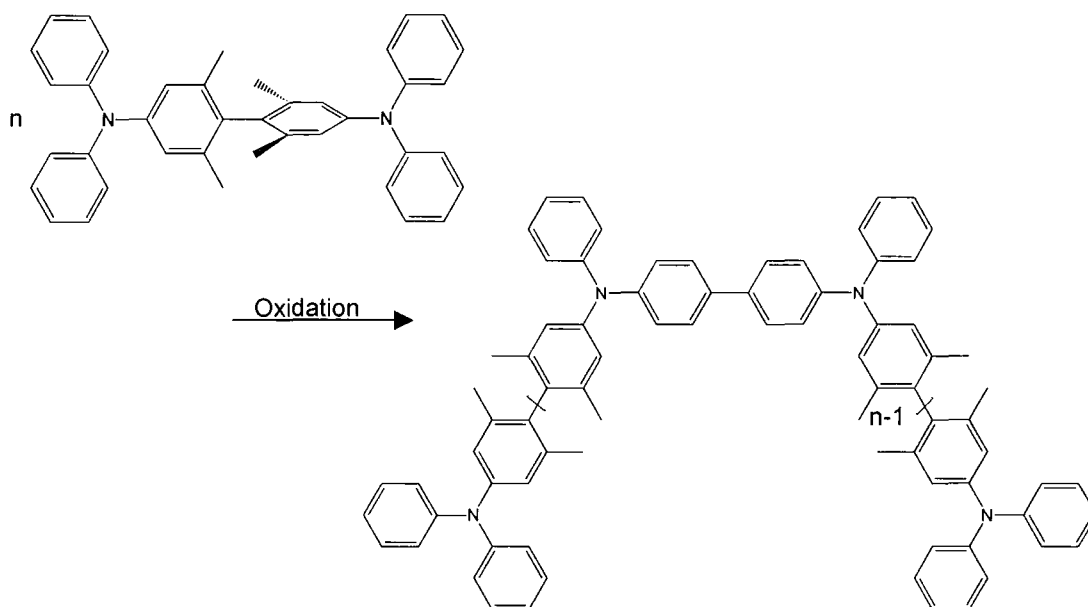
Consideration of the spectroelectrochemical and electrochemical results across **1**, **28**, **30** and **32** and comparison with unhindered diamines indicates that the dominant factor in the stability of the redox products lies in the relative conformational flexibility of the biphenyl diamine moiety.

The introduction of the methyl groups around the C(1)-C(1#) bond serves to decrease the thermodynamic stability of the oxidised forms, as evidenced by the increase in oxidation potentials. The introduction of steric constraints which limit free rotation of the diarylamine unit about the N-C(4) bond do not affect the thermodynamic stability of the cation in the same manner, although the chemical reactivity is affected.

It is also clear that the kinetic stability of the oxidised forms of the more restricted systems **28**, **30** and **32** is dependent upon the presence of substituents at the peripheral

aryl ring *para* positions, as the analogous (4-methylphenyl) substituted materials **29**, **31** and **33** studied in Chapter 4 showed no sign of reactivity.

The spectroscopic profiles of the products derived from electrochemical oxidation of **28**, **30** and **32** are indicative of a unrestricted tetraarylbenzidine moiety, and a likely reaction scheme is given in Scheme 6.2.



Scheme 6.2 The proposed reaction scheme for the coupling of the restricted diamines

Guided by the electrochemical and spectroelectrochemical results, preparative scale chemical oxidation of **30** was undertaken using an equimolar quantity of SbCl_5 in CH_2Cl_2 . The addition of the oxidising agent was marked by an instant deep blue colouration of the solution, which rapidly faded to orange. Two absorption bands at 480 and 1400 nm were observed, consistent with the tetraaryl biphenyl diamine motif, and entirely consistent with the profile observed spectroelectrochemically for $\mathbf{1}^+$.

The reaction mixture was allowed to stir for 1 hr at ambient temperature, before being quenched by addition of SnCl_2 . Filtration of the reaction mixture through a silica pad to remove the tin and antimony by-products gave a colourless solution from which a white solid (**71**) was obtained after concentration and precipitation into ethanol.

In the ^1H NMR spectrum of the resulting white solid, singlet resonances at δ 2.20 and δ 6.91 ppm characteristic of the 2,2',6,6'-tetramethyl biphenyl diamine fragment were observed. In the aromatic region, an AA'BB' resonance centred at δ 7.13 ppm indicated the presence of a 4,4'-disubstituted-1,1'-biphenyl moiety in the product, **71**. This suggestion is further supported by the UV/Vis spectrum of **71** prepared in this manner, which was characterised by two absorption bands at 315 and 351 nm, similar to the spectral profile of **1**, and other simple TPD-type molecules.

Estimates of the molecular weight of the material **71** obtained from several reactions by GPC against polystyrene standards fell in the range 1740 (3-mer) to 30,500 (58-mer) depending upon the rate of addition of the oxidising agent and the concentration of the reagents. While the conditions were not optimised, it is clear that oxidation of **30** is a viable method for the production of oligo and polymeric derivatives.

6.3 Conclusion

Both the electrochemical and chemical oxidation of “twisted TPDs” such as **28**, **30** and **32** provide a polymeric material with discrete TPD type units incorporated into the backbone. The availability of polymeric materials from precursors with varying numbers and position of methyl groups enhances the possibility of synthesising a polymer by this method with the required physical and electrochemical properties required for device application.

References for Chapter 6

- 1 P. M. Borsenberger, W. Mey, and A. Chowdry, *J. Appl. Phys.*, 1978, **49**, 273.
- 2 M. Stolka, J. F. Yanus, and D. M. Pai, *J. Phys. Chem.*, 1984, **88**, 4707.
- 3 S. Heun and P. M. Borsenberger, *Physica B*, 1995, **216**, 43.
- 4 M. V. d. Auwerer and F. C. D. Schryver, *J. Phys. Chem.*, 1993, **97**, 8808.
- 5 C. Adachi, K. Nagai, and N. Tamoto, *Appl. Phys. Lett.*, 1995, **66**, 2679.
- 6 Y. Kuwabara, H. Ogawa, H. Inada, N. Noma, and Y. Shiota, *Adv. Mater.*,
1994, **6**, 677.
- 7 H. Tanaka, S. Tokito, Y. Taga, and A. Okada, *Chem. Commun.*, 1996, 2175.
- 8 S. Tokito, H. Tanaka, A. Okada, and Y. Taga, *Appl. Phys. Lett.*, 1996, **69**, 878.
- 9 S. Tokito, H. Tanaka, K. Noda, A. Okada, and Y. Taga, *Appl. Phys. Lett.*,
1997, **70**, 1929.
- 10 F. Ullmann, *Ber. Dtsch. Chem. Ges.*, 1903, **36**, 2382.
- 11 H. B. Goodbrand and N.-X. Hu, *J. Org. Chem.*, 1999, **64**, 670.
- 12 H. B. Goodbrand, in 'United States Patent 5,654,482', 1997.
- 13 H. B. Goodbrand, in 'United States Patent 5,648,539', 1996.
- 14 S. Gauthier and J. M. J. Fréchet, *Synthesis*, 1987, 383.
- 15 A. Petr, C. Kvarnström, L. Dunsch, and A. Ivaska, *Synth. Met.*, 2000, **108**,
245.
- 16 C. Kvarnström, A. Petr, P. Damlin, T. Lindfors, A. Ivaska, and L. Dunsch, *J.*
Solid State Electrochem, 2002, **6**, 505.
- 17 M.-K. Leung, M.-Y. Chou, Y. O. Su, C. L. Chiang, H.-L. Chen, C. F. Yang,
C.-C. Yang, C.-C. Lin, and H.-T. Chen, *Org. Lett.*, 2003, **5**, 839.
- 18 R. Fáber, G. F. Mielke, P. Rapta, A. Staško, and O. Nuyken, *Collect. Czech.*
Chem. Commun, 2000, **65**, 1403.

Chapter Seven

Fluorescence, Raman and ESR Studies

7.1 Introduction

The use of advanced spectroscopic methods was applied to a study of a selection of compounds in order to obtain further information on both the neutral and oxidised forms of the material. Emission and excitation spectroscopy together with Raman spectroscopy were used to obtain further information on the chromophore responsible for the UV/Vis absorption spectra. ESR spectra were recorded of both pre-oxidised samples, and as spectroelectrochemical experiments, to investigate the electronic spin-state of the oxidised forms of **23**, **26** and **59**. The author participated in these studies led by the groups of Beeby (Durham, fluorescence), Smith (Strathclyde, Raman) and McInnes (Manchester, ESR)

7.2 Fluorescence spectra

The absorption, emission and excitation spectra of **23** are presented here. As described in Chapter 3, the UV/Vis absorption consists of a single peak at 303 nm. The emission spectrum obtained by irradiation at 300nm exhibits a single peak at 375 nm.(Figure 7.1) The excitation spectrum was collected with the detector set to record emission only at 375 nm, with irradiation across the range 200 to 365 nm. The spectrum contains a peak at 300 nm.

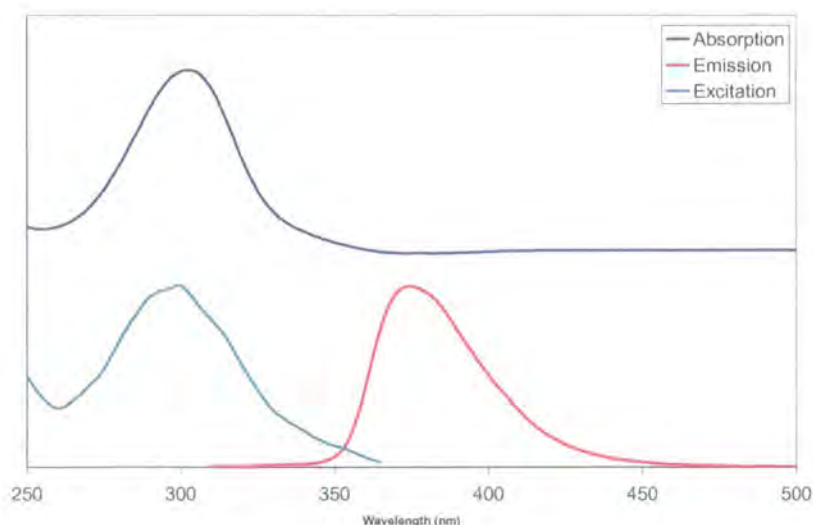


Figure 7.1 Absorption, emission and excitation spectra of **23**

The emission spectrum of **1** resembled the mirror image of the absorption spectrum with a set of bands at 405 nm.(Figure 7.2) The excitation spectrum also contained

more features than the triarylamine **23**, with bands at 311 and 350 nm being observed. (Figure 7.2) The spectra of **26** were essentially identical to those of **1**, as would be expected of such closely related compounds.

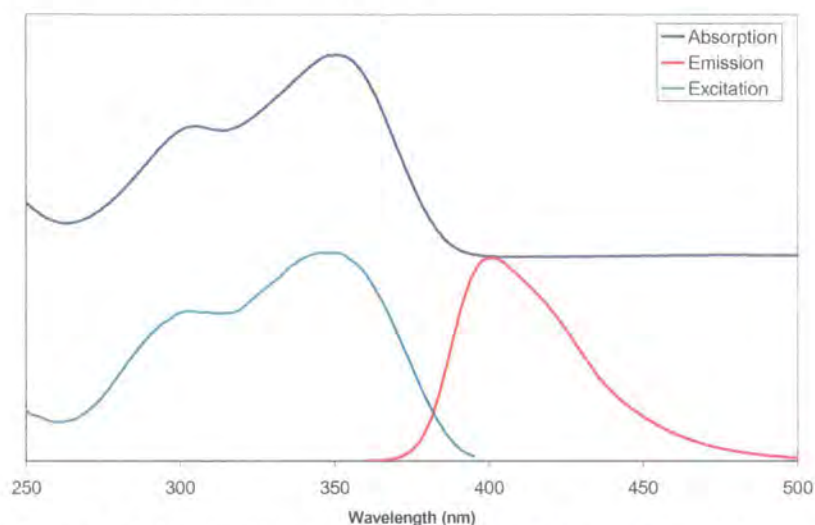


Figure 7.2 Absorption, emission and excitation spectrum of **1**

Having seen the effect of introducing methyl groups about the central C-C bond on the absorption spectra of the 2,2',6,6'-tetramethyl and 3,3'-dimethyl substituted biphenyl diamines, **28** and **31** (Chapter 4) investigation into the effect on the emission and excitation spectra was undertaken. The emission spectrum of **31** contained a single band at 367 nm, (Figure 7.3) however it was in the excitation spectra that the real differences became evident. (Figure 7.3) Only two features were apparent in the spectrum, bands at 242 and 306 nm, closely resembling the excitation spectrum of **23**. This further supports the hypothesis that the 2,2',6,6'-tetra methyl substitution pattern about the biphenyl is de-coupling the two nitrogen centres.

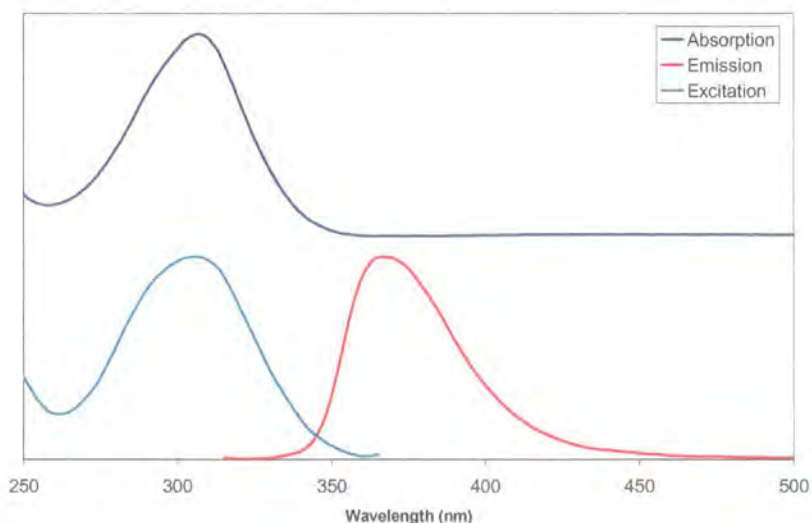


Figure 7.3 Absorption, emission and excitation spectrum of **31**

The effect of the 3,3'-dimethyl substitution pattern on the emission and excitation spectra was also studied. The excitation spectrum was again the more informative, showing a marked difference to the unsubstituted materials **1** and **26**. There were two bands present at 300 and 340 nm, similar to the spectra of **1** and **26** however the relative intensities of the bands were altered. (Figure 7.4) This is consistent with the change in intensities of bands in the absorption spectrum noted in Chapter 4.

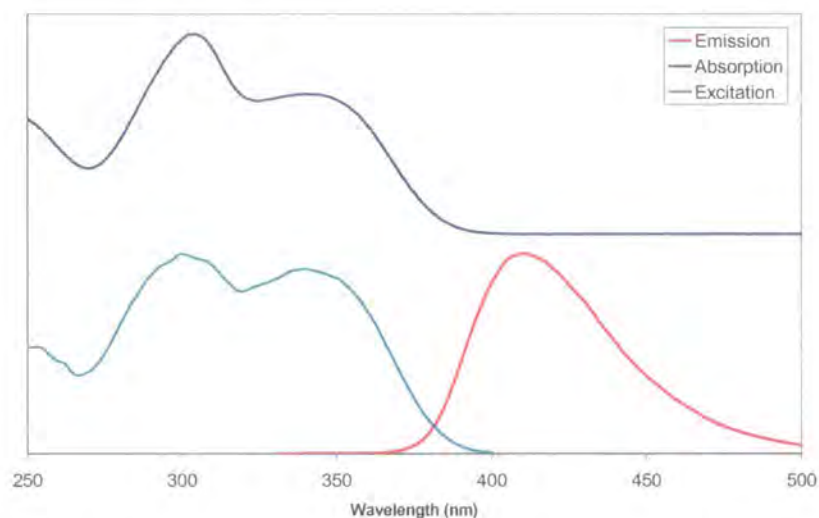


Figure 7.4 Absorption, emission and excitation spectrum of **33**

7.3 Electron Spin Resonance Studies

ESR studies on charge transfer complexes of triarylamine with iodine have reported a triplet with ^{14}N hyperfine splitting of approximately 14 Gauss. Increasing the temperature from room temperature to 150 °C produced better resolution and allowed the super-hyperfine structure to be observed. The following explanation was offered for the spectra observed. The three peaks observed at room temperature were undoubtedly associated with the interaction of the hole in the $[(\text{C}_6\text{H}_5)_3\text{N}]^+$ radical cation with the nuclear magnetic moment of the nitrogen. The appearance of the super-hyperfine structure as the temperature of the system is raised was probably due to the partial resolution of the hydrogens on the phenyl groups.¹ The recording of the ESR spectrum of triarylamines can be complicated by the reactivity of the $[(\text{C}_6\text{H}_5)_3\text{N}]^+$ radical cation which is discussed in more detail below. For this reason the experiments have been repeated using trianisylamine and tri(4-bromophenyl)amine which have stable radical cations. These also displayed a triplet splitting pattern.²

Our attempts to replicate the ESR spectrum by oxidation of **23** produced only a broad poorly defined triplet. (Figure 7.5) The experiment was repeated at both reduced and elevated temperatures in the range (243-303 K) with no discernible improvement in the appearance of the spectrum.

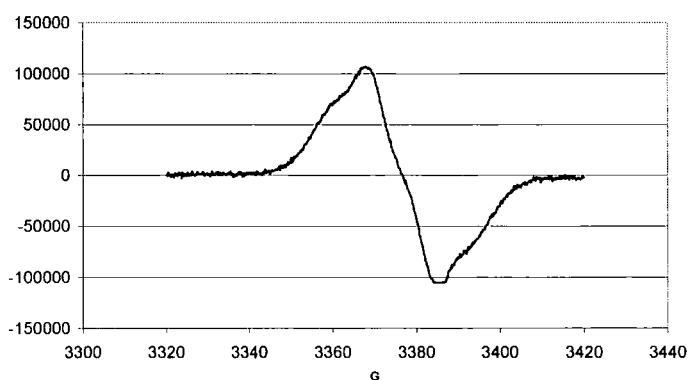


Figure 7.5 The ESR spectrum of $23^{+\bullet}$ in CH_2Cl_2 at 258K

It was through electrochemical ESR studies that the reaction scheme of the dimerisation of triphenylamine to tetraphenyl-1,1'-biphenyl-4,4'-diamine was first elucidated. ESR studies on both chemically and electrochemically oxidised

tetraphenyl-1,1'-biphenyl-4,4'-diamine have since revealed a pentet splitting pattern which is consistent with coupling of the unpaired electron to two equivalent ^{14}N nuclei.^{2,3} (Figure 7.6)

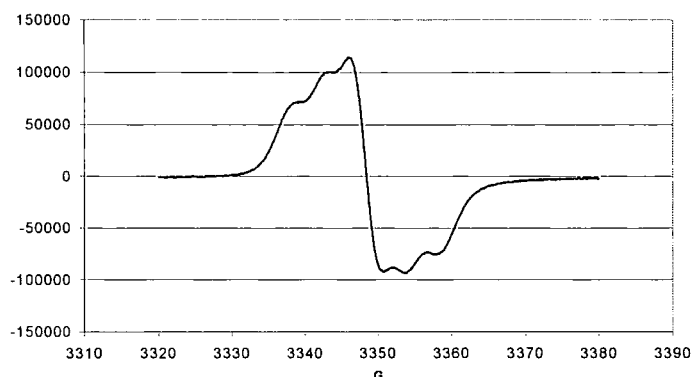


Figure 7.6 The ESR spectrum of 26^{+1} in CH_2Cl_2 at 298K

The dication 26^{+2} was ESR silent with no signal being observed across the range of the instrument.

A spectroelectrochemical investigation of the ESR response of the trimeric material **59** was undertaken by means of an *in situ* ESR spectroelectrochemical rig. This electrochemical set-up enabled ESR spectra to be recorded during oxidation. (Figures 7.7-7.9)

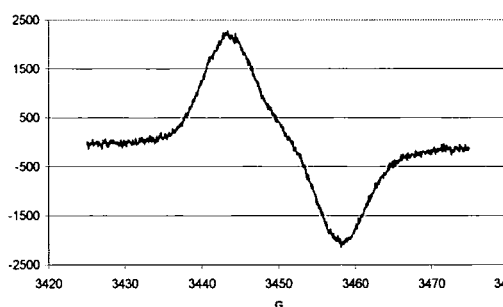


Figure 7.7 ESR spectrum of 59^{+1}

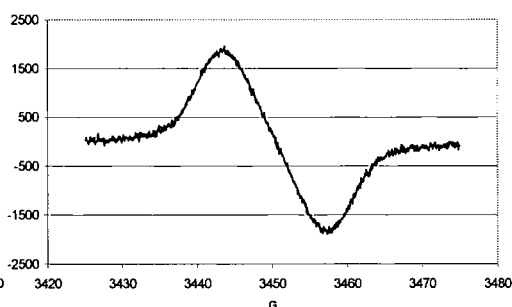


Figure 7.8 ESR Spectrum of 59^{+2}

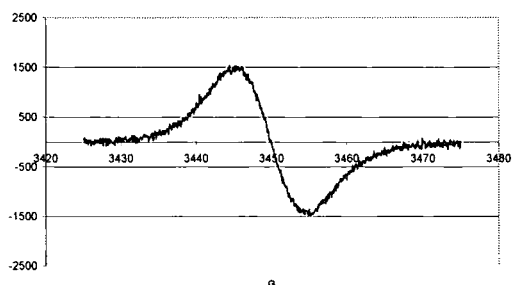


Figure 7.9 ESR Spectrum of 59^{+3}

The ESR spectrum of **59** during various stages of oxidation was recorded with the intention of attempting to identify the environment of the unpaired spins present in the different oxidation states. Unfortunately the spectra displayed very little difference, and no clear hyperfine splitting. This made interpretation impossible, although it is worth noting that there are characteristic wave shapes and intensities to the spectra of the differing oxidation states. Difficulties in isolating the trimeric materials in the intermediate oxidation states +1 and +2 in this cell made further investigations problematic.

7.4 Raman Analysis of Charge Transfer Materials

(A joint study carried out with Rachael Littleford, University of Strathclyde.)

7.4.1 Introduction

Raman spectroscopy offers an alternative method through which to interrogate the structure of these tetraaryl biphenyl diamine systems.⁴⁻⁸ While the neutral forms of these molecules are readily accessible, it is far harder to isolate the radical species although the successful studies in Chapter 3 suggest that many more of these radical cations may be isolable than is commonly thought.

Raman spectroelectrochemical techniques which allow the generation of these species in solution in the spectrometer beam path *in-situ* provide a solution to the problems in obtaining the radical samples for study, and can be used to provide a molecularly specific fingerprint of the generated molecule.⁹⁻¹²

7.4.2 Aims

The overall aim is to follow the formation of both monocations and dications of charge transfer materials, specifically **1** and **26**, generated inside an OTTLE cell, using Raman and resonance Raman spectroscopy. In combination with a calculated Raman spectrum of **1**, the frequencies and displacements of each vibration will provide information on the structure and electronic structure of the cations *in-situ* in solution, indicating if the radical cations are best described in terms of a symmetrical structure with a fully delocalised radical as suggested by the analysis of the NIR band and DFT calculations (Chapter 3) or if the rate of electron transfer is sufficiently slow to allow the observation of a valence trapped “mixed-valence” state.¹³

7.4.3 Results and Discussion

For 1^{n+} , excitation with 514.5 nm radiation is in the envelope of the absorption band at 477 nm. Although the excitation wavelength is towards the lower frequency side of the absorption band, this will be close to the 0 to 0 and 0 to 1 vibronic band frequencies, and consequently should be effective in creating resonance enhancement. Resonance conditions are encountered with the chromophore of the dication when the sample is excited at 632.7 nm, this is due to the excitation wavelength being within the absorption envelope with the maximum at 732 nm. With the dication, the 632.7 nm band is on the high energy side of the absorption band. This will correspond to a higher vibronic level of the band and consequently weaker resonance enhancement is to be expected. The results are similar for 26^{n+} a slight frequency shift of the absorption maximum occurs, although the monocation chromophore will still be resonant with 514.5 nm excitation and the dication resonant with 632.7 nm excitation.

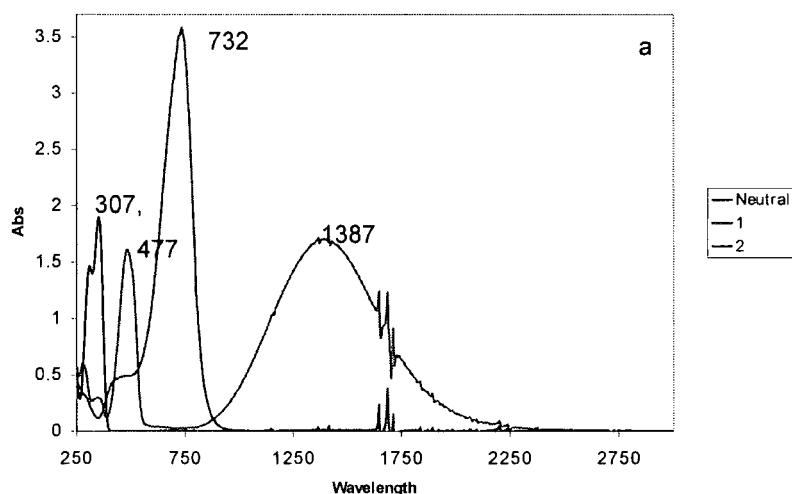


Figure 7.10 Electronic spectrum of 1

7.4.3.1 DFT calculations

Theoretical Raman spectra of the neutral **1** species were calculated by Tackley using DFT methods and compared with the experimental Raman spectrum of the neutral **26**. Although the experimental result is from a molecule with an extra methyl group, in the region 1800 to 4000 cm^{-1} there is close agreement between the calculated and observed frequencies. The largest deficit for any clearly assigned band was 18 cm^{-1} ,

and a fit of the most intense 10 bands gave an average error of 7.9 cm^{-1} . However, calculated intensities are poor, often a common factor in DFT calculations. A similar comparison of the **1** monocation theoretical spectrum and the **26** monocation experimental spectrum is shown in figure 7.11. The largest deficit for any band was 9 cm^{-1} , with an average error of 4.7 cm^{-1} . Thus, the assignments as made by the DFT calculations can be used with some confidence. The full list of calculated bands together with the experimental frequencies of the Raman active bands is given in Appendix A.

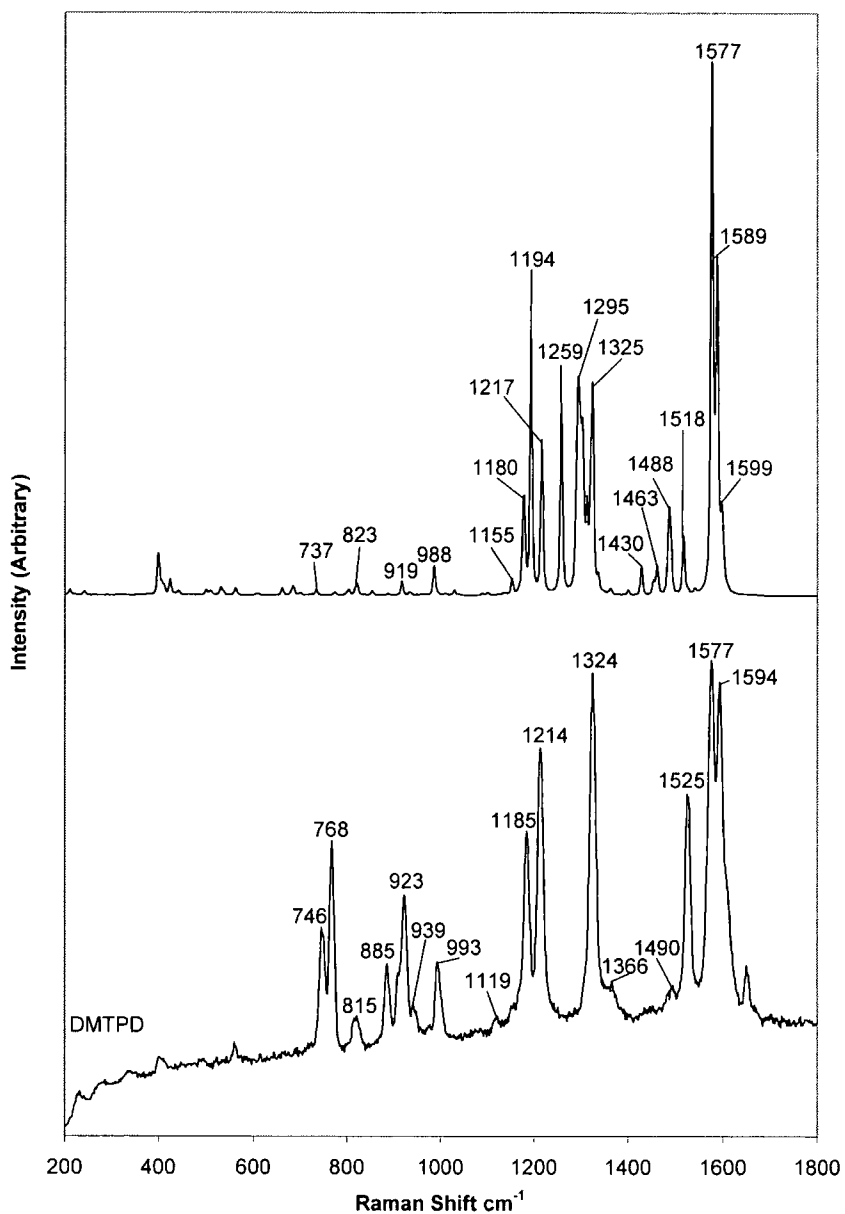


Figure 7.11 Predicted Raman spectrum of **1** cation and experimental Raman spectrum of **26** cation with 514.5 nm excitation

7.4.3.2 Raman Spectra of Solid State 26^{n+} ($n=0,1$)

The Raman spectra of neutral **26** and of the mono cation as $[26]SbCl_6$ in the solid state are given in figure 7.12. There are clear differences in the spectra. Three bands can be identified and assigned from the DFT calculation in what is essentially the quadrant stretch region for phenyl ring systems between 1550 cm^{-1} and 1620 cm^{-1} . Two of these bands, at 1614 and 1606 cm^{-1} can be identified clearly in the neutral species with the largest band being the 1606 cm^{-1} band. However, in the cation, this band although still the most intense, has a reduced intensity relative in particular to the band at 1614 cm^{-1} . There are a number of other differences as can be seen in figure 7.12, but the predominant differences are the relative intensity changes in the bands at about 1300 cm^{-1} and 1200 cm^{-1} . Both the relatively intense band at 1324 cm^{-1} in the cation and the relatively intense band at 1294 cm^{-1} in the neutral species arise from a combination of C-N and C-C stretches on the entire ring system. Generally, it is these ring stretches rather than the C-H displacements that are effective in resonance Raman enhancement. The reason for this is that enhancement is caused when the vibrational displacements take the nuclear skeleton from its geometry in the ground electronic state into the geometry in the excited electronic state. This is most likely to occur in a $\pi \rightarrow \pi^*$ or $n \rightarrow \pi^*$ transition of the type described here when nuclear motion of the carbon nitrogen skeleton occurs.

Through comparison of the experimental spectra with the calculated data, the main peaks, and the associated molecular motions can be assigned. The main difference between the 1324 cm^{-1} mode and the 1294 cm^{-1} mode is that the 1324 cm^{-1} mode has larger C-N and C-C displacements on the peripheral rings. A similar picture is obtained for the other pair of vibrations at 1214 cm^{-1} and 1182 cm^{-1} . Thus the resonant enhancement in the mono cation is favoured by contributions from C-N and C-C stretches of the outer phenyl rings.

These observations suggest that the electron density in the π to π^* transition which leads to the absorption band at 472 nm covers at least the outer phenyl rings and the nitrogen atoms.

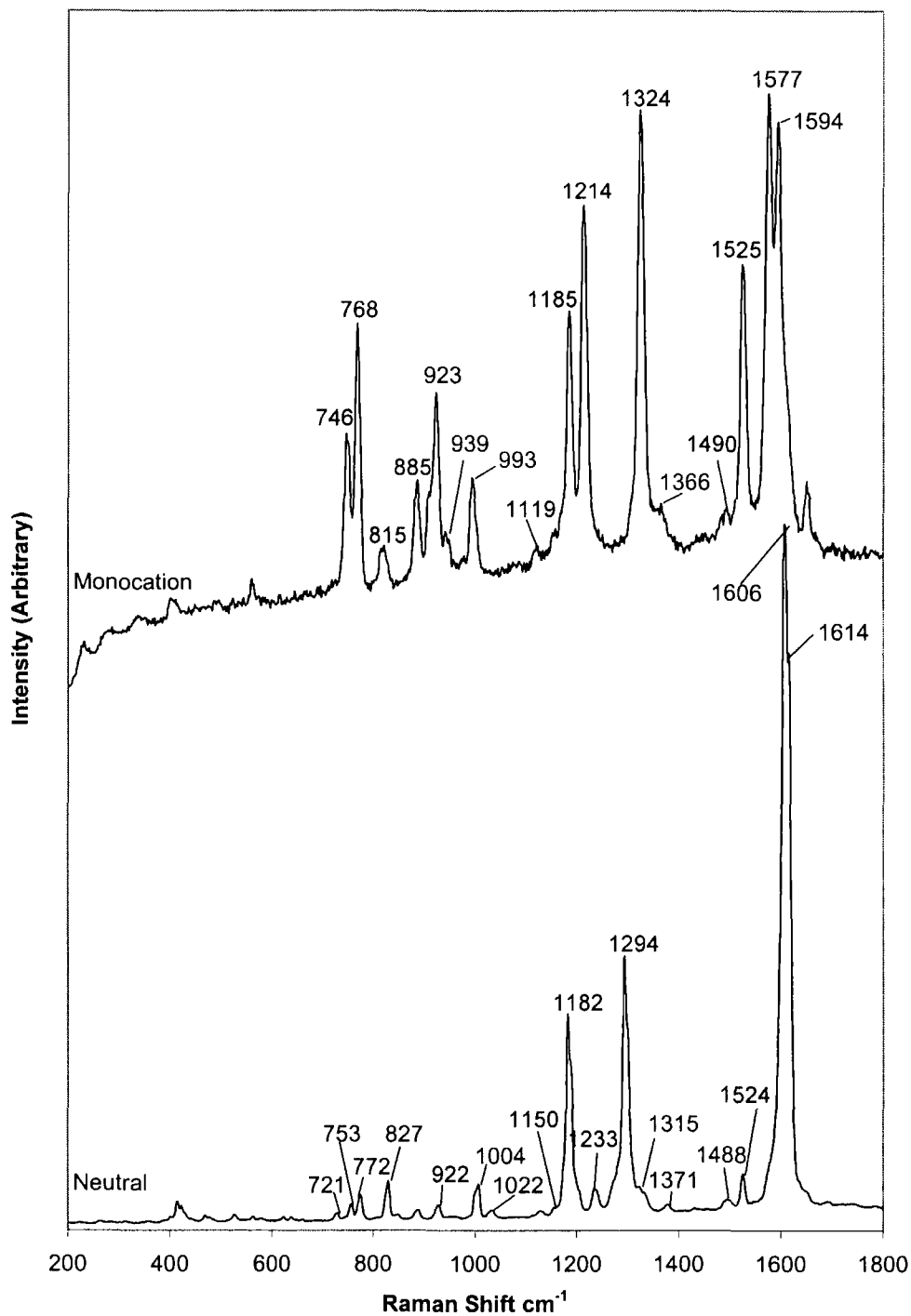


Figure 7.12 Experimental Raman spectrum of **26** (a) neutral and (b) monocation. Excitation at 514.5 nm

7.4.3.3 Spectroelectrochemical Raman Data

The results of an OTTLE experiment using a solution of **26** in CH_2Cl_2 with supporting electrolyte are shown in figure 7.13. Together with an obvious increase in the intensity of the sharp Raman scattering due to resonance enhancement when the cations are formed, there is clear evidence of overtones in the region between 1600 and 3200 cm^{-1} and a clear emission spectrum. The presence of overtones is common for resonant systems since the usual selection rules are relaxed.

The emission spectrum can be used to follow the formation of the cations as the voltage is changed. The emission from 632.7 nm excitation is likely to arise from the dication since it has an absorption band in that frequency region. Emission from the monocation would not be expected to be efficient as there is no absorption band close in frequency to the laser excitation wavelength of 632.7 nm. The band grows in at potentials at and above that at which the dication is produced. This is as expected since the dication will continue to form through diffusion of residual monocations to the electrode surface.

A more complicated situation arises with 514.5 nm excitation. In addition to emission from the dication which is at the same absolute frequency as that obtained with 632.7 nm excitation, there appears to be emission from the monocation with a maximum at approximately 2500 cm^{-1} lower than the excitation frequency. This is slightly unusual because there is a lower energy excited state for the monocation. However, Raman scattering uses a high power laser, and emission from higher excited states is known. This will be helped by the larger energy separation between this state (472 nm) and the state in the near infra-red (1327 nm). This emission is broad compared to that of the dication. However, emission from the dication occurs at a remarkably low voltage, and peaks at a lower voltage than for 632.7 nm excitation. Smith and Littleford suggest that this occurs through energy transfer from the relatively long lived higher excited state of the monocation, transferring energy efficiently to the excited state of the dication. Hence, the dication emission arises from two processes, emission stimulated by collisional processes with the monocation, and emission from direct absorption of the laser beam into a very high vibronic excited state arising from the band with a maximum at 742 nm, or the weaker with a maximum at 492 nm.

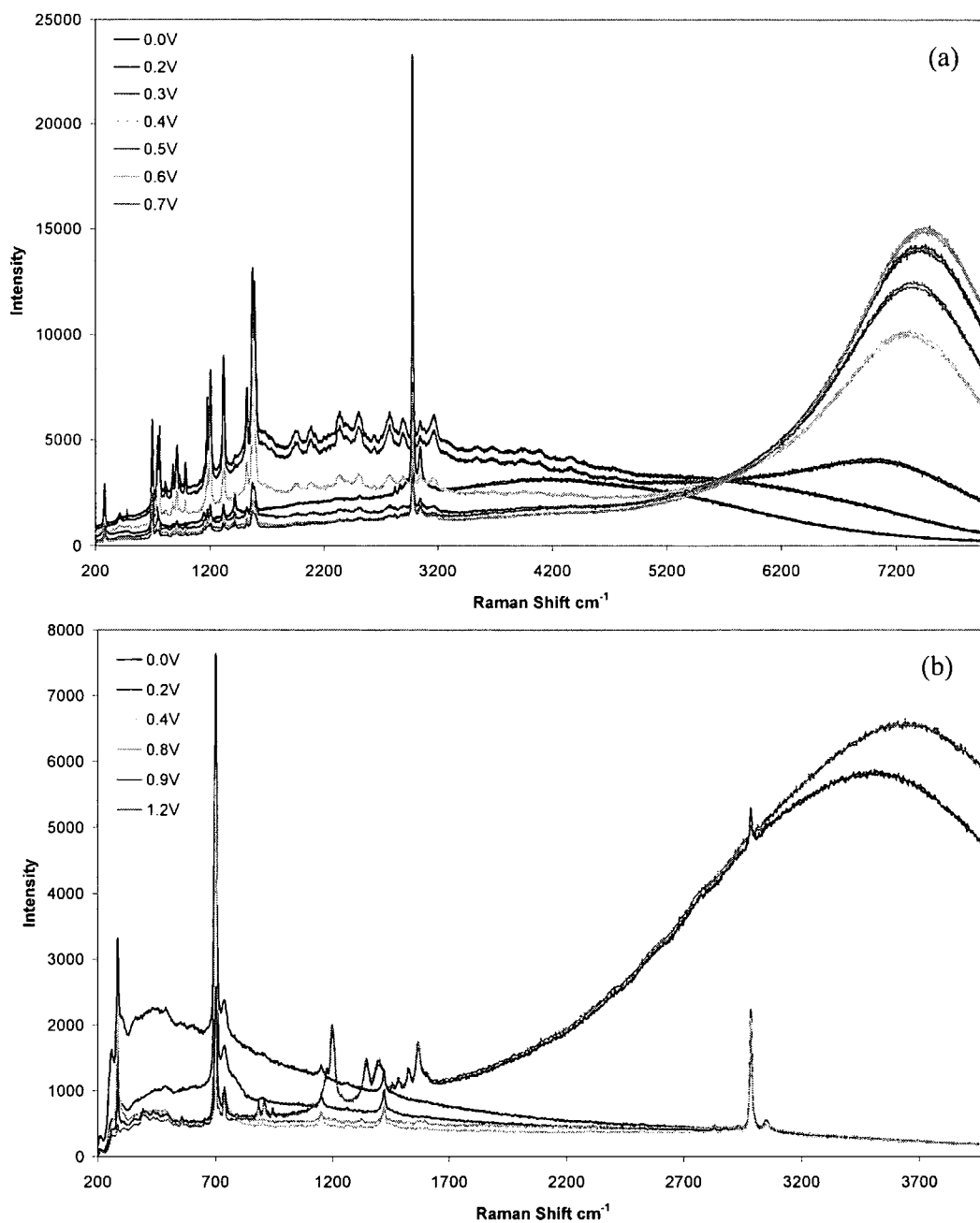


Figure 7.13 Raman spectra showing the generation of the **26** cation and dication *in-situ* using an OTTLE cell. Excitation at (a) 514.5 nm and (b) 632.7 nm

Figure 7.14 shows an expanded plot of the Raman data in the region below 1800 cm^{-1} . There is obvious agreement between the spectrum from the monovalent radical at 0.3 V in the OTTLE cell and the same radical in the solid state. Small frequency differences may be attributed to instrumental error. There are only very minor intensity changes.

The frequency of the Raman active modes of the dication are similar but not identical to those of the monocation. However, there are significant intensity changes. In particular, there are changes in the 1600 cm^{-1} region and in the 1200 cm^{-1} region. The apparent rise in the number of other bands such as the band at 1413 cm^{-1} merely indicate the much weaker enhancement from this radical since the band at 1413 cm^{-1} is from the solvent. However, the band at 1592 cm^{-1} in the theoretical calculation has greater displacements on the periphery of the molecule. This may suggest that the difference between the monocation and the dication is that somewhat more of the electron density is on the peripheral rings in the dication.

Less intense spectra were obtained from the dication than from the cation radical with 514.5 nm excitation. However, with 632.7 nm excitation more intense spectra are obtained at higher voltages. On the basis that this is the dication this effect is explained by the fact that the dication is to a greater extent in resonance with the main 742 nm band when excited at 632.7 nm . There is no effective resonance band to produce a Raman effect for the monocation with 632.7 nm excitation.

The enhancement pattern however, is not the same as that found with 514.5 nm excitation. This is because it is more in resonance with the lower frequency 742 nm electronic band in the spectrum of the divalent ion. However, some noticeable similarities are present. In particular, the band at 1569 cm^{-1} (1592 cm^{-1} in the theoretical calculations) is again the most strongly enhanced band in the quadrant stretching region. This confirms the conclusion that a significant fraction of electron density is on the periphery of the molecule for the cationic species. Similar conclusions can be drawn from the fact that the band at 1200 cm^{-1} is relatively intense. However, the band at 1317 cm^{-1} is now weak and the bands at 1343 and 1395 cm^{-1} are relatively much more intense. The band at 1395 cm^{-1} is of particular interest. The main displacement shown in the DFT calculated Raman stretching modes

calculation are of large methyl C-C stretches. Again this would emphasise the presence of significant electron density at the peripheral parts of the molecule.

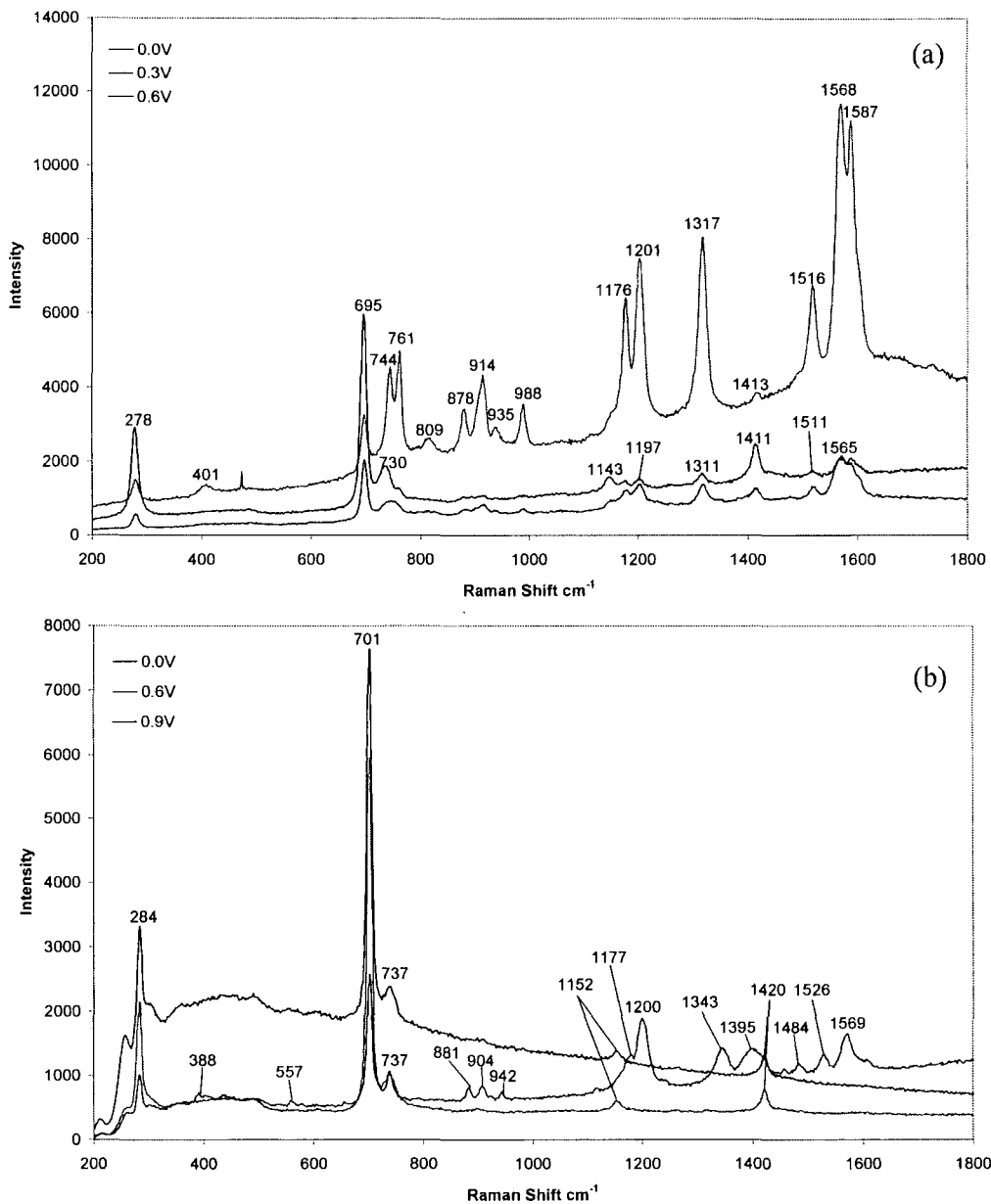


Figure 7.14 Selected Raman spectra showing the electrochemical generation of the **26** cation and dication in the OTTLE cell. Excitation at (a) 514.5 nm and (b) 632.7 nm

Figures 7.15 and 7.16 show the results of an OTTLE experiment using **1**. Due to resonance enhancement an obvious increase in the intensity of the sharp Raman scattering occurs when the cations are formed. Excitation at 632.7 nm shows very little resonance enhancement from the monocation as expected, with an increase in intensity as the dication is formed.

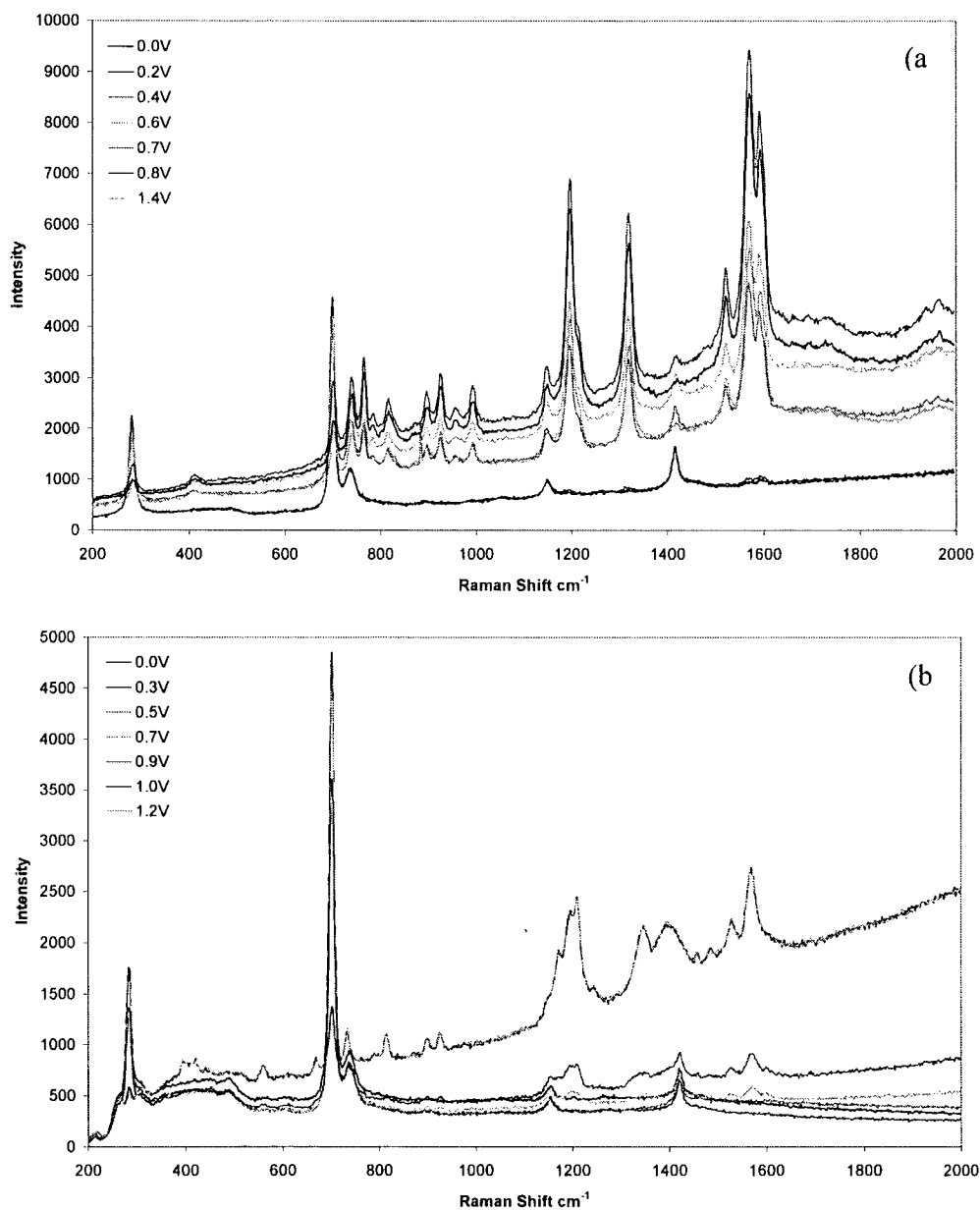


Figure 7.15 Raman spectra showing the generation of the **1** cation and dication *in-situ* inside an OTTLE cell. Excitation at (a) 514.5 nm and (b) 632.7 nm

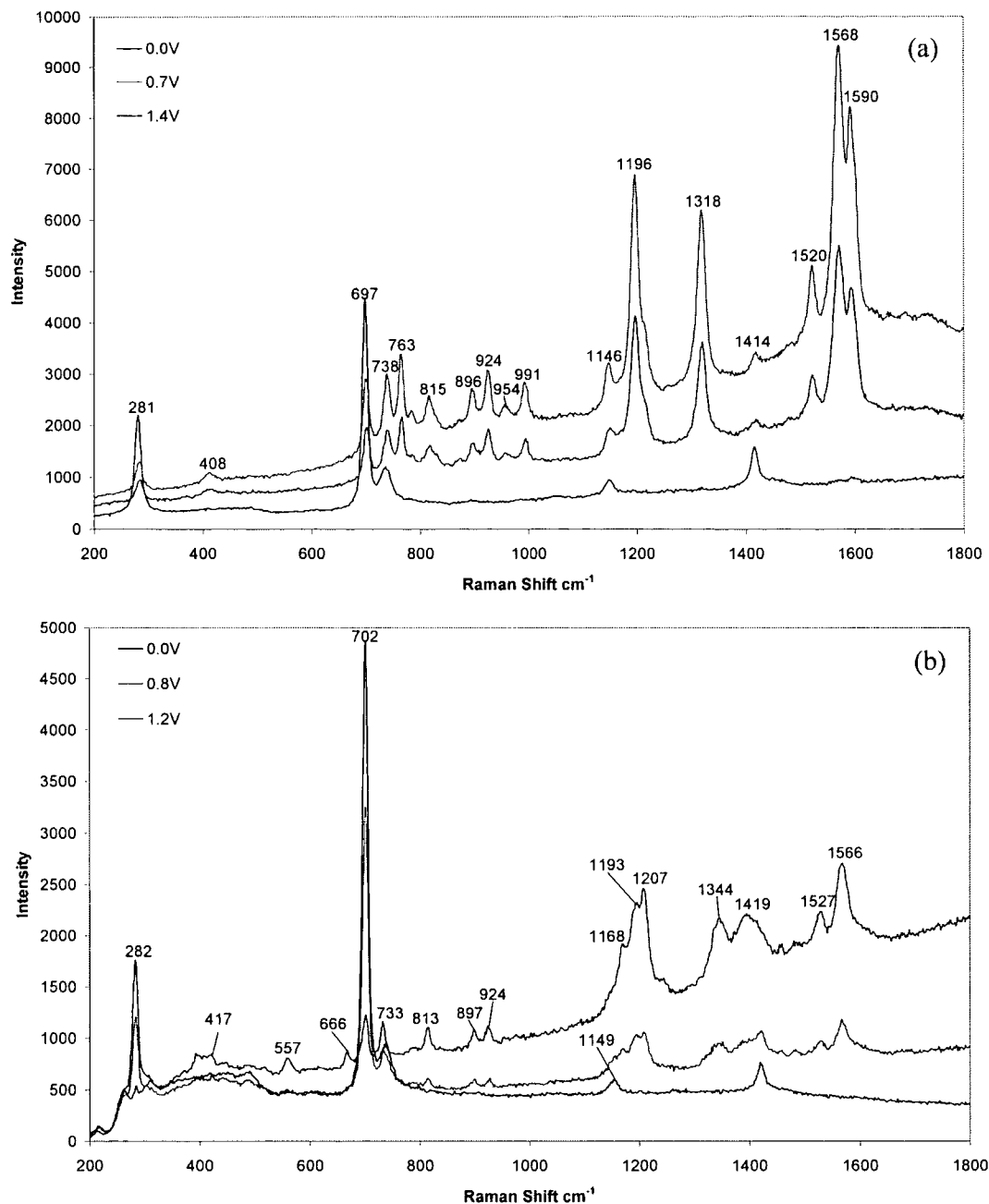


Figure 7.16 Selected Raman spectra showing the generation of the **1** cation and dication *in-situ* inside an OTTE cell. Excitation at (a) 514.5 nm and (b) 632.7 nm

7.4.4 Conclusion

The use of an OTTLE cell combined with Raman spectroscopy provides a complimentary technique to generate and monitor the formation of radical species of model charge transfer materials. In conjunction with DFT calculations it is possible to predict that the nature of the radical cations are best described in terms of a symmetrical structure with a fully delocalised radical structure, with significant electron density on the outer rings of the dicationic system. This data compliments that obtained from spectroelectrochemical UV-Vis-NIR studies.

The Raman scattering from the three oxidation states of both the materials studied are clearly different, allowing discrimination between the neutral, mono- and dicationic species. The signal to noise ratio from the radicals under resonance conditions is very good. This suggests it may be possible to detect the radicals *in-situ* in a device at low concentrations, this is not a trivial experiment however and would require significant further study. With a tunable laser it would be possible to obtain resonance profiles for the monocation and dication, providing an effective method to probe the structures of these species.

7.4.5 Experimental

1 and **26** were supplied by the synthetic team at Avecia.

[**26**] SbCl_6 was prepared by oxidation of **26** with a 0.1 M solution of SbCl_5 in CH_2Cl_2

7.4.5.1 Spectroelectrochemical studies

Spectroelectrochemical studies were carried out in an OTTLE cell (quartz, 1 mm pathlength) fabricated at the University of Durham, using a 0.5 mM solution of the material of interest with supporting electrolyte of tetrabutylammonium tetrafluoroborate (0.1 M) in freshly distilled dichloromethane at room temperature. The potential was increased in a stepwise manner, allowing Nernstian equilibrium to occur at each potential, evidenced by a drop in current prior to each spectral acquisition.

7.4.5.2 Raman analysis

The OTTLE cell was mounted in the beampath of the spectrometer and focussed on a pore within the gauze working electrode using the microscope.

Raman spectra were collected using Renishaw 2000 microprobe systems with a Spectra-Physics model 163 argon-ion laser providing excitation at 514.5 nm, and a Spectra-Physics model 127 helium-neon laser providing excitation at 632.7 nm. A Vantacon macrosampler attachment was employed in the analysis. Solid state spectra were the result of three 10 s accumulations. Spectroelectrochemical solution state spectra were collected for 1 s, 1 accumulation

A silicon standard was analysed before Raman scattering was collected in order to assess the systems performance.

References for Chapter 7

- 1 D. N. Stamires and J. Turkevich, *J. Am. Chem. Soc.*, 1963, **85**, 2557.
- 2 E. T. Seo, R. F. Nelson, J. M. Fritsch, L. S. Marcoux, D. W. Leedy, and R. N. Adams, *J. Am. Chem. Soc.*, 1966, **88**, 3498.
- 3 W. H. Bruning, R. F. Nelson, L. S. Marcoux, and R. N. Adams, *J. Phys. Chem.*, 1967, **71**, 3055.
- 4 V. Guichard, A. Bourkba, O. Poizat, and G. Buntinx, *J. Phys. Chem.*, 1989, **93**, 4429.
- 5 R. E. Hester and K. P. J. Williams, *J. Chem. Soc., Faraday Trans. 2*, 1981, **77**, 541.
- 6 G. Buntinx and O. Poizat, *J. Chem. Phys.*, 1989, **91**, 2153.
- 7 V. Guichard, O. Poizat, and G. Buntinx, *J. Phys. Chem.*, 1989, **93**, 4436.
- 8 V. Guichard, A. Bourkba, M.-F. Lautie, and O. Poizat, *Spectrochim. Acta*, 1989, **45A**, 187.
- 9 F. Hartl, T. L. Snoeck, D. J. Stufkiens, and A. B. P. Lever, *Inorg. Chem.*, 1995, **34**, 3887.
- 10 J.-S. Yu, C. Yang, and H.-Q. Fang, *Anal. Chim. Acta*, 2000, **420**, 45.
- 11 P. A. Mosier-Boss, R. Newbery, S. Szpak, S. H. Lieberman, and J. W. Rovang, *Anal. Chem.*, 1996, **68**, 3277.
- 12 L. Kavan, L. Dunsch, and H. Kataura, *Chem. Phys. Lett.*, 2002, **361**, 79.
- 13 J. T. Hupp and R. D. Williams, *Acc. Chem. Res.*, 2001, **34**, 808.

Chapter Eight

Experimental Procedures

8.1 Experimental Procedures

All reactions were carried out under a nitrogen atmosphere in flame-dried glassware. Solvents were dried from an appropriate agent and distilled. Di(4-methylphenyl)amine, 2,2' dimethylbenzidine dihydrochloride and *ortho*-dichlorobenzene were purchased from Aldrich, diphenylamine, carbazole, fluorene, 18-crown-6 and K_2CO_3 were purchased from Avocado, 5-nitro-*meta*-xylene was purchased from Lancaster. All commercial reagents were used as received.

8.2 Instrumentation

Mass spectra were recorded on a Micromass Autospec instrument operating in EI mode. [M] is used to denote the molecular ion.

NMR spectra were recorded on the following machines at frequencies listed unless stated otherwise; Varian XL-200 (1H), Varian Unity-300 (1H and $^{13}C\{^1H\}$) or Varian VXR-400 (1H , ^{13}C , 1H - 1H COSY and 1H - ^{13}C HETCOR). All chemical shifts are reported in δ (ppm). 1H NMR spectra were referenced to residual protio impurity in the solvent $CHCl_3$, 7.26 ppm. ^{13}C NMR spectra were referenced to the solvent resonance $CDCl_3$, 77.0 ppm. All spectra were recorded at ambient temperature. The abbreviations have been used for multiplicities: s (singlet), d (doublet), t (triplet), m (multiplet), br (broad).

UV-Visible spectra were recorded on a Varian Cary-5 spectrophotometer

Electron spin resonance measurements were recorded on a Bruker EMX ESR spectrometer equipped with a Bruker x-band microwave bridge.

Emission and excitation spectra were recorded on a Perkin Elmer LS-50B luminescence spectrometer.

Elemental analysis was performed by the microanalytical service within the Department of Chemistry at the University of Durham.

8.3 General Procedure

For preparation of the series of Ullmann Condensation reaction products detailed below, we found the most effective and consistent preparative method to be that employing 18-crown-6 as a phase transfer agent and utilising *ortho*-dichlorobenzene as the solvent.¹ The general procedure was as follows: To a 100ml round-bottomed flask containing *ortho*-dichlorobenzene (10 ml) equipped with a magnetic follower, a nitrogen gas purge and a reflux condenser were added diphenylamine (5.5 mmol), diiodobiphenyl (2.5 mmol), K₂CO₃ (20 mmol), copper powder (5.0 mmol) and 18-crown-6 (0.5 mmol). The reaction mixture was rapidly heated to the reflux temperature of 180 °C and maintained at that temperature for 12-24 hrs. The reaction mixture was cooled and filtered to remove the inorganic residues. The crude reaction mixture was then reduced in volume *in vacuo* and purified by column chromatography.

***N,N,N',N'*-tetra(phenyl)-(1,1'-biphenyl)-4,4'-diamine (19)**

Diphenylamine (0.916 g, 5.43 mmol), diiodobiphenyl (1.0 g, 2.46 mmol), K₂CO₃ (2.72 g, 19.68 mmol), copper powder (0.34 g, 5.3 mmol) and 18-crown-6 (0.13 g, 0.49 mmol) were dissolved in *ortho*-dichlorobenzene (10 ml) and heated at reflux for 18.5 hrs. The crude reaction mixture was treated with MeOH, producing a precipitate. The solid was collected, dried and recrystallised from CH₂Cl₂. (0.68 g, 56%)

¹H NMR (CDCl₃) δ 7.48 (d, *J*_{AB} = 9Hz, 4H, Ha/Hb),

7.16 (pseudo t, *J*_{HH} = 15Hz, 8H, Hd),

7.03 (d, *J*_{HH} = 9Hz, 8H, Hc),

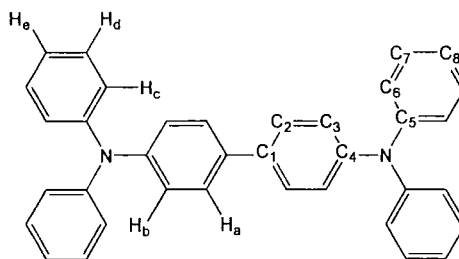
7.03 (d, *J*_{HH} = 9Hz, 4H, Ha/Hb),

6.93 (t, *J*_{HH} = 14 Hz, 4H, He)

¹³C NMR (CDCl₃) δ 147.71 (C5), 146.73 (C4), 134.74 (C1), 129.25 (C2), 127.29 (C3), 124.30 (C7), 124.08 (C6), 122.81 (C8)

EI MS *m/z* 488 [M]⁺

m.p. 220-222°



***N,N,N',N'*-tetra(4-methylphenyl)-(1,1'-biphenyl)-4,4'-diamine (27)**

A solution of diiodobiphenyl (2.0 g, 4.93 mmol), di(4-methylphenyl)amine (2.14 g, 10.85 mmol), K_2CO_3 (5.44 g, 39.44 mmol), copper powder (0.67 g, 10.6 mmol) and 18-crown-6 (0.29 g, 0.99 mmol) in *ortho*-dichlorobenzene (10 ml) was heated at reflux for 15 hrs. The reaction mixture was filtered and the solvent volume reduced *in vacuo*. The crude mixture was purified by column chromatography (silica, hexanes). (1.25 g, 47%)

1H NMR ($CDCl_3$) δ 7.31 (d, $J_{HH} = 8$ Hz, 4H, Ha/Hb),

6.97 (m, 20H), 2.2 (s, 12H, CH_3)

^{13}C NMR ($CDCl_3$) δ 147.22 (C5), 145.54 (C4),

134.20 (C1), 132.61 (C8), 130.08 (C2), 127.28 (C3),

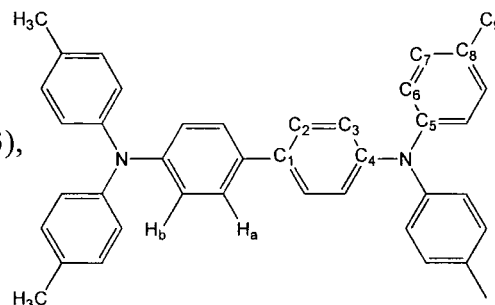
124.74 (C7), 123.16 (C6), 21.07 (C9)

EI MS m/z 544 $[M]^+$, 349 $[M-NAr_2]^+$

m.p. 203-205°

Analysis $C_{40}H_{36}N_2$

Calculated. C%, 88.19; H%, 7.66; N% 5.14 and found: C% 88.18; H% 7.74; N% 4.49

**2,2'-Dimethyl-4,4'-diiodobiphenyl (52)^{2, 3}**

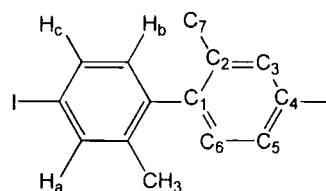
2,2'-Dimethylbenzidine dihydrochloride (10 g, 35.0 mmol) was dissolved in a 10% H_2SO_4 solution and cooled to 10 °C. A $NaNO_2$ solution (6.31 g, 91 mmol in 67 ml H_2O) was added dropwise whilst maintaining a temperature of 8 °C. This solution was stirred for 30 mins, after which it was poured into a stirred solution of KI_3 (KI, 100 g, 671 mmol; I_2 , 110 g, 436 mmol) and stirred for 10 hrs. Thereafter, sodium hydrogen sulfite was added with stirring, until gas evolution ceased. The solution was filtered and the organic material extracted with Et_2O (5 x 100 ml). This solution was washed with a further portion of sodium hydrogen sulfite solution, dried ($MgSO_4$) and the solvent removed *in vacuo* to afford the crude product which was sufficiently pure for subsequent reactions. (10.75 g, 68.5%)

^1H NMR (CDCl_3) δ 7.56 (s, 2H, H_a), 7.48 (d, $J_{\text{HH}} = 8$ Hz, 2H, H_b/H_c), 6.72 (d, $J_{\text{HH}} = 8$ Hz, 2H, H_b/H_c), 1.93 (s, 6H, CH_3)

^{13}C NMR (CDCl_3) δ 139.99, 138.76, 138.23, 134.82, 130.88, 93.16, 19.50

EI MS m/z 434 $[\text{M}]^+$, 306 $[\text{M}-\text{I}]^+$, 180 $[\text{M}-2\text{I}]^+$

m.p. 83-84°



***N,N,N',N'*-tetraphenyl-(2,2'-dimethyl)-(1,1'-biphenyl)-4,4'-diamine (28)**

A stirred solution of 2,2'-dimethyl-4,4'-diiodobiphenyl (**52**) (1.0 g, 2.3 mmol), diphenylamine (0.78 g, 4.6 mmol), K_2CO_3 (2.54 g, 18.4 mmol), copper powder (0.58 g, 9.2 mmol) and 18-crown-6 (0.12 g, 0.46 mmol) in *ortho*-dichlorobenzene (10 ml) was heated at reflux for 20hrs. The reaction mixture was filtered and the solvent volume reduced *in vacuo*. The crude mixture was purified by column chromatography (silica, hexanes/ CH_2Cl_2) to afford the title compound as a yellow powder. (0.38 g, 35%)

^1H NMR (CDCl_3) δ 7.22 (s, 2H, H_a) 7.19 (m, 8H, H_d), 7.06 (m, 8H, H_e), 6.93 (m, 2H, H_b/H_c), 6.92 (m, 4H, H_f), 6.85 (m, 2H, H_b/H_c), 1.94 (s, 6H, CH_3)

^{13}C NMR (CDCl_3) δ 147.95 (C7), 146.48 (C4),

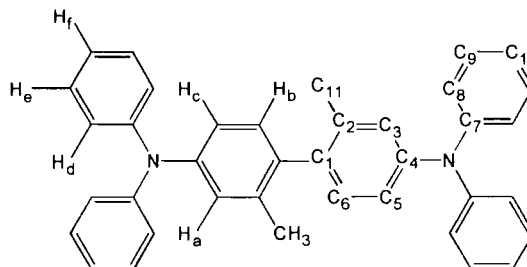
137.10 (C1), 135.93 (C2), 130.40 (C3),

129.17 (C9), 125.10 (C5), 124.17 (C8)

122.64 (C6), 121.23 (C10), 20.06 (C11).

EI MS m/z 516 $[\text{M}]^+$, 349 $[\text{M}-\text{NPh}_2]^+$

m.p. 206-209°



***N,N,N',N'*-tetra(4-methylphenyl)-(2,2'-dimethyl)-(1,1'-biphenyl)-4,4'-diamine (29)**

To prepare the title compound 2,2'-dimethyl-4,4'-diiodobiphenyl (**52**) (2.17 g, 5.0 mmol), di(4-methylphenyl)amine (2.36 g, 12.0 mmol), K_2CO_3 (5.52 g, 40.0 mmol), copper powder (0.68 g, 10.75 mmol) and 18-crown-6 (0.27 g, 1.0 mmol) were dissolved in *ortho*-dichlorobenzene (10 ml) and heated at reflux for 45 hrs. The reaction mixture

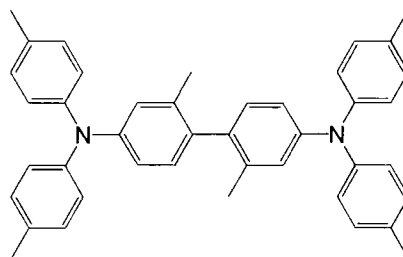
was filtered and the solvent volume reduced *in vacuo*. The crude mixture was purified by column chromatography (silica, hexanes). (2.35 g, 82%)

$^1\text{H NMR}$ (CDCl_3) δ 7.05 (m, Ar, 22H), 2.32 (s, 12H, ArCH₃), 1.99 (s, 6H, biphenyl CH₃)

$^{13}\text{C NMR}$ (CDCl_3) δ 145.79, 144.54, 135.90, 134.08, 131.06, 129.27, 128.76, 123.43, 122.79, 118.96, 19.78, 19.05

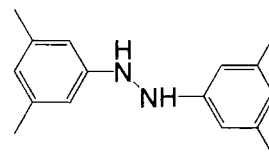
EI MS m/z 572 [M]⁺, 377 [$\text{M}-\text{NAr}_2$]⁺, 286 [M]²⁺

m.p. 248-250°



3,3'-5,5'-Tetramethyl hydrazobenzene⁴

An aqueous solution of NaOH (0.75 mmol, 100 ml) was added dropwise to a boiling suspension of zinc dust (25.0 g, 0.38 mol) in EtOH (40ml) containing 5-nitro-1,3-xylene. The rate of addition was adjusted in order to maintain a vigorous reflux. After addition of the alkali the reaction was maintained at reflux for 4 hrs. The solution was filtered into an acetic acid solution (30%,150 ml) into which sodium metabisulfite (0.5 g,)had been dissolved. The yellow filtrate was cooled and the precipitate collected and immediately dissolved in boiling petroleum ether (150 ml), the organic layer was decanted from the slight water layer, and allowed to cool, producing white needles of the crude product which was used without further purification in the synthesis of 2,2',6,6'-tetramethyl-4,4'-diaminobiphenyl. (6.9 g, 87%)



2,2',6,6'-Tetramethyl-4,4'-diaminobiphenyl (39)⁴

To a boiling solution of HCl (300 ml, 10%) through which N₂ was being bubbled, 3,3'-5,5'-tetramethyl hydrazobenzene (6.9 g, 28 mmol) was added with vigorous stirring. The solution was refluxed for 5hrs, after which heating was discontinued and the solution was allowed to cool overnight. After filtration to remove any azo derivatives the yellow solution was boiled with charcoal for 30mins then filtered again. The now colourless solution was treated with a 20% NaOH solution until cloudiness appeared, a saturated

sodium acetate solution (50 ml) was then added to complete the precipitation. The pinkish solid obtained was extracted with ether, producing a red solution which was dried over MgSO₄ the solvent was then removed and the residue extracted into hot benzene (20 ml), which was treated with hexanes (50 ml). On cooling buff coloured crystals of the product were obtained. (2.55 g, 39%)

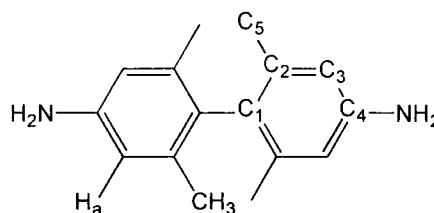
¹H NMR (CDCl₃) δ 6.48 (s, 4H, Ha), 3.48 (br, 4H, NH₂), 1.82 (s, 12H, CH₃)

¹³C NMR (CDCl₃) δ 138.54 (C4), 137.80 (C1),

136.48 (C2), 136.39 (C3), 19.53 (C5)

EI MS *m/z* 240[M]⁺, 225 [M-NH₂]⁺, 210 [M-2NH]⁺

m.p. 166-167° (lit. 167-168°)



2,2',6,6'-Tetramethyl-4,4'-diiodobiphenyl (53)^{2,3}

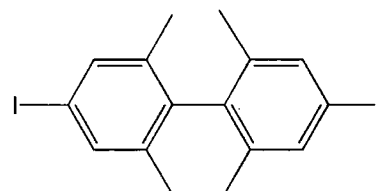
A solution of KI₃ was prepared by dissolving KI (27.5 g, 166 mmol) and I₂ (42 g, 166 mmol) in H₂O (275 ml) and stirring overnight. A stirred solution of 2,2',6,6'-tetramethyl-4,4'-diaminobiphenyl (39) (2.0 g, 8.3 mmol) in 10% H₂SO₄ was cooled to 10 °C. A NaNO₂ solution (1.26 g, 18.3 mmol in 12 ml H₂O) was added dropwise whilst maintaining a temperature of 8 °C. This solution was stirred for 30 minutes, after which it was then poured into the stirred solution of KI₃. The mixture was stirred for a further 30 minutes then heated to reflux until I₂ vapour was observed, the solution was then allowed to cool and sodium hydrogen sulfite was added with stirring until gas evolution ceased. The solution was filtered and the organics extracted into Et₂O (5 x 100ml). This solution was washed with a further portion of sodium hydrogen sulfite solution, dried (MgSO₄) and the solvent removed *in vacuo* to afford the crude product (2.93 g, 77%) which was sufficiently pure to be used in the subsequent reactions.

¹H NMR (CDCl₃) δ 7.48 (s, 4H, Ar), 1.83 (s, 12H, CH₃)

¹³C NMR (CDCl₃) δ 138.75, 138.01, 136.69, 136.60, 19.62

EI MS *m/z* 462 [M]⁺, 336 [M-I]⁺, 209 [M-2I]⁺

m.p. 194-196° (lit. 199-200°)



***N,N,N',N'*-tetra(phenyl)-(2,2',6,6'-tetramethyl)-(1,1'-biphenyl)-4,4'-diamine (30)**

A stirred solution of 2,2',6,6'-tetramethyl-4,4'-diiodobiphenyl (**53**) (2.0 g, 4.33 mmol), diphenylamine (1.61 g, 9.5 mmol), K₂CO₃ (5.52 g, 40.0 mmol), copper powder (0.6 g, 9.3 mmol) and 18-crown-6 (0.23 g, 0.86 mmol) in *ortho*-dichlorobenzene (10 ml) was heated at reflux for 19 hrs. The reaction mixture was filtered and the solvent volume reduced *in vacuo*. The crude mixture was treated MeOH and placed in the freezer, producing a pale precipitate, which was collected and recrystallised from benzene/hexanes, (1.64 g, 70%).

¹H NMR (CDCl₃) δ 7.26 (pseudo t, *J*_{HH} = 16 Hz, 8H, H_c), 7.12 (d, *J*_{HH} = 7 Hz, 8H, H_b), 7.00 (t, *J*_{HH} = 14 Hz, 4H, H_d),

6.86 (s, 4H, H_a), 1.86 (s, 12H, CH₃)

¹³C NMR (CDCl₃) δ 148.34 (C5), 146.24 (C4),

137.14 (C1), 135.07 (C2), 129.37 (C7),

124.19 (C6), 123.63 (C5), 122.48 (C5),

20.24 (C9)

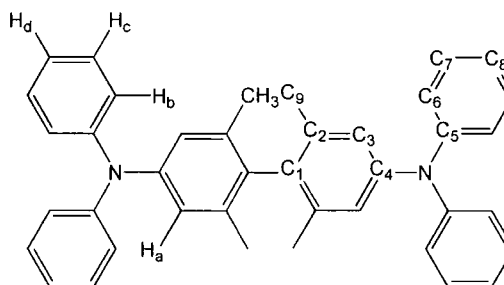
EI MS *m/z* 544 [M]⁺, 377 [M-NAr₂]⁺

Analysis C₄₀H₃₆N₂

Calculated. C%, 88.19; H%, 6.66; N% 5.14 and found: C% 87.80; H% 6.95; N% 5.05

***N,N,N',N'*-tetra(4-methylphenyl)-(2,2'-dimethyl)-(1,1'-biphenyl)-4,4'-diamine (31)**

A stirred solution of 2,2',6,6'-tetramethyl-4,4'-diiodobiphenyl (**53**) (2.0 g, 4.33 mmol), di(4-methyl)phenylamine (1.87 g, 9.52 mmol), K₂CO₃ (4.78 g, 34.63 mmol), copper powder (0.59 g, 9.3 mmol) and 18-crown-6 (0.27 g, 1.0 mmol) in *ortho*-dichlorobenzene (10 ml) was heated to reflux for 18 hrs. The reaction mixture was filtered and the solvent volume reduced *in vacuo*. The crude mixture was purified by column chromatography (silica, hexanes, CH₂Cl₂), (0.29 g, 11%).



$^1\text{H NMR}$ (CDCl_3) δ 6.99 (d, $J_{\text{AB}} = 8$ Hz, 8H, Hb), 6.93 (d, $J_{\text{AB}} = 8$ Hz, 8H, Hc), 6.73 (s, 4H, Ha), 2.25 (s, 12H, ArCH₃),

1.76 (s, 12H, biphenyl CH₃)

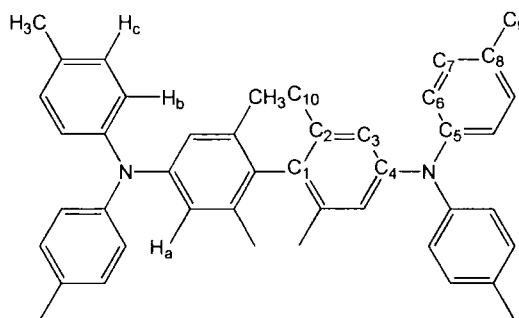
$^{13}\text{C NMR}$ (CDCl_3) δ 146.88 (C5), 146.10 (C4),

132.08 (C1), 130.89 (C2), 130.07 (C8),

128.06 (C3), 124.55 (C7), 122.56 (C6),

21.16 (C9), 20.34 (C10)

EI MS m/z 600[M]⁺, 405 [M-NAr₂]⁺



3,3'-dimethyl-4,4'-diiodobiphenyl (**54**)^{2, 3}

Potassium iodide (104.5 g, 0.63 mol) and iodine (104 g, 0.41 mol) were dissolved in water (375 ml) and stirred overnight to give an aqueous solution of KI₃. 3,3'-dimethylbenzidine (6.13 g, 0.029 mol) was dissolved in 10% sulphuric acid and cooled to 10°C. A solution of sodium nitrite (5.92 g, 0.086 mol in 60 ml H₂O) was added dropwise, maintaining a temperature between 6-8°C. This solution was then stirred for 30mins after which it was poured into the potassium tri-iodide solution. The reaction mixture was heated to reflux until evolution of iodine vapour was observed. The solution was cooled to room temperature and sodium bisulfite was added until gas ceased evolving. The organic layer was then extracted with benzene (3x200 ml), which was washed with sodium sulfite, dried and the solvent removed *in vacuo*, producing a pale yellow powder. Yield: 4.92g, 0.011mol, 40%

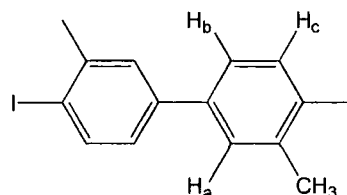
$^1\text{H NMR}$ (CDCl_3) δ 7.76 (d, $J_{\text{HH}} = 8$ Hz, 2H, Ha), 7.33 (d, $J_{\text{HH}} = 2$ Hz, 2H, Hb), 6.97 (dd, $J_{\text{HH}} = 11$ Hz, 2H, Hc), 2.41 (s, 6H, CH₃)

$^{13}\text{C NMR}$ (CDCl_3) δ 141.88, 140.33, 139.33,

128.21, 125.92, 100.21, 28.23

EI MS m/z 433[M]⁺, 306[M-I]⁺, 178[M-2I]⁺

m.p. 102-104°



***N,N,N',N'*-tetraphenyl-(3,3'-dimethyl)-(1,1'-biphenyl)-4,4'-diamine (32)**

3,3'-Dimethyl-4,4'-diiodobiphenyl (**54**) (1.0 g, 2.3 mmol), diphenylamine (0.92 g, 5.75 mmol) K₂CO₃ (2.54 g, 18.43 mmol), copper powder (0.31 g, 4.94 mmol), and 18-crown-6 (0.12 g, 0.46 mmol) were dissolved in *ortho*-dichlorobenzene (10 ml) and heated to reflux for 18 hours. The solution was filtered and the solvent removed *in vacuo*, the residue was dissolved in MeOH and placed in the freezer, producing a pale yellow precipitate. Purified by chromatography (silica, hexanes/CH₂Cl₂), (0.42 g, 36%).

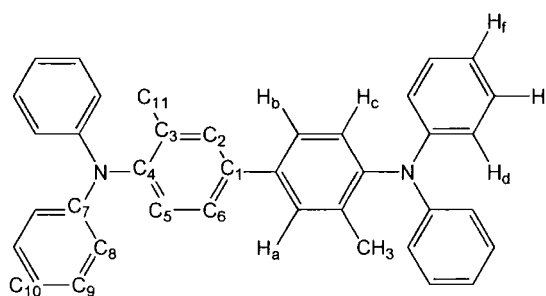
¹H NMR (CDCl₃) δ 7.52 (d, *J*_{HH} = 2 Hz, 2H, Ha), 7.47 (dd, *J*_{HH} = 8 Hz, 2H, Hb), 7.26 (pseudo t, *J*_{HH} = 8 Hz, 8H, He), 7.21 (d, *J*_{HH} = 8 Hz, 2H, Hc), 7.05 (d, *J*_{HH} = 8 Hz, 8H, Hd), 6.97 (t, *J*_{HH} = 14 Hz, 4H, Hf), 2.12 (s, 6H, CH₃)

¹³C NMR (CDCl₃) δ 147.48 (C7),

144.65 (C4), 138.03 (C1), 136.53 (C3),
130.21 (C2), 129.75 (C5), 129.07 (C9),
125.83 (C6), 121.69 (C8), 121.51 (C10),
18.83 (C11).

EI MS *m/z* 516 [M]⁺, 349 [M-NPh₂]⁺

m.p. 174-176°

***N,N,N',N'*-tetra(4-methylphenyl)-(3,3'-dimethyl)- 1,1'-biphenyl-4,4'-diamine (33)**

3,3'-Dimethyl-4,4'-diiodobiphenyl (**54**) (1.0 g, 2.3 mmol), di(4-methylphenyl)amine (1.0 g, 5.07 mmol), K₂CO₃ (2.54 g, 18.43 mmol), copper powder (0.31 g, 4.94 mmol), and 18-crown-6 (0.12 g, 0.46 mmol) were dissolved in *ortho*-dichlorobenzene and heated to reflux for 27 hours. The solution was filtered and the solvent removed *in vacuo*, the residue was recrystallised from MeOH in the freezer. The yellow precipitate was purified by flash chromatography (SiO₂, CH₂Cl₂/hexane 1:9), (0.43 g, 33%).

^1H NMR (CDCl_3) δ 7.38 (m, 2H, Ha), 7.19 (m, 4H, Hb/Hc), 6.88 (m, 16H, Hd/He), 2.22 (s, 12H, CH_3), 2.00 (s, 6H, CH_3)

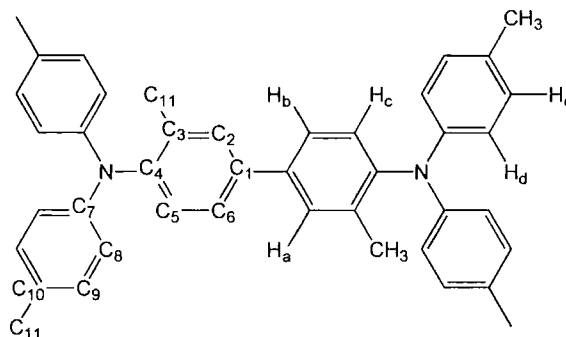
^{13}C NMR (CDCl_3) δ 145.35 (C7), 144.97 (C4), 137.61 (C1), 136.19 (C3), 130.72 (C2), 130.04 (C5), 129.59 (C9), 129.35 (C6), 125.62 (C8), 121.69 (C10), 20.68 (C11), 18.91 (C12).

EI MS m/z 572[M] $^+$, 480[M-Ar] $^+$, 377[M-NAr $_2$] $^+$

m.p. 170-172 $^\circ$

Analysis $\text{C}_{42}\text{H}_{40}\text{N}_2$

Calculated. C%, 88.07; H%, 7.03; N% 4.89 and found: C% 86.68; H% 7.42; N% 4.59



9,9-diethylfluorene (55)^{5, 6}

Fluorene (8.3 g, 0.05 mol) in thf (120 ml) at -78°C was treated dropwise with BuLi (65.6 ml of 1.6M soln. in hexanes, 0.10 mol). The mixture was stirred at -78°C for 45 mins, then bromoethane (10.9 g, 0.10 mol) was added dropwise. The solution was then allowed to warm to room temperature and stirred for a further 3 hrs. The now brown solution was poured into H_2O (300ml), and the organics extracted with Et_2O , washed with brine then dried (MgSO_4) and the solvents removed *in vacuo*, leaving an orange oil, which was used without further purification in the synthesis of 9,9-diethyl-2,7-diiodofluorene.(11.07 g, 99%)

^1H NMR (CDCl_3) δ 7.22 (m, 8H, Ar), 1.92 (q, $J_{\text{HH}} = 20\text{Hz}$, 4H, CH_2), 0.218 (t, $J_{\text{HH}} = 16\text{Hz}$, 6H, CH_3)

9,9-diethyl-2,7-diiodofluorene (56)⁷

To a stirred solution of 9,9-diethylfluorene (55) (5.5 g, 24.7 mmol) and finely divided I_2 (6.92 g, 27.3 mmol) in acetic acid (100 ml), a mixture of red fuming nitric acid (2 ml) and conc. sulfuric acid (10 ml) was added dropwise. The mixture was stirred for 30mins then poured into H_2O (700 ml), neutralised with a sodium hydrogen carbonate solution and the

organics extracted with Et₂O. The solution was washed with a sodium thiosulfate solution, dried (MgSO₄) and the solvents removed *in vacuo*, producing an off white solid of **56** which was used without further purification. (3.56 g, 30%)

¹H NMR (CDCl₃) δ 7.49 (m, 2H, Ar), 7.26 (m, 2H, Ar), 7.11 (s, 2H, Ar), 1.82 (q, *J*_{HH} = 20Hz, 4H, CH₂), 0.16 (t, *J*_{HH} = 16Hz, 6H, CH₃)

¹³C NMR (CDCl₃) δ 150.79, 140.35, 136.12, 132.45, 121.69, 93.04, 56.30, 32.72, 8.27

EI MS *m/z* 474 [M]⁺, 347 [M-I]⁺, 222 [M-2I]⁺

***N,N,N',N'*-tetraphenyl-9,9-diethyl-2,7-diaminofluorene (34)**

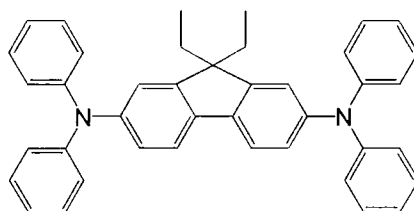
9,9-Diethyl-2,7-diiodofluorene (**56**) (1.5 g, 3.15 mmol), diphenylamine (1.17 g, 6.93 mmol), K₂CO₃ (3.48 g, 25.21 mmol), copper powder (0.43 g, 6.77 mmol), and 18-crown-6 (0.17 g, 0.63 mmol) were dissolved in *ortho*-dichlorobenzene and heated to reflux for 18hrs. The solution was filtered and the solvent removed *in vacuo*. Purified by chromatography (silica, hexanes/CH₂Cl₂) (0.531 g, 30%)

¹H NMR (CDCl₃) δ 7.0 (m, 26H), 1.72 (q, *J*_{HH} = 21Hz, 4H), 0.29 (t, *J*_{HH} = 14Hz, 6H)

¹³C NMR (CDCl₃) δ 151.28, 146.48, 144.32, 130.55, 129.86, 129.11, 127.72, 123.84, 122.33, 119.54, 56.25, 32.55, 8.56

EI MS *m/z* 556 [M]⁺, 404 [M-2Ph]⁺, 389[M-N Ph₂]⁺

m.p. 191-193°



***N,N,N',N'*-tetra(4-methylphenyl)-9,9-diethyl-2,7-diaminofluorene (35)**

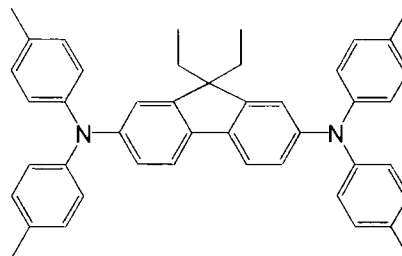
9,9-diethyl-2,7-diiodofluorene (**55**) (1.5 g, 3.15 mmol), di(4-methylphenyl)amine (1.37 g, 6.93 mmol), K₂CO₃ (3.48 g, 25.21 mmol), copper powder (0.43 g, 6.77 mmol), and 18-crown-6 (0.17 g, 0.63 mmol) were dissolved in *ortho*-dichlorobenzene and heated to reflux for 18hrs. The solution was filtered and the solvent removed *in vacuo*, the residue was recrystallised from MeOH in the freezer, producing a red powder.(0.87 g, 45%)

^1H NMR (CDCl_3) δ 7.0 (m, 22H), 2.2(s, 12H), 1.71 (q, $J_{\text{HH}} = 24\text{Hz}$, 4H), 0.29 (t, $J_{\text{HH}} = 15\text{Hz}$, 6H)

^{13}C NMR (CDCl_3) δ 151.28, 145.72, 142.58, 132.80, 130.56, 130.02, 127.97, 124.56, 121.69, 56.43, 32.81, 21.04, 18.31, 8.83,

EI MS m/z 612 $[\text{M}]^+$, 417 $[\text{M}-\text{NAr}_2]^+$

m.p. 187-189°



4,4'-dicarbazole-1,1'-biphenyl (36)

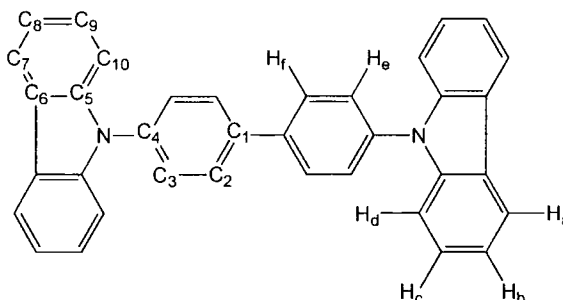
Carbazole (0.90 g, 5.42 mmol), diiodobiphenyl (1.0 g, 2.46 mmol), K_2CO_3 (2.72 g, 19.7 mmol), copper powder (0.43 g, 6.77 mmol), and 18-crown-6 (0.13 g, 0.49 mmol) were dissolved in *ortho*-dichlorobenzene and heated to reflux for 19.5hrs. The solution was filtered and the solvent removed *in vacuo*, the residue was recrystallised from MeOH in the freezer, producing a white powder. (0.94 g, 79%)

^1H NMR (CDCl_3) δ 8.18 (d, $J_{\text{HH}} = 8\text{ Hz}$, 4H, H_a), 7.93 (d, $J_{\text{HH}} = 8\text{ Hz}$, 4H, H_c), 7.73 (d, $J_{\text{HH}} = 8\text{ Hz}$, 4H, H_f), 7.53 (d, $J_{\text{HH}} = 8\text{ Hz}$, 4H, H_d), 7.47 (pseudo t, $J_{\text{HH}} = 15\text{ Hz}$, 4H, H_c), 7.33 (t, $J_{\text{HH}} = 15\text{ Hz}$, 4H, H_b)

^{13}C NMR (CDCl_3) δ 140.82 (C5), 139.30 (C4), 137.25 (C1), 128.52 (C2), 127.49 (C3), 126.02 (C10), 123.50 (C6), 120.38 (C7), 120.08 (C8), 109.83 (C10).

EI MS m/z 484 $[\text{M}]^+$

m.p. 270-272°



Trimeric Triarylamine Synthesis

Bis(4-bromophenyl)phenylamine (60)

The bis(4-bromophenyl)phenylamine was prepared by a modified Ullmann condensation using 1,10 phenanthroline and CuCl.⁸⁻¹⁰ A 500ml flanged flask fitted with overhead stirrer, thermometer, nitrogen inlet and condenser topped with a non-return gas outlet was charged with the aniline (18.62 g, 0.2 mol), 4-bromiodobenzene (141.5 g, 0.5 mol), 1,10-phenanthroline (7.20 g, 0.04 mol) and *ortho*-xylene (80 ml). The flask was heated with stirring to 100°C and then the KOH (79.6 g, 1.42 mol), and CuCl (4.03 g, 0.03 mol) added. The temperature was then increased to ensure reflux. The reaction was monitored through the use of HPLC and after 2.5 hrs the heating was discontinued and the solution allowed to cool. The resulting mixture was poured into water (500 ml) and toluene (400 ml), neutralised with acetic acid (400 ml) and filtered. The organic layer was extracted and the solvent removed *in vacuo*. The brown residue was purified by flash chromatography from silica eluting with hexane. The fractions were identified by means of HPLC and those containing product recrystallised from MeOH until a white crystalline solid was obtained. (13.92 g, 17.3%, 95% pure by HPLC)

¹H NMR (CDCl₃) δ 7.34 (d, *J*_{HH} = 9 Hz, 4H, Hd/He),

7.26 (pseudo t, *J*_{HH} = 16 Hz, 2H, Hb), 7.06 (m, 3H, Hc/Ha),

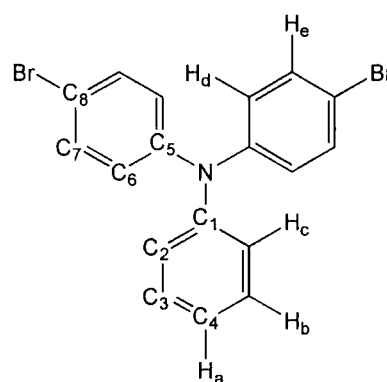
6.93 (d, *J*_{HH} = 9Hz, 4H, Hd/He).

¹³C NMR (CDCl₃) δ 146.48 (C5), 132.35 (C1),

132.15 (C8), 124.94, 129.42, 125.50,

125.41, 124.16

m.p. 70-73°

**4-bromophenyl bis(4-methylphenyl)amine (61)**

Ditolylamine (29.58 g, 0.15 mol), 4-bromo-iodobenzene (63.65 g, 0.225 mol) and 1,10 phenanthroline (5.40 g, 0.03 mol) were dissolved in *ortho*-xylene (60 ml) and heated under nitrogen to 100°C at which point the potassium hydroxide (59.46 g, 1.06 mol), and copper chloride (2.17 g, 0.022 mol) were added and the heating continued until reflux

was evident. The reaction was monitored by HPLC and after 3hrs the reaction observed to be complete. The reaction mixture was poured into water (350 ml) and toluene (350 ml), the solution was then neutralised with acetic acid (40 ml) and filtered. The organic layer was extracted, dried and the solvents removed *in vacuo* and the residue purified by flash chromatography (SiO₂, Hexane). The product was precipitated from MeOH. (30.81 g, 60%, 96% pure by HPLC)

¹H NMR (CDCl₃) δ 7.20 (d, *J*_{HH} = 8 Hz, 2H, Ha/Hb),

7.00 (d, *J*_{HH} = 9 Hz, 4H, Hc/Hd),

6.90 (d, *J*_{HH} = 9 Hz, 4H, Hc/Hd),

6.82 (d, *J*_{HH} = 9 Hz, 2H, Ha/Hb),

2.24 (s, 6H, CH₃)

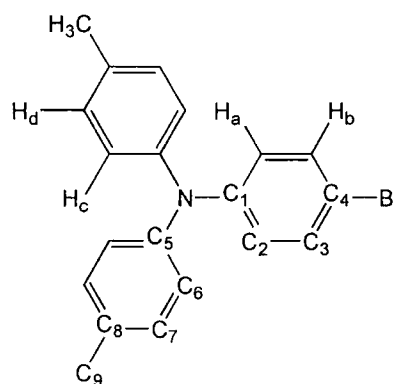
¹³C NMR (CDCl₃) δ 147.44 (C1),

144.95 (C5), 132.94 (C8), 131.93,

130.01, 124.94, 124.94, 124.69,

124.37, 123.92, 113.62, 20.85 (C9)

m.p. 98-100°



4-boronic acid bis(4-methylphenyl)phenylamine (62)

To a flame dried 250ml flask fitted with magnetic stirrer, nitrogen inlet, thermometer and bubbler, 4-bromophenyl bis(4-methylphenyl)amine (**61**) (10.0 g, 0.028 mol) and tetrahydrofuran (150 ml) were added, and cooled to -78°C. Butyllithium (1.6M in hexane 12.2 ml, 0.028 mol) was added dropwise over a period of 25 minutes. The solution was stirred for 30 minutes at -78°C, then trimethylborate (6.45 ml, 0.057mol) was added dropwise over 20 minutes.¹¹ After a further hour stirring at -78°C, the solution was allowed to warm to room temperature and stirred overnight, after which time the solution had gained a yellow colouration. The solution was then poured into tetrahydrofuran (150 ml), acidified with HCl (2M, 600 ml) and stirred for 1.5hrs. The organic layer was then extracted with diethyl ether (3x300 ml), and the extracts washed with saturated brine (300 ml) then dried and the solvent removed *in vacuo*. The solid was washed with hot hexane, leaving 4-boronic acid bis(4-methylphenyl)phenylamine as a pale grey powder which

was dried in the oven overnight. The product was identified by comparison of HPLC retention time with an authentic sample. (5.92 g, 67%,)

***N,N*-bis[4'-(bis {4-methylphenyl}amine)-1,1'-biphenyl-4] *N*-phenylamine (63)**

A 250ml flask equipped with nitrogen inlet, mechanical stirrer and condenser topped with bubbler were charged with 4-boronic acid bis(4-methylphenyl)phenylamine (**62**) (4.0 g, 12.6 mmol), bis(4-bromophenyl)phenylamine (**60**) (2.3 g, 5.7 mmol), tetrakis (triphenylphosphine) palladium (0.20 g, 0.171 mmol) and sodium carbonate (12.93 g, 122 mmol) were dissolved in toluene (125 ml) and water (40 ml). The reaction mixture was heated at reflux overnight with vigorous stirring in order to mix the two phases. After 18 $\frac{1}{4}$ hrs at reflux heating was discontinued and the solution allowed to cool. The organic layer was separated, washed with water (2x100 ml), dried and the solvent removed *in vacuo* then the residue purified by flash chromatography on silica, gradient elution, from hexane to 20% CH₂Cl₂ /80% hexane, producing *N,N*-Bis[4'-(bis {4-methylphenyl}amine)-1,1'-biphenyl-4] *N*-phenylamine as a white powder. (0.85 g, 19%, 96% by HPLC)

¹H NMR (CDCl₃) δ 7.38-6.94 (several m, 37H, aromatic H), 2.25 (s, 12H CH₃)

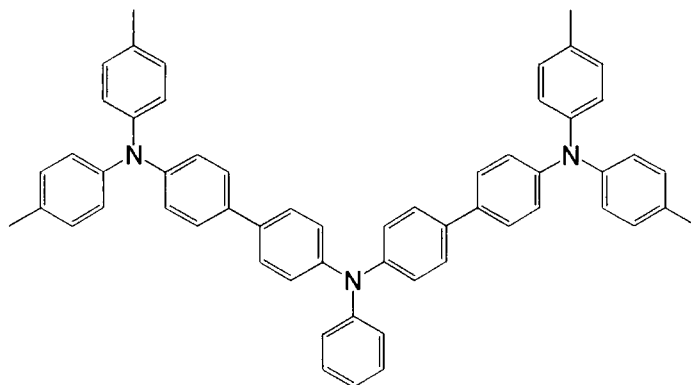
¹³C NMR (CDCl₃): δ 147.86, 147.41, 146.67, 145.51, 135.25, 134.22, 133.97, 132.72, 130.12, 129.51, 127.48, 127.38, 124.82, 124.56, 124.48, 123.07, 21.16

EI MS *m/z* 787 [M]⁺, 696 [M-Ar]⁺, 592 [M-NAr₂]

m.p. 148-150°

Analysis C₅₈H₄₉N₃

Calculated. C%, 88.40; H%, 6.26; N% 5.33 and found: C% 88.13; H% 6.27; N% 5.19



References for Chapter 8

- 1 S. Gauthier and J. M. J. Fréchet, *Synthesis*, 1987, 383.
- 2 S. F. Nelsen, R. F. Ismagilov, K. E. Gentile, and D. R. Powell, *J. Am. Chem. Soc.*, 1999, **121**, 7108.
- 3 A. Helms, D. Heiler, and G. McLendon, *J. Am. Chem. Soc.*, 1992, **114**, 6227.
- 4 R. B. Carlin, *J. Am. Chem. Soc.*, 1945, **67**, 928.
- 5 M. Ranger, D. Rondeau, and M. Leclerc, *Macromol.*, 1997, **30**, 7686.
- 6 B. Tsuie, J. L. Reddinger, G. A. Sotzing, J. Soloducho, A. R. Katritzky, and J. R. Reynolds, *J. Mater. Chem.*, 1999, **9**, 2189.
- 7 R. C. Bansal, E. J. Eisenbraun, and R. J. Ryba, *Oppi Briefs*, 1987, **19**, 258.
- 8 H. B. Goodbrand and N.-X. Hu, *J. Org. Chem.*, 1999, **64**, 670.
- 9 H. B. Goodbrand, in 'United States Patent 5,648,539', 1996.
- 10 H. B. Goodbrand, in 'United States Patent 5,654,482', 1997.
- 11 M. Nicolas, B. Fabre, J. M. Chapuzet, J. Lessard, and J. Simonet, *J. Electroanal. Chem.*, 2000, **482**, 211.

Conclusions

The work contained in this thesis describes the synthesis and structural characterisation of a library of model hole transport materials, and has demonstrated that conformation, as well as inductive effects, can be used to manipulate:

- the oxidation potential of the materials
- the thermodynamic stability of the oxidation products derived from these compounds
- the electronic structure of the oxidation products as evidenced by the shifts in shape and energy of the UV-Vis-NIR absorption bands and DFT calculations.

This thesis also presents an insight into conformational factors which relate to the reorganisation energy associated with the oxidation of polyaryl amine dimers and oligomers through both experimental structure, and computational studies. Similar factors may contribute to the barriers to hole transport in the bulk material.

A study of trimeric and oligomeric materials revealed unexpected and previously unreported reactivity for the higher oxidation states of materials with an odd number of nitrogen centres. Synthesis and study of a number of derivatives revealed the reactive sites of these materials to be confined to the *para* position of the peripheral aryl rings.

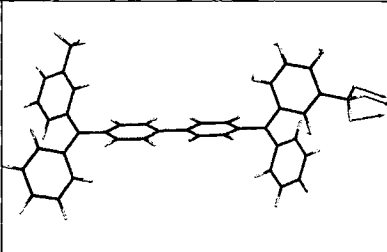
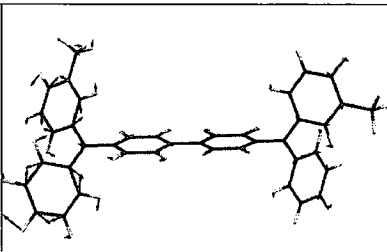
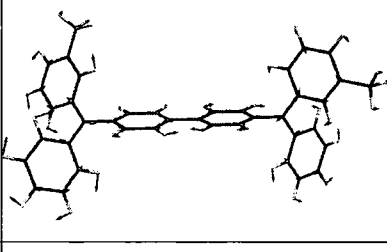
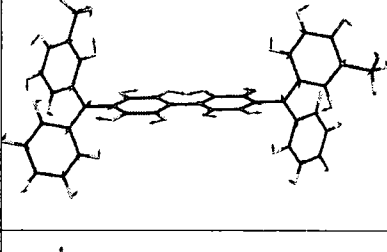
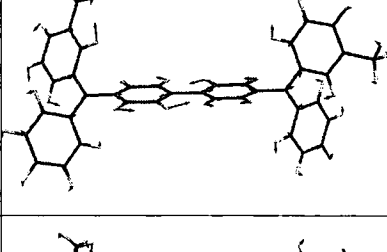
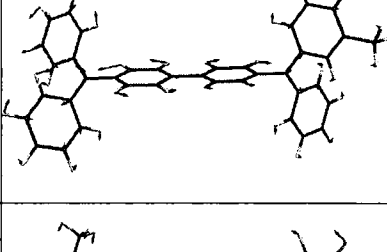
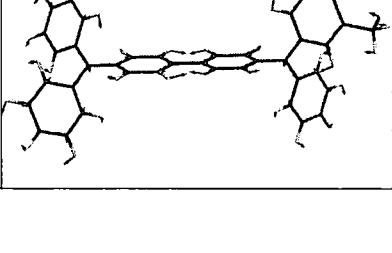
The reactivity of compounds with an odd number of nitrogen centres, and dimeric systems where the nitrogen centres are effectively localised, was exploited, and a novel electrochemical polymerisation of TPD type monomers was developed.

Appendix A Experimental and Computational Raman Data

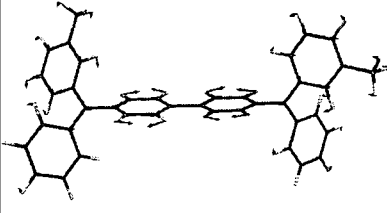
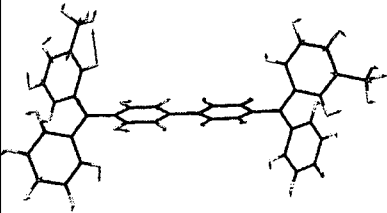
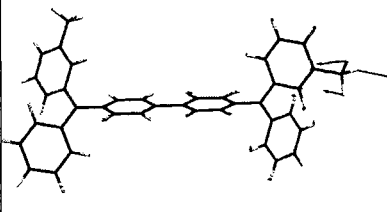
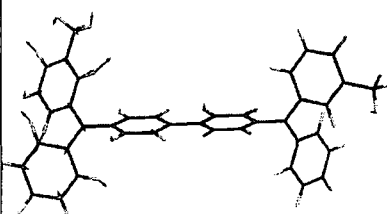
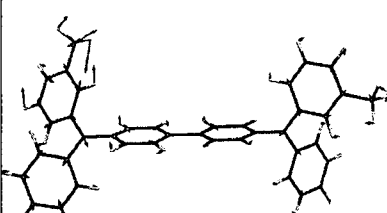
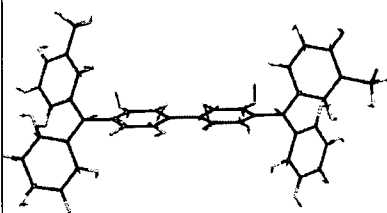
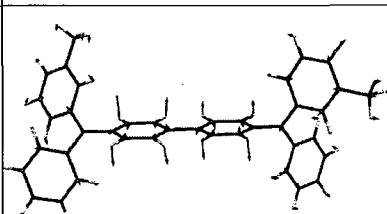
DFT calculation of **26** (neutral) (RBPW91/6-31G (d))Experimental results of **26** (neutral) with excitation at 514.5, 632.8, 785 nm

Calculated vibrations / cm^{-1}	Experimental vibrations / cm^{-1}	Assignment	Visualisation of vibration
1619 (s)	1614 - 1610	Quadrant stretch of biphenyl and all phenyl rings coupled with C-N stretches and methyl C-C stretches	
1608 (s)	1606 (s) 1606 (s) 1604 (s)	Quadrant stretch of biphenyl and all phenyl rings coupled with C-N stretches and methyl C-C stretches	
1592 (sh, m)	- - -	LHS of molecule quadrant stretch of phenyl rings coupled with C-N stretches. Small biphenyl stretch with associated C-N stretches. No movement on RHS phenyl rings.	
1523 (m)	1524 (w) 1520 (w) 1522 (w)	Large biphenyl stretch with associated C-C and C-N stretches. Very little stretch from phenyl rings at ends of molecule	
1495 (w)	1488 (w) 1483 (w) 1483 (w)	Large C-N stretches on LHS of molecule with associated phenyl C-C stretches and methyl C-C stretch. Small biphenyl stretch with C-C phenyl stretches. Small C-N and associated C-C stretches on RHS of molecule	

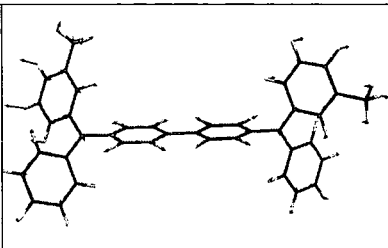
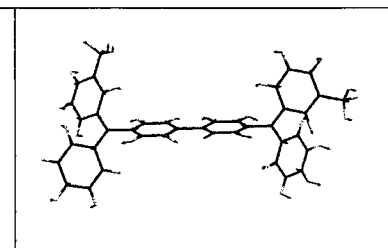
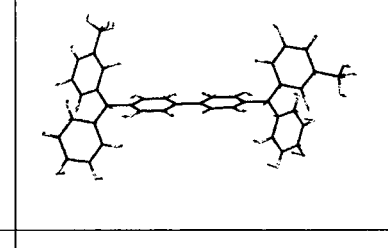
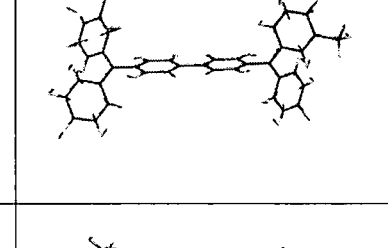
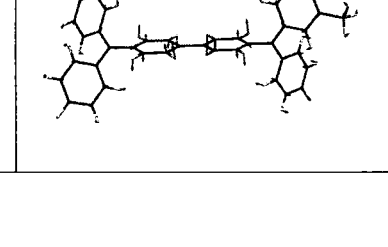
Appendix A: Experimental and Computational Raman Data

1396 (w)	- - -	Large methyl C-C stretch on RHS of molecule with C-H wagging. No other movement	
1362 (w)	1371 (w) 1364 (w) 1372 (w)	Large C-C stretches from LHS phenyl rings with associated C-N stretches. Small biphenyl stretch with C-C phenyl stretches. Small C-N and associated C-C stretches on RHS of molecule	
1325 (w)	1322 (sh, w) - 1323 (sh, w)	Whole molecule C-N and C-C stretches on biphenyl and phenyl rings. Larger movement on end phenyl rings	
1314 (w)	1315 (sh, w) 1312 (sh, w) 1315 (sh, w)	Whole molecule C-N and C-C stretches on biphenyl and phenyl rings. Larger movement on middle biphenyl rings	
1291 (s)	1294 (s) 1292 (s) 1292 (s)	Whole molecule C-N and C-C stretches on biphenyl and phenyl rings. Larger movement on middle biphenyl rings	
1282 (sh, s)	- - 1269 (sh,w)	Whole molecule C-N and C-C stretches on biphenyl and phenyl rings.	
1219 (w)	- - 1191 (sh, w)	Quadrant stretch of biphenyl rings with associated C-N stretches. C-N stretches from outer phenyl rings with associated C-C stretches.	

Appendix A: Experimental and Computational Raman Data

1190 (s)	1182 (s) 1181 (s) 1181 (s)	Quadrant stretch of biphenyl rings with associated C-N stretches. C-N stretches from outer phenyl rings with small associated C-C stretches.	
1157 (m)	1150 (sh, w) 1150 (sh, w) 1151 (sh, w)	C-C and C-H wagging with associated C-N stretches across whole molecule	
1039 (w)	1022 (w) 1022 (w) 1026 (w)	Large methyl C-C stretch on RHS of molecule with C-H wagging. No other movement	
986 (m)	1004 (w) 998 (m) 999 (m)	Large C-C stretches on LHS phenyl rings with some C-H wagging and associated C-N stretches. Very little movement from rest of molecule	
961 (w)	- 947 946	C-C stretches and C-H wagging from LHS phenyl rings with C-N stretches and large methyl C-C stretch. Smaller C-C stretches from biphenyl rings and RHS phenyl rings with some C-H wagging and C-N stretches.	
916 (w)	922 (w) 919 (w) 922 (w)	C-H wagging from inner biphenyl rings and outer phenyl rings with associated C-C and C-N stretches.	
809 (w)	827 (m) 821 (m) 823 (m)	Large C-H wagging from biphenyl rings with associated C-C and C-N stretches. Small C-H wagging from outer phenyl rings with associated C-C and C-N stretches	

Appendix A: Experimental and Computational Raman Data

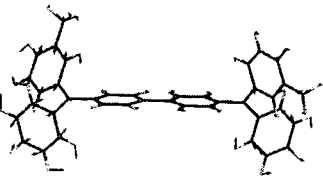
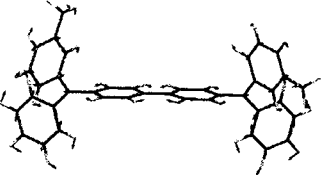
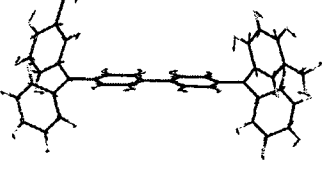
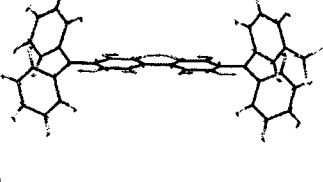
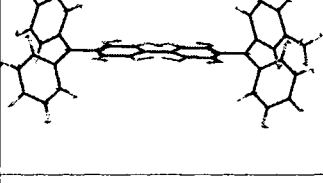
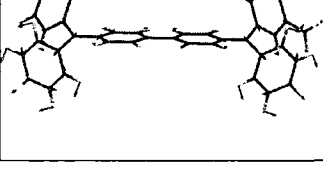
767 (sh, w)	772 (w) 766 (w) 768 (m)	Small C-C and C-H wagging with associated C-N stretches across whole molecule	
754 (w)	753 (sh, w) 746 (sh, w) 750 (m)	C-C and C-H wagging with associated C-N stretches across whole molecule	
733 (w)	721 (w) 718 (w) 721 (w)	C-C and C-H wagging with associated C-N stretches across whole molecule	
664 (w)	- - 632 (w)	Biphenyl C-C stretch with associated C-C phenyl stretches in middle rings and C-N stretches. C-N and C-C stretches from outer phenyl rings with some C-H wagging	
410 (m)	413 (w) 408 (w) 409 (m)	Large C-H wagging and C-C stretches on biphenyl rings with associated C-N stretches. Smaller C-H wagging and C-C stretches on end phenyl rings	

s = strong m = medium w = weak sh = shoulder

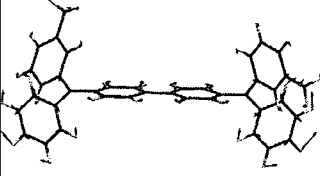
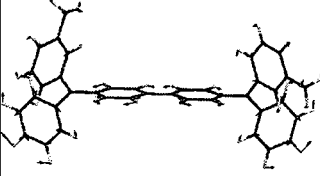
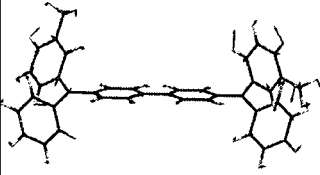
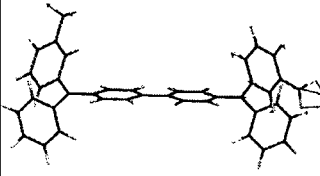
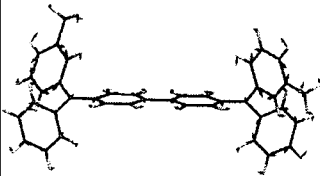
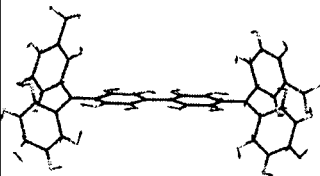
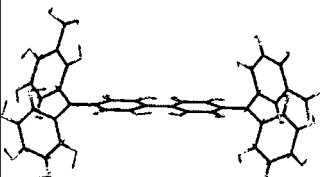
Appendix A: Experimental and Computational Raman Data

DFT calculation of **26** cation (UBPW91/6-31G (d))

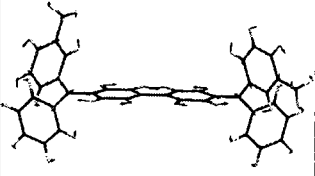
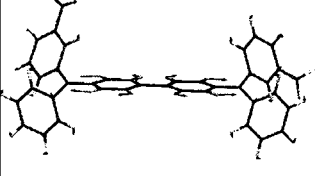
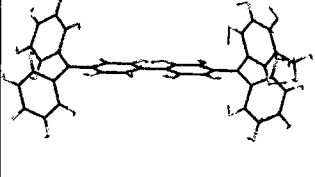
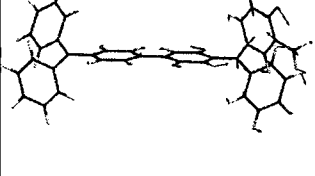
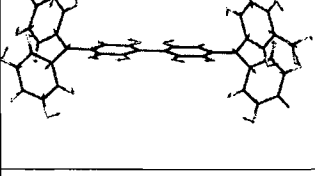
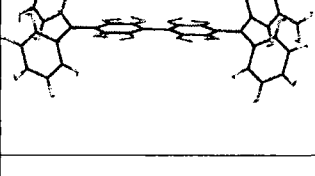
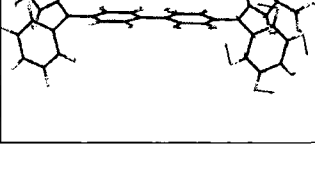
Experimental results of **26** cation with excitation at 514.5, 632.8, 785 nm

Calculated vibrations / cm^{-1}	Experimental vibrations / cm^{-1}	Assignment	Visualisation of vibration
1597 (sh, m)	- - -	Quadrant stretch of biphenyl and all phenyl rings coupled with C-N stretches and methyl C-C stretches and biphenyl rings	
1589 (s)	1599 (s) 1594 (s) 1596 (m)	Large biphenyl stretch with associated C-C and C-N stretches. Smaller stretches from phenyl rings at ends of molecule	
1577 (s)	1580 (s) 1576 (s) 1578 (s)	Quadrant stretch of biphenyl rings with associated C-N stretches. C-C stretches from phenyl rings with associated C-N stretches	
1541 (w)	- - -	Large C-C stretches on biphenyl rings with associated biphenyl stretch and C-N stretches. Small C-N and C-C stretches on outer phenyl rings	
1517 (m)	1527 (m) 1525 (s) -	Large biphenyl stretch with associated C-C and C-N stretches from inner phenyl rings. Small C-N and C-C stretches on outer phenyl rings	
1487 (m)	1495 (sh, w) 1491 (w) 1490 (w)	Large C-N stretch from unsub. outer phenyl ring with associated C-C stretches. Small C-C stretches from sub. outer phenyl ring and biphenyl rings	

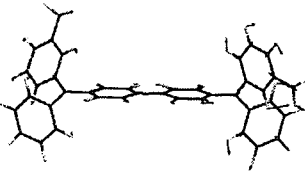
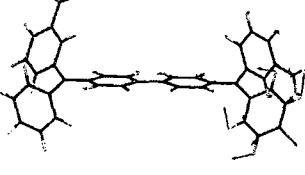
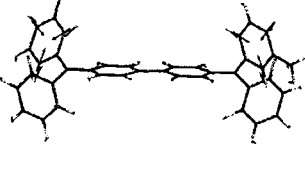
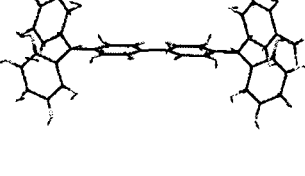
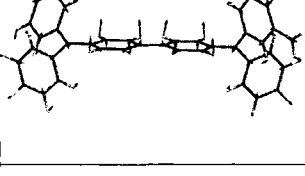
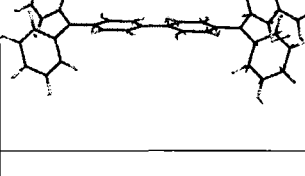
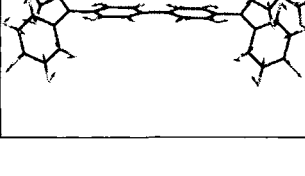
Appendix A: Experimental and Computational Raman Data

1462 (m)	- - -	Whole molecule C-N and C-C stretches on biphenyl and phenyl rings	
1454 (sh, w)	- - -	Whole molecule C-N and C-C stretches on biphenyl and phenyl rings	
1429 (m)	- - -	Large C-C stretches on sub. phenyl rings with associated C-N stretches. Smaller C-C and C-N stretches from unsub phenyl rings and biphenyl	
1400 (w)	- - -	Large methyl C-C stretch on RHS of molecule with associated small C-C and C-N stretches	
1363 (w)	- - -	Large asymmetric C-C stretches from sub. phenyl and biphenyl rings coupled with C-N stretches. Smaller C-C stretches from unsub. phenyl rings with C-N stretches	
1337 (sh, w)	1354 (sh, m) 1351 (sh, w) 1365 (s)	Large C-C stretches on unsub. phenyl rings and biphenyl with C-N stretches. Smaller C-C stretches from sub. phenyl rings with C-N stretches	
1325 (s)	1328 (s) 1324 (s) 1326 (s)	Whole molecule C-N and C-C stretches on biphenyl and phenyl rings	

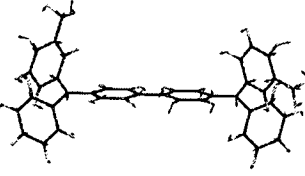
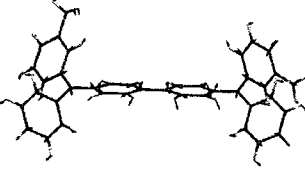
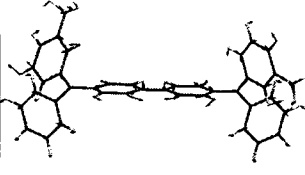
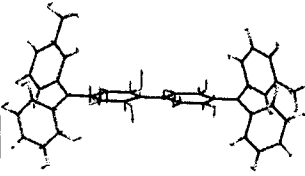
Appendix A: Experimental and Computational Raman Data

1313 (m)	- - -	Whole molecule C-N and C-C stretches on biphenyl and phenyl rings. Larger movement on middle biphenyl rings	
1304 (sh, s)	- - -	Large biphenyl stretch with associated C-C stretches from inner phenyl rings and C-N stretches. Small C-C and C-N stretches from outer phenyl rings	
1294 (s)	1293 (sh, m) - -	Large C-N stretches on RHS of molecule with associated C-C stretches from RHS phenyl rings. Small C-N and C-C stretches from LHS rings	
1259 (s)	- - -	Large C-N stretches from RHS outer phenyl rings with C-C stretches. Smaller C-N stretches on RHS inner phenyl ring with small associated c-C stretches	
1217 (s)	1215 (s) 1214 (s) 1216 (s)	Quadrant stretch of biphenyl rings with associated C-N stretches. C-N stretches from outer phenyl rings with associated C-C stretches and large methyl C-C stretches	
1194 (s)	1184 (s) 1184 (s) -	Quadrant stretch of biphenyl rings with associated C-N stretches. C-N stretches from outer phenyl rings with small associated C-C stretches.	
1178 (m)	- - -	Large quadrant stretches from phenyl rings on RHS of molecule with C-N stretches	

Appendix A: Experimental and Computational Raman Data

1154 (w)	- - -	C-C and C-H wagging on RHS of molecule with associated C-N stretches	
1030 (w)	- - -	Large C-C stretches on unsub. phenyl ring on RHS with some C-N stretch. Small C-C and C-N stretches from other two phenyl rings on RHS	
986 (m)	1001 (w) 993 (m) -	Large C-C stretches from sub. phenyl rings on each end of molecule coupled with C-N stretches. Small C-N and C-C stretches from other phenyl rings	
918 (w)	926 (m) 923 (s) -	C-H wagging from inner biphenyl rings and outer phenyl rings with associated C-C and C-N stretches.	
822 (w)	816 (w) 815 (w) -	Large C-H wagging from biphenyl rings with associated C-C and C-N stretches. Small C-H wagging from outer phenyl rings with associated C-C and C-N stretches	
685 (w)	- - -	Large C-H wagging and C-C stretches from RHS sub. phenyl ring with associated C-N stretch. Small C-N stretches from other two phenyl rings on RHS with C-C stretches and C-H wagging	
662 (w)	- - -	Biphenyl C-C stretch with associated C-C phenyl stretches in middle rings and C-N stretches. C-N and C-C stretches from outer phenyl rings with some C-H wagging	

Appendix A: Experimental and Computational Raman Data

562 (w)	- 558 562	C-H wagging and C-C stretches across whole molecule with associated C-N stretches	
530 (w)	- - -	C-H wagging and C-C stretches across whole molecule with associated C-N stretches	
424 (w)	- - -	C-H wagging and C-C stretches with C-N stretches across whole molecule	
400 (m)	413 398 405	Large C-H wagging and C-C stretches on biphenyl rings with associated C-N stretches. Smaller C-H wagging and C-C stretches on end phenyl rings	

s = strong m = medium w = weak sh = shoulder

First Year Introduction Courses: October 2000

The courses consist of one hour lectures on the services available in the department.

1. Department Safety
2. Safety Matters
3. Electrical appliances and Infrared Spectroscopy
4. Chromatography and Microanalysis
5. Atomic Absorption and Inorganic Analysis
6. Library Facilities
7. Mass Spectroscopy
8. Nuclear Magnetic Resonance
9. Glass Blowing Techniques
10. Introduction to Computing Facilities

Examined Lecture Courses: October 2000 to April 2001

Three courses were attended consisting of one hour lectures followed by a written examination in each.

1. Electroanalytical Techniques, Dr. R. Katakya
2. Lasers in Chemistry, Dr. A. Beeby
3. NMR Techniques, Dr. A. Kenwright

**Research Colloquia, Seminars and Lectures Organised by the
Department of Chemistry**

Only lectures attended by the author during the period October 2000 - September 2003 are shown

2000

- October 25 Dr S.F. Campbell, Former Senior Vice President of Pfizer
Science, art and drug discovery. A personal perspective
- November 7 Dr C. Ludman, Durham University
Explosions - A demonstration lecture
- November 8 J.P.L. Cox, Bath University
Cosmic: a universal, DNA-based language for communicating with aliens and other intelligent lifeforms
- November 22 Dr Wayne Hayes, University of Reading
Synthesis of Novel Dendrimers and Hyperbranched Polymers
- November 28 Professor C. Steward, Heriot-Watt University
Commercial and technological developments in the international brewing industry
- December 6 Professor Richard Compton University of Oxford
Dual activation approaches to electroanalysis: ultrasound, microwaves and laser activation

2001

- January 10 Professor S. P. Armes
School of Chemistry, Physics and Environmental Science, University of Sussex
Micelles, reversed micelles and shell-crosslinked micelles based on tertiary amine methacrylates
- January 24 Dr Andrew deMello, Department of Chemistry, Imperial College, London
Chemical Integrated Circuits: organic synthesis and analysis on a small scale

Appendix B – Courses, Lectures, Colloquia and Conferences Attended

- May 2 Dr. AWG Platt, University of Staffordshire
Transition Metal Complexes of Alkylsulfonated phosphines and their Antitumor Properties
- October 9 Dr Roy S Lehrle, Birmingham
Forensics, Fakes and Failures
- October 31 Dr Colin Raston, School of Chemistry, Univ of Leeds
Towards benign supramolecular chemistry: synthesis - self organisation
- November 6 Dr Cliff Ludman, Durham University
Explosions - a demonstration lecture
- November 14 Professor John Goodby, Department of Chemistry, University of Hull
Supramolecular liquid crystals - multipodes and dendrimers
- November 20 Professor Peter Atkins
A Century of Physical Chemistry
- 2002
- February 26 Dr Mike Griffin, Forensic Science Service, Metropolitan Police
Smack, Crack, Speed and Weed: A forensic chemists tale
- 2003
- February 12 Professor Paul Raithby, Department of Chemistry, University of Bath
Adventures in Organometallic Polymer Chemistry
- February 25 Professor Brian Tighe, Aston Biomaterials (supported by the North East
Polymer Association)
Blood Sweat and Tears: Problems in the design of Biomaterials
- March 5 Professor Neil Connelly, School of Chemistry, University of Bristol
Redox-active Metal Alkyne and Related Complexes: Structure, Bonding and
Reactivity

Conferences and Symposia attended

Posters[†] and ‡Oral presentations

30th May-4th June 2002 Fifth International Symposium on Functional π -Systems,
University of Ulm/Neu-Ulm, Germany[†]

13th –18th July 2002 Metal Containing Molecules, 2nd Chianti Electrochemistry
Meeting, Siena, Italy[†]

9th-10th September 2002 Universities of Scotland Inorganic Conference, Edinburgh
University, Scotland‡

7th-12th November 2002 Research Councils' Graduate Schools Programme, Derby

10th January 2003 Avecia/Departmental Poster Competition[†]

19th February 2003 New Strategies in Metal Chemistry: Organometallics, Clusters,
Nanoparticles and Catalysis, Dalton Division, Symposia,
University of Nottingham

8th-9th May 2003 Avecia Case symposium, Grassmere, Lake District‡

25th June 2003 Department Post Graduate Symposia‡

1st-2nd September 2003 Universities of Scotland Inorganic Conference, University of
Strathclyde, Scotland^{††}

